

Sensorless Quasi-static Piezoelectric Actuator for Micro-Robotics

Présentée le 4 septembre 2020

à la Faculté des sciences et techniques de l'ingénieur
Laboratoire d'actionneurs intégrés
Programme doctoral en robotique, contrôle et systèmes intelligents

pour l'obtention du grade de Docteur ès Sciences

par

Louis Antoine MASSON

Acceptée sur proposition du jury

Prof. J.-P. R. Kneib, président du jury
Prof. Y. Perriard, directeur de thèse
Prof. B. Lemaire-Semail, rapporteuse
Prof. C. Espanet, rapporteur
Prof. P. Muralt, rapporteur

I don't know where I'm going from here, but I promise it won't be boring.

— David Robert Jones

Remerciements

Bien que je puisse être fier du travail de thèse que j'ai effectué, ce serait une exagération de prétendre d'en être l'unique responsable. Je tiens à exprimer dans ces quelques lignes ma sincère reconnaissance à toutes les personnes qui ont rendu ce travail possible.

En premier lieu, je remercie le Prof. Yves Perriard du fond du coeur pour avoir cru en moi et pour m'avoir fourni le cadre et les ressources nécessaires à la poursuite d'une thèse. D'autre part, je suis également reconnaissant pour le soutien académique et l'apport d'un esprit scientifique qui m'ont été consacrés par le Dr. Yoan Civet. Cette reconnaissance s'étend également à Paolo Germano pour son intuition d'ingénieur et son soutien technique. Je tiens à remercier de surcroît la superbe équipe des collègues du LAI et du CAM pour la bonne ambiance et le soutien mutuel au travers de toutes ces années. Et tout particulièrement, merci à mon très cher ami, le Dr. Florian Copt, sans qui je n'aurais jamais été au courant de cette opportunité de thèse, et avec qui j'ai pu collaborer sur quelques belles réalisations techniques.

J'ai eu la chance de défendre ma thèse face à un jury d'exception qui a su suivre et critiquer tout l'acheminement de mon approche scientifique, et qui a su me poser les judicieuses questions qui ont permis de perfectionner mon travail de recherche. Merci donc au président du jury, Prof. Jean-Paul Kneib, et aux rapporteurs qui ont assisté à ma défense, Prof. Betty Lemaire-Semal, Prof. Christophe Espanet, et Prof. Paul Muralt.

L'axe appliqué et l'orientation ingénierie de cette thèse a été rendue possible grâce à un projet Innosuisse (anciennement CTI) qui lui a fourni un contexte industriel et stimulant. À cette fin, je souhaite exprimer ma gratitude envers Imina Technologies SA, et tout particulièrement au Dr. Benoît Dagon et à Guillaume Boetsch.

Sur une note plus personnelle, je n'en serais pas là aujourd'hui sans l'amour inconditionnel et le soutien inébranlable de mes parents, Jacques Masson et Tanja Masson-Zwaan, mes frères Nicolas et Laurent, ma soeur Émilie, et toute ma famille étendue. J'espère particulièrement avoir pu rendre fier mon grand-père, Dr. Ton Zwaan, qui n'est plus des nôtres et qui a su instiller en moi dès un jeune âge l'ambition d'aller aussi loin que possible dans mon éducation. Enfin merci à toi Amandine, mon amour, d'avoir accepté de me suivre dans cette aventure, et d'avoir su m'épauler à travers les moments les plus difficiles comme les plus heureux.

Neuchâtel, le 8 juillet 2020

Louis Antoine Masson

Abstract

Research interest into the miniaturisation of micro-robots has soared in recent years due to the availability of suitable integrated actuators. The reduction in size of these components is achieved through the implementation of Self-Sensing Actuation (SSA). This approach foregoes the need for external sensors which increase the encumbrance of micro-robots. The SSA approach is all the more relevant with piezoelectric actuators due to the reversible properties of piezoelectricity. The present thesis endeavours to explore the topic of piezoelectric SSA by applying a focus on the fundamental theory supporting the approach. It would then be possible to determine how a piezoelectric actuator could be tailored for SSA, particularly at the quasi-static ranges of frequencies that characterise robotic manipulation tasks.

A general model describing the piezoelectric actuator as a system with electro-mechanical inputs and outputs has been formulated: the inputs are the force and the voltage, resulting in a displacement and accumulated electrical charge as outputs. It is shown that all piezoelectric actuators follow this model form, which can be summarised through the description of three parameters: the stiffness, the capacitance, and a coefficient named β . The latter describes the electro-mechanical coupling between charge accumulation and force, and is the most critical characteristic when aiming for high precision SSA. It is then demonstrated through dynamic modelling of piezoelectric actuators using bond graph models that the performance of the position and force sensorless estimation is intimately tied to these three actuator characteristics. Since these are a function of the actuator's design parameters, the self-sensing performance may be drastically improved at the design level.

By deriving design guidelines from an actuator design study based on an analytical model, a SSA demonstration prototype is developed. A batch of piezoelectric benders are manufactured with sub-mN sensorless estimation accuracies in mind. A test environment supporting these actuators is designed with the specific goals of determining their parameters experimentally, and of providing the grounds for the testing of diverse SSA implementations. After a measurement campaign providing a statistical appreciation for the parameters of the actuator batch, a calibrated self-sensing implementation approach is discussed. With this approach, it is shown that force estimation accuracies of 0.25 mN for durations of up to 60 s are within the grasp of these actuators tailored to SSA. Longer durations that guarantee high estimation accuracies would be acquired by focusing more research effort into the delicate task of measuring minute electrical charges.

Abstract

In light of some inconsistencies between model predictions and experimental data, an updated model is proposed: the error of the β coefficient and the stiffness are reduced to 3% and 12% respectively. From this model describing parameters with non-monotonic characteristics, a multi-objective optimisation study is proposed to simultaneously optimise an actuator design for high sensitivity and low estimation error. The resulting piezoelectric actuator design provides a β coefficient of -4.62 nC/mN , corresponding to a sensitivity increase of 52% compared the previously fabricated actuator, and a sensitivity increase by a factor of $\times 9.5$ compared to a commercial actuator of similar morphology.

Keywords:

Self-sensing actuation, sensorless, piezoelectric actuator, micro-robotics, quasi-static.

Résumé

La miniaturisation des micro-robots a suscité un intérêt grandissant dû à la disponibilité d'actionneurs intégrés. La diminution en taille de ces composants est principalement propulsée par le développement d'Actionnement Auto-Sensible (AAS). Cette approche a franchi l'actionneur de la nécessité de capteurs externes, dont l'encombrement va à l'encontre de la miniaturisation. L'AAS est d'autant plus pertinente quand il s'agit de l'implémenter avec des actionneurs piézoélectriques, dû à la réversibilité de leurs propriétés. La thèse ci-présentée a pour vocation d'explorer le sujet de l'AAS en s'appuyant sur la théorie fondamentale régissant cette méthode. Il devient possible de déterminer comment la conception d'un actionneur piézoélectrique peut être adaptée à des applications AAS, en particulier à des gammes de fréquences quasi-statiques qui caractérisent les manipulations micro-robotiques.

Une forme générale de modèle décrivant les entrées et sorties électro-mécaniques de l'actionneur piézoélectrique est définie : la force et la tension sont des entrées, et il en résulte une déformation et une accumulation de charges en sortie. Il est montré que toute morphologie d'actionneur suit ce modèle général. Ce dernier est décrit par trois paramètres : la raideur, la capacité, et un coefficient β . Ce dernier décrit le couplage électro-mécanique entre l'accumulation de charges et la force, et il constitue la caractéristique la plus critique pour implémenter un AAS de haute précision. Il est alors démontré au travers d'une modélisation par graphes de liaison que la performance de l'estimation de position et de force est intimement liée à ces trois paramètres. Ceux-ci étant liés à leur tour à la morphologie de l'actionneur, il en vient que la performance AAS peut être conséquemment améliorée au stade de la conception d'actionneur.

En utilisant des critères de conception déduites d'une étude d'un modèle analytique, un prototype de démonstration visant des précisions \leq mN est mis en place. Un environnement de test est conçu pour développer des stratégies d'AAS. Une campagne de mesure est menée afin de fournir une vue statistique des paramètres du lot d'actionneurs. Dès lors, une implémentation AAS utilisant d'une méthode de calibration pour la mesure de charges est présentée. Il est ainsi montré que l'estimation de la force résultant de la méthode calibrée présente une précision de 0.25 mN pour des durées d'expérience jusqu'à 60 s. Il convient de préciser qu'une telle précision peut être garantie pour des durées plus longues à condition de consacrer plus d'effort dans la recherche de mesures de charges de faible ordre de grandeur.

Résumé

Suite à l'observation d'écarts entre prédictions théoriques et mesures, un modèle révisé permet de réduire les écarts pour le coefficient β et la raideur à 3% et 12% respectivement. Les fonctions du modèle décrivant les paramètres ne présentant pas de caractéristique monotone, une opportunité d'étude d'optimisation a été saisie. Cela permet de proposer une conception d'actionneurs maximisant la sensibilité décrite par β tout en minimisant l'erreur résultant de la mesure de charges. La conception d'un actionneur piézoélectrique optimisé résultant de cette étude révèle un coefficient β de l'ordre de -4.62 nC/mN , soit un accroissement de 52% par rapport aux actionneurs précédemment fabriqués. Par rapport à un actionneur commercial étudié précédemment, cela correspond de plus à un accroissement d'un facteur $\times 9$.

Mots-clés :

Actionnement Auto-Sensible, sans capteur, actionneur piézoélectrique, micro-robotique, quasi-statique.

Contents

Remerciements	i
Abstract (English/Français)	iii
List of Figures	xi
List of Tables	xv
Introduction	1
1 An introductory look into piezoelectric self-sensing actuation	9
1.1 Introduction	9
1.2 Voltage measurement bridge	10
1.2.1 Operating principle	10
1.2.2 Improvements for quasi-static operation	13
1.3 Charge and current measurement	17
1.3.1 Operating principle	17
1.3.2 Measurement strategies	19
1.3.3 Improvements for quasi-static operation	23
1.4 Impedance related and hybrid approaches	27
1.4.1 Impedance measurement	28
1.4.2 Hybrid observers	30
1.5 Overview and conclusions	31
2 Framework for the development of sensorless piezoelectric actuators	35
2.1 Introduction	35
2.2 General model for charge-based self-sensing	36
2.2.1 Definition of the general model	36
2.2.2 Experimental characterisation of a piezoelectric actuator	38
2.3 Dynamic modelling of a piezoelectric self-sensing system	41
2.3.1 Piezoelectric actuator modelling	41
2.3.2 Mechanical interface modelling	45
2.3.3 Charge amplifier modelling	47
2.3.4 Complete bond graph model	48
2.4 Evaluation of piezoelectric self-sensing capabilities	50

2.4.1	Case study: Approach and manipulation of a high mass sample	50
2.4.2	Discussion on the tradeoff of actuator design and self-sensing performance	58
2.5	Conclusion	60
3	Novel approach to high resolution self-sensing actuator design	63
3.1	Introduction	63
3.2	Defining a scope for self-sensing piezoelectric actuation	64
3.2.1	Mechanical tests	65
3.2.2	Electrical tests	67
3.2.3	Discussion of the results	68
3.3	Analytical modelling of a piezoelectric cantilever	69
3.3.1	Modelling approach	70
3.3.2	Determination of the deformation strains	73
3.3.3	Constitutive equations of the piezoelectric actuator	76
3.4	Self-sensing actuator design	79
3.4.1	Design considerations and objectives	79
3.4.2	Analysis of the objective function	81
3.4.3	Design guidelines for piezoelectric self-sensing benders	85
3.5	Conclusion	86
4	Prototype fabrication and self-sensing performance assessment	87
4.1	Introduction	87
4.2	Prototype design and assembly	88
4.2.1	Fabrication of an actuator batch	88
4.2.2	Self-sensing test environment	90
4.3	Identification of the actuation and self-sensing parameters	92
4.3.1	Capacitance measurement	93
4.3.2	Step response	93
4.3.3	Free stroke	95
4.3.4	Flexure testing	96
4.3.5	Results overview	98
4.4	Self-sensing actuation	100
4.4.1	Calibrated approach	101
4.4.2	Discussion on the resulting SSA performance	103
4.5	Conclusion	105
5	Definite improvement of self-sensing performance through optimisation	107
5.1	Introduction	107
5.2	Reconsidering the design assumptions on actuator topology	108
5.2.1	Description of the topology and associated design parameters	108
5.2.2	Influence of the electrodes and isolation layers	109
5.2.3	Updating the model for the monomorph bender	111
5.2.4	Experimental validation of the complete model	114

5.3	Multi-objective optimisation study based on the complete model	115
5.3.1	Optimisation problem definition	115
5.3.2	Multi-Objective Optimisation	119
5.3.3	Closing remarks of the optimisation study	125
5.4	Conclusion	129
Conclusion and perspectives		131
A	Equations of piezoelectricity	137
A.1	History of piezoelectric discovery	137
A.2	Equations	138
A.3	Deriving a model	140
B	Introduction to bond graph modelling	143
B.1	Power conjugated variables	144
B.2	Power bonds	146
B.3	Concept of computational causality	146
B.4	Bond graph elements	147
B.4.1	Elements and their constitutive equations	147
B.4.2	Summary	152
C	Charge measurement techniques for high impedance devices	155
C.1	Parasitic effects inherent to the supporting electronics	155
C.2	Parasitic effects inherent to the piezoelectric actuator	157
C.3	Parasitic effects caused by environmental contributions	157
Bibliography		161
Nomenclature		167
Curriculum Vitae		171

List of Figures

1	Examples of micro-robotic applications	2
2	Examples of commercial prober solutions	3
3	Examples of integrated micro-robots	4
4	Photos of the miBot, source: Imina Technologies S.A.	5
1.1	Electrically equivalent model of a piezoelectric actuator.	10
1.2	Self-sensing actuator circuit for rate of strain and strain sensing.	11
1.3	Proposals for updated bridges to extend the self-sensing bandwidth.	14
1.4	Robust self-sensing actuator bridge for strain sensing.	16
1.5	Operating principle of charge or current based SSA for the estimation of the mechanical state of the actuator.	18
1.6	Rate of strain sensing hardware using current measurement.	19
1.7	Sensorless position estimation system through charge measurement SSA. . . .	20
1.8	Charge amplification circuit for sensorless position estimation.	21
1.9	Updated system for dynamic displacement estimation.	25
1.10	Dynamic component of the displacement estimator.	25
1.11	Complete system for dynamic displacement and force estimation.	27
1.12	Self-sensing approach for strain sensing with permittivity measurement. . . .	29
1.13	Schematic of the measurement setup for the hybrid observer.	31
1.14	Best results in terms of maximum relative error in the state of the art.	33
2.1	System representation of the actuator and the self-sensing estimator.	36
2.2	Structure of the test bench used to characterise the CMBP03 actuator.	39
2.3	Results of the CMBP03 characterisation.	40
2.4	Graphical representation of the full system considered for bond graph modelling.	41
2.5	Graphical representation of the multiport C node for the piezoelectric actuator.	42
2.6	Equivalent models expanding the multiport C node of the piezoelectric actuator.	44
2.7	Overview schematic of the mechanical interface.	45
2.8	Piecewise characteristics of the mechanical interface.	46
2.9	Bond graph model of the mechanical interface.	46
2.10	Schematic and bond graph representations of the charge amplifier.	47
2.11	Considered piezoelectric drive and charge measurement circuit.	48
2.12	Complete bond graph model of the self-sensing system with feedback loop. . .	49
2.13	Simplified bond graph of the piezoelectric actuator in contact with a sample. .	52

List of Figures

2.14	Considered actuators for the case study.	53
2.15	Manipulation simulation with the Noliac CMBP03 and custom actuators. . . .	54
2.16	Bond graph of the charge amplification with added parasitic effects.	56
2.17	Simulated force and displacement estimations for the case study.	58
3.1	SEM images of the micro-pillars.	64
3.2	Cross-sectional schematic of a micro-pillar.	64
3.3	Micro-pillars deformed in compression and in flexure.	66
3.4	Mechanical tests on multiple micro-pillars.	66
3.5	Plastic deformation of the titanium probe tip.	67
3.6	I-V curves for the micro-pillars after successive loadings and successive sweeps.	68
3.7	Schematic of the piezoelectric monomorph bender.	70
3.8	Representation of the strains in the piezoelectric bender, due to the piezoelectric effect and to the mechanical bending.	70
3.9	Modelling methodology for the piezoelectric monomorph bender.	72
3.10	Representation of the intersection between the objective function for different values of n with the solution plane satisfying the constraint.	83
3.11	Partial derivatives of f with respect to L and w	84
4.1	Structure and topology of the fabricated actuator.	88
4.2	Structure of the self-sensing prototype.	90
4.3	Overview of the mechanical structure.	91
4.4	Sub-systems of the self-sensing prototype.	91
4.5	Photo and schematic of the fabricated actuator	92
4.6	Displacement measurements for the step response experiment	94
4.7	Qualitative observation of the creep on the expected displacement.	95
4.8	Displacement measurements for the free stroke experiment.	96
4.9	Force, charge, and displacement measurement results for the flexure experiment.	97
4.10	Comparison between the characterisation results and the model predictions. .	99
4.11	Calibration of the self-sensing approach.	102
4.12	Photos of the force sensor positioned close to the bender's tip.	103
4.13	Self-sensing force estimation result for three separate approach runs.	104
5.1	Considered monomorph topology in the case where $N = 2$; electrodes in black, piezoelectric layers of the upper and lower areas in grey, and isolation layers in red.	109
5.2	Effect of the decrease in h and N parameters on the η_e and η_i thickness ratios.	110
5.3	Representation of the frame of reference and of the strains in sections of the actuator stack: piezoelectric strain in red and mechanical strain in blue.	112
5.4	Graphical representation of the ϵ_f and f_β objective functions for a $N = 1$ and layer thickness h ; w_{\max} (Purple), w_{\min} (Red).	122

5.5	Illustration of the four cases considered by the algorithm for $h = 50 \mu\text{m}$, with the valid design space for (L, w) drawn in green, the solution chosen by the algorithm circled in black, and the solution that is considered the worst as a red dot.	124
5.6	Pseudocode of the (L, w) solution correction algorithm.	124
5.7	Evolution of the objective functions f_β and ϵ_f , design parameters L and w , and constraint functions F and C_p , and after the application of the correction algorithm.	126
5.8	Evolution of f_β and ϵ_f as a function of N ; the optimal solution for each objective function is circled in black, and the points making up each Pareto front in emboldened.	127
5.9	Representation of all solution ranges for different values of N , with the leftmost extremity of each range corresponding to the solution chosen by the optimisation algorithm; the Pareto efficient points of the Pareto frontiers for each h are circled in black.	128
A.1	Integration surface used in the application of Gauss' law.	140
B.1	Tetrahedron of state [33], and relationship between its variables.	145
B.2	Graphical representation of a power bond.	146
B.3	Graphical representation of activated bonds (i.e. signals).	146
B.4	Standard graphical representation for the causality of a power bond.	147
B.5	Bond graph node for a 0-junction with 4 ports.	148
B.6	Bond graph node for a 1-junction with 4 ports.	148
B.7	Expected causality for 0-junctions and 1-junctions.	149
B.8	Bond graph nodes for 2-port C elements.	149
B.9	Bond graph nodes for 2-port I elements.	150
B.10	Bond graph nodes for R elements.	150
B.11	Bond graph nodes for ideal energy sources and sinks.	151
B.12	Bond graph nodes for transformers (TF).	151
B.13	Bond graph nodes for gyrators (GY).	152
B.14	Examples of modulated elements: modulated (a) transformer, (b) gyrator. . . .	152
C.1	Charge components and parasitic charges.	156
C.2	Effect of the airflow on the charge measurement.	158
C.3	Photos of the enclosure surrounding the prototype.	159
C.4	Schematic of the double shielding for the electronics.	159

List of Tables

1.1	Sensorless displacement and force estimation accuracies of strategies observed throughout the state of the art.	33
2.1	Model predictions, measured values, and relative error for the parameters of the constitutive equations of the CMBP03 multi-layer bender.	40
2.2	Intermediate power conjugated variables within the piezoelectric actuator. . .	44
2.3	Actuator parameters for the CMBP03 and the NAC2011-H11.	53
2.4	Simulation parameters of the case study.	57
3.1	Physical parameters of the actuator design.	80
3.2	Evolution of the partial derivative of f with respect to w	84
4.1	Final actuator specifications.	89
4.2	Inspection of the fabrication results.	89
4.3	Results of the capacitance measurements.	93
4.4	Extrapolated parameters of the fitted curves for the unit response experiment. .	95
4.5	Extrapolated β slopes and maximum displacements δ_{\max} for the free stroke experiment.	96
4.6	Extrapolated β and K slopes for the flexure experiment.	97
4.7	Results overview of the actuator characterisation experiments.	98
4.8	Comparison between <i>model 1</i> , <i>model 2</i> , and the measurement results.	99
5.1	Reminder of the experimental results presented in Chapter 4.	115
5.2	Actuator morphology parameters.	118
5.3	Summary of the optimal solutions for each possible value of h	129
A.1	Constitutive equation parameters for three elementary deformations.	141
B.1	Power conjugated variables pertaining to multiple physics domains.	145
B.2	Summary of the bond graph elements and their constitutive equations.	153

Introduction

Background and motivation

Since the advent of micro-scale electronics and mechanical systems, most notably in the field of silicon semiconductor technology, the discipline of micro-robotics has gained traction. Not only is it a relevant research topic garnering a large number of scientific disciplines, but it also attracts interest for its potential, present and future, industrial applications. As for all devices, systems developed at the nm–mm scale need to be tested, characterised, manipulated, inspected, or sometimes assembled. Micro-robots are thus needed to complete these tasks, and are required to cover minuscule displacements and provide careful manipulation forces.

When approaching a research topic, it is convenient to properly define it as well as the scope that it encompasses. To do so, it is proposed to consider the definition of micro-robots brought forward by H. Bleuler in [3], where he can be quoted as such:

Micro-robots are either machines of small proportions (from a few cm^2 to a few μm^2), and / or are machines that have been designed to interact with small sized objects (from a few mm to a few μm).

According to this definition, micro-robots are related to the micro-scale world either through their own volume, or through the dimensions of the object they are designed to interact with. The present manuscript will mainly concern itself with the latter definition, even though it is not mutually exclusive with the former. Similarly, nano-robotics may be defined in the same manner as micro-robotics when downsizing the scale of the scope provided in the definition by three orders of magnitude.

The main challenge in the way of a micro-robot's use resides in the newfound relevance of phenomena that could be considered as negligible at the macro-scale: van der Waals forces, static electricity, surface tension, thermal conditions, and airflow. Even though tasks at the mm scale are perfectly handled by most modern industrial robots, the aforementioned physical effects cause the performance of a robot to become seemingly unpredictable when delving into smaller scales. To counter these effects that have a negative effect on a micro-robot's ability to fulfil its tasks, a closed control loop must be implemented.

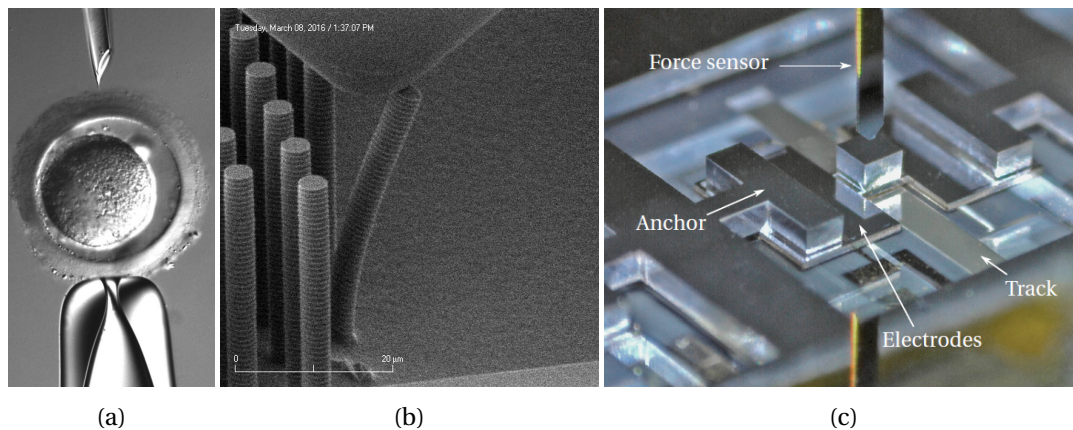


Figure 1 – Examples of micro-robotic applications; (a) Cytoplasmic injection, source: Leica Microsystems, (b) Mechanical testing of semiconductor micro-pillars, (c) Characterisation of a MEMS relay for the reconfiguration of synchronous motors [8].

The applications of micro-robots in the industry are numerous and multi-disciplinary, being used in materials science, mechanical, electrical, biological, and optical applications. With some examples taken from the state of the art as illustrated in Fig. 1, a non-exhaustive list of tasks performed by these devices follows:

- Micro-electronics characterisation (e.g. nanotransistors)
- Nanostructure characterisation (e.g. nanowire, nanotubes)
- Microelectromechanical Systems (MEMS) characterisation
- Small object inspection under a Scanning Electron Microscope (SEM)
- Micro-assembly and manipulation of small devices
- Optic fiber positioning
- Cytoplasmic injection

The number of use cases for micro-robotics is ever expanding due to the improvements made in terms of accuracy, automation, and miniaturisation, as well as the growing demands of the research community and industries for devices capable of interacting with the micro-scale. A brief overview of the categories of micro-robots that complete these tasks is necessary to define the scope of research of this thesis.

Micro-robotic solutions

Following the previous definition of micro-robots [3], there are two categories of micro-robots interacting with micro-scale objects that may be identified: stations, and integrated robots.

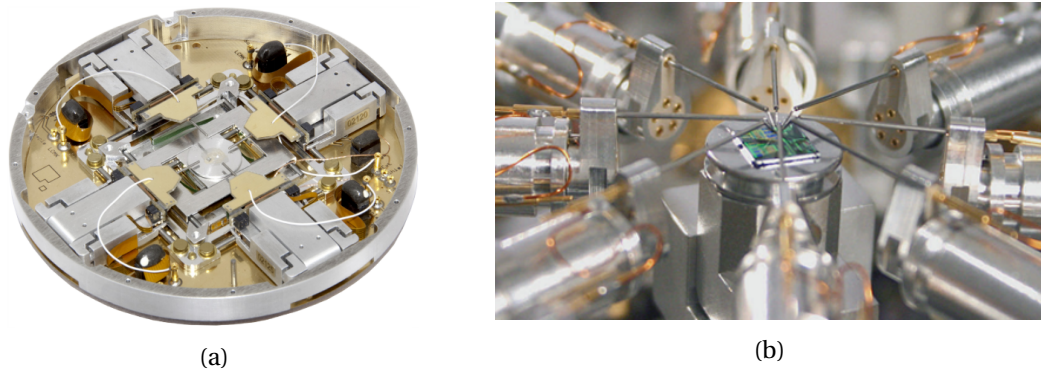


Figure 2 – Examples of commercial prober solutions;
(a) Kleindiek nanotechnik Prober Shuttle (PS4), (b) Zyvex nProber.

Stations are devices of large volume, potentially up to several m^3 in bulk (Fig. 2). As per their name, they are generally stationary in that they are of fixed configuration. They provide a controlled environment in which their actuators may operate with precision, and feature an ensemble of calibrated sensors that allow for closed-loop control. The sensing schemes that are used in stations may either be proprioceptive, or exteroceptive, providing a wide array of sensing possibilities for the system. They are therefore optimised machines designed for specific tasks (e.g. 4-point probe electrical characterisation of micro-electronics on wafers), and are cutting edge in terms of performance. In their fixed configuration, they are however limited in the applications that they can tackle, as the possibility of swapping tools is usually limited to the device constructor's design. Their use at a lower scale than high volume industrial applications is also compounded by the large costs of such complete systems. The first micro-robots that have been used in the industry are related to this type of configuration, as small displacements may be more easily achieved in controlled environments.

In opposition to probing stations, the latest advancements in micro-robots have paved the way towards the development of integrated solutions that are capable of working in constrained volumes. They feature a single end effector, as opposed to the multitude of end effectors that are simultaneously controlled by most probing stations, and they do not come in their own controlled working environment. The sensors that are provided are proprioceptive rather than exteroceptive, providing readings that are internal to the system (e.g. motor speed, joint angles, etc.). Such examples of these robots may be seen in Fig. 3 with the Delta-Cube [18], or the Sugar-Cube Delta robots (CSEM), where the widely used delta-robot kinematic chain is adapted to micro-robotics in low volume robots: the Delta-Cube has an edge of 11 cm, and the Sugar-Delta pushes it even further with an edge of 20 mm. The use of flexible joints becomes the norm at this scale to provide elements of the kinematic chain, as miniaturisation of typical components (e.g. joints, ball bearings) is impossible past a certain point.

The strengths of miniaturised micro-robotics lie in their flexibility and thus adaptability to different applications. Such micro-robots have been deployed in various environments, which

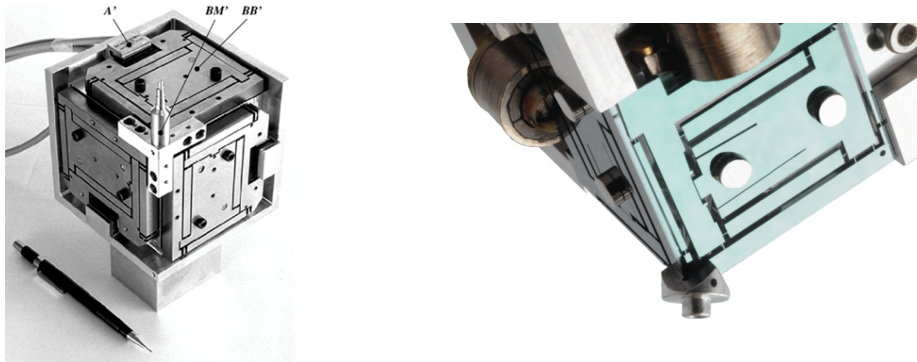


Figure 3 – Examples of integrated micro-robots; (left) Delta-cube micro-robot with 11 cm edges [18], (right) Sugar-cube delta robot with 20 mm edges (CSEM).

are constrained in terms of working volume or working conditions, such as vacuum chambers, Scanning Electron Microscope (SEM), [5] [59] [34], or Magnetic Resonance Imaging (MRI) scanners [44]. Their reduced costs of acquisition, maintenance, and repair make them attractive for academic purposes as much as for large scale industrial applications.

Limitations to micro-robotic miniaturisation

Following the preceding introduction, the drawback of integrated micro-robots that stands out the most is the difficulty of reconciling increased miniaturisation with high accuracy and performance. Sensors are necessary to ensure that the mechanical state (i.e. position, velocity, force) of an actuator matches the target state. This is because of the unpredictability brought about by the fact that sub- μm manipulations answer to rules of physics that are not present at the macro-scale. These phenomena may not always be accurately modelled for compensation in feedforward control approaches, therefore sensors providing direct information on an actuator's state are necessary to overcome them. The miniaturisation of a system entails reducing its encumbrance volume while preserving its performance and accuracy as much as possible. This includes reducing the encumbrance of the sensors that are necessary to preserve the accuracy of the system, inexorably leading to the aforementioned drawback of integrated robots over their stationary counterparts.

Some micro-robots have been implemented without proprioceptive sensors, such as the miBot my Imina Technologies SA featuring 4 degrees of freedom controlled by stick-slip piezoelectric actuators. These robots are manipulated by human operators with ease using a visual feedback, and some amount of automation may be brought to them by using said visual feedback in combination with image processing to determine the displacement of the actuator. Despite these approaches to control, the lack of proper sensors limit the automation capabilities of these micro-robots, therefore holding these devices back when it comes to large scale integration within the industry.



Figure 4 – Photos of the miBot, source: Imina Technologies S.A.

Overcoming the limitations through collocated control

To counteract this limitation, the notion of collocated control has been brought forward. Such a control scheme requires the use of *sensorless* or *self-sensing* actuators, foregoing the need for external sensors. In the present manuscript, the principle of Self-Sensing Actuation (SSA) is defined as the capability of deriving the current state of an actuator as it is being driven without the use of external sensors. The state of the actuator can be defined in accordance to the target application, but it typically includes the position of the actuator, its velocity, and its applied force. The exploration of self-sensing actuation has sprung from the fruits of a collaboration between the Integrated Actuators Lab (EPFL-LAI) and an industrial partner, Imina Technologies S.A., through CTI project # 18318.1 P FIW-IW. The purpose of this collaboration aimed to investigate on how to bring sensorless capabilities to the miBot (Fig. 4), a promising micro-robotic solution proposed by the industrial partner.

Achieving self-sensing with a transducer requires to exploit its multi-physics characteristics. Most actuators are driven by an electrical or thermal signal to produce a mechanical deformation, and byproduct signals originating from the actuator in either physics domains may be measured by the control system of the actuator. Knowledge of the transducer's properties may then allow to derive its current state from the measurement of these signals. In the case of byproduct electrical signals (e.g. currents, voltages), they may be measured directly from the drive electronics of the actuator, hence the lack of need for external sensors. Self-sensing has been successfully implemented with different types of actuators: Omar Scaglione has demonstrated this approach with synchronous motors [55], while Markus Flückiger has done so for piezoelectric ultrasonic motors [14], and finally Daniel Grivon has demonstrated the sensing possibilities that lie within magneto-rheological valves [16].

Among the multitude of actuators that are used in micro-robotics, piezoelectric transducers are particularly suited to this approach, owing to the reversibility of their properties. Additionally, piezoelectric actuation offers numerous advantages to micro-robotic manipulation:

- **Resolution of motion:** the minute displacements (1 nm — 100 μm) that can be achieved under high applied voltages (10 V — 100 V) allow for piezoelectric actuators to achieve high precision motion. The resulting sensitivity of the actuator's output with respect

to the control signal is ideal for the fine motions that are required for micro-robotic applications, e.g. manipulation of μm -sized objects.

- **Miniaturization potential:** piezoelectric actuators impose less encumbrance compared to other means of actuation due to the strains achieved with small actuators, positively affecting the miniaturization possibilities of a given robotic system. This is further strengthened by the fact that the control electronics for a piezoelectric actuator can be implemented outside of the working area of the robot, especially relevant when operating in confined workspaces.

The present thesis will seek to investigate the matter of piezoelectric SSA for the advancement of miniaturisation in micro-robotics. With a comprehensive approach to understanding the theory behind achieving *self-sensing* within piezoelectric actuators, an approach to providing ultra-high accuracy sensorless actuators will be presented with the aim of developing a prototype. The detection of force and position thresholds will be considered at first, with the future prospect of using the prototype for high accuracy force and position control.

Thesis outline

Before undertaking any steps in this endeavour, an evaluation of the current advancements of piezoelectric self-sensing in modern research is required. As such, Chapter 1 shall begin with a complete introductory look into how self-sensing has been implemented in piezoelectric actuators up to now. Three main approaches will be discerned: voltage measurements, current and charge measurements, and finally impedance evaluations which are often combined with one of the latter two. With an application goal in mind, and by deduction from the qualitative appreciation of the strengths and weaknesses of each approach, the current or charge measurement approach is considered for the remainder of this thesis.

Following the observation that most self-sensing attempts with piezoelectric actuators have been made with commercially available actuators, the research focus shifts towards a top-down approach in Chapter 2. The goal is to develop a comprehensive understanding of piezoelectric SSA with a framework comprised of two models: a general form of analytical model describing piezoelectric actuators and their input / output signals, and a dynamic model constructed from Bond Graph Models (BGM). The use of BGM to understand the dynamic behaviour of a piezoelectric actuator, allowing for the description of the estimation performance of the system, is a novelty brought forward by this chapter. It allows to shine some insight into the relationship between actuator parameters, i.e. stiffness, capacitance, and the estimation accuracy of the mechanical state.

With the self-sensing theory presented in the SSA framework, Chapter 3 moves on to the design of a piezoelectric SSA device. Before settling on an actuator morphology, experiments are performed on samples with tasks that would typically be performed by micro-robots. Their purpose is to highlight a scope for the actuation and sensing performances of the actuator

in terms of displacement and applied force. Once the actuator morphology is settled, the establishment of an analytical model according to the general model defined in Chapter 2 is demonstrated. The analytical model is then used to maximise the estimation resolution of the prototype, as design parameters shall be derived from this study.

From this point, all the tools to design and assemble a self-sensing prototype are in hand. The guidelines derived from the design study are hence used in Chapter 4 to manufacture a batch of piezoelectric actuators. The prototype is then designed around this actuator design, with a test environment providing feedback on the electro-mechanical inputs and outputs of the piezoelectric actuator. This makes it possible to validate in real-time the output of the sensorless estimation for the mechanical state of the actuator. This prototype is then used to provide a statistical evaluation of the actuator's characteristics by experimenting on an ensemble of six actuators. The results of the characterisation are finally used in an attempt to implement the sensorless force estimation of the self-sensing actuator manipulation a sample.

Finally, Chapter 5 investigates a discrepancy that may be observed between the model predictions and the measured values for the actuator's parameters. The importance of previously neglected features of the actuator stack such as the electrode thicknesses and isolation layers is evaluated and found to be responsible for large drifts in designs with very thin piezoelectric layers and small number of layers. A newer and more complete model for the actuator morphology defined in Chapter 3 is provided. The verified accuracy and non-linearity of the new complete analytical model provides a new opportunity to study the optimal design parameters for a self-sensing piezoelectric actuator. A novel approach to designing self-sensing piezoelectric actuators is devised by considering the actuator as a sensor, and by defining functions for its *sensitivity* and its *accuracy*. A full multi-objective optimisation study is provided, and the Pareto frontier of the optimisation problem is provided.

Photographic credits

- Fig. 1a: photographic rights held by Leica Microsystems, image downloaded from <https://www.leica-microsystems.com/fr/applications/> on April 24, 2020.
- Fig. 2a: photographic rights held by Kleindiek Nanotechnik, image downloaded from <https://www.nanotechnik.com/ps4.html> on April 24, 2020.
- Fig. 2b: photographic rights held by Zyvex Instruments, image downloaded from www.zyvex.com/Products/nProber_features.html on May 23, 2016.
- Fig. 3: photographic rights of right photo held by the Swiss Center for Electronics and Microtechnology (CSEM), image downloaded from <https://www.polymedia.ch/RP/Articles/view/742> on April 24, 2020.
- Fig. 4: photographic rights held by Imina Technologies S.A., images downloaded from <https://www.imina.ch/> on April 24, 2020.

1 An introductory look into piezoelectric self-sensing actuation

1.1 Introduction

The first step in designing a high precision and sensorless piezoelectric actuator for micro-robotics is to study the current advancements of academic research on the matter. Self-Sensing Actuation (SSA) is a relatively recent topic, with the first publications on the topic dating back to 1990, and with a large amount of breakthrough that has been brought in the past decade. Before going into the specifics of sensorless piezoelectric actuators, it is convenient to have some theoretical background. For the sake of brevity for this chapter, a summary of the theory of piezoelectricity and piezoelectric modelling are provided in Appendix A.

As discussed in the Introduction of this thesis, piezoelectric actuators present a multitude of perks in terms of miniaturisation and displacement accuracy. The downside to these strengths are the unfortunate parasitic effects that are inherent to the properties of piezoelectric materials such as voltage-displacement hysteresis, creep effect, and dielectric absorption, which have to be taken into account to guarantee an acceptable accuracy [51]. This is all the more relevant when attempting to achieve high accuracy for micro-robotic applications, as tools need to be precisely positioned, and exerted manipulation forces need to be controlled in a way that objects are not damaged. Hence the need for sensors is a hurdle to the integration of piezoelectric actuators in micro-robots and, ultimately, to their miniaturization. It has been suggested in the Introduction that SSA is a potential solution to this problem by enabling the precise operation of actuators without the need for external sensors.

The following sections will discuss the methods that are present in scientific literature to this day regarding SSA with quasi-static piezoelectric actuators. Piezoelectric SSA may be categorised depending on the nature of the electrical signal that is measured to provide a state estimation, as it can be a voltage, a current, or an impedance. Three main axes of research have been identified according to this type of criteria, and they will each be presented: voltage-based SSA, current or charge-based SSA, and impedance-based SSA, the latter being often associated with one of the other strategies in hybridised approaches. A summary of the scientific literature's progress on these topics will then be provided.

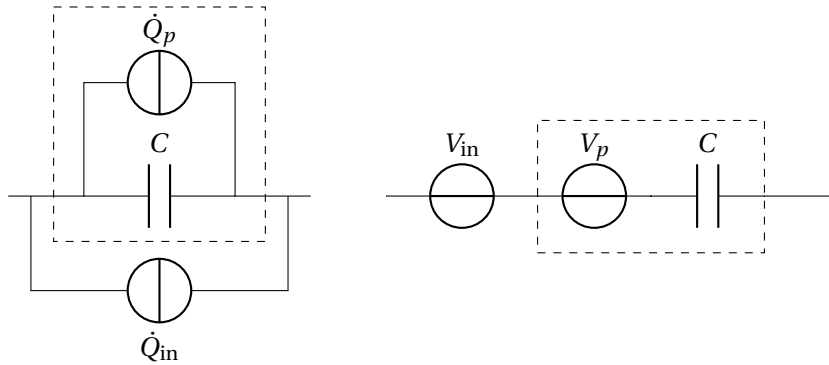


Figure 1.1 – Electrically equivalent model of a piezoelectric actuator.

1.2 Voltage measurement bridge

One of the first contributions to piezoelectric SSA was made in 1992 by Dosch and Inman [31], describing the voltage measurement bridge as a means to determine the mechanical state of an actuator. The use-case for SSA presented in this first publication is the damping of vibrating piezoelectric cantilevers. While this does not directly pertain to SSA with quasi-static piezoelectric actuators, it does demonstrate how the state of a piezoelectric actuator can be determined by simply measuring a voltage. The work of Dosch and Inman nonetheless serves as a good starting point to explain the operating principle of the approach. Subsequent works have attempted to reconcile the approach with quasi-static applications with some degree of success. These will be discussed once an overview of the approach for high frequency applications has been laid out.

The following section will present the working principle of the voltage measurement bridge, along with short analyses of the basic strain and rate of strain sensing bridges, followed by an overview of the improvements that have been made on the method in order to improve its quasi-static performance.

1.2.1 Operating principle

In order to be able to derive the state of an actuator through voltage measurements, a relationship between the mechanical state (i.e. strains) and the electrical state (i.e. electric fields) must be established. This is done by Dosch and Inman with the assumption that the actuator's electrical behaviour can be modelled through an electrically equivalent model (Fig. 1.1).

This simple model consists of the actuator's internal capacitance C_p in series with a voltage source V_p , the latter modelling the effect of the electric displacement field D within the piezoelectric material. This electric displacement field is a result of the strain within the piezoelectric material through a linear relationship, and it is linearly related to the electric field and, therefore, to the voltage V_p . Thus a linear relationship can be established between the V_p voltage of the electrically equivalent model (Fig. 1.1) and the mechanical state of the

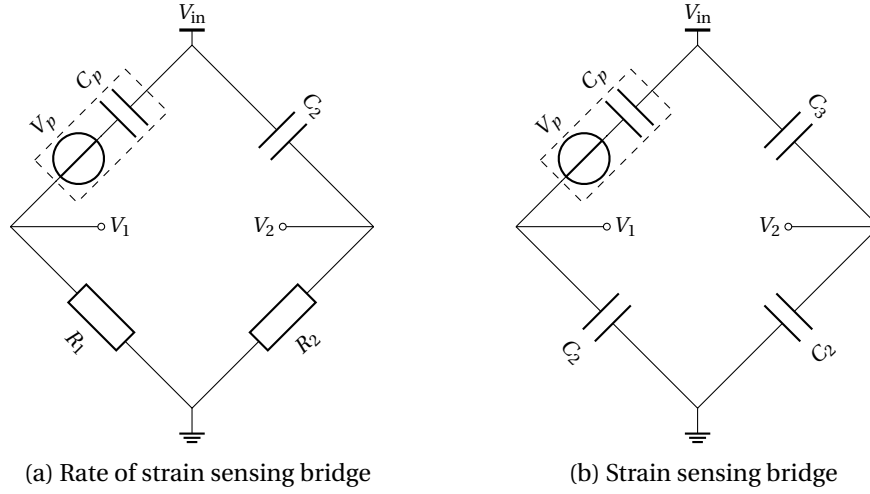


Figure 1.2 – Self-sensing actuator circuit for rate of strain and strain sensing.

actuator. As voltages can generally be measured with ease, this provides a plausible approach to estimating the state of the actuator during its operation. Determining the internal piezoelectric voltage V_p while actuator is being driven by a voltage V_{in} would make it possible to estimate the actuator's mechanical state, opening the door to achieving SSA with piezoelectric actuators. Only the rightmost electrically equivalent model in Fig. 1.1 will be used, as it takes into consideration the internal piezoelectric voltage V_p that is targeted by the approach.

A challenge arises from this due to the fact that the voltage source V_p is in series with an internal piezoelectric capacitance C_p , being internal to the piezoelectric actuator. This makes it impossible to directly measure the V_p voltage, and the solution brought by Dosch and Inman to this hurdle is the use of voltage measurement bridges: two bridges that can be used to estimate either the rate of strain or the strain of an actuator have been proposed. These circuits take advantage of the aforementioned electrically equivalent model of the piezoelectric actuator (Fig. 1.1). They can be described as Wheatstone bridges wherein the piezoelectric actuator has been placed on one of the branches of the bridge (Fig. 1.2a — 1.2b). On the condition that their branches are properly balanced, the voltage output of these bridges yields the voltage V_p , which leads to the estimation of the electrical displacement field D and, consequently, the mechanical state of the actuator.

Rate of strain sensing bridge

The first electrical circuit to be considered is the rate of strain sensing bridge seen in Fig. 1.2a. The upper half bridge is composed of the piezoelectric actuator, modelled with the capacitance C_p and voltage source V_p , and of a capacitance C_2 . The lower half of the bridge consists of resistors R_1 and R_2 . The sensing voltage V_s consists of the difference in electrical

Chapter 1. An introductory look into piezoelectric self-sensing actuation

potential between V_2 and V_1 , both of which can be expressed as follows using phasors:

$$\underline{V_2} = \underline{V_{in}} \cdot \frac{j\omega R_2 C_2}{1 + j\omega R_2 C_2} \quad \underline{V_1} = (\underline{V_{in}} - \underline{V_p}) \cdot \frac{j\omega R_1 C_p}{1 + j\omega R_1 C_p} \quad (1.1)$$

Which yields the following expression for the sensing voltage V_s :

$$\underline{V_s} = \underline{V_{in}} \cdot \left(\frac{j\omega R_2 C_2}{1 + j\omega R_2 C_2} - \frac{j\omega R_1 C_p}{1 + j\omega R_1 C_p} \right) + \underline{V_p} \cdot \frac{j\omega R_1 C_p}{1 + j\omega R_1 C_p} \quad (1.2)$$

This expression can be greatly simplified with proper balancing of the measurement bridge. In that regard, imposing the condition that $C_p R_1 = C_2 R_2$ will suppress the first half of Eq. 1.2. By moving into the frequency domain through the transformation $s = j\omega$ and by applying the condition that $\omega R_1 C_p \ll 1$, one can come to the following development:

$$\underline{V_s}(s) = s R_1 C_p V_p(s) \quad \xleftrightarrow{\mathcal{L}} \quad v_s(t) = R_1 C_p \cdot \dot{v}_p(t) \quad (1.3)$$

It can be concluded that, should the aforementioned conditions be met, the sensing voltage V_s is proportional to the derivative of the piezoelectric voltage V_p . As the latter is proportional to the strain, these equations can be used in order to determine the rate of strain of the piezoelectric material.

Strain sensing bridge

The second bridge seen in Fig. 1.2b, used for direct strain sensing, is a variation of the first bridge. The lower half bridge is replaced with identical capacitors C_2 . The same approach to determine the sensing voltage V_s is applicable here, with expressions for the $\underline{V_2}$ and $\underline{V_1}$ phasors in the following form:

$$\underline{V_2} = \underline{V_{in}} \cdot \frac{C_3}{C_2 + C_3} \quad \underline{V_1} = (\underline{V_{in}} - \underline{V_p}) \cdot \frac{C_p}{C_2 + C_p} \quad (1.4)$$

The bridge can be balanced, and the expression for the sensing voltage V_s simplified, if the condition $C_p = C_3$ is met. In this case, the following transformation from the frequency domain to the time domain can be made:

$$\underline{V_s} = \underline{V_p} \cdot \frac{C_p}{C_p + C_2} \quad \xleftrightarrow{\mathcal{L}} \quad v_s(t) = v_p(t) \cdot \frac{C_p}{C_p + C_2} \quad (1.5)$$

Consequently, the sensing voltage V_s is proportional to the piezoelectric voltage V_p by a factor dependent on the choice of C_2 , and is thus directly proportional to the strain of the piezoelectric material. The balancing of such a measurement bridge is unfortunately a much

more delicate matter than in the case of the rate of strain sensing bridge. The condition of $C_p = C_3$ is harder to achieve due to the difficulty of imposing a strict tolerance on passive components such as capacitors. Furthermore, the capacitance of the piezoelectric actuator C_p must be precisely known in order to match it with C_3 , which is made more difficult by the fact that the impedance of a piezoelectric material may change as a function of its strain.

Raw performance of voltage measurement bridges

In order to verify the performance of this approach, Dosch and Inman have performed a validation test using the rate of strain measurement bridge [31]. This bridge was used to create a feedback loop so that a regulator could use the rate of strain in order to suppress the vibrations of a piezoelectric actuator. The latter is a monomorph cantilever of dimensions $38.74 \times 2.29 \times 0.081 \text{ cm}^3$, initially excited at a frequency of 20 Hz. The vibration was reduced to 5% of its initial amplitude within 0.3 s for the first mode of vibration and 0.9 s for the second mode, demonstrating a successful self-sensing actuation implementation.

This approach is however held back by one caveat, as the electrically equivalent model that has been considered (Fig. 1.1) is rather simplistic. It does not account for the parasitic effects that are typically present in piezoelectric materials: hysteresis, creep, dielectric absorption, etc. These effects aren't as impactful at higher frequencies of operation, hence the good performance achieved for the stabilization of vibrating actuators. Quasi-static implementations of this SSA approach, however, will be held back by these effects by causing a drift over time between the estimated and the real physical state of the actuator.

Another difficulty arising from this approach is the complexity of balancing the branches required to isolate the sensing signal from the actuation signal in the bridge's output. The impedance of the piezoelectric actuator must be accurately measured before attempting to match the opposed branch to its capacitance C_p . Furthermore, the impedance of a piezoelectric actuator at quasi-static frequencies (typically less than 1 Hz) are not trivially modelled. This is compounded by the fact that the impedance of a piezoelectric actuator is not constant and is influenced by several internal and external parameters: strain, electric field, ambient temperature, relative humidity, etc. The voltage measurement bridge is therefore vulnerable to external conditions, and its output may become unpredictable.

1.2.2 Improvements for quasi-static operation

Despite the difficulties faced by the implementation of a voltage measurement bridge, this approach to self-sensing actuation has been successfully used in various high frequency applications and, to a certain extent, quasi-static ones. Some solutions have come up to compensate for these downfalls and make the quasi-static application more promising. These improvements and their effect on quasi-static performance will be discussed further in the following sections.

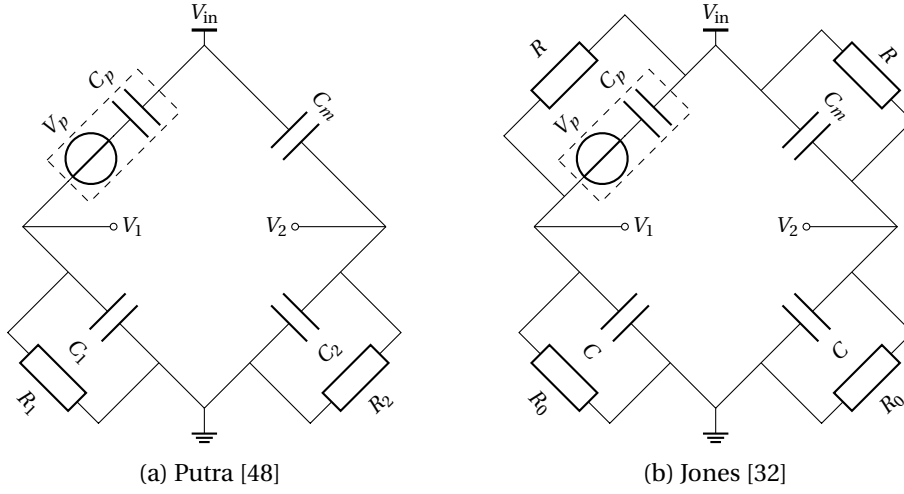


Figure 1.3 – Proposals for updated bridges to extend the self-sensing bandwidth.

Extending the self-sensing bandwidth

As previously mentioned, the main flaw of the measurement bridge approach to piezoelectric self-sensing actuation is the simplistic electrically equivalent model that is used to approximate the electrical behaviour of the piezoelectric actuator. In reality, the impedance of the piezoelectric material has a resistive component which is the cause for leakage currents. These currents inevitably result in a deviation over time in the estimation of the sensing voltage with respect to the real value of the strain or rate of strain. This deterioration over time causes the method to be unsuitable for quasi-static applications.

Some proposals have gone into possible solutions to increase the bandwidth of the measurement bridge. In 1994, the design of a piezoelectric linear stack actuator used in the micropositioning of small segments of a satellite dish is discussed by Jones et al. [32]. They consider the implementation described by Dosch, as it was a promising solution to a lightweight actuation system that could satisfy stringent requirements on operating frequencies from Direct Current (DC) to 3 kHz. Jones acknowledged the issue of DC drift incurred in a purely capacitive bridge and its effect on a micropositioning device, and proposes a modification in which resistors are added in parallel to each branch (Fig. 1.3b). Similarly to the strain sensing bridge, the sensing voltage V_s in Fig. 1.3b is isolated from the actuation voltage V_{in} if the condition $C_p = C_m$ is met, and the same equation as Eq. 1.5 can be found. An additional condition on the resistors to eliminate the drift component burdening the sensing voltage V_s can be found by studying the transfer function of each half-bridge, and can be expressed as follows:

$$\frac{C_1}{C_1 + C_2} = \frac{R_2}{R_1 + R_2} \quad (1.6)$$

Rather than improving the bridge's accuracy at lower frequencies, Putra et al. have pondered on how extend the bandwidth to higher frequencies in 2008 [48]. In this work, a self-sensing

piezoelectric linear stack actuator for a micro-dispensing system injecting and depositing microliters of fluids on samples is presented. The nature of its task requires the actuator to be capable of handling fast switching trajectories, hence the need for extending the bandwidth to higher frequencies. Putra proposes an updated rate of strain sensing bridge (Fig. 1.3a) in which parallel resistors are only placed in the lower legs of the measurement bridge. This approach was also presented by Pang et al. in 2006 [6].

The following conditions must be met in order for the bridge to be balanced: $C_p = C_m$, $C_1 = C_2$ and $R_1 = R_2$. Meeting those conditions, the sensing voltage V_s is isolated from the actuation signal V_{in} , and the bridge functions is a high-pass filter:

$$\frac{V_s}{V_p} = \frac{j\omega R_1 C_p}{1 + j\omega R_1 (C_p + C_1)} \quad (1.7)$$

The cut-off frequency of the bridge is increased as a consequence of this modification, extending the bandwidth of the self-sensing actuation to higher frequencies. This approach allows the self-sensing bridge to be able to accurately perform fast switching trajectories, but it is however less suitable for low frequency and quasi-static operations such as micro-positioning and micro-manipulation.

Compensation of impedance variations

The issue that causes the most unpredictability in the bridge measurement implementation is the sensitivity of the method to external parameters. This is mainly due to the fact that the actuator's impedance being influenced by its environment causes the bridge to become unbalanced. In this situation, the sensing voltage is no longer isolated from the actuation signal, and it loses its direct relationship to the electric field, and therefore the strain, within the piezoelectric material. Adjusting resistors while the actuator is being driven is possible with the use of digital potentiometers, but the adjustment of capacitors is another matter.

In addition to compensating the DC drift to improve quasi-static performance, Jones makes this observation with regards to the long term accuracy of the bridge. Matching the capacitance of the piezoelectric actuator with a reference capacitor on the other half-bridge is critical to isolate the sensing voltage V_s from the actuation signal V_{in} , until it inevitably became unbalanced. It was first thought that the actuator's capacitance changed due to the deformation of the material, but overall this effect has been proven to have a negligible impact on the capacitance change. Instead, the change may be due to the modification of the piezoelectric material's property, more specifically the permittivity ϵ , under the influence of an electric field. This made it difficult to model and compensate for the changes in impedance of the actuator. Jones therefore proposes to replace the reference capacitor leg of the half-bridge with another identical piezoelectric actuator which will be subject to the same applied voltages. The reference capacitance would therefore match the capacitance of the piezoelectric actuator at all times, and the non-linearities of the piezoelectric properties can thus be compensated.

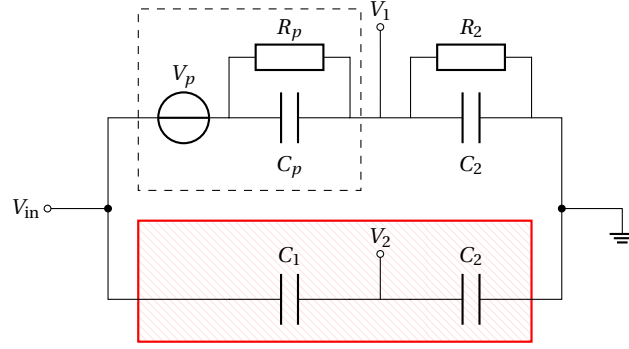


Figure 1.4 – Robust self-sensing actuator bridge for strain sensing.

Replacing the reference capacitance of the half-bridge opposed to the self-sensing actuator is an elegant solution in that it is passively regulated. Other attempts at increasing the robustness of the bridge have used analog computers to replace the passive half-bridge by simulating its output. This has been proposed by Takigami et al. in 1998 [57], as illustrated in Fig. 1.4. The active half-bridge makes use of the previously discussed improvement by adding parallel resistors to both branches to compensate the drift caused by leakage currents, improving the self-sensing accuracy during quasi-static operations. Ignoring the presence of the analog computer for now, the sensing voltage V_s of the measurement bridge presented in Fig. 1.4 can be found by finding the expression of the $\underline{V_2}$ and $\underline{V_1}$ phasors:

$$\underline{V_2} = \underline{V_{in}} \cdot \frac{C_1}{C_2 + C_1} \quad \underline{V_1} = (\underline{V_{in}} - \underline{V_p}) \cdot \frac{R_2}{R_2 + R_p \frac{1+j\omega R_2 C_2}{1+j\omega R_p C_p}} \quad (1.8)$$

The bridge can be balanced, and the expression for the sensing voltage V_s simplified, if the conditions $C_p R_p = C_2 R_2$ and $C_1 = C_p$ are met. In this case, the following transformation from the frequency domain to the time domain can be made:

$$\underline{V_s} = \underline{V_p} \cdot \frac{C_p}{C_p + C_2} \quad \xleftrightarrow{\mathcal{L}} \quad v_s(t) = v_p(t) \cdot \frac{C_p}{C_p + C_2} \quad (1.9)$$

The first condition (i.e. $R_2 C_2 = R_p C_p$) can be controlled with ease by implementing R_2 as a digital potentiometer that can be adjusted online and using a fixed capacitance C_2 . However, the second condition (i.e. $C_1 = C_p$) is not as easy to control and fine-tune. Despite the availability digitally tunable capacitors, matching with accuracy the evolving capacitance C_p of the piezoelectric actuator with these devices remains a complex issue. This is where the solution of implementing an analog computer in the stead of the passive half-bridge, composed of C_1 and C_2 , gains merit. Since the potential V_2 is not dependent on the piezoelectric voltage V_p , the gain of the passive half-bridge is simulated by means of this analog computer. Since it is possible to design the analog computer to match the gain to the evolution of the piezoelectric capacitance C_p online, this approach becomes more robust to external conditions that

previously limited the potential of the bridge measurement implementation. This approach foregoes the need for another piezoelectric actuator as a reference capacitance, making it less costly to implement.

1.3 Charge and current measurement

The first approach to SSA that has been presented has discussed the use of voltage measurements for the deduction of the electrical field within the piezoelectric material, which in turn can be used to deduce the strain of the actuator.

In the same year that Dosch and Inman have published their paper on voltage measurement bridges, Hagood and Anderson have offered an alternative approach to piezoelectric SSA [17]. They provide insight into the relationship between the current flowing between the shorted electrodes of a strained piezoelectric actuator and the strain rate of the actuator. It is thus hypothesised that the capability of isolating and quantifying the current flowing through the actuator due to its deformation may lead to an accurate estimation of the rate of strain. As was the case for the publication of Dosch and Inman, the approach presented by Hagood and Anderson had been intended for high frequency applications. This research topic has nonetheless garnered significant interest, as multiple improvements have been brought to this approach to make it viable for quasi-static applications.

The following paragraphs will first present the basics of the charge or current measurement SSA approach, then will discuss all the quasi-static performance improvements that have been brought over the years.

1.3.1 Operating principle

Through the application of the theory of piezoelectricity, a system of two constitutive equations can be determined for a given actuator. This system describes the state of the actuator in the mechanical and electrical domains along with the mutual interactions of these two domains. It may be expressed when considering the matrix form of the piezoelectric equations:

$$\begin{bmatrix} \mathbf{S} \\ \mathbf{D} \end{bmatrix} = \begin{bmatrix} \mathbf{s}^E & \mathbf{d} \\ \mathbf{d}_t & \boldsymbol{\epsilon}^T \end{bmatrix} \begin{bmatrix} \mathbf{T} \\ \mathbf{E} \end{bmatrix} \quad (1.10)$$

where \mathbf{D} is the electric displacement field matrix, \mathbf{E} is the electric field matrix, \mathbf{T} is the stress matrix and \mathbf{S} is the strain matrix. The properties of the piezoelectric material are described by its permittivity matrix $\boldsymbol{\epsilon}$, its compliance matrix \mathbf{s} , and its piezoelectric coefficients matrix \mathbf{d} . The $(\cdot)^E$ superscript denotes a constant electric field E , the $(\cdot)^T$ superscript denotes a constant stress T , and the $(\cdot)_t$ subscript denotes a matricial transpose.

Through these equations, Hagood and Anderson demonstrate that the current flowing through an actuator is related to its rate of strain [17]. Similarly, it can be shown that the electric charges

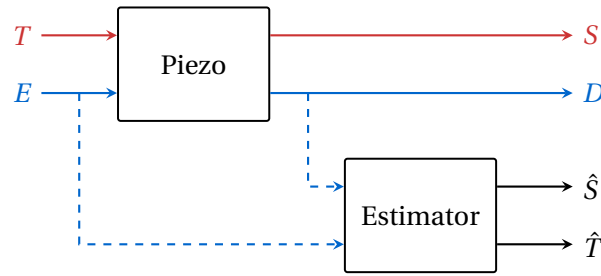


Figure 1.5 – Operating principle of charge or current based SSA for the estimation of the mechanical state of the actuator (mechanical quantities in red, electric quantities in blue).

accumulated by an actuator is related to its strain. This can be explained by considering the system of equations in Eq. 1.10. The electrical and mechanical states of the actuator are both influenced by the driving electric field E and the strain T perceived by it. The application of both those quantities, considered as inputs to the piezoelectric system, influence the strain S and the electric displacement field D considered as outputs of the same system. The applied electric field E and resulting electric displacement field D can be tied to measurable electric quantities, namely voltages for E and charges (and by extension currents) for D through the application of Gauss' law. These electrical signals are readily available within the drive electronics of the actuator and do not require additional external sensors to be measured.

This approach to modelling the piezoelectric actuator is relevant when considering SSA, since sensorless actuators are designed to behave simultaneously as actuators and as sensors. The principle of operation of charge / current self-sensing is illustrated as a system in Fig. 1.5. With E and D being available from within the drive electronics, it is possible to measure both of these quantities without the use of external sensors. The model of the piezoelectric actuator determined through the development of Eq. 1.10 can then be used to provide an estimation of the strain \hat{S} and the stress \hat{T} . This approach thus provides a way to derive the mechanical state of the actuator from the knowledge of the driving voltage that is applied to it and the measurement of its current, or accumulated charges.

To demonstrate their approach, Hagood and Anderson have performed an experiment with a piezoelectric cantilever of dimensions $33 \times 2.54 \times 0.32 \text{ cm}^3$. The goal of the experiment was to stabilise the vibrating cantilever without the use of external sensors, by using a current measurement SSA approach. After defining the constitutive equations for a cantilevered piezoelectric actuator, they have proposed to amplify the current within the driving circuit, as shown in Fig. 1.6. The output voltage of the current amplifier is then used by a Fourier analyser to determine the current strain of the actuator. A second current amplification stage is used in parallel to the amplification of the actuator's current. It is connected to a reference capacitor approximating the actuator's capacitance and is subject to the same voltage. This is done in order to negate the current flow caused by the application of a driving voltage, and is used to subtract this unwanted contribution from the output of the actuator's current amplification. In this manner, only the current caused by the deformation of the actuator is measured.

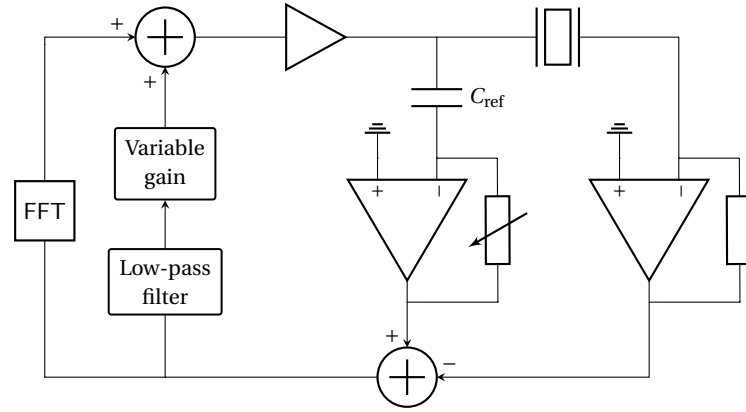


Figure 1.6 – Rate of strain sensing hardware using current measurement.

The transfer function of the system designed by Hagood and Anderson had been evaluated for frequencies ranging from 10 Hz to 1 kHz. This led to the conclusion that the first modes of vibration were successfully attenuated to 1% of their initial amplitude. This experiment has thus proven successful in demonstrating the validity of the current measurement SSA approach, and in showing that it is possible to use piezoelectric materials to achieve self-sensing actuation.

Due to the high frequency nature of the application proposed in this publication, the authors have not concerned themselves with the parasitic effects of piezoelectricity (i.e. creep, hysteresis) and have assumed linear properties of the material. As such, this approach is unsuitable to quasi-static operation as is, and requires additional improvements to extend its bandwidth to lower frequencies. Similarly to the voltage measurement bridge, this approach also calls for special care in the choice of its components. The reference capacitor needs to match precisely the internal capacitance of the piezoelectric material, which is not constant depends on several parameters that are external to the actuator.

1.3.2 Measurement strategies

As discussed in the presentation of the operating principle, it is possible to achieve this type of piezoelectric SSA either through current or charge measurements. In the following paragraphs, examples of these two strategies and what the choice of either entails in terms of SSA performance will be discussed in the context of quasi-static applications.

Charge amplification

Some of the most significant contributions to the field of charge and current based SSA have come from the FEMTO-ST Institute (France), starting with the publication of Ivan in 2009 on the use of current integration, or charge amplification, for sensorless position estimation [27]. The approach of charge amplification instead of current measurement is favoured under the stipulation that it is easier to detect small variations in position through this method. For

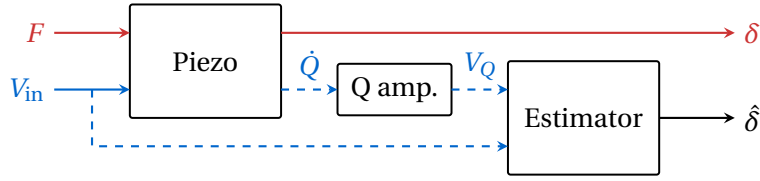


Figure 1.7 – Sensorless position estimation system through charge measurement SSA.

slight variations, and therefore small rates of strain, the current flowing through the actuator may be too low to properly detect.

This publication is aimed specifically at quasi-static applications using piezoelectric actuators, and has led to multiple publications in the subsequent years iterating on this particular SSA approach. A piezoelectric bimorph cantilever is considered in this article, with the aim of deriving the deflection δ of the bimorph's free tip when it is subject to an applied voltage V_{in} . Instead of using current measurements, it is proposed to use charges measurement instead. The reason for this approach is that the model that Ivan has used for this actuator directly ties the accumulate electric charges Q to the displacement δ of the free tip. This is more convenient when considering quasi-static applications than the rate of strain that would be obtained through current measurements.

To provide a sensorless estimation of the deflection, the system presented by Ivan consists of two main components, both illustrated in the system diagram in Fig. 1.7. These two systems are the following:

- A **charge amplification circuit** is connected in series with the piezoelectric actuator, and provides analog integration of the current $i(t)$ flowing through the actuator. This is done with the operational amplifier set-up in Fig. 1.8, and its instantaneous output voltage $v_Q(t)$ is proportional to the amount of charges accumulated by the actuator at a given point in time.
- A **data processing system** is connected to the output of the charge amplifier and to a measurement of the applied voltage V_{in} , and it implements the inverse model of the piezoelectric actuator. With the knowledge of the charge Q deduced from V_Q and the voltage V_{in} , it provides an estimation $\hat{\delta}$ for the deflection of the bimorph's free tip.

While the charges may be measured by an electrometer connected to the piezoelectric actuator in series while it is being driven, Ivan has instead provided a design of his own. The custom circuit, illustrated in Fig. 1.8, consists of an operational amplifier with a capacitor C in its feedback loop. Since the integration of the current over long periods of time can lead to the saturation of the operational amplifier, it is necessary to include a resistor with a digitally controlled switch k . This parallel resistor discharges the integrating capacitor C when

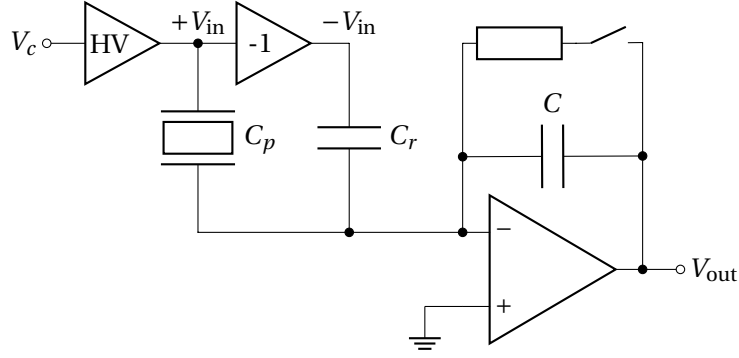


Figure 1.8 – Charge amplification circuit for sensorless position estimation.

necessary. The output voltage of this amplifier can be written as:

$$V_{\text{out}} = -\frac{1}{C} \int_0^t i(t) dt = -\frac{Q}{C} \quad (1.11)$$

where $i(t)$ is the instantaneous current flowing through the actuator, C the reference capacitance, and t the duration of the measurement since the beginning of the experiment, and Q the charge of the device under test.

The accumulated charges Q measured by the charge amplification circuit has two components, such that $Q = Q_p + Q_e$. An electrical component $Q_e = C_p V_{\text{in}}$ which is caused by the application of the driving voltage V_{in} on the piezoelectric actuator of capacitance C_p , and a mechanical component Q_p which is caused by the deformation of the piezoelectric material. In the context of self-sensing being used to estimate the mechanical state of the actuator, only Q_p is of relevance. Depending on the considered piezoelectric actuator's characteristics, it may be that the Q_e is up to three order of magnitudes higher than Q_p . With the operational amplifier saturating over a given amount of charges, this causes much of the dynamic range of the charge measurement to be taken up by this parasitic charge.

The charge amplification circuit attenuates the electrical component Q_e through the inclusion of the reference capacitor C_r . By verifying the condition that $C_r = C_p$, and by applying to C_r a voltage opposite to the actuation voltage (i.e. $-V_{\text{in}}$), the charge accumulated by C_r opposes the charge Q_e accumulated by C_p . This reduces the contribution of the applied voltage V_{in} to the measured charges, and therefore increases the dynamic range of the charge measurement by a significant margin. Note that the reference capacitor C_r does not necessarily to perfectly match the piezoelectric capacitance C_p . As long as the C_r and C_p capacitances are accurately characterised prior to the integration to the charge amplification circuit, it reduces the amount of parasitic charges output by the circuit. Let ΔC be the difference in capacitance between C_r and C_p , the final output of the voltage measurement circuit is as follows:

$$V_{\text{out}} = -\frac{Q_p + C_p V_{\text{in}} - C_r V_{\text{in}}}{C} = -\frac{Q_p + \Delta C V_{\text{in}}}{C} \quad (1.12)$$

Foregoing the use of such a capacitor is possible depending on the actuator's capacitance and the amplitude of the applied voltage, but it will make it more difficult to guarantee high estimation accuracy. This is especially relevant when attempting to estimate low applied forces. As an example, Fallahinia has presented a similar SSA implementation for position estimation without using a reference capacitor in the charge amplification circuit [12]. This charge amplification approach has been used in the follow-up articles released by the FEMTO-ST Institute which will be discussed later [52] [45] [46].

Current measurement

The more direct approach to the SSA strategy presented in this section is, as presented by Hagood and Anderson, current measurement. This can be done in a multitude of ways, such as measuring the current through a shunt resistor, amplifying the current through an operational amplifier, or using a current probe. For small and low frequency deformations of the piezoelectric material, the rate of strain within the actuator will be minimal, which will inevitably be the case in quasi-static manipulation applications. The currents that flow through the actuator will expectedly be of low amplitude, hence complex to measure. Nonetheless, some attempts have been made to use current measurement for quasi-static SSA with piezoelectric actuators.

A current measurement approach where the current is measured within the actuator's driving circuit before being digitally integrated has been discussed by Ivan [26]. While no specifics are given as to how the current was measured in this approach, Ivan describes at length the different compensations for non-linearities (i.e. hysteresis, creep) that were necessary to guarantee reliable information for the SSA estimation. In this publication, a piezoelectric cantilever subject to an applied voltage V_{in} and to an external force F_{ext} is determined. The aim of the SSA implementation is to provide an estimation for both the displacement δ and the external force F_{ext} on the basis of the current measurement coupled with an inverse model of the piezoelectric actuator.

Another practical approach to SSA with piezoelectric actuators and current measurement can be seen in the development of a manipulation tweezer for Magnetic Resonance Imaging (MRI) applications by McPherson in 2011 [43], and improved further in 2014 [44]. The considered actuator is a linear stack nested within a rhombus mechanism, allowing the actuator to close the tips of a tweezer together. This kinematic chain provides strain amplification within the piezoelectric material, and a reduced force application at the tips of the tweezer. The ingenuity of this setup improves the resolution of the SSA implementation, as the increased strain within the piezoelectric actuator for a given applied force at the tweezer's tips increases the amount of current that will flow through the actuator. The SSA implementation presented by McPherson makes use of direct current measurement by measuring the voltage on a shunt resistor. The actuator is modelled with a system of constitutive equations describing the relationship between the measured current, the applied voltage, and the variations in displacement. There are several downfalls to current measurement through a shunt resistor. Chief of these is that the use of a shunt resistor results in a decrease of actuator efficiency due to the passive

component's dissipation of power in the form of heat. Additionally, the sensing signal is affected by the shunt resistor even for resistor values lower than the actuator's impedance. The estimated displacement and force thus slightly differ to the true displacement and force experienced by the actuator.

1.3.3 Improvements for quasi-static operation

As was the case for voltage measurement bridges, the first implementation of piezoelectric SSA on the basis of charge or current measurements was presented with high frequency applications in mind. This comes with limitations to the performance in quasi-static scenarios, due to the assumption of a linear piezoelectric model and the absence of parasitic effects such as hysteresis. The following paragraphs will go into the improvements that have been made to this SSA approach to make it suitable for quasi-static applications.

Compensation of material non-linearities

For quasi-static actuation, one of the key issues identified in piezoelectric materials is the hysteretic relationship between its deformation and the electric field. This is most noticeable when measuring the voltage-displacement characteristic of the actuator. Hysteresis could be suppressed by modelling it, much like it is done in feedforward approaches to piezoelectric actuation and control. Mathematical operators are used to model the hysteresis of an actuator, and the inverse model may then be used to compensate for it.

This is the approach presented by Badel [2] [1], where the hysteresis compensation already common in feedforward approaches is combined with charge based self-sensing. While the charge is used in this study, it is not directly measured. Instead, a shunt resistor is connected in series with the piezoelectric actuator and its voltage is measured to determine the current flowing through the actuator. The charge is then deduced by integrating the current digitally. The purpose of this SSA implementation is to achieve sensorless position sensing. By considering an electrically equivalent model of the piezoelectric actuator based Fig. 1.1 onto which the hysteresis operator was added, an empirical model of the actuator is formulated. The parameters of this model are then experimentally identified. As specified by the author, any kind of hysteresis operator could be used. They propose to use an operator that they have designed themselves. For reference, other publications like those of Ivan [26], Fallahinia [12] [11], Mansour [35] and Islam [24] have used the Prandtl-Ishlinskii hysteresis model to great effect.

The creep effect corresponds to a drift that occurs on a piezoelectric actuator after a DC voltage step has been applied to it, and causes the displacement of the actuator to slightly change over time (i.e. over several hundreds of seconds). Much like voltage steps on capacitors in electrical theory, the creep effect is more prevalent with greater DC voltage steps, and its speed decreases logarithmically over time. This effect is caused by the same material properties responsible

for hysteresis. Creep compensation is briefly discussed by Ivan in his charge measurement implementation [26], where an Auto Regressive and Moving Average Exogenous (ARMAX) model is used to predict the effect of creep. The data processing system used by Ivan takes into account these non-linearities of the piezoelectric material, and reverses their effect on the current or charge measurement output by implementing their reverse model. The charge measurement through current integration presented by Ivan is noted to be self-compensated for material non-linearities (hysteresis, creep) due to the nature of the charge-displacement relationship being less hysteretic than that of voltage-displacement [27]. However, subsequent publications have nonetheless made use of these aforescribed compensations to reach for increased SSA accuracies.

Compensation of external non-linearities

Aside from inaccuracies caused by piezoelectric material non-linearities at quasi-static frequencies, other time dependent phenomena have a negative impact on the performance of the piezoelectric actuator. This is especially true in manipulation tasks where a position or force must be held for a long amount of time (i.e. several minutes). This is caused by external actors, typically by the driving circuit itself. They will affect the measurement circuit of the sensorless actuator, and adding inaccuracies to the current or charge measurement. This inevitably causes a drift in the force or position estimation of the SSA actuator over time, and will cause the self-sensing function of a sensorless actuator to become dysfunctional.

The first cause of drift that can be identified is the presence of leaking resistance within the piezoelectric actuator and the driving circuit itself. With driving voltages being applied to the piezoelectric actuator, this leaking resistance will cause a current to flow through the measuring circuit, and will be added to the current produced by the actuator. While these currents are of low amplitude and could generally be ignored, the currents that are caused by the actuator's deformation are of a similar order of magnitude for sufficiently small deformations. Thus these leaking currents cannot be disregarded, especially considering that their amplitude will increase along with the voltage, while the current produced by the strain on the piezoelectric material will remain the same. The second cause for drift in charge or current measurement is the presence of bias currents from the input of measuring circuits. These currents are also of low amplitude and are generally constant. Nonetheless, they cannot be ignored for quasi-static applications where the self-sensing estimation needs to be operational for long periods of time.

In the work of Ivan [27], and in the subsequent publications by Rakotondrabe [52] [45] [46], the SSA estimation is implemented within a data processing system (Fig. 1.7). In addition to providing a force and position estimation, this system takes into account the aforescribed external non-linearities. Ivan and Rakotondrabe proceed to compensate for the drift caused leakage and bias currents empirically. The leakage resistance of the electric circuit and the charge amplifier's bias current are experimentally determined, with experimental protocols diminishing the contribution of other non-linearities (i.e. creep, hysteresis). With the knowledge

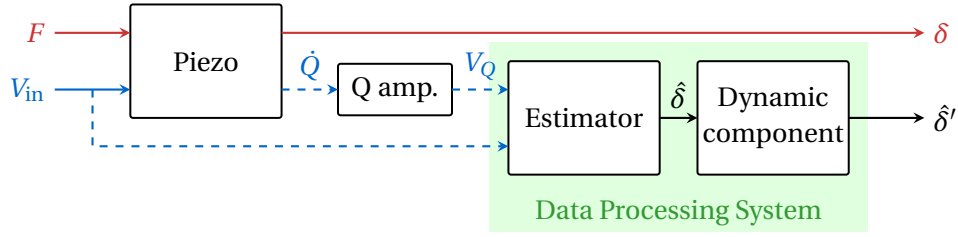


Figure 1.9 – Updated system for dynamic displacement estimation [52].

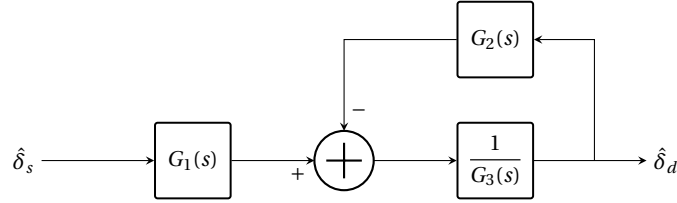


Figure 1.10 – Dynamic component of the displacement estimator [52].

of these parameters, measuring the time since the start of the current integration allows the data processing system to determine the amount of drift caused by these effects on the charge measurement by integrating these drift currents. This estimation of the drift is then subtracted to the measurement signal output by the charge amplifier, before the latter is used by the estimator. In addition to these, Rakotondrabe also compensates for the dielectric absorption of the piezoelectric actuator's equivalent capacitance through a linear transfer function in the Laplace domain.

Another source of error that can be introduced to the charge measurement may be caused by external electrostatic and electromagnetic interferences affecting the electronics. This becomes relevant when measuring nano-scale electric charges, when aiming for increased SSA resolutions. As these may not be deterministically modelled, the only solution is to provide proper shielding to the drive and measurement electronics of the piezoelectric actuator.

Improvement of the dynamic performance of the estimation

None of the models that have been discussed in the present section have taken into account the transient part of the piezoelectric actuator's deformation. Even though the estimation can be made to be accurate after a sufficiently long period of time, the estimator will be inaccurate for the first moments after a step of input voltage. In micro-robotic manipulation tasks, this problem may become dire. Piezoelectric actuators which are flexible may have strong overshoot characteristics when they are applied voltage. Uncompensated overshoot may cause damage to the actuator itself or to the manipulated sample, both of which are generally fragile. On top of overshoot, the actuator may keep oscillating for a long duration after a step response, and this oscillation needs to be removed to provide a better estimation accuracy. Dynamic position and / or force estimation coupled with robust control is therefore necessary

for static high precision estimation and control of self-sensing piezoelectric actuators. Static in this context refers to frequencies that are 10 to 100 times lower than the first resonance frequency of the actuator.

The charge measurement SSA implementations for displacement estimation presented by Ivan were proven not to be accurate for changes that occurred under 0.2 s [26] [27]. The topic of dynamic control for accurate high precision estimation forms the main topic of the follow-up article by Rakotondrabe [52]. An improvement to the estimation system presented by Ivan is proposed by adding a dynamic component within the data processing system (Fig. 1.9). The estimator, as presented earlier, only implements the reversal of the piezoelectric actuator's model and eventually applies drift corrections to the charge measurement. Its output is then used by the dynamic component, cascaded with the estimator, in order to provide dynamic corrections to the displacement estimation.

The dynamic component of the displacement estimation is implemented as a Linear Time Invariant (LTI) model in the Laplace domain, as illustrated in Fig. 1.10. The transient response of the actuator can be modelled with another LTI model in the form of $\delta(s) = K \cdot D(s)$, where K is a static gain and $D(s)$ is a dynamic part. By considering the output of the charge amplifier $V_Q(s) = H(s) \cdot V_{in}(s)$, the gains $G_1(s)$, $G_2(s)$ and $G_3(s)$ of the dynamic component can be analytically expressed as a function of K , $D(s)$ and $H(s)$. Then, while observing the displacement step response of the piezoelectric actuator for a given step of applied voltage V_{in} , the K and $D(s)$ parameters of the actuator's LTI model can be determined. Once K , $D(s)$ and $H(s)$ are empirically determined through experimental data, the full transfer function of the dynamic component can therefore be determined. This approach presented by Rakotondrabe has led to good performances for the dynamic displacement estimation. Alongside this contribution to dynamic estimation, a robust H_∞ synthesis approach has been used for the design of the controller, which is further developed in a follow-up publication [46].

The upgrade to the dynamic estimation suggested by Rakotondrabe has significantly improved the transient performance of the SSA estimation [52]. However, it was implemented with only displacement sensing in mind, and does not provide an estimation for the force applied by the actuator. An accurate and dynamic estimation of both force and displacement are necessary for proper manipulation task, so as not to damage an object when the actuator comes into contact with it. The previous publication by Ivan provided a dual estimation on force and displacement with poor dynamic performances [26], but the improvement suggested by Rakotondrabe is not suitable to improve it. Dynamic estimation such as the system presented in Fig. 1.10 presents more complexity when considering both force and displacement. This is the topic of another publication presented by Rakotondrabe, providing a new approach to obtaining dynamic estimation for the complete mechanical state of the actuator [45].

Before making contact with the object to manipulate, the tip of actuator is free and the applied force is null, hence the former is only a function of the applied voltage. Once the tip of the actuator touches the object to manipulate, the displacement becomes a function

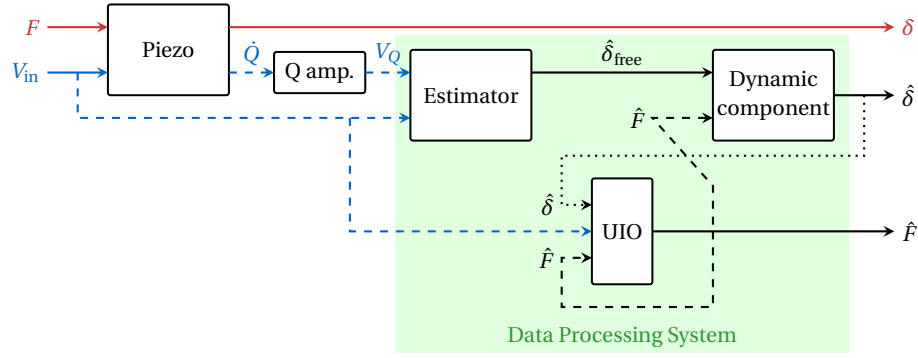


Figure 1.11 – Complete system for dynamic displacement and force estimation [45].

of both the applied voltage and the applied force. Using the previously discussed dynamic free displacement estimation [52], the dynamic real displacement of the actuator cannot be determined without the dynamic force estimation. Furthermore, it is not possible to determine the dynamic force on the basis of the dynamic free displacement estimation alone without knowledge of the object's stiffness. This becomes obvious when observing the model of the actuator: the piezoelectric actuator may be represented as a system with voltage and force as inputs, along with displacement and charges as outputs. One of the inputs of the piezoelectric system, the force, is a desired output for the SSA estimator. Hence the proposal of Rakotondrabe in a subsequent publication to use an Unknown-Input-Observer (UIO) approach [45] to extend the dynamic performance to the force estimation (Fig. 1.11).

This type of observer takes into consideration a perturbation signal that is an unknown input to the system, in this case the applied force F . The UIO observer makes use of the actuator state of the previous time step to provide the next dynamic estimation. To that end, the applied voltage V_{in} and the dynamic estimation of the displacement $\hat{\delta}$ are used as inputs to the UIO, and the dynamic force estimation \hat{F} is fed back into the UIO in a feedback loop. Furthermore, the dynamic force estimation \hat{F} is also fed to the dynamic component of the displacement estimation, so that the dynamic real displacement may be deduced. With this approach, Rakotondrabe has succeeded in providing a simultaneous force and displacement estimation with satisfying static and dynamic performances. The time delay introduced by the signal processing strategies isn't discussed in detail in these publications, and it may be prudent to consider the effect of such a delay on the estimator's dynamic performance.

1.4 Impedance related and hybrid approaches

The present section will provide a few other options for piezoelectric SSA that have been noticed in the state of the art. Rather than measuring voltages, charges or currents, these approaches have considered determining the impedance of the piezoelectric actuator, tying this measurement to the mechanical state of the actuator. While they may not necessarily offer the same accuracy as the two main topics that have been previously discussed, they

offer an interesting alternative. This is most notable when considering hybridised approaches that have combined impedance measurements with one of the previously discussed SSA approaches.

1.4.1 Impedance measurement

The idea of using impedance measurement to derive the current state of the actuator has been suggested early on to integrate self-sensing capabilities into Piezoelectric Ultrasonic Motors (PUM). One of the first examples of this approach may be seen in the thesis of Péclat [49] and a follow-up patent [50]. This approach was then further explored by Flückiger, with the aim of optimising piezoelectric actuator morphologies in order to improve their mechanical performance as well as their impedance-based self-sensing performance [13] [14].

The impedance measurement is particularly well adapted to PUM due to the high frequency of actuation, near the resonance frequency of the piezoelectric actuator. It has been noted that the impedance of the actuator could be related to its current strain, which is related to the amount of displaced mass and the compliance of the rotor's guidance rail. Much like optical encoders for traditional electric motors, mechanical features along the rotor's guidance could be used to modulate the PUM's impedance. The impedance could be determined during the PUM's operation by tracking the resonance frequency of the actuator, which was done with a Phase-Locked Loop controller (PLL). Measuring the impedance while the PUM was operated made it possible to provide an estimation of the position of the rotor. The first implementation of such an approach led to a rotor position estimation with a resolution of 60°.

Evidently, this approach is not adapted to quasi-static application due to the necessity of driving the piezoelectric actuators at high frequencies. Similar approaches have nonetheless stemmed from the observation that the mechanical state and the electrical impedance of the actuator are related. A first proposal for using impedance measurement, or rather permittivity measurement to be exact, for low frequency piezoelectric actuators (i.e. less than 1 Hz) was suggested by Ishikiriyama to overcome the hysteresis and creep effects when controlling the displacement of an actuator [61]. As discussed in Section 1.2.2, when attempting to improve the quasi-static performance of voltage-based SSA approaches, Jones made the observation that changes in the impedance of the piezoelectric material were due to a change in material properties such as permittivity under the influence of an applied electric field [32]. In that regard, Ishikiriyama notes that the displacement-voltage hysteresis has a similar profile to the permittivity-voltage hysteresis within the piezoelectric actuator. Using this similarity, it is possible to provide a relationship between the free tip of a piezoelectric actuator and the measurement of its permittivity. The relationship between permittivity and displacement is then used to provide an estimation of the mechanical state of the actuator.

The main hurdle to the implementation of this impedance-based SSA approach is the measurement of the impedance itself. While it could be done by tracking the resonance frequency of the piezoelectric actuators in PUM, other means must be elaborated to achieve this with quasi-

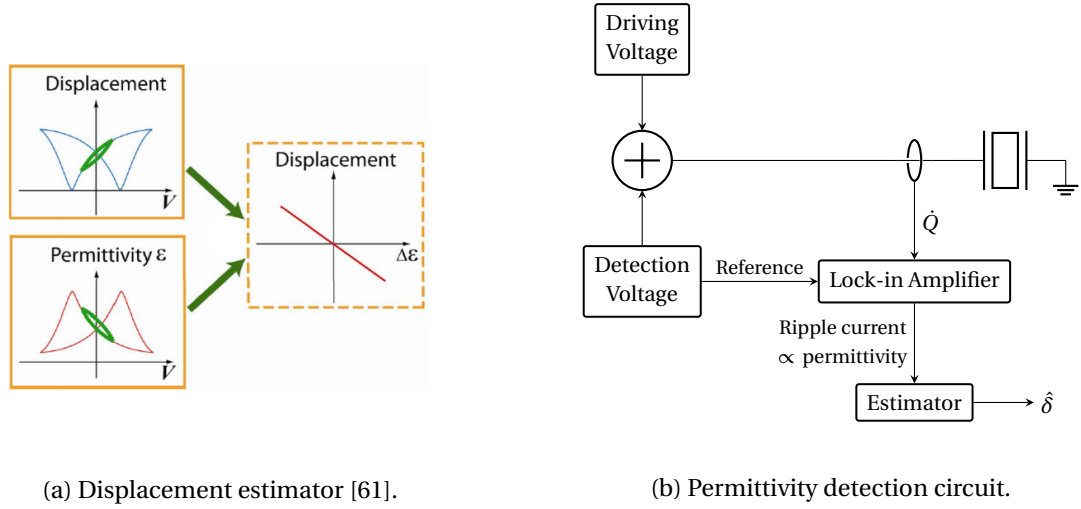


Figure 1.12 – Self-sensing approach for strain sensing with permittivity measurement.

static actuators. Ishikiriyama has thus proposed the permittivity measurement procedure illustrated in Fig. 1.12. The actuator is driven with two superimposed signals: a low frequency and high amplitude driving voltage, and a high frequency and low amplitude detection voltage. The detection voltage is of sufficiently low amplitude so as not to affect the mechanical state of the actuator. The output current of the actuator is then measured, and its high frequency component is separated from the main signal by means of a lock-in amplifier. The phase difference between the detection voltage and the detection current provides information on the capacitance of the actuator, and therefore of its permittivity.

The end result of Ishikiriyama's approach is that the creep is successfully suppressed. Although no clear information is provided on the attainable positioning accuracy of this approach, some follow-up publications have attempted to improve on this aspect. These improvements start with Ikeda's implementation of high precision position control for the same bimorph piezoelectric actuator [21]. In comparison to Ishikiriyama's setup, the novelty of this approach resides in the use of a differential current measurement method to improve the position estimation. The considered actuator is a bimorph piezoelectric cantilever comprised of two piezoelectric layers of identical polarisation. Each piezoelectric layer is subjected to an opposite electric field to deform them in opposition, creating a push-pull interaction between the layers and amplifying the motion of the actuator: a positive or negative change in permittivity for a given layer will be reflected by an opposite change in the other layer.

With differential current measurement, the difference between the detection currents flowing through each layer will therefore provide a signal corresponding to the double of the permittivity change. Furthermore, the signal of interest for the permittivity measurement self-sensing approach is the change of permittivity itself, as it is related to the change in displacement. In Ishikiriyama's approach, the measurement range was tuned for the absolute value of the permittivity, which is greater than the permittivity change by a factor of 10. Since the dif-

ferential current measurement is used, with the resulting signal being directly related to the permittivity change instead of its absolute value, Ikeda indicates that it is possible to lower the measurement range to that of the difference itself. These two improvements have provided a better Signal-to-noise ratio (SNR), hence increasing the accuracy of the positioning.

This implementation is not limited to bimorph actuators, however it may only be applied in push-pull types of configurations featuring piezoelectric material being deformed in opposite manners. Saigusa has followed up on this self-sensing approach with a configuration using two piezoelectric linear stacks attached to an end effector, with one actuator pushing the end effector and with the other actuator pulling it [54]. Applying differential current measurement for the permittivity change detection of the two actuators has provided good positioning results in this implementation. More recently, Suzuki has attempted to use the permittivity measurement self-sensing approach for contact detection. While the force couldn't be estimated, it has been shown that it is possible to detect the moment the piezoelectric actuator comes in contact with another object by observing a change in admittance [56]. The approach remained empirical in the determination of what constitutes contact, which is reminiscent of Flückiger's work on self-sensing PUM [13].

1.4.2 Hybrid observers

Literature on impedance measurement for SSA is not as diverse as for voltage or current measurement approaches in the context of quasi-static applications. Despite the lack of research popularity, some hybrid approaches have stemmed from this, combining the non invasive impedance measurement with current or charge measurements in an attempt to pursue better estimators. An example of this angle of research is laid out in Islam's work on hybrid observers for sensorless position and force estimation. In a first publication, Islam presents evidence for a linear relationship between the capacitance of the actuator and its displacement [23]. This relationship is in the form of $C_p = C_{p0} + xC_{px}$, where x is the displacement of the actuator, C_{p0} the capacitance at rest (i.e. zero displacement) and C_{px} the slope of the displacement-capacitance characteristic. In another publication, Islam discusses an approach to measuring the capacitance of the actuator while it is operational [22]. It is reminiscent of the setup provided by Ishikiriya as it superposes a detection voltage onto the driving voltage [61], but instead uses high and low pass filters to separate the detection signal from the driving signal. It is then theoretically possible to implement a self-sensing estimation of the displacement relying solely on capacitance measurement, however it has to be noted that capacitance measurement is a low frequency operation and the output of this method is affected by noise. As opposed to current or charge-based self-sensing approaches, it is however hysteresis free and is also unaffected by some of the difficulties that arise when measuring small currents (e.g. leaking and bias currents).

Due to the nature of the capacitance measurement making use of a high frequency and low amplitude detection signal, it can be used in conjunction with charge or current measurement.

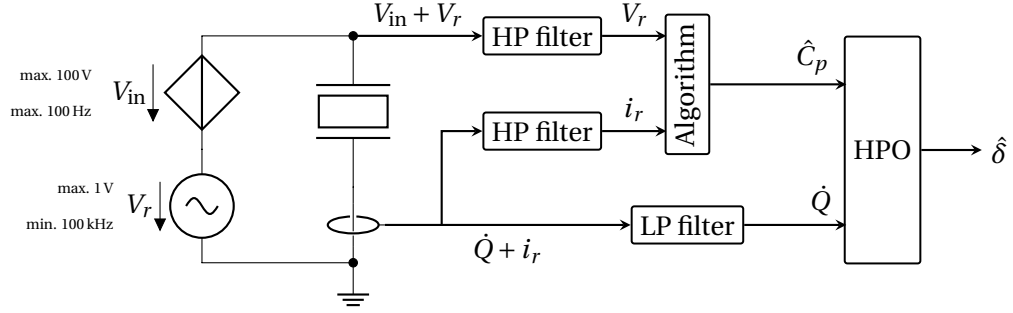


Figure 1.13 – Schematic of the measurement setup for the hybrid observer.

This could help alleviate the low frequency and noise issues that plague the capacitance measurement approach ($x = f(C_p)$), as this estimation could be combined with that of the well proven charge-based SSA estimation method ($x = f(Q)$). This forms the premise for a hybrid displacement observer for piezoelectric SSA, which is brought to fruition in a subsequent publication [24]. A schematic of this setup is shown in Fig. 1.13. Results of the hybrid observer are encouraging when it comes to quasi-static applications. The capacitance-based estimation allows to correct the drift over time that naturally occurs with the charge-based estimation. Force estimation with hybrid observers suitable for micro-robotics is successfully demonstrated by Fallahinia [11], with forces ranging up to 500 mN.

1.5 Overview and conclusions

The merits of Self-Sensing Actuation (SSA) are undebatably beneficial for the advancement of miniaturisation in micro-robotics. While ample research has gone into the feedforward control of piezoelectric actuators allowing for sensorless position control, this approach is unreliable when aiming for manipulation tasks. While the behaviour of the actuator and its non-linear properties may indeed be modelled in advance, lack of knowledge of the manipulated object's stiffness and moment of contact with the object renders the interaction non-deterministic. This therefore justifies the need for sensorless force and position estimation for the context of manipulation tasks. The possibility of sensorless estimation of piezoelectric actuators is a boon, as it allows for accurate control without the burden of sensors, while overcoming the limitations of feedforward approaches. A large panel of contributions to Self-Sensing Actuation with piezoelectric actuators has been presented and discussed in this chapter. As a reminder, sensorless estimation of the mechanical state (i.e. displacement, force) of a piezoelectric actuator may be approached by measuring various electrical signals that are present in the actuator's drive electronics. In this state of the art, the key identified electrical signals that can be measured are current, which may be associated with charges, voltage and impedance.

Voltage measurement approaches, referred to as voltage-based SSA, attempt to estimate the electric displacement field within the piezoelectric material. Through the equations of

piezoelectricity, it can be demonstrated that this field is related to the current strain of the material, and can therefore be used to determine the mechanical state of the actuator. The estimation of this electric displacement field is generally done with the help of a measurement bridge similar to Wheatstone bridges, where the piezoelectric actuator is placed on one of the branches. When the branches of this bridge are properly balanced, its output will be proportional to either the strain or the rate of strain depending on the bridge's configuration. Despite the ease with which this strategy is implemented, this first approach is held back by some difficulties impacting its quasi-static accuracy, most notably when it comes to the balancing of the bridge itself. While some improvements to the method have been discussed and good results for the displacement estimation have been observed, the quasi-static force estimation is lackluster in the implementations that are seen throughout the state of the art.

Alternatively, strategies relying on current or charge measurement, referred to as current or charge-based SSA, have shown a lot of promise for quasi-static displacement and force estimation. Through the equations of piezoelectricity, an actuator may be modelled as a system with two inputs, applied voltage and external force, culminating into two outputs, displacement and accumulated charges. In these approaches, the only addition to the actuator's driving electronics is a measurement circuit in series for the estimation of the charge and the current. With the knowledge of the voltage applied to the actuator and this measurement circuit's output, the inverse model of the piezoelectric actuator may be used to derive the actuator's mechanical state. The range, accuracy and dynamic performance of this strategy may be reinforced with measures such as the inclusion of a reference capacitor, as well as error compensation algorithms for drifts that typically affect measurements with high impedance devices. The current and charge-based strategies have been shown to simultaneous force and displacement estimation as well, a strong advantage for manipulation tasks where both of these physical quantities must be controlled.

Finally, strategies that use the estimation of the piezoelectric actuator's impedance are referred to as impedance or capacitance-based approaches. The properties of the piezoelectric material are affected by the electric field that has been applied to it, as well as by its strain. It is the former relationship that this strategy intends to make use of, and provides an estimation of the actuator's mechanical state on the basis of the impedance measurement within the drive electronics. Due to the complexity in accurately modelling the impedance of the piezoelectric actuator, this approach is by default empirical in its nature. The relationship between impedance, displacement and force must first be experimentally evaluated for a given actuator in order to use this approach. The efficacy of this approach is further compounded by the difficulty in accurately estimating the impedance of the actuator while it is being operated, and this may be a low frequency process. One redeeming quality to this approach is its compatibility with other SSA strategies, as it may be integrated with another form of measurement to form a hybrid strategy. This has been seen most notably in the combination of capacitance measurement and charge measurement, compensating the weaknesses and playing to the strengths of each strategy.

Table 1.1 – Sensorless displacement and force estimation accuracies of strategies observed throughout the state of the art; Morphology key is (B) for Bender and (LS) for Linear Stack).

Year	Morph.	Position estimation			Force estimation			τ	Ref.
		Range	Abs.	Rel.	Range	Abs.	Rel.		
Voltage-based SSA									
1998	B	-	-	-	20 mN	1 mN	5%	10 s	[57]
2008	B	30 μm	5 μm	16.6%	-	-	-	160 s	[48]
Current and charge-based SSA									
2008	LS	-	-	-	390 N	20 N	5%	30 s	[1]
2009	B	-	-	-	1.15 mN	0.16 mN	8%	100 s	[26]
2009	B	69 μm	0.38 μm	0.55%	-	-	-	1000 s	[27]
2010	B	8 μm	0.4 μm	5%	-	-	-	300 s	[52]
2013	B	-	-	-	10 mN	0.1 mN	1%	15 s	[45]
2014	LS	2.5 mm	400 μm	16%	100 mN	12 mN	12%	30 s	[44]
2015	B	3.1 μm	0.2 μm	6%	3 mN	0.2 mN	6%	200 s	[46]
2015	B	77 μm	6.2 μm	8%	-	-	-	10 s	[12]
2017	B	15 μm	0.26 μm	0.2%	-	-	-	300 s	[25]
2017	LS	30 μm	1.8 μm	6%	550 N	44 N	8%	0.3 s	[35]
Impedance-based and hybrid (*) SSA									
2011	B	80 μm	0.4 μm	0.5%	-	-	-	10 s	[21]
2014*	B	30 μm	0.72 μm	2.4%	-	-	-	0.5 s	[24]
2015	LS	8 μm	0.1 μm	1.25%	-	-	-	150 s	[54]
2018*	LS	-	-	-	500 mN	14 mN	2.8%	20 s	[11]

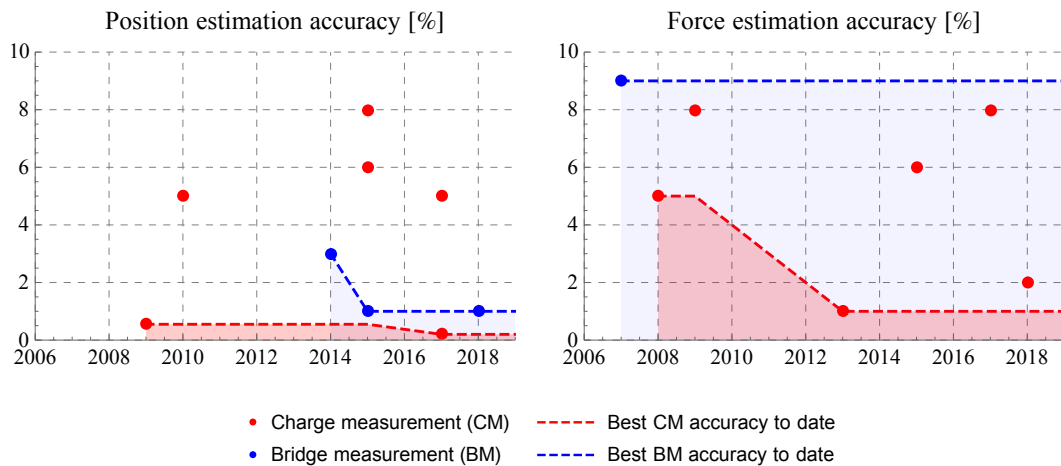


Figure 1.14 – Best results in terms of maximum relative error in the state of the art.

In the interest of comparing the quasi-static performance of each strategy for either position or force estimation, a compilation of the accuracy results that may be observed throughout the state of the art is shown in Tab. 1.1. For each result, the actuator morphology is provided, along with the displacement and force range, maximum absolute error, and maximum relative error that have been observed within the estimation. In addition to the sensing performances, the experimental duration τ is also given to provide a sense of each publication's quasi-static performance. It should be noted that only papers with clear statement of the resulting maximum error were compiled. This is by no means an exhaustive summary of the results that have been obtained in the field of piezoelectric SSA.

At first glance, the methodologies providing the most results are the current and charge-based strategies. These are also the only implementations that successfully demonstrate a complete estimation of the mechanical state, i.e. an estimation of both force and displacement. The accuracies for these implementations have steadily improved over the years, with sub- μm and sub-mN accuracies being demonstrated in some cases. Being a more recent topic, hybrid and impedance-based approaches have offered less results so far, but their estimation accuracy for either parameter have been promising. In these examples, displacement estimation accuracies have been lower than $1\text{ }\mu\text{m}$, with one case being as low as 100 nm . Accuracies in force estimation have not been on par with those of charge-based implementations as of yet, but hybrid approaches using charge measurement could hypothetically achieve this. As for voltage-based SSA, few papers have offered conclusive results. This topic has been more popular in high-frequency applications, but its quasi-static performance hasn't been as encouraging as those of the other strategies.

Moving forward, it is clear that the strategies that will be considered for the design of high precision piezoelectric SSA will rely on charge measurement. If necessary, capacitance measurement can supplement the approach in order to improve its long duration accuracy. One aspect that has been overlooked so far is the design of the actuator itself. Most of the publications that have been studied in this state of the art have used commercially available actuators, and not much consideration has gone into how the design of the actuator and the SSA are related. This forms the train of thought for the following chapters of this thesis.

The following publications by the author are related to this chapter:

- Masson, L. and Perriard, Y. (2019c). Study of self-sensing actuation strategies for quasi-static piezoelectric actuators. In *2019 22nd International Conference on Electrical Machines and Systems (ICEMS)*, pages 1–5, Harbin, China. IEEE

2 Framework for the development of sensorless piezoelectric actuators

2.1 Introduction

Three main approaches to Self-Sensing Actuation (SSA) with piezoelectric actuators have been discussed in the previous chapter. They may be categorised by the electrical signals that are measured: voltage measurement, charge or current measurement, and impedance measurement. The merits of each of these approaches to SSA in quasi-static applications have been discussed, and it has been determined that charge-based approaches had shown the greatest potential for high precision SSA.

Before developing such a high precision sensorless piezoelectric actuator, it is imperative to understand how the design of the piezoelectric device affects not only its performance as an actuator, but also its self-sensing performance. The former can be evaluated in a variety of manners depending on the intended application of the actuator: e.g. free range of displacement, blocking force, energy considerations. The self-sensing performance would be evaluated as the ease and accuracy with which the mechanical state of the actuator can be derived from the electrical measurements. In the case of charge-based self-sensing, a good self-sensing performance would therefore imply a higher sensitivity in terms of accumulated charges under the effect of a mechanical force or displacement. The aspects of an actuator design that favour that accumulation of electrical charge need to be understood before that optimising these aspects in the face of tradeoffs that may need to be taken into account.

The present chapter provides a framework for understanding the stakes of actuator design in charge-based SSA, starting with the definition of a general model that describes the signals, both mechanical and electrical in nature, tied to a piezoelectric actuator. Development for a dynamic model using Bond Graphs Modelling (BGM) will then be provided for piezoelectric actuators in micro-robotic applications. The novelty of using BGM to model a complete SSA system provides insight into the relationship between design parameters and SSA performance, helping understand the multi-physics interactions within the system. Based on a simulation using this BGM, a discussion on the self-sensing possibilities offered by given design is held.

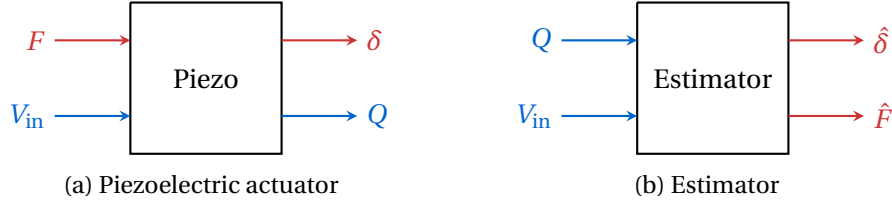


Figure 2.1 – System representation of the piezoelectric actuator and the self-sensing estimator; mechanical signals in red, electrical signals in blue.

2.2 General model for charge-based self-sensing

In the following sections, the piezoelectric actuator will be considered as a system with two input signals and two output signals. The inputs are physical quantities that describe the interaction between the piezoelectric actuator and its environment. They consist of the applied voltage V_{in} as of the external force F . Therefore, the output signals consist of the resulting displacement δ and the accumulated charges Q , both of which are a function of the two input signals through the constitutive equations of the system. The system representation of the piezoelectric actuator is illustrated in Fig. 2.1a.

These constitutive equations of the system representing the piezoelectric actuator form the basis for the general model. Knowledge of these equations may then be used to derive an estimator for the piezoelectric actuator. The system representing the estimator, as illustrated in Fig. 2.1b, takes the measured charges Q and applied voltage V_{in} signals as inputs, and outputs the estimated mechanical state of the actuator. This state is defined by the force \hat{F} and the displacement $\hat{\delta}$, where the hat symbol indicates that the variable is an estimation of the real physical quantity.

2.2.1 Definition of the general model

The modelling approach that is used to derive the general form of model for any charge-based self-sensing actuator, along with a reminder on the equations of piezoelectricity, is provided in Appendix A. As introduced in this section, the outputs δ and Q of the piezoelectric actuator system (Fig. 2.1a) may be written as a function of F and V_{in} . It can be shown that the constitutive equations for the piezoelectric actuator, which intuitively share a similar form to that of the piezoelectricity tensor equations (Eq. 3.2), may be written as follows:

$$\delta = f(F, V_{in}) = \frac{1}{K}F + \beta V_{in} \quad Q = g(F, V_{in}) = \beta F + C_p V_{in} \quad (2.1)$$

where C_p is the capacitance of the actuator at rest, K the stiffness of the actuator in its strain direction, and β a coefficient that may be expressed either in $[C/N]$ or in $[m/V]$. The β coefficient is related to the electromechanical coupling of the actuator. It is used to describe the charge accumulation as a function of the applied force, as well as the amount of displacement for a given applied voltage. As the other parameters, C_p and K , it is related to the actuator

2.2. General model for charge-based self-sensing

design parameters (i.e. dimensions, layer configuration) and to the material's properties, more specifically to its piezoelectric coefficients d_{ij} which describe the electromechanical coupling within the material.

As they describe the outputs of a multi-port system (Fig. 2.1a), the constitutive equations may be written in matrix form as follows:

$$\begin{pmatrix} \delta \\ Q \end{pmatrix} = \begin{pmatrix} \frac{1}{K} & \beta \\ \beta & C_p \end{pmatrix} \begin{pmatrix} F \\ V_{\text{in}} \end{pmatrix} \quad (2.2)$$

The estimator system, providing an approximation of the force \hat{F} and the displacement $\hat{\delta}$ from the measurement of the voltage V_{in} and the charge Q , can be derived from Eq. 2.2. The constitutive equation of the estimator system may also be written in matrix form as such:

$$\begin{pmatrix} \hat{F} \\ \hat{\delta} \end{pmatrix} = \begin{pmatrix} \frac{1}{\beta} & -\frac{C_p}{\beta} \\ \frac{1}{K\beta} & \beta - \frac{C_p}{K\beta} \end{pmatrix} \begin{pmatrix} Q \\ V_{\text{in}} \end{pmatrix} \quad (2.3)$$

It can be shown that these equations will remain identical for any type of actuator topology, with the parameters C_p , K , and β of the equations determined as a function of material properties and actuator design parameters. Intuitively, it can be said that attempting to increase the β coefficient through actuator design will lead to a more accurate self-sensing estimator. By doing so, the amount of measurable charges that are caused by the application of a force F is increased, effectively increasing the sensitivity of the self-sensing actuator. However, as it will be evidenced in later chapters of this thesis, the solution is not as simple as maximising the β coefficient, as a tradeoff will need to be made between accurate force estimation and accurate displacement estimation. Parasitic charge measurement effects caused by the capacitive nature of the piezoelectric material will impose more tradeoffs on the actuator design as well.

To illustrate how the model differs from one actuator topology to another, the parameters of the constitutive equations for three different types of piezoelectric deformation are provided in Appendix A. The actuators in Tab. A.1 are referred to as elementary due to their simple configuration. They are not multi-layered examples of piezoelectric actuators, which is the configuration for most modern piezoelectric actuators due to the increased mechanical performances it provides. These monolithic actuators may be stacked (i.e. layered) an arbitrary number of times N in order to provide increased ranges of motions for a given driving electric field, causing the constitutive equation parameters to be modified as a function of N . When optimising actuators for self-sensing actuation in the later chapters of this thesis, the parameter N representing the number of layers shall be considered as a critical variable, as it greatly affects the actuator's characteristic.

2.2.2 Experimental characterisation of a piezoelectric actuator

Following the definition of a general model, it has been possible to derive it for various actuator topologies (Tab. A.1). To validate this modelling practice, this form of model is experimentally verified on a commercial piezoelectric actuator.

To achieve this, a test bench is designed, allowing for the characterisation of commercial piezoelectric actuators (Fig. 2.2). It is proposed to achieve this characterisation by measuring the output state of the actuator (Q, δ) according to Fig. 2.1a when the input variables (F, V_{in}) are varied manually across a pre-defined experience matrix. The measurement points are spread out across this experiment matrix with F varying from 0 to 250 mN and with V_{in} varying from 0 to 10 V. The resulting $\delta = f(F, V_{in})$ and $Q = g(F, V_{in})$ are then fitted to planes for which equations are in the form of $y = aF + bV_{in} + c$, where c is the residue of the fit.

The commercial piezoelectric actuator that is considered for this experiment is Noliac's CMBP03 multi-layer bender (Fig. 2.14). The test bench is driven by a STM32F446 micro-controller, and the latter controls and interfaces with instruments (Fig. 2.2b) that measure the actuator's mechanical and electrical states at all times:

- **Interferometer:** An SP 2000 interferometer by SIOS, with a measurement resolution of 20 pm and a range of 2 m, is used for measuring the displacements of the actuator. It requires a reflective surface to accurately measure displacement, hence the mirror included in the design of the mechanical interface (Fig. 2.2a).
- **Force Sensor:** The UF1 force sensor by LCM Systems, with a measurement accuracy of 1 mN and a range of 220 mN, is used in two ways: to measure the strain on the actuator, and to manually apply a given amount of force with the help of a micrometric screw (Fig. 2.2b) and a low stiffness mechanical interface (Fig. 2.2a).
- **Electrometre:** The Keithley 6517A electrometre serves the purpose of charge amplification, and is connected in series with the piezoelectric actuator and its power supply. While the accuracy and range of the instrument is dependant on the calibre that is used (i.e. from ± 10 nC to ± 20 μ C), the accuracy of the nC-scale charge measurement will be impacted by other considerations, e.g. proper shielding, leakage currents, etc.

The CMBP03 acutator is a multi-layered monomorph cantilever of length L and width w . Both sections of the monomorph bender are each built with $N = 12$ piezoeceric layers of height $h = 67 \mu\text{m}$, with alternating electrodes between each. The model for this actuator has been derived in [36], and its constitutive equations may be written as such:

$$\begin{aligned} \delta &= \frac{1}{32} d_{31} \frac{L^2}{h^2} V_{in} + \frac{s_{11}}{3456} \frac{L^3}{wh^3} F \\ Q &= \left(12\epsilon_{33} \frac{Lw}{h} + \frac{33}{2} d_{31}^2 \frac{Lw}{hs_{11}} \right) V_{in} + \frac{1}{32} d_{31} \frac{L^2}{h^2} F \end{aligned} \quad (2.4)$$

2.2. General model for charge-based self-sensing

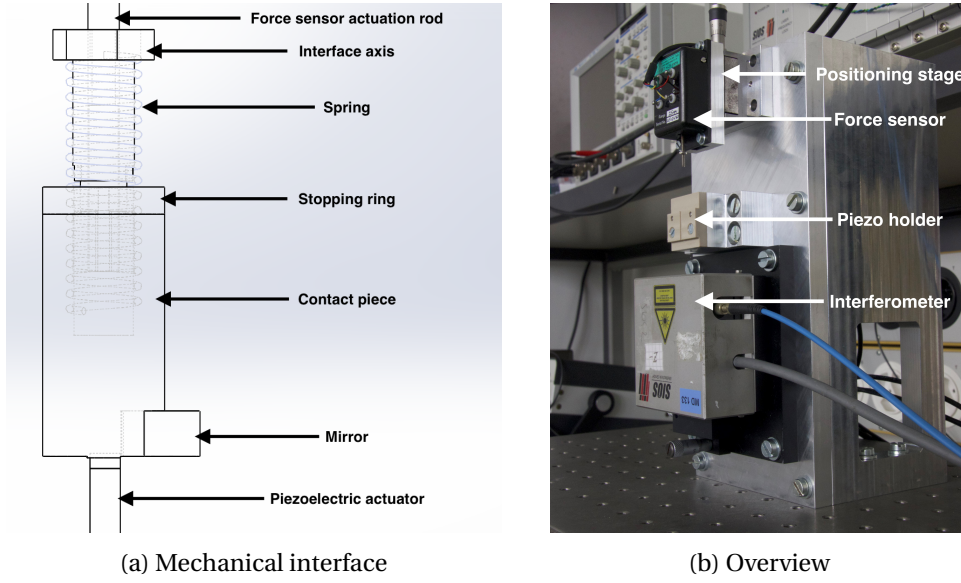


Figure 2.2 – Structure of the test bench used to characterise the CMBP03 actuator.

The model parameters have been computed for the CMBP03, and are shown in Tab. 2.1. The result of the measurements across the experiment matrix of (F, V_{in}) system inputs may be seen in Fig. 2.3, with the measured displacement in Fig. 2.3a and the measured sensing charge in Fig. 2.3b. Note that the measured displacement δ' is opposed to the model displacement of the actuator δ , such that $\delta = -\delta'$. This needs to be taken into account when identifying the actuator's parameters. Let Q_p be the component of the actuator's charge accumulation that can be attributed to the application of the force F . It is measured by connecting in parallel a reference capacitor C_r with an opposed supply voltage $(-V_{in})$, and by making sure that it matches the capacitance of the piezoelectric actuator. This allows to reduce the amount of charges that are measured, as the application of a voltage greatly increases the accumulated charges. In this manner, the expected charge range fits completely within the available calibres on the Keithley 6517A electrometre.

Through post-processing, the data for Q_p can be converted to the total amount of charges Q on the actuator through the knowledge of the value of the reference capacitor C_r and the applied voltage, such that $Q = Q_p + C_r V_{in}$. The measurement data for both δ and Q are fitted to a plane, as the general model is assumed to be linear by definition:

$$\begin{aligned}\delta_{[nm]} &= -8.9E^{-14} - 486.1 \cdot V_{in}[V] + 17.54 \cdot F_{[mN]} \\ Q_{[nC]} &= -44.89 + 331.1 \cdot V_{in}[V] - 0.4074 \cdot F_{[mN]}\end{aligned}\tag{2.5}$$

The fit for the displacement δ is satisfactory, as the average residue is negligible in face of the other fitting coefficients. The same cannot be said for the charge measurement however, with an average residue of -44.89 nC. This was to be expected, as nC-scale measurements are sensitive to several parameters: leakage currents, bias current of the charge amplifier, and

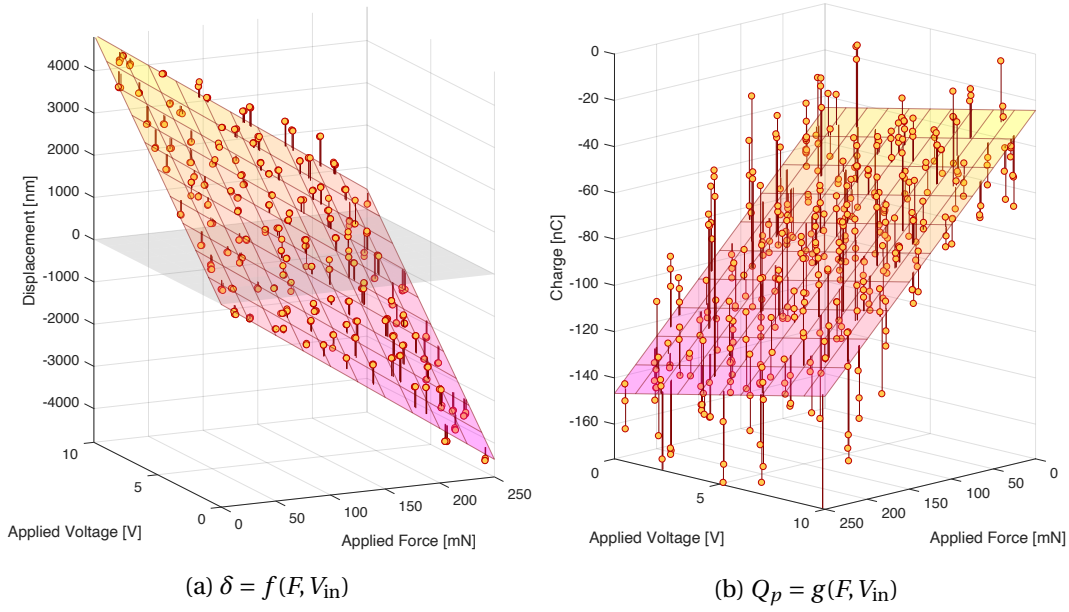


Figure 2.3 – Results of the CMBP03 characterisation.

Table 2.1 – Model predictions, measured values, and relative error for the parameters of the constitutive equations of the CMBP03 multi-layer bender.

Parameter	Unit	Model	Measured	Error
K	mN/ μ m	52	57	9.6%
C_p	nF	398	331	20.2%
β_δ	pC/mN	-521	-486	6.7%
β_Q	pC/mN		-407	21.9%

non-linearities of the piezoelectric material such as hysteresis and creep. Moreover, the measurement of the voltage applied to the actuator and the reference capacitor presented noise, which made the post-processing of Q_p to determine Q less accurate. Despite this offset and the apparent measurement noise in Fig. 2.3b, the fit is still convenient enough to determine the model parameters empirically. The experimental value of the model parameters in Eq. 2.4 may be extracted from the equations of the fitted planes in Eq. 2.5. The resulting parameters are shown in Tab. 2.1 alongside the model predictions. The β_δ and β_Q parameters refer to the β estimates provided by the displacement and the charge measurement respectively. A relative error of 21.9% between measurements and model predication is satisfactory, considering that the properties of the piezoelectric material are provided with a tolerance of $\pm 20\%$.

These measurements validate the model predictions for the commercial actuator. It shows that the general model mainly described by three parameters, i.e. K , C_p , and β , may be used to describe the state of piezoelectric actuators. With a valid form of general model in hand, it is now possible to use it in more advanced modelling techniques.

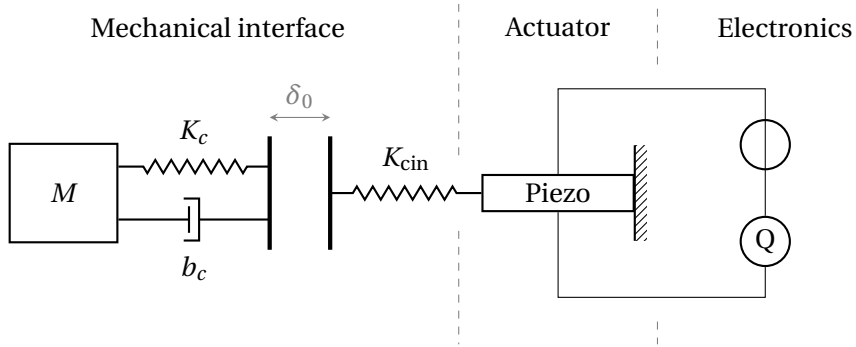


Figure 2.4 – Graphical representation of the full system considered for bond graph modelling.

2.3 Dynamic modelling of a piezoelectric self-sensing system

Bond Graph Modelling (BGM) is an elegant approach to understanding complex systems where multiple domains of physics interact. It is a top-down approach which aims to model a system by considering the flow of power between its components, and it introduces the concept of computational causality. This is useful as it allows the bond graph user to derive the constitutive equations of complex systems with ease. The constitutive equations generated by bond graph models are typically differential equations, and are thus particularly well suited to explain the dynamic behaviour of a system. A brief introduction to bond graph modelling is provided in Appendix B of this thesis. For a deeper understanding of the subject matter, it is suggested to refer to the excellent works of Borutzky [4], Gawthrop [15], and Karnopp [33].

The BGM approach is considered for the dynamic modelling of piezoelectric SSA systems. The novelty of this tool applied to piezoelectric SSA might provide further insight into the relationship between the design parameters of an actuator and the sensorless estimation performance, all while helping understand the physics that drive this kind of electromechanical system. A straightforward implementation of this type of model for a charge-based self-sensing system shall be demonstrated in this section. For a complex system, the bond graph can be built by studying each of its subsystems and by connecting their respective bond graphs together. The complete system that will be studied in this section is illustrated in Fig. 2.4. It features three subsystems: the piezoelectric actuator, its drive electronics, and the mechanical interface. The latter is comprised of the target object to be manipulated coupled with an element simulating its contact stiffness, and of the compliant mechanism supporting the piezoelectric actuator. The following paragraphs will detail the establishment of the BGM for each system component, followed by a complete BGM representation of the system.

2.3.1 Piezoelectric actuator modelling

Modelling a piezoelectric actuator with the bond graph approach necessitates an inspection of the power-conjugated variables at play. As manifested in the equations of piezoelectricity, a piezoelectric transducer behaves simultaneously as a spring in the mechanical domain and as



Figure 2.5 – Graphical representation of the multiport C node for the piezoelectric actuator.

a capacitor in the electrical domain, with energy being exchanged between the two domains. The efforts related to the mechanical and electrical domains, respectively the force F and the applied voltage V_{in} , can be tied to a generalised displacement, respectively the displacement δ and the accumulated charge Q . If the piezoelectric actuator is considered massless, the system representing it may therefore be considered as a multiport C node, with F and V_{in} as efforts, associated to the flows $\dot{\delta}$ and \dot{Q} .

The multiport C store approximating the piezoelectric actuator is illustrated in Fig. 2.5 in two equivalent representations. Notice that both power bonds connected to this node are oriented towards it. This implies that the piezoelectric actuator does not merely convey energy from one physics domain to another like most transducers, but instead it stores energy and exchanges it with its surrounding environment. Multiport nodes other than transformers (**TF**) and gyrators (**GY**) have not been discussed previously when introducing bond graph models, and thorough theoretical definitions may be found in [4] [15]. They behave much like the 1-port C store nodes that have been discussed in that their constitutive equations may be written in matrix form as follows:

$$\mathbf{q} = \Phi_C(\mathbf{e}) \quad (2.6)$$

where \mathbf{q} is a vector of generalised displacements, \mathbf{e} a vector of their associated efforts, and Φ_C a matrix defined by the constitutive equations of the multiport C node.

This form of constitutive equations for the multiport C node of the piezoelectric actuator are readily available in the present context. Indeed, the constitutive equations of the general model for charge-based SSA that have been discussed earlier in this chapter may be identified with the expression in Eq. 2.6:

$$\underbrace{\begin{pmatrix} \delta \\ Q \end{pmatrix}}_{\mathbf{q}} = \underbrace{\begin{pmatrix} K^{-1} & \beta \\ \beta & C_p \end{pmatrix}}_{\Phi_C} \underbrace{\begin{pmatrix} F \\ V \end{pmatrix}}_{\mathbf{e}} \quad (2.7)$$

In bond graph modelling, energy stores must be considered as energy conservative. This can be verified by one of two methods defined by the reciprocity condition. The first is to verify that Φ_C is a symmetric matrix. The second, which is a corollary to the first, is to verify the following condition imposed on all efforts and generalised displacements of the node:

$$\frac{\partial e_i}{\partial q_j} = \frac{\partial e_j}{\partial q_i} \quad (2.8)$$

The Φ_C matrix in Eq. 2.7 verifies both of these conditions. These constitutive equations are

2.3. Dynamic modelling of a piezoelectric self-sensing system

therefore adequate for an energy store, and the multiport C node considered to approximate the piezoelectric actuator is appropriate. Due to the Φ_C matrix being invertible, it is possible to calculate its inverse Φ_C^{-1} and express the constitutive equations in the form of $\mathbf{e} = \Phi_C^{-1}(\mathbf{q})$. Let Δ be the determinant of Φ_C , leading to the following constitutive equations:

$$\Phi_C^{-1} = \frac{1}{\Delta} \begin{pmatrix} C_p & -\beta \\ -\beta & K^{-1} \end{pmatrix} \quad \ni \quad \Delta = \frac{C_p}{K} - \beta^2 \quad (2.9)$$

$$F = \frac{C_p}{\Delta} \delta - \frac{\beta}{\Delta} Q \quad V_{in} = -\frac{\beta}{\Delta} \delta + \frac{1}{K\Delta} Q \quad (2.10)$$

These equations can now be used to deduce the bond graph model of the piezoelectric actuator. This is done by expanding the multiport C element into a transformer conveying the exchange of energy between the electrical and mechanical domains. This transformer can then be connected to 1-port C stores in each physics domain through a 0-junction or a 1-junction, depending on which power conjugated variable must be propagated. The model can be represented in up to four equivalent models according to two design considerations:

- The first of these considerations is the direction of the power conveyed by the transformer: commonly, the power is directed from the mechanical to the electrical domain in the case of sensors, and from the electrical to the mechanical domain in the case of actuators. In the context of piezoelectric SSA, even though the piezoelectric material is also used for its sensing properties, it mainly functions as an actuator.
- Secondly, it has to be decided in which physics domains the 0-junction and the 1-junction will be placed. This is merely a matter of which power conjugated variables need to be propagated throughout the model for convenience, and will largely depend on how the actuator's bond graph will be connected to other systems's bond graphs.

Given the actuator convention for the direction of the power conveyed by the transformer, the two types of model that can be derived for the multiport C node are illustrated in Fig. 2.6. On the one hand, the type 1 model (Fig. 2.6a) propagates the effort F on the mechanical side and the flow \dot{Q} on the electrical side. On the other hand, the type 2 model (Fig. 2.6b) propagates the flow δ on the mechanical side and the effort V_{in} on the electrical side. What becomes apparent in these two models are the internal effort and flow power conjugated variables that describe the power exchanges that are internal to the piezoelectric actuator. They provide an enhanced understanding for the piezoelectric actuator working in a self-sensing system. For instance, the V_p component of the voltage apparent in the type 1 model (Fig. 2.6a) corresponds to the electrical field resulting from a strain that is sought to be measured in the voltage measurement bridge approaches presented in Chapter 1. Similarly, the \dot{Q}_p component of the current apparent in the type 2 model (Fig. 2.6b) corresponds to the charges that need to be isolated in charge-based approaches in order to provide an estimate of displacement. A summary of all these power conjugated variables and their meaning is given in Tab. 2.2.

Chapter 2. Framework for the development of sensorless piezoelectric actuators

Table 2.2 – Intermediate power conjugated variables within the piezoelectric actuator.

Variable	Expression	Description
V_p	$-\frac{\beta}{C_p}F$	Voltage resulting from the application of a force F , in the absence of an applied voltage.
\dot{Q}_p	$K\beta\dot{\delta}$	Current resulting from a rate of strain $\dot{\delta}$, in the absence of an applied voltage.
F_p	$K\beta V_{in}$	Reaction force of the constrained actuator under an applied voltage V_{in} , in the absence of an applied force.
$\dot{\delta}_p$	$-\frac{\beta}{C_p}\dot{Q}$	Rate of strain resulting from a current \dot{Q} , in the absence of an applied force.
V_e	$V_{in} - V_p$	Component of the internal voltage contributing to the general displacement Q .
\dot{Q}_e	$\dot{Q} - \dot{Q}_p$	Reaction current to the application of an external voltage V_{in} while the actuator is constrained by a force F .
F_m	$F + F_p$	Component of the internal constraint contributing to the general displacement δ .
$\dot{\delta}_m$	$\dot{\delta} + \dot{\delta}_p$	Reaction rate of strain to the application of an external force F while the actuator is driven by a voltage V_{in} .

While both models are equivalent in terms of constitutive equations and interaction with elements connected to its power ports, a model type will be chosen that will allow to conveniently connect it with other subsystems. The piezoelectric actuator will be connected in series with its power supply and the charge amplification circuit, thus the flow \dot{Q} will be shared among these subsystems. A similar reasoning can be made for the mechanical side, as the actuator will interact with its surroundings through the application of manipulation forces; the effort F will be shared with these subsystems. On the basis of these considerations, the type 1 model illustrated in Fig. 2.6a will be used throughout the following developments.

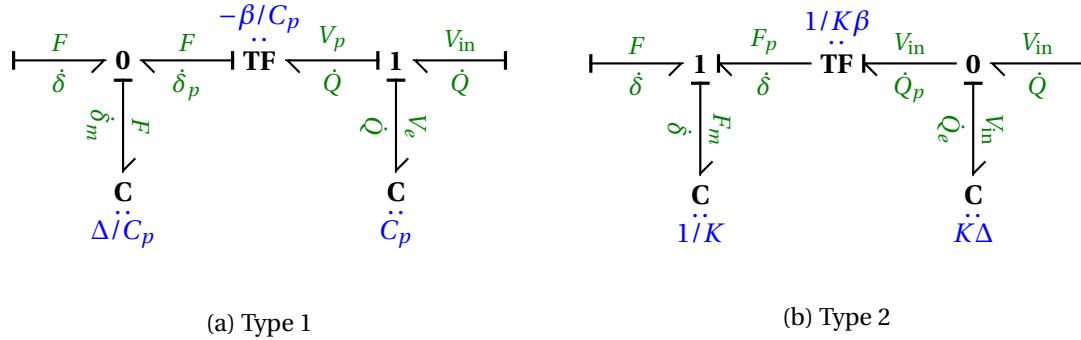


Figure 2.6 – Equivalent models expanding the multiport C node of the piezoelectric actuator.

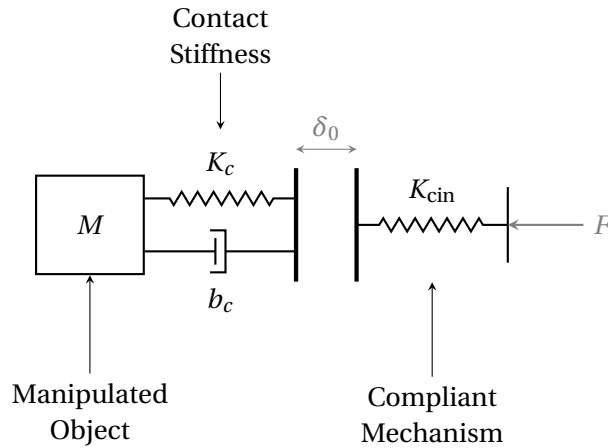


Figure 2.7 – Overview schematic of the mechanical interface.

2.3.2 Mechanical interface modelling

The mechanical interface subsystem consists of multiple components which might be present in a microrobotic manipulation task. Illustrated in Fig. 2.7 are the various components that will be considered as part of the interface:

- **Sample target:** The object that is the very subject of the micro-manipulation task. It is considered to have a mass labelled as M . If the mass is sufficiently great for the momentum produced by the actuator to be considered inconsequential, it may be considered grounded for the simplification of this model, i.e. $M \rightarrow \infty$.
- **Contact stiffness:** This element is considered massless, and simply provides a way to simulate the contact stiffness of the sample target. It consists of a spring of stiffness K_c and a damper of coefficient b_c in parallel. Should the model require simplification, they can be omitted from it provided that the contact between the micro-robot's end effector and the target sample can be considered rigid.
- **Compliant mechanism:** Piezoelectric actuators are seldom used on their own in micro-robot designs, but are instead integrated into a kinematic chain which either amplifies the displacement or the force they can provide. Such a compliant mechanism is characterised by its stiffness K_{cin} .

At $t = 0$ of the manipulation operation, the micro-robot is generally not already in contact with the target sample. The distance between the robot's end effector and the target sample is characterised in Fig. 2.7 by the parameter δ_0 . The force F applied by the piezoelectric actuator will be null until the moment it has achieved a displacement of $\delta = \delta_0$. When the displacement of the end effector $\delta = \delta_0$, the characteristic behaves like that of a spring of stiffness K_{mec} if dampers are neglected. As shown in Fig. 2.8, this implies a discontinuity in the F - δ characteristic of the mechanical interface. This would entail the need to provide two

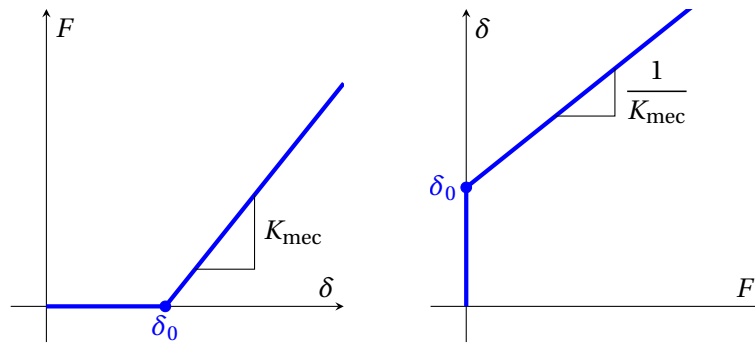


Figure 2.8 – Piecewise characteristic of the mechanical interface.

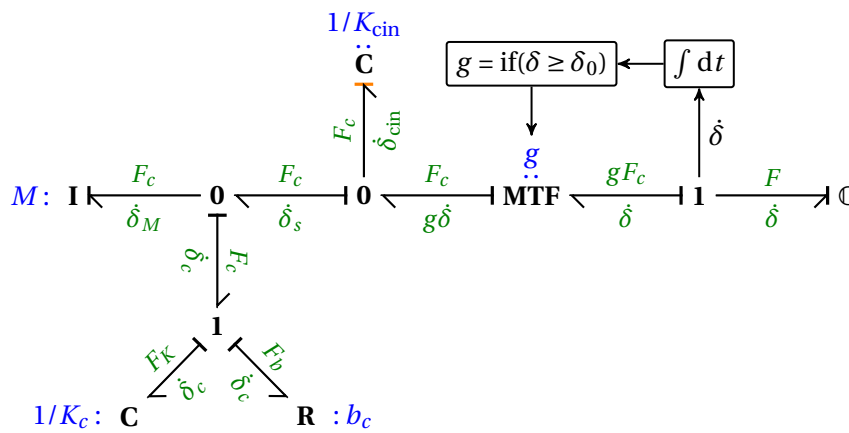


Figure 2.9 – Bond graph model of the mechanical interface.

separate models to account for the parts of the piecewise characteristic: one for the approach of the end effector to the target sample, and another once they are in contact.

Fortunately, there exists a way to provide a unique bond graph describing the complete characteristic of the mechanical interface. As demonstrated in [4], should the speed of the state transition from one mode to another be greater than that of the other dynamics present in the system, a piecewise characteristic (e.g. Fig. 2.8) may be considered a good approximation of the system. With this assumption in mind, the fast mode switching can be simulated by a modulated transformer (**MTF**) with a Boolean variable g . A signal arrow is taken from a 1-junction propagating the velocity $\dot{\delta}$, which is then integrated to provide the current displacement δ , before finally being fed into a Boolean operator. The Boolean variable g resulting from this operation is a value of 1 should the condition be verified, in this case if $\delta \geq \delta_0$. When this condition is not met, the g returns as 0 and the modulated transformer is effectively switched off, cutting off the piezoelectric bond graph from the mechanical interface bond graph.

Using this representation for the piecewise characteristic of the mechanical interface, its bond graph model is defined as illustrated in Fig. 2.9. The multiport C energy store that is connected to the extremity of the bond graph model corresponds to the piezoelectric actuator. It should

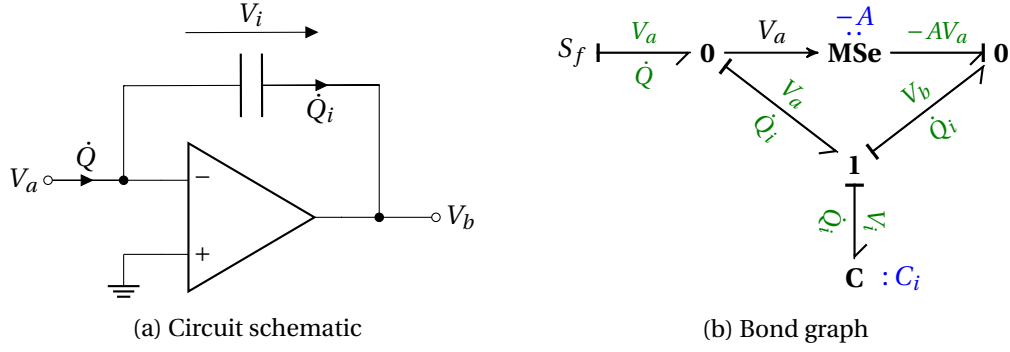


Figure 2.10 – Schematic and bond graph representations of the charge amplifier.

be noted that there are no power sources in the model of this subsystem, since energy is provided by the piezoelectric actuator, represented by a multiport C node in Fig. 2.9, when it is driven by an electrical power source. It is equally worthy of note that the causality for the compliant mechanism 1-port C node (K_{cin}) has been reversed to an integral causality. This change, marked in red, is necessary to avoid any causal conflict on the 0-junction connecting the compliant mechanism to the target sample and its contact stiffness.

2.3.3 Charge amplifier modelling

Charge-based SSA has been introduced in Chapter 1, and the topic of charge measurement has been discussed. The most common approach is to use a charge amplifier, consisting of an operational amplifier with an integrating capacitor C_i in its feedback loop (Fig. 2.10a). This approach will thus be implemented for the self-sensing system bond graph. An operational amplifier may be represented in a bond graph model as a modulated effort source (MSe) as shown in Fig. 2.10b. When the positive terminal of the operational amplifier is grounded, the input voltage V_a is taken from an input 0-junction and is fed by a signal arrows into the modulated effort source, which then amplifies it by a factor of $-A$. Let Q_i be the amount of charges accumulated by the integrating capacitor C_i and V_b be the output voltage of the charge amplifier. The following may be written when applying the constitutive equation of the 1-port C node characterising the C_i capacitor:

$$\dot{Q}_i = \frac{d}{dt} (C_i V_i) = -C_i \left(1 + \frac{1}{A}\right) \dot{V}_b \quad (2.11)$$

In ideal conditions, the operational amplifier has a high gain such that $A \rightarrow \infty$, and no bias current are present on its input terminals such that $\dot{Q}_i = \dot{Q}$. The output voltage of the amplifier is thus written as follows:

$$V_b = -\frac{1}{C_i} Q \quad (2.12)$$

To increase the dynamic range of the charge measurement, a reference capacitor C_r supplied

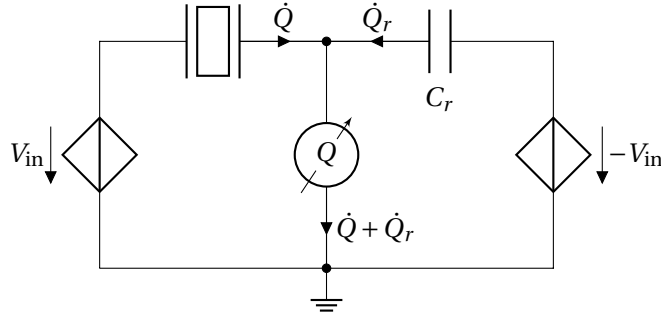


Figure 2.11 – Considered piezoelectric drive and charge measurement circuit.

by an opposed voltage $-V_{in}$ is usually included in the drive circuit (Fig. 2.11). In this setup, the current that is integrated by the charge amplifier is equal to $\dot{Q}_i = \dot{Q} + \dot{Q}_r$. The charge Q accumulated by the piezoelectric actuator has a mechanical component which depends only of the applied force F , as well as of an electric component which depends only of the applied voltage V_{in} . Depending on actuator design, the latter may end up being several orders of magnitude greater than the mechanical component of the charge, upon which charge-based SSA relies. When the reference capacitor C_r approximates as accurately as possible the internal capacitance of the piezoelectric C_p , the electric component of the charges is cancelled out. This results in an increased dynamic range for the charge measurement, as the integrating capacitor C_i will saturate less quickly.

2.3.4 Complete bond graph model

With the description of the separate subsystems as bond graph models now in hand, the complete bond graph of the self-sensing system can now be assembled by connecting the bond graphs together. The result of this combination may be seen in Fig. 2.12. The causalities of the 1-port C energy stores characterised by C_p , Δ/C_p , C_r and K_{cin} have all been changed from integral to differential to avoid causal conflicts on their adjacent 0- and 1-junctions.

A force and displacement estimator with a feedback loop to the controlled voltage sources has been connected to the output of the charge amplifier to represent the control scheme of the self-sensing system. More details could be brought into the model, and more specifically into the bond graph of the piezoelectric actuator. Up to this point, developments have assumed energy conservative and linear characteristics for this type of transducer. However, in practice, the linearity is impacted by parasitic effects such as hysteresis and creep. Some publications such as [60] have attempted to design bond graphs that model the behaviour brought forward by these phenomena: a Kelving-Voigt model is used to design the creep bond graph, and a Maxwell-Slip model is used to design the hysteresis bond graph. For the sake of brevity of the mathematical developments that will ensue, the phenomena of creep and hysteresis are neglected. They are complex phenomena that cannot be modelled analytically rather than empirically, and are thus incompatible with the analytical approach provided here.

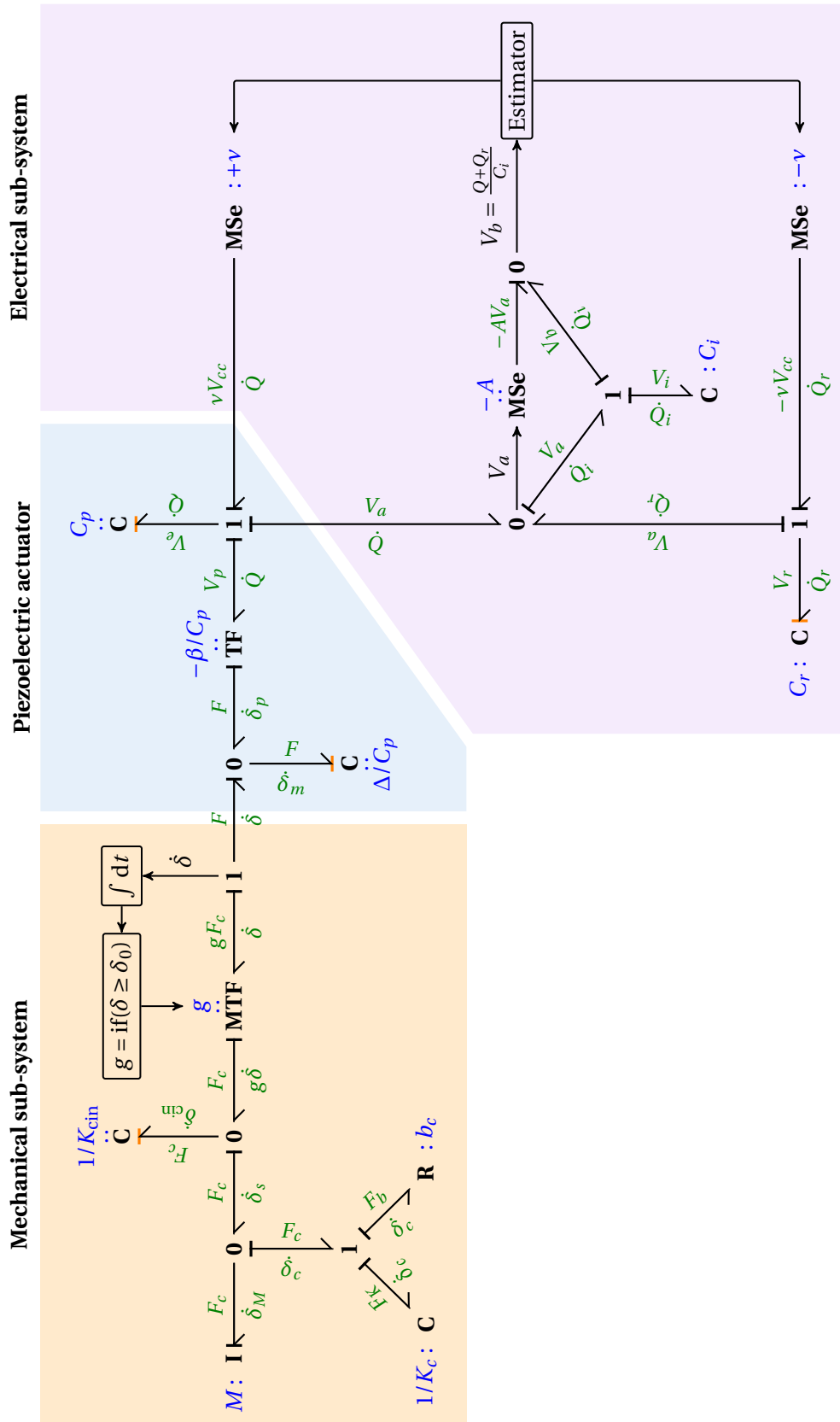


Figure 2.12 – Complete bond graph model of the self-sensing system with feedback loop.

Another simplification that has been made, due to the use of the general model in Section 2.2, is that the actuator consists of a single block of piezoelectric material. In reality, piezoelectric actuators are stacked to produce increased displacements for a given applied voltage. Other publications such as [53] have sought to model each piezoelectric layer as a separate bond graph, and to assemble all these layer bond graphs together. These approaches could be used to expand on the complete bond graph shown in Fig. 2.12. However, a well designed and accurate model for the self-sensing piezoelectric actuator accounts for these layers, and the bond graph can be simplified accordingly by using the general form of the model.

2.4 Evaluation of piezoelectric self-sensing capabilities

Following its definition in Fig. 2.12, the complete bond graph of the self-sensing system provides a powerful tool for assessing various aspects of its inner workings. Deriving the equations of the system from its bond graph and solving the resulting system of equations allows for a user to determine the total energy of the system, given the knowledge of the energy stores that are represented in the bond graph. In the same manner, under specific use cases for the self-sensing system, the bond graph may also be used to provide constitutive equations that will describe the manipulation parameters, i.e. displacement and force. Finally, the bond graph may be used to derive dynamic state equations of the system in the form of $\dot{\mathbf{x}} = \mathbf{Ax} + \mathbf{Bu}$, where \mathbf{x} is the state vector and \mathbf{u} the input vector of the system. This approach allows the bond graph user to solve the dynamic equations in a typical state-space problem, paving the way to robust force and displacement controllers. The system's bond graph model will be used to assess the feasibility of self-sensing with piezoelectric actuators. This will serve to underline the possible tradeoffs in actuator design that will need to be made in order to achieve high precision sensorless estimation.

2.4.1 Case study: Approach and manipulation of a high mass sample

To provide an example of the application of bond graphs while examining the self-sensing capabilities of piezoelectric actuators, it is proposed to consider a typical case study. When the actuator is at rest, i.e. $F = 0$ and $V_{in} = 0$, at the beginning of an operation, the assumption will be made that micro-manipulation tasks are divided into two phases.

- **Approach phase (a):** The end effector of the actuator at rest is set within a given distance to the sample target defined as δ_0 . During this phase, the applied voltage V_{in} is gradually increased so that the end effector will approach the sample target, while the self-sensing estimator will track the displacement δ . The operation transitions into the next phase once the end effector of the actuator has travelled a distance of $\delta = \delta_0$.
- **Contact phase (b):** The end effector is in contact with the surface of the target sample of mass M , and the exerted manipulation force F exerted is now controlled by the applied voltage. During this phase, a minute displacement δ still occurs as the compliant

2.4. Evaluation of piezoelectric self-sensing capabilities

mechanism and the target sample's surface are deformed. The self-sensing estimator at that point will be able to track both thanks to the measurement of charge and voltage.

The problem is simplified by neglecting the damping nature of the sample's surface, resulting in the contact stiffness K_c being connected in series with the compliant mechanism's stiffness K_{cin} . The equivalent stiffness K' and the total system stiffness K_e may thus be written as:

$$K' = \left(\frac{1}{K_c} + \frac{1}{K_{cin}} \right)^{-1} \quad K_e = \left(\frac{1}{K} + \frac{1}{K'} \right)^{-1} \quad (2.13)$$

Furthermore, it is assumed that the target sample's mass M is great enough that the momentum produced by the actuator may be considered inconsequential. This implies that the target sample will not be moved by the actuator, and the latter shall only apply a force on it. Note that further studies may be done with a defined mass M , and that they shall be required to study the design of dynamic force control algorithms for the actuator. However, the previous assumption is sufficient for a clear discussion on the separate force and displacement estimation capabilities of self-sensing piezoelectric actuators. Based on the previous assumptions, the complete bond graph illustrated in Fig. 2.12 may be simplified as seen in Fig. 2.13. From the mechanical side of the bond graph, the following equations can be written:

$$F = \frac{C_p}{\Delta} \int \dot{\delta}_m dt \quad (2.14) \quad \dot{\delta}_k = -\frac{\dot{F}}{K'} \quad (2.17)$$

$$\dot{\delta} = -\dot{\delta}_k - \dot{\delta}_M \quad (2.15) \quad \dot{\delta}_p = -\frac{\beta}{C_p} \dot{Q} \quad (2.18)$$

$$\dot{\delta}_m = \dot{\delta} + \dot{\delta}_p \quad (2.16) \quad \dot{\delta}_M = 0 \quad (2.19)$$

Similarly, the following equations may be defined from the electric side of the bond graph:

$$\dot{Q} = C_p \dot{V}_e \quad (2.20)$$

$$V_p = -\frac{\beta}{C_p} F \quad (2.21) \quad V_{in} = V_e + V_p \quad (2.22)$$

The equations pertaining to the approach phase of this case study, denoted by the subscript a , may be trivially derived from the general form of the self-sensing model defined in Sec. 2.2:

$$\begin{aligned} F_a(t) &= 0 \\ \delta_a(t) &= \beta V_{in}(t) \\ Q_a(t) &= C_p V_{in}(t) \end{aligned} \quad (2.23)$$

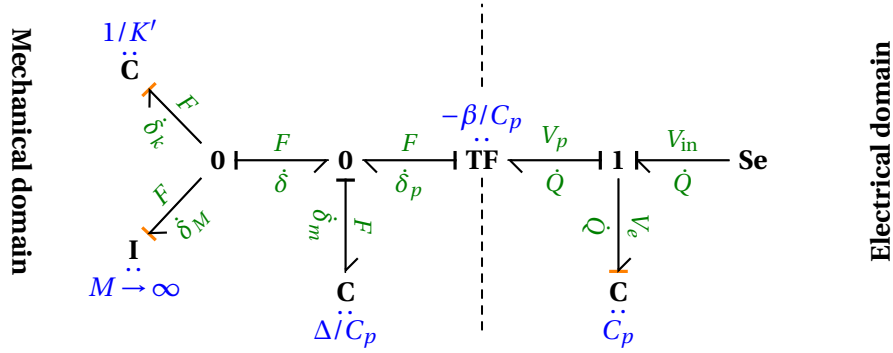


Figure 2.13 – Simplified bond graph of the piezoelectric actuator in contact with a sample.

From the set of equations Eq. 2.20 – 2.22, and according to the linear properties of differentiation, the following equation for the current may be established:

$$\dot{Q} = C_p \dot{V}_{in} + \beta \dot{F} \quad (2.24)$$

The expression of the force is found by integrating $\dot{\delta}_m$ in Eq. 2.14. The latter rate of displacement may be obtained by combining the bond graph equations Eq. 2.15 – 2.19 with the expression of the current in Eq. 2.24. This leads of the following development:

$$F(t) = -\frac{\beta C_p}{\Delta} \int_{t_0}^t \dot{V}_{in}(t) dt - \left(\frac{\beta^2}{\Delta} + \frac{C_p}{\Delta K'} \right) \int_{t_0}^t \dot{F}(t) dt \quad (2.25)$$

This integral is solvable on the condition that the boundary conditions at $t = t_0$, the moment the piezoelectric actuator is set into contact with the target sample, are known. Since the displacement of the actuator at that point in time is $\delta = \delta_0$, the following boundary conditions may be derived from Eq. 2.23:

$$F(t = t_0) = 0 \quad V_{in}(t = t_0) = \frac{\delta_0}{\beta} \quad (2.26)$$

Finally, the equations pertaining to the contact phase of this case study, denoted by the subscript b , may be established. Solving the integral in Eq. 2.25 with the proper boundary conditions and then using the new expression of the force in Eq. 2.15 and Eq. 2.24 yields:

$$\begin{aligned} F_b(t) &= K_e \delta_0 - K_e \beta V_{in}(t) \\ \delta_b(t) &= \left(1 - \frac{K_e}{K'} \right) \delta_0 + \frac{K_e}{K'} \beta V_{in}(t) \\ Q_b(t) &= \beta K_e \delta_0 + \left(C_p - \beta^2 K_e \right) V_{in}(t) \end{aligned} \quad (2.27)$$

2.4. Evaluation of piezoelectric self-sensing capabilities

Table 2.3 – Actuator parameters for the CMBP03 and the NAC2011-H11.

Parameter	Symbol	Unit	CMBP03	NAC2011-H11
Stiffness	K	mN/ μ m	51	761
Compliant stiffness	K_{cin}	mN/ μ m	255	3805
Capacitance	C_p	nF	398	80
Leakage resistance	R_L	G Ω	4	38
Charge coefficient	β	pC/mN	522	49

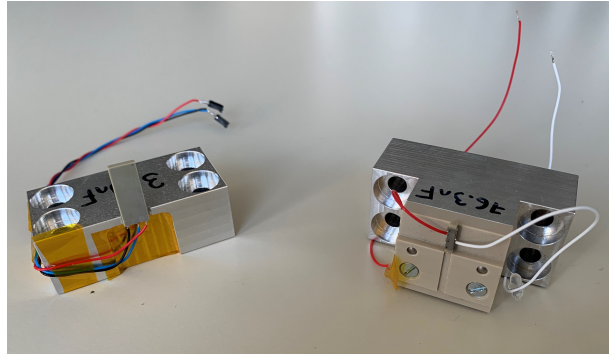


Figure 2.14 – Considered actuators for the case study: Noliac CMBP03 multilayer bender (left), and Noliac NAC2011-H11 multilayer linear actuator (right).

Simulation of the actuator state

Before proceeding with a discussion on the self-sensing possibilities brought forward by piezoelectric actuators, a simulation based on the previously defined case study is proposed. The purpose of this simulation is to observe the evolution of the state of the piezoelectric actuator, i.e. the force F , the displacement δ , and the accumulated charge Q , during the approach and contact phases of the case study. This will provide a basis of comparison between the simulated estimator's outputs and the actual values for the state of the actuator.

Two commercial piezoelectric actuators available on the market at the date of the publication of this thesis will be considered for this simulation. The two actuators of varying topologies, both manufactured by Noliac, are the CMBP03 multilayer cantilever and the NAC2011-H11 multilayer stack that have been discussed in Sec. 2.2, and illustrated in Fig. 2.14. The former provides bending motion while the latter provides linear motion. While both offer similar ranges of motion in the order of the μ m, they have been chosen due to their vastly different actuator parameters, namely capacitance, stiffness, and charge coefficient β . The measured parameters for both of these actuators may be found in Tab. 2.3. For this simulation, the compliant mechanisms associated with each actuator will arbitrarily be assigned a stiffness equal to $\times 5$ its respective stiffness.

In the simulated case study, the end effector of each actuator is set within a distance of $\delta_0 = 1 \mu\text{m}$ of the target sample. It is assumed that the contact stiffness of the target sample is

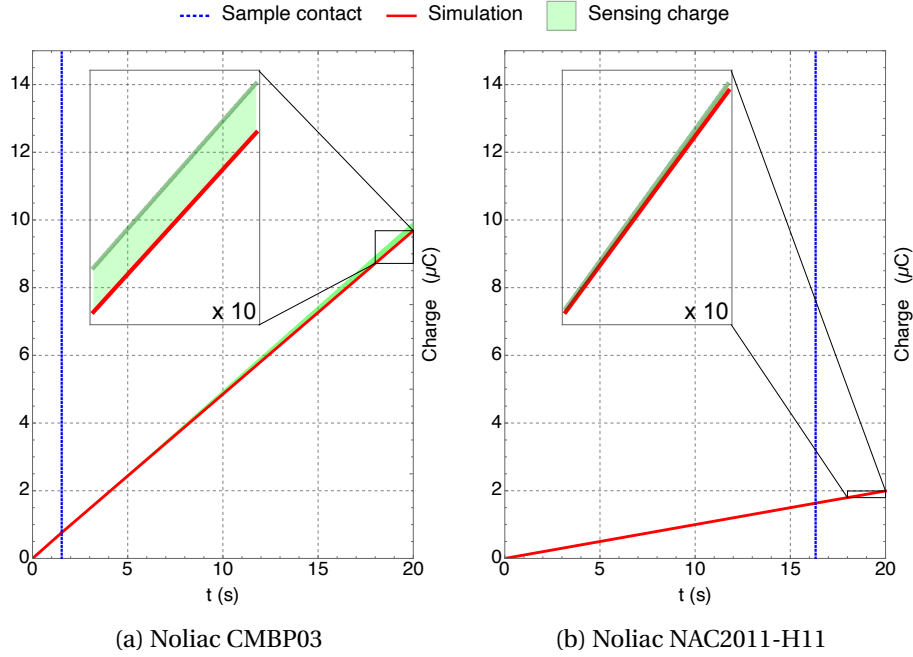


Figure 2.15 – Manipulation simulation with the Noliac CMBP03 and custom actuators.

significantly greater than that of the actuator or its compliant mechanism, and will therefore be neglected during the contact phase. To mitigate estimation inaccuracies caused by the charge measurement when discussing the self-sensing prospects of both actuators, it is proposed to drive both actuators with the same voltage levels, and for the same duration. The actuators are therefore supplied with a ramping voltage that linearly increases from 0 V to 25 V in a time frame of 20 s. The result of this simulation can be seen in Fig. 2.15 for the two candidate actuators. As expected, due to the difference in charge coefficients β , the CMBP03 reaches the target sample earlier (i.e. $t_0 = 1.53$ s) than the NAC2011-H11 (i.e. $t_0 = 16.32$ s).

The simulated curves (Fig. 2.15) for the charge of both actuators are seemingly linear, but their slope is slightly altered after making contact with the sample. This is due to the fact that the accumulated charge has an electrical component caused by the application of the drive voltage, and a mechanical component caused by the stress on the piezoelectric material. The green area of the charge curves in Fig. 2.15 corresponds to the mechanical component of the total accumulated charge. This charge, referred in the following paragraphs as the sensing charge, is the information that needs to be extracted by the self-sensing system in order to evaluate the force F and the displacement δ . The plots in Fig. 2.15 serve well to illustrate how the electrical component of the charges caused by the capacitive nature of piezoelectric actuators is greater than the sensing charge by several orders of magnitude. This is why the charge measurement is one of the most critical aspects of charge-based self-sensing.

The evolution of the state other state variables, δ , and F , calculated through Eq. 2.27, falls within expectations (Fig. 2.17). The displacement increases linearly until contact, after which

the slope is modified due to the total system stiffness. Even though the end effector has made contact with the target sample, the piezoelectric actuator continues to deform and compresses the compliant mechanism. As for the force, it remains null until contact, after which it increases linearly along with the increase in voltage.

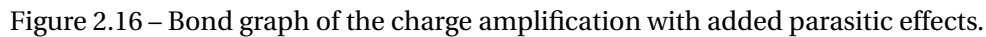
Simulation of the force and displacement estimation output

To understand the critical nature of the charge measurement, the case study is complemented with a simulation of it accounting for typical errors that arise with this type of approach. Force and displacement estimations as they would be implemented in a self-sensing system are provided on the basis of this simulated charge measurement, providing grounds for discussing the potential for self-sensing piezoelectric actuators in micro-robotics. To establish the equation for the simulated charge measurement, it is necessary to describe the phenomena that affect it. The two parasitic effects that will be considered in these paragraphs are the bias current i_b and the leakage current \dot{Q}_L , defined as follows:

- **Leakage current:** Despite piezoelectric materials featuring high resistances, typically in the order of the $G\Omega$, leakage currents may be observed. In quasi-static applications, the presence of leakage currents over long periods of time will cause the charge amplification to drift significantly from the intended sensing charge.
- **Bias current:** Measuring instruments making use of operational amplifiers are affected by bias currents, albeit of small amplitude (i.e. fA – nA). This bias current is added to the current \dot{Q} originating from the piezoelectric actuator, and also contributes to a measurement drift over time observed in the charge amplifier.

Both effects have been added to the bond graph model of the charge amplifier subsystem (Fig. 2.16). The bias current is modelled on a bond graph as a flow source adding a current of i_b to the input of the charge amplifier. The chosen value for this bias current is taken from the worst case value provided by the Keithley 6517A electrometre manual, as this is the instrument that has been used throughout this thesis' experiments for charge measurements. The leakage resistance is modelled by a resistor R_L connected to the piezoelectric actuator in parallel. On a bond graph, this is equivalent to connecting both the R node of R_L and the piezoelectric subsystem to a 0-junction, which propagates the input voltage. The leakage current therefore results from a voltage drop of V_{in} across this resistor. In order to provide an approximation of each considered actuator's leakage resistance, data will be taken from Hooker's study on piezoelectric material properties [20]: a steady resistivity on the order of magnitude of $10^9 \Omega/\text{cm}$ has been measured at frequencies of 100 Hz for temperatures between -150°C and 50°C . From this, the leakage resistances R_L of each actuator has been estimated thanks to the knowledge of each actuator's topology (Tab. 2.3)

As observed in the previous paragraphs, the electrical component of the charge is greater than the sensing charge by several orders of magnitude (Fig. 2.15). This justifies the use of a


$$V_{\text{out}} = -\frac{1}{C_i} \int \dot{Q}_i dt = -\frac{1}{C_i} \int (\dot{Q} + \dot{Q}_L + \dot{Q}_r + i_b) dt \quad (2.28)$$
$$Q_i = \int_{t_0}^t \dot{Q} dt - C_r V_{\text{in}} + \int_{t_0}^t i_b dt + \frac{1}{R_L} \int_{t_0}^t V_{\text{in}} dt \quad (2.29)$$
$$\begin{aligned} Q_{i,a}(t) &= C_d V_{\text{in}}(t) + i_b t + \frac{\gamma}{2R_L} t^2 \\ Q_{i,b}(t) &= \left(C_d - \beta^2 K_e \right) V_{\text{in}}(t) + \beta K_e \delta_0 + i_b t + \frac{\gamma}{2R_I} t^2 \end{aligned} \quad (2.30)$$

2.4. Evaluation of piezoelectric self-sensing capabilities

Table 2.4 – Simulation parameters of the case study.

Parameter	Symbol	Unit	Value
Experiment time	τ	s	20
Maximum voltage	V_{\max}	V	25
Voltage slope	γ	V/s	1.25
Sample distance	δ_0	μm	1
Bias current	i_b	fA	4

where C_d is the difference between the piezoelectric actuator's capacitance C_p and the reference capacitor C_r , such that $C_d = C_p - C_r$. Matching the capacitance of the piezoelectric actuator at rest is not trivial. This is not an issue as long as the reference capacitor is accurately characterised, but it is ideal that it matches the actuator as close as possible in order to reduce the capacitance difference C_d . In these simulations, it is assumed that C_r can be matched with C_p within 1% of its value. This does not affect the precision of the self-sensing system, as the C_r capacitor is only used as a means to fit the sensing charge into the dynamic range of the coulombmeter, but defining a value is necessary to proceed with the simulation.

As a reminder, the equations for a simple force and displacement estimator based on the measurements of sensing charge and applied voltage were discussed in Sec. 2.2. This estimator does not account for the parasitic effects that affect the charge measurement, therefore using the simulated charge measurement with these equations will evidence the impact of these effects on the estimations:

$$\hat{F} = \frac{1}{\beta} Q - \frac{C_p}{\beta} V_{\text{in}} \quad \hat{\delta} = \frac{1}{K\beta} Q - \frac{\Delta}{\beta} V_{\text{in}} \quad (2.31)$$

Notwithstanding the charge measurement drifts, the charges accumulated by the piezoelectric actuator are equivalent to $Q = Q_i - Q_r$. This equivalence, combined with Eq. 2.30, may be used in Eq. 2.31 to provide an equation for the simulated force and displacement estimations:

$$\hat{F}(t) = \frac{1}{\beta} Q_i(t) - \frac{C_d}{\beta} V_{\text{in}}(t) \quad \hat{\delta}(t) = \frac{1}{K\beta} Q_i(t) + \frac{K\beta^2 - C_d}{K\beta} V_{\text{in}}(t) \quad (2.32)$$

Note that these estimator equations only rely on the actuator's own parameters (i.e. K , C_p , β) and on the reference capacitor C_r , but is independant of the other system parameters such as the compliant mechanism's stiffness K_{cin} or the contact stiffness K_c . This is convenient in that it allows the self-sensing system to determine the actuator state without having to characterise the objects that are to be manipulated.

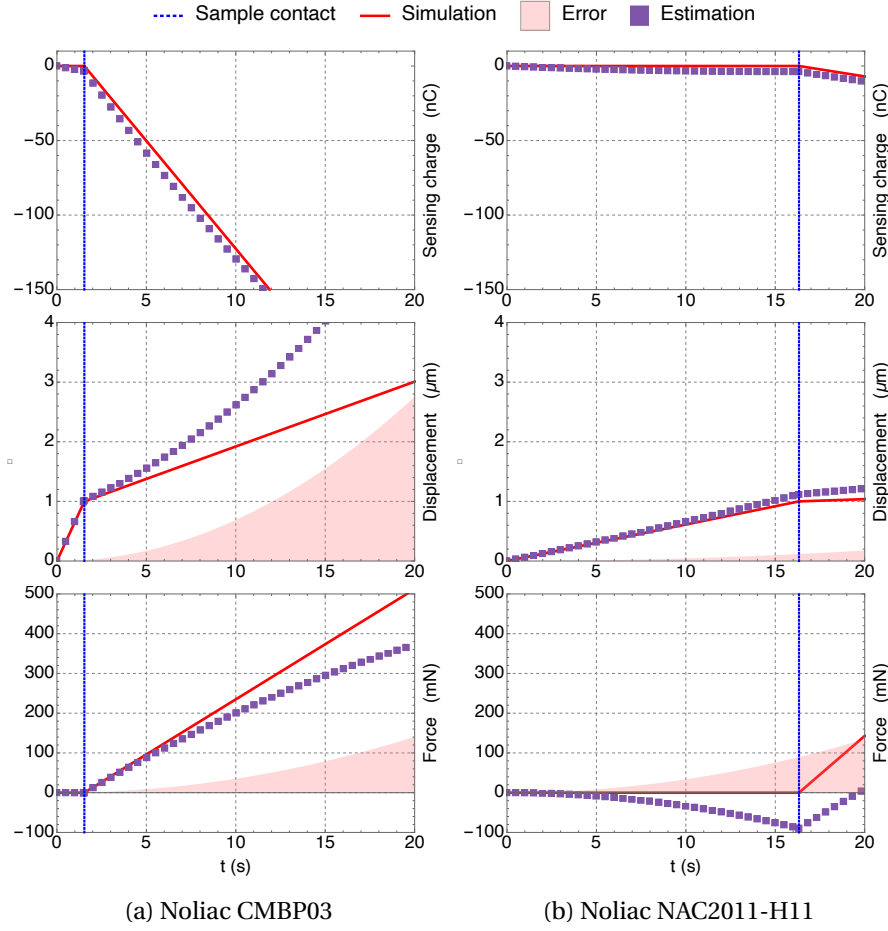


Figure 2.17 – Simulated force and displacement estimations for the case study.

2.4.2 Discussion on the tradeoff of actuator design and self-sensing performance

The estimator functions in Eq. 2.32 have been used to simulate the estimator output for the CMBP03 and NAC2011-H11 actuators in this case study. The results are provided in Fig. 2.17. The parameters that have been used to generate the simulated curves are provided in Tab. 2.4. It has been stated that the most critical aspect of the charge-based SSA approach is the charge measurement. More specifically, it is the accurate extraction of the sensing charge that withholds information on the actuator's mechanical state. From the analytical simulations for the CMBP03 and NAC2011-H11 actuators, this sensing charge for the target application of the simulation is typically in the range of 10 nC – 100 nC for displacements up to 3 μm and forces of up to 500 mN. Depending on the target applications (i.e. lower displacements and forces) and the actuator design, the sensing charge may even be lower than this.

The estimation simulation (Fig. 2.17) illustrates how important it is to compensate for the parasitic currents that affect the extraction of the sensing charge. The measurement of the sensing charge, which corresponds to the output of the charge amplifier in the topmost graph

of Fig. 2.17, shows a slight drift over time caused by the parasitic currents. The difference in capacitance C_d will also add a drift between the integrated charge Q_i and the actual sensing charge, albeit not a problematic drift since it can be compensated at the level of the estimator (Eq. 2.32 so long as C_r is properly characterised. This drift will cause the charge amplifier to saturate faster¹, reducing the dynamic range of the charge measurement.

The CMBP03 multilayer bender is the most flexible of the two actuators, featuring a lower stiffness and a greater β . However, its large piezoelectric layer area of $21 \times 7.9 \text{ mm}^2$ cause it to have a lower leakage resistance and a greater capacitance, making it more prone to charge measurement drift. In terms of displacement, it provides a quick approach to the target sample for the same driving signal ($t_0 = 1.53 \text{ s}$). The displacement error for the bender remains low during the approach phase, however it accumulates swiftly after that point. After $t = 20 \text{ s}$, the relative error approaches 100% of the actual displacement, rendering the displacement estimation unusable. As for the force, the relative error is lower than 1% for the first 5 s of the simulation, and remains lower than 30% after $t = 20 \text{ s}$.

The NAC2011-H11 multilayer linear actuator has a greater stiffness and a lower β coefficient, causing it to reach the target sample at a slower pace ($t_0 = 16.32 \text{ s}$). Thanks to its smaller piezoelectric layer area of $2 \times 2 \text{ mm}^2$, it features a greater leakage resistance and a lower capacitance. The displacement estimation accuracy is more promising than that of the bender, as the maximum relative error after $t = 20 \text{ s}$ is under 20%. The same could not be said for the relative error of the force estimation, as it is greater than 100% for most of the simulation.

To better understand the impact of actuator parameters on these estimation errors, a closer look at the analytical expressions of the errors should be taken. It can be demonstrated that this expression remains identical for both phases of the case study, and that for a ramping drive voltage in the form of V_{in} it can be written as follows:

$$\epsilon_\delta = \delta(t) - \hat{\delta}(t) = -t^2 \frac{\gamma}{2KR_L\beta} - t \frac{i_b}{K\beta} \quad \epsilon_F = F(t) - \hat{F}(t) = -t^2 \frac{\gamma}{2R_L\beta} - t \frac{i_b}{\beta} \quad (2.33)$$

Some conclusions can be made with regards to actuator parameters that affect self-sensing accuracy. From Eq. 2.33, it is apparent that for increased F and δ estimation accuracy, the leakage resistance R_L and the β coefficient both need to be as high as possible. Additionally, the actuator stiffness K also affects the displacement estimation accuracy, as a greater stiffness lowers the estimation error ϵ_δ . This is apparent with the better estimation results for the NAC2011-H11, with a stiffness greater than the CMBP03 stiffness by one order of magnitude. The fact that the capacitances C_r and C_p do not appear in Eq. 2.33 corroborates with the earlier statement that those only affect the dynamic range of the measurement, as long as they are both properly characterised.

¹For instance, the widest calibre offered by the Keithley 6517A electrometre is $\pm 2 \mu\text{C}$, with the smallest being $\pm 10 \text{ nC}$. Being able to use smaller calibers without saturating the charge amplifier brings increased resolution to the charge measurement, and therefore to the actuator state estimation.

Note that the examples in Fig. 2.17 show the results that would be obtained without compensating the parasitic currents, and that the error in estimations may be reduced with such compensations. Serious efforts to implement accurate charge-based self-sensing must account for some form of compensation to increase the long term accuracy. It is, however, a complex matter to accurately characterise currents that are in the fA – nA range, and errors over long periods of measurement are to be expected.

2.5 Conclusion

So far in the scientific literature pertaining to charge-based SSA, a concise effort to build a framework for understanding their performance hasn't been witnessed. This chapter provides such an approach to charge-based self-sensing by offering a bottom-up construction of piezoelectric SSA theory. As an introduction to this theory, a general model compatible with any type of piezoelectric actuator has been defined. The form of this model offers the convenience of deriving the estimator equations for the displacement and the force. This general model has been verified experimentally with a test bench aiming to characterise a commercial actuator, showing that the model is accurate within 22% of the measured data. This relative error can be attributed to the fact the properties of the piezoelectric material are provided by the manufacturer with tolerances of $\pm 20\%$. To that end, it has been noted that further characterisations of actuators following that model should require systematic testing across batches of actuators to provide a statistical appreciation of the model fit.

Following up on the presentation of a general model, a new angle of study for self-sensing piezoelectric actuators has been proposed. The Bond Graph Modelling (BGM) approach has been taken to provide dynamic models for a complete piezoelectric SSA system. This complete system is comprised of the piezoelectric actuator, the manipulated object, and the drive and measurement electronics. The causal aspect of bond graphs provides differential equations describing the system energetically, providing a sense of the multi-physics interactions that occur between the sub-components of the complete system. While BGM have been used to formulate a theoretical understanding, their use may be expanded later on to derive the system's response to a given control input in the frequency domain. Therefore, the BGM approach laid out in this chapter may be used to design robust controllers for sensorless actuators. The theory provided by bond graphs has been then used to study a typical use case for sensorless piezoelectric actuators in micro-robotics, paving the way to a discussion between actuator morphology and self-sensing performance.

From the moment the general model was established with the actuator's parameters, i.e. K , C_p , and β , it has been hypothesised that the design parameters and topology of an actuator will greatly influence the self-sensing performance. The simulation resulting from this case study has been applied to two different commercial piezoelectric actuators: Noliac's CMBP03 bender and NAC2011-H11 linear actuator. The simulated outputs of the SSA estimator (Fig. 2.17) offer different results and prospects for each of the two actuators, despite their similar displacement

and force ranges. In broad terms, it can be said that the NAC2011-H11 multilayer linear actuator with greater stiffness is more suitable for displacement estimation, while the CMBP03 multilayer bender with lower stiffness is more suitable for force estimation. In reality, the self-sensing prospects of one given actuator design is more complex than merely considering the β , K or R_L parameters. The latter not only depend of the piezoelectric material's properties, but also of the actuator's topology and type of deformation, i.e. compression/traction, flexion, shear deformations.

With this newfound comprehension of piezoelectric SSA theory in hand, the next step of this research has been to provide a methodology to design optimal self-sensing piezoelectric actuators for given applications. It is clear that the force application and displacement requirements will greatly vary from one type of practical application to another, so too will the sensorless estimation requirements.

The following publications by the author are related to this chapter:

- Masson, L., Civet, Y., Germano, P., and Perriard, Y. (2017). Design of a generalised charge-based self-sensing model for quasi-static piezoelectric actuators. In *2017 20th International Conference on Electrical Machines and Systems (ICEMS)*, pages 1–6, Sydney, Australia. IEEE

3 Novel approach to high resolution self-sensing actuator design

3.1 Introduction

With the introduction of Self-Sensing Actuation (SSA) theory, it has been shown that the morphology and design parameters of piezoelectric actuators are critical in determining their self-sensing performance. Most works of piezoelectric SSA in the scientific literature presented in Chapter 1 make use of readily available commercial actuators to implement their approach. While the results provided by these implementations are promising in terms of estimation accuracy, greater results could be obtained by using appropriately designed actuators. Hence the proposal for the development of a self-sensing actuator prototype starting from the ground up, using analytical models as discussed in Chapter 2.

Before designing a prototype, the scope of its actuation and self-sensing capabilities should first be defined in order to properly constrain the design. To that end, experiments are undertaken on samples that could be typically manipulated in micro-robotic applications. These experiments seek to determine the required resolution for the force and displacement estimations so that the actuator may fulfil its tasks without the need for external sensors. The minimum actuator performances (e.g. blocking force, free displacement stroke) are also defined, as a tradeoff might need to be studied between these two different types of performances.

With some order of magnitude for the estimation resolutions in mind, it is then possible to proceed with the prototype modelling and design. The modelling is based on an actuator morphology that is considered to be suitable for the studied micro-robotic samples. The novelty of the modelling approach consists in considering the number of layers of the stacked actuator as a design variable that may be tuned in order to influence the final actuator parameters. Finally, the design based on the actuator model may be performed by attempting to maximise predefined design goals. The maximisation of these goals represented by an objective function is constrained by requirements on the actuator performance and by the boundaries of the design parameters.

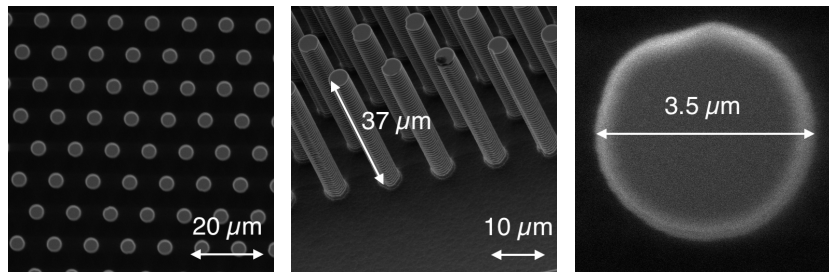


Figure 3.1 – SEM images of the micro-pillars.

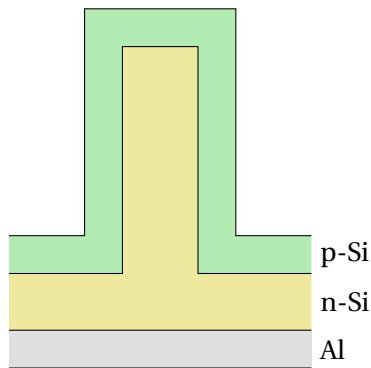


Figure 3.2 – Cross-sectional schematic of a micro-pillar.

3.2 Defining a scope for self-sensing piezoelectric actuation

Before pursuing the endeavour of designing a self-sensing actuator for micro-robotic applications, it is necessary to have a grasp on the orders of magnitude for the displacements and forces at play at first. Hence the initial step of studying samples that could potentially be the target of micro-robotic manipulation, in order to delimit the scope of the self-sensing and actuation needs of the task.

The samples that have been considered for these tests are silicon micro-pillars that are $37\text{ }\mu\text{m}$ in height and $3.5\text{ }\mu\text{m}$ in diameter. These micro-pillars are arranged in a high density "forest", as illustrated in Fig. 3.1. As seen in the cross sectional schematic in Fig. 3.2, the outer surface of the micro-pillars consists of p-type doped silicon (green), and the interior consists of n-type doped silicon (yellow). The bottom of the wafer is coated by an aluminum electrode (gray), serving as an electrode to the P-N junction that is the micro-pillar. By connecting the probes of a measuring instrument to the top of a micro-pillar and to the bottom electrode of the wafer, one may characterise this individual micro-pillar by means of I-V curves. Special care has been taken to ensure that no oxydation of the micro-pillars would take place, as this would hinder the accuracy of their electrical characterisation.

The battery of experiments that have been performed on these micro-pillars may be divided into two categories, which are defined as follows:

- **Mechanical tests** have been undertaken to determine the upper boundaries of the scope of force and displacement control. By mechanically characterising the micro-pillars, the maximum force causing the breaking points of the pillars and the electrical probe are sought out. To that end, compression and flexure tests have been produced by a nanoindenter within the chamber of a Scanning Electron Microscope (SEM).
- **Electrical tests** have been conducted on a large number of samples in order to establish a relationship between the applied force and the quality of the electrical measurements. The purpose of these tests is to understand the resolution of the sensorless force estimation that would be required to properly characterise these micro-pillars. These tests are also performed in a SEM chamber, and a thin electrode adapted to these micro-pillars has been attached to the nanoindenter. The electrical characterisation is performed with a Keithley 2400 electrometer.

3.2.1 Mechanical tests

A diamond point is attached to the nanoindenter in order to manipulate the micro-pillars without affecting their compliance. The nanoindenter features a closed loop control on both position and force, and simultaneously records measurements for both of these states. All the tests are performed within the chamber of a SEM in order to visually position the diamond point with respect to the pillars. To mechanically characterise the micro-pillars, compression and flexure tests have been performed on them using the diamond point mounted on the nanoindenter while recording the displacement and the force perceived by the latter. These deformations are illustrated in the SEM imagery of Fig. 3.3. A strain-stress curve of the samples may then be established, providing information on the stiffness of the samples, and more importantly on their breaking point.

Compression tests were the simplest experiment that could be performed on the micro-pillars. In this procedure, the diamond point is initially positioned on top of the pillar with the help of SEM imagery (Fig. 3.3). It is then moved downward at a steady rate in a position control loop until the visible rupture of the pillar prompts the end of the experiment. The experiment has been reproduced across seven different micro-pillars. With the measurements of the force and the displacement perceived by the nanoindenter, a type of stress-strain curve may be established for these micro-pillars. An example of four of those curves may be seen in Fig. 3.4. The experiment presented great repeatability in the results, as the average of the estimation Young's modulus for all pillars is 137 GPa for a standard deviation of 6.2 GPa. Finally, the yield strength for all micro-pillars has been observed to be in the 22–24 mN range.

Contrary to the compression tests, flexure tests are slightly more complicated to perform due to the dimensions of the diamond point. To perform these tests, the micro-pillars were slightly preloaded axially with the diamond point, then the latter was displaced by the nanoindenter laterally to induce the flexure of the micro-pillar (Fig. 3.3). The axial load is kept constant throughout the experiment by adapting the vertical displacement of the diamond point, and

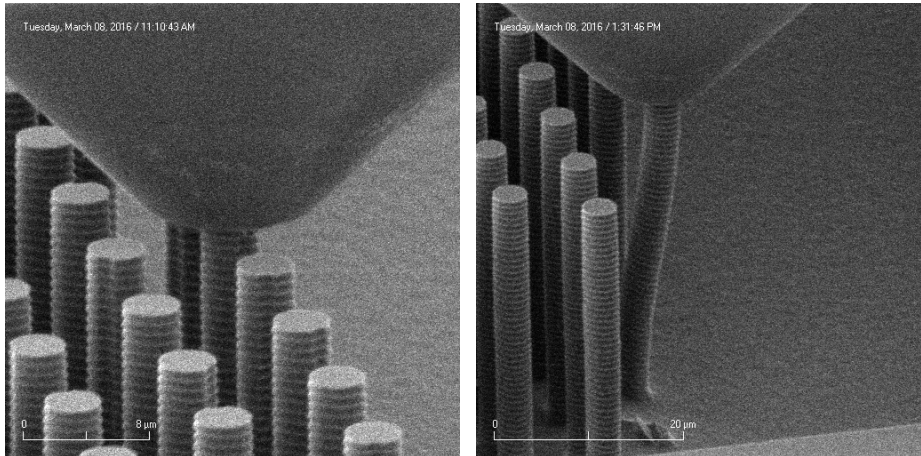


Figure 3.3 – Micro-pillars deformed in compression (left) and in flexure (right).

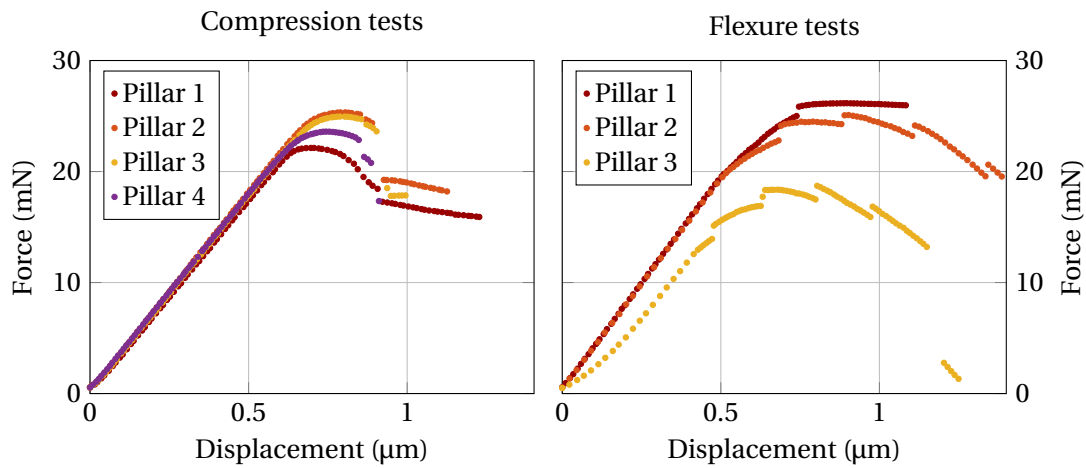


Figure 3.4 – Mechanical tests on multiple micro-pillars.

the experiments is ended as soon as the micro-pillar has ruptured. The characterisation curves on three of the successful flexure attempts are shown in Fig. 3.4. The results of the flexure tests show less repeatability than that of the compression tests: a stick-slip motion can be seen in some iterations as the diamond point slides across the top of the micro-pillar (e.g. Pillar 3 in Fig. 3.4). The average Young's modulus determined from the flexure tests is of 139 GPa for a standard deviation of 9.8 GPa. The yield strength of the micro-pillars in flexure deformation is equally similar to that of compression deformation, and is estimated to be of 20 mN.

While no mechanical characterisation has been performed on the thin titanium probes used for the electrical measurements, the forces that would deform the probe past its elastic limit have been qualitatively estimated. This has been done by progressively loading the top of a micro-pillar with the electric probe mounted on the nanoindenter, and visually evaluating the presence of plastic deformation on the probe tip. The experiment has been ended when plastic deformation was apparent at a force of 2 mN and a displacement of 2.75 μm (Fig. 3.5).

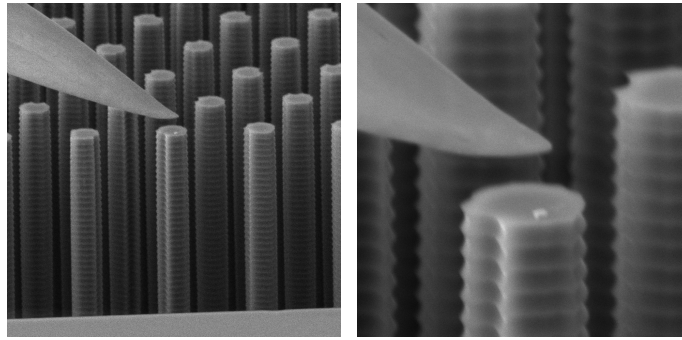


Figure 3.5 – Plastic deformation of the titanium probe tip.

Correlation between SEM imagery and the load measurement data points to an elastic limit of approximately 1.15 mN for the titanium probe tip. It is also possible to observe damage on the surface of the micro-pillar's top (Fig. 3.5, right photo). Therefore, to use these titanium probes to electrically characterise the micro-pillars, the applied force must be controlled without exceeding this elastic limit.

3.2.2 Electrical tests

For the electrical tests, the diamond point is replaced by a titanium probe which is mounted at a fixed 30° angle with respect to the surface of the micro-pillar's top. This probe is connected to the high terminal of an electrometer, while the low terminal of the latter is connected to the bottom electrode of the silicon wafer. The electrometer that is used for the I-V characterisation is a Keithley 2400, and is capable of sourcing a voltage while measuring the current. Through voltage sweeps, it is possible to draw the I-V curves that electrically characterise the P-N junction of a micro-pillar. The tests are still executed within the chamber of a SEM in order to visually position the probe on top of the micro-pillars (Fig. 3.5).

To outline a relationship between the force applied by the probe and the quality of the electrical contact, a micro-pillar has been loaded at different loads and subjected to I-V sweeps. To compare the various I-V curves, the dynamic resistance at a given voltage is evaluated for each sweep as the basis for a comparison. The estimation of the dynamic resistance at 0.5 V for different I-V sweeps shows that increasing the applied force past a certain point has no effect on increasing the repeatability of the electrical characterisation. Aside from the considerations on the chemical compositions of the probe and the sample, this seems to indicate that as long as the load is sufficient, it is possible to do accurate electrical measurements on the micro-pillar. The minimal amount of force that is required for this task has been identified to be of 0.3 mN, as no current would pass through the measurement electronics below this limit.

The repeatability of these voltage sweeps has been assessed in two manners. The first has consisted of executing five successive voltage sweeps between –2 V and 2 V at a fixed load of 0.5 mN, and with a current cutoff of ± 0.5 A for protection. The second method varies the

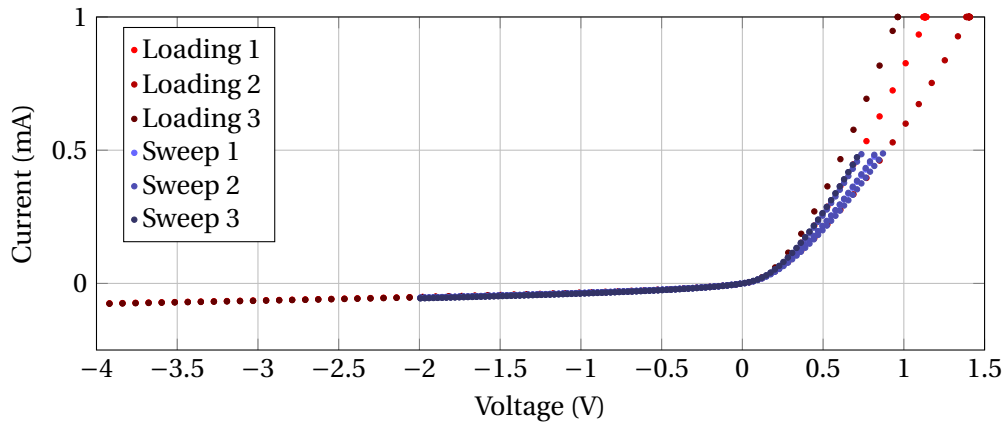


Figure 3.6 – I-V curves for the micro-pillars after successive loadings and successive sweeps.

measurement repeatability through successive loadings and unloadings of a micro-pillar: a sample is loaded with a force of 0.5 mN, a voltage sweep between -4 V and 4 V is realised, then the pillar is unloaded. The resulting I-V curves may then be compared to extrapolate the effect of mechanical fatigue on the electrical measurement. These loading and unloading steps are repeated ten times, with the voltage sweeps being done during each iteration. The resulting I-V curves for some iterations of both of these experiments are plotted side by side in Fig. 3.6. The mean dynamic resistance evaluated at 0.5 V is of 984Ω . With the given applied force and probe angle parameters, it can be said that the repeatability of the measurement with successive sweeps is coherent, and that a force of 0.5 mN is suitable. It can be noted however that the measurements with successive loadings of the micro-pillar do lead to a decreased measurement repeatability, indicating that a high positioning accuracy and repeatability is necessary.

3.2.3 Discussion of the results

Valuable information on the actuation and sensing scope of the self-sensing actuator has been obtained through measurements with samples that would typically be manipulated by such a device. Conclusions can be made for the displacement and the force separately.

Given the dimensions of the micro-pillars, being $37 \mu\text{m}$ in height and $4 \mu\text{m}$ in diameter, a free stroke on the order of at least $25 \mu\text{m}$ is proposed for the prototype actuator that is to be designed. A higher range would be advantageous for more flexibility in the device's potential use cases, however this can be remedied by achieving coarse positioning with another, less precise, actuator. Not much information has been obtained in these measurements on what would constitute an acceptable position estimation resolution. However, given the displacements required to characterise the micro-pillars with stress-strain curves in Fig. 3.4, an accuracy of $0.1 \mu\text{m}$ would be ideal for the self-sensing actuator's estimation requirements.

Given the yield strength of the micro-pillars, an actuator that would need to manipulate

and characterise these samples would need to apply forces of up to 24 mN. However, the force must be controlled with accuracy. On the one hand, no current will flow through the sample until sufficient force is applied. The required amount of force to establish a proper electrical contact has been identified at approximately 0.3 mN. On the other hand, instruments like thin platinum probes used in electrical measurements are damaged beyond forces of up to 1.15 mN. Ideally, the self-sensing piezoelectric actuator would need to aim for a force estimation resolution in the order of 0.1 mN.

These values are to be taken into account in the following chapters, especially when coming up with an actuator design for the self-sensing prototype.

3.3 Analytical modelling of a piezoelectric cantilever

In section 3.2, a typical case study for micro-manipulation tasks has been observed with the electrical characterisation of 25 μm long and 4 μm wide silicon micro-pillars. For such samples, and considering the thin measurement probes that were used for their characterisation, it has been concluded that the force must be controlled in a way that it does not exceed 1.2 mN, while also allowing for accurate force application within the 0.3 – 0.5 mN range. To achieve this feat, not only would a self-sensing piezoelectric actuator be required to guarantee a force sensing resolution on the order of 0.1 mN, but a low blocking force would also be desirable to protect the manipulated objects.

Additionally, some insight into the impact of actuator morphology and design, and more specifically of the resulting characteristics K , C_p , and β , on self-sensing performance has been provided in Chapter 2. It had been observed that a greater stiffness is only beneficial to displacement estimation. While a lower stiffness had no impact on the force estimation, it lowers the blocking force of the actuator. This results in lower manipulation forces, such that low stiffness actuators are more suitable for the handling of fragile objects. This line of thought applied to the micro-pillar case study, along with the large presence of this morphology in the self-sensing scientific literature (e.g. [27] and [46]), has led to the choice of monomorph benders for the development of a high resolution self-sensing actuator. In addition to the convenience in terms of low stiffness that this morphology comes with, in contrast with traction or shearing stack actuators, the SSA implementations in the scientific literature provide points of reference. The performance of the actuator designed for self-sensing will be able to be compared with other self-sensing bender examples.

The first step to designing a high accuracy self-sensing actuator is to derive its constitutive equations from its defined morphology, and therefore the expression of its model parameters. As the fabrication of the actuator has been taken into account as the next step, inspiration has been taken from the morphology of the Noliac CMBP03 multi-layer bender used in Chapter 2 so that the fabrication process of this commercial company may be used. The monomorph bender is illustrated in Fig. 3.7, and is a multi-layer configuration composed of $2N$ layers of piezoceramic interspersed with electrodes. These layers are divided into two areas: an upper

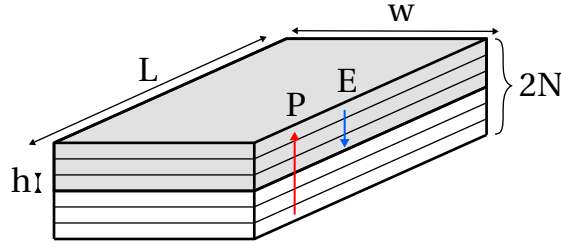


Figure 3.7 – Schematic of the piezoelectric monomorph bender [41].

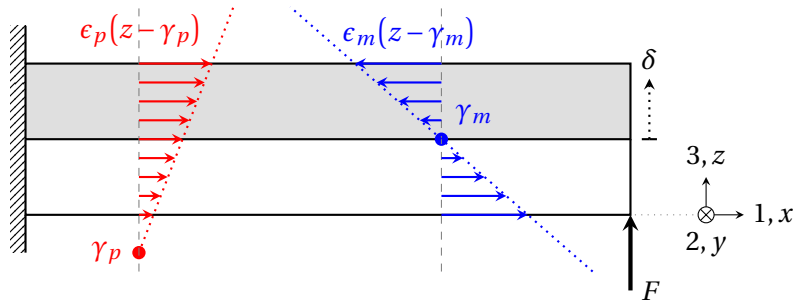


Figure 3.8 – Representation of the strains in the piezoelectric bender, due to the piezoelectric effect (red) and to the mechanical bending (blue).

area (grey) of N layers which is electrically activated by an electric field and thus deformed, and a lower (white) area of N layers which is passively deformed and which causes the flexure of the beam. As a positive electric field E in the upper area is opposed to the material's polarisation P , the area expands along its length due to the negative sign of the d_{31} piezoelectric constant. As shown in Fig. 3.7, let L be the length of the layers, w their width, and h their individual thicknesses.

The configuration of this actuator makes it possible to use it as a bimorph bender as opposed to a monomorph bender. With a bipolar supply and the coulombmeter in series to the actuator, the mechanical contributions to the charge accumulation (i.e. the sensing charge) will cancel each other out in the upper and lower active areas, shown in white and grey in Fig. 3.7. Indeed, one area would be working in compression while the other would be working in traction. Such implications indicate that separate electronics to drive and sense would be required for each area. This falls outside of the scope of this chapter, however it may be considered as a possible venue of investigation to extend the capabilities of self-sensing pieoelectric actuators further.

3.3.1 Modelling approach

As discussed in Chapter 2, the piezoelectric actuator may be considered as a system with two inputs and two outputs, coupling signals from the mechanical and electrical domains. The inputs are the force F applied on the bender's tip, and the actuation electric field E . Due to the electromechanical coupling present in piezoelectric materials, both of the output

displacement δ and the output charge Q are a function of these inputs. As per the general model for self-sensing piezoelectric actuators established in Chapter 1, the expected result of the analytical model is a system of two constitutive equations:

$$\begin{cases} \delta = \beta V_{\text{in}} + \frac{1}{K} F \\ Q = C_p V_{\text{in}} + \beta F \end{cases} \quad (3.1)$$

where the outputs δ and Q are related to the inputs through the actuator's characteristics. These are its mechanical stiffness K , its capacitance C_p , and its β coefficient.

The actuator parameters β , C_p , and K , in the constitutive equations are all to be expressed as a function of the actuator's dimensions and the material properties of the piezoelectric and electrode layers. This shall provide a level of control upon these parameters when designing the actuator. The key to determining these parameters is to express the x -coordinate strain $S_1(z)$ relative to the z -coordinate along a vertical section of the bender.

The strain is caused by two separate effects, illustrated in Fig. 3.8, with mechanical deformation on the one hand caused by the application of the force F (in blue), and piezoelectric deformation on the other hand caused by the application of an electric field E within the piezoelectric material (in red). The principle of superposition may be applied in this case, due to the supposed linearity of the piezoelectric effect, and therefore the total strain along a section of the beam may be written as the sum of the mechanical strain $S_{1,m}(z)$ and of the piezoelectric strain $S_{1,p}(z)$. The strains are to be expressed in generic forms in relation to the reference frame defined in Fig. 3.8. Respectively, the strains $S_{1,m}$ and $S_{1,p}$ are defined by the position of their neutral planes γ_m and γ_p (i.e. where the strain is null), and by their slope relative to the z -coordinate ϵ_m and ϵ_p .

A methodology for determining the two strains and, by deduction, the total strain, is represented in the schematic of Fig. 3.9. After writing the piezoelectricity theory equations for an actuator morphology, the mechanical strain is determined by considering the applied voltage V_{in} to be zero and by applying classical bending theory to the piezoelectric bender. Conversely, by considering the applied force F to be zero, the piezoelectric strain may be determined by solving Euler's laws of motion at equilibrium with the sum of the internal forces F_{int} and internal moments M_{int} within a section of the bender.

With the former demonstration for the generic form of the strain S_1 , the latter may then be inserted into the piezoelectricity equations for the actuator to derive the electric displacement field D under the effects of both the force F and applied voltage V_{in} . The amount of charges Q accumulated on the layer electrodes may therefore be deduced by applying Gauss' law to the electric displacement field D . As for the total displacement, according to bending theory, it is calculated through the double integration throughout the length L of the slope of the strain slope. By superposition, the sum of the strain slopes $\epsilon_{\text{tot}} = \epsilon_p + \epsilon_m$ is integrated.

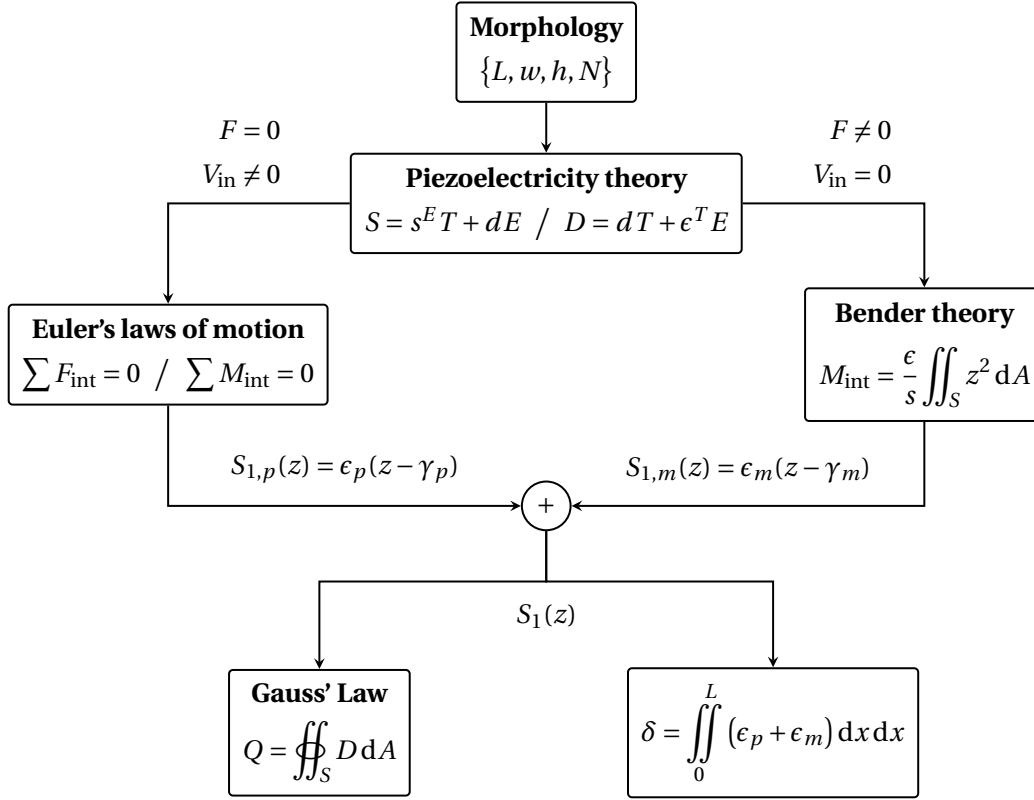


Figure 3.9 – Modelling methodology for the piezoelectric monomorph bender.

Applying the equations of piezoelectricity

The first step for modelling the piezoelectric actuator after defining its morphology is to apply the piezoelectric equations to the considered configuration (Fig. 3.9). This provides the expressions for the stress T and the electric field D in each area of the actuator (Fig. 3.7).

The piezoelectric equations are written in tensor form as such (Appendix A):

$$\begin{cases} S = s^E T + dE \\ D = dT + \epsilon^T E \end{cases} \quad (3.2)$$

where the state of the material is described by the strain tensor S , the stress tensor T , the electric displacement field D , and the electric field E . The material properties are represented in matrix form by the compliance s , the permittivity ϵ , and the piezoelectric coefficient tensor d . The superscripts T and E respectively denote a zero or constant stress and electric field when evaluating a given parameter.

The schematic in Fig. 3.8 illustrates the sign convention used for the following demonstration. The referential frame is set at the bottom of the bender, and indexes **1**, **2** and **3** respectively correspond to the **x**, **y** and **z** axes. Let the superscript u denote the active piezoelectric layers

in the upper area, and let l denote the inactive piezoelectric layers in the lower area. On the one hand, the electric field in the piezoelectric layers of the upper area can be expressed as $E_3^u = V_{in}/h$ and is opposed to the piezoelectric polarisation. On the other hand, the electric field in the piezoelectric layers of the lower area E_3^l is null. Since the upper piezoelectric layers are driven in opposition to their polarisation, the terms multiplied by the d_{31} coefficient are assigned a "-" sign. The following piezoelectricity equations may be derived:

$$\begin{aligned} S_1^u &= -d_{31}E_3^u + s_{11}T_1^u & D_3^u &= \epsilon_{33}E_3^u - d_{31}T_1^u \\ S_1^l &= s_{11}T_1^l & D_3^l &= d_{31}T_1^l \end{aligned} \quad (3.3) \quad (3.4)$$

The expressions for the stresses T_1^u and T_1^l , with the strains replaced by the generic form of the strain S_1 , may be used to determine the parameters of the strain (i.e. neutral plane and slope). With the stresses updated with the parameters of the strain equations, the equations for the electric displacement fields D_3^u and D_3^l are then used in the application of Gauss' Law. Note that only D_3^u shall be used, as the lower area is short circuited and is only used as a passive deformation layer.

3.3.2 Determination of the deformation strains

Piezoelectric strain

The parameters of the piezoelectric strain $S_{1,p}(z)$ will first be evaluated. As represented in Fig. 3.8, let γ_p be the position of the neutral plane and ϵ_p be the slope of the strain along a section of the actuator stack. In the frame of reference defined in Fig. 3.8, the total strain caused by the piezoelectric effect $S_{1,p}$ can therefore be expressed as follows:

$$S_{1,p}(z) = \epsilon_p(z - \gamma_p) \quad (3.5)$$

When considering Euler's law of momentum for a section of the beam at equilibrium, the sum of internal forces and moments is zero. From this statement, it is possible to find the expressions for ϵ_p and γ_p by solving the following system of equations:

$$\begin{cases} F_{int} = F_l + F_u = 0 \\ M_{int} = M_l + M_u = 0 \end{cases} \quad (3.6)$$

The force F_i exerted on each area of the actuator stack can be obtained by integrating the stress T_1^i across the section of the actuator stack, where i denotes the upper or lower area:

$$F_i = \iint_A T_1^i dA \quad (3.7)$$

The moment M_i on each area of the actuator stack can be expressed in a similar manner by

integrating the stress T_1^i , multiplied by the distance z to the neutral plane, across the surface of the beam section:

$$M_i = \iint_A T_1^i z \, dA \quad (3.8)$$

Using the expressions of the layer strains S_1^i in Eq. 3.3, it is possible to develop the expressions for the stresses T_1^i . These can then be used to express the forces and the moments described by Eq. 3.7 and Eq. 3.8. By using the frame of reference described in Fig. 3.8, these expressions of force and moment can be used in conjunction with the system of equation in Eq. 3.6 to find the expression of the slope of the internal strain ϵ_p and of the position of the neutral plane γ_p .

With the expressions of the stresses deduced from Eq. 3.3, it is thus possible to calculate the internal forces and moments in the upper and lower areas of the beam section. Since the number of layers N is a design variable, it is necessary to express the total forces and moments as the sums of all layers:

$$F_l = \sum_{n=1}^N \int_{\gamma_p+(n-1)h}^{\gamma_p+nh} \frac{w}{s_{11}} \epsilon_p z \, dz \quad (3.9)$$

$$F_u = \sum_{n=N+1}^{2N} \int_{\gamma_p+(n-1)h}^{\gamma_p+nh} \frac{w}{s_{11}} (\epsilon_p z + d_{31} E_3^u) \, dz$$

$$M_l = \sum_{n=1}^N \int_{\gamma_p+(n-1)h}^{\gamma_p+nh} \frac{w}{s_{11}} \epsilon_p z^2 \, dz \quad (3.10)$$

$$M_u = \sum_{n=N+1}^{2N} \int_{\gamma_p+(n-1)h}^{\gamma_p+nh} \frac{w}{s_{11}} (\epsilon_p z + d_{31} E_3^u) z \, dz$$

Finally, the total force F_{int} and the total moment M_{int} are deduced from Eq. 3.9 and Eq. 3.10. The following expressions can be given for these two internal physical quantities:

$$F_{\text{int}} = \frac{Nw}{s_{11}} (2\epsilon_p h(\gamma + hN) + d_{31} V_{\text{in}}) \quad (3.11)$$

$$M_{\text{int}} = \frac{Nw}{6s_{11}} (4\epsilon_p h(3\gamma^2 + 6\gamma hN + 4h^2 N^2) + 3d_{31} V_{\text{in}}(2\gamma + 3hN))$$

Solving the system of equations Eq. 3.6 derived by Euler's Law of momentum, along with Eq. 3.11, yields the following results for the expressions of ϵ_p and γ :

$$\epsilon_p = -\frac{3d_{31}}{4Nh^2} V_{\text{in}} \quad (3.12) \quad \gamma = -\frac{Nh}{3} \quad (3.13)$$

which yields the final expression of the piezoelectric strain caused by the actuation signal V_{in} , with respect to the reference frame defined in Fig. 3.8:

$$S_{1,p}(z) = -\frac{3d_{31}}{4Nh^2} V_{\text{in}} \left(z + \frac{Nh}{3} \right) \quad (3.14)$$

Due to the fact that the d_{31} piezoelectric coefficient is negative, the slope of the piezoelectric strain is positive (Fig. 3.8). This implies that a positive applied voltage V_{in} will cause the tip of the bender to move downwards with respect to the reference frame. It is therefore expected for δ to be negative when a positive voltage is applied in the absence of force.

Mechanical strain

The mechanical strain $S_{1,m}$ will now be evaluated. As represented in Fig. 3.8, let γ_m be the position of the neutral plane and ϵ_m be the slope of the strain. In the frame of reference defined in Fig. 3.8, the total strain caused by the mechanical deformation $S_{1,m}(z)$ can be expressed as follows:

$$S_{1,m}(z) = \epsilon_m(z - \gamma_m) \quad (3.15)$$

The assumption can be made that the bender is symmetrical and that the external force F is applied orthogonally to the bender. This prompts the statement that the neutral plane of the mechanical deformation is situated at the center of the section of the actuator stack, leading to the following expression of its position γ_m in the frame of reference:

$$\gamma_m = Nh \quad (3.16)$$

The slope of the strain ϵ_m is related to the moment of inertia I of the bending section of the actuator stack. The moment of inertia of a solid is evaluated by integrating z^2 across the surface of its section with respect to its rotation axis, i.e. the neutral plane of its flexure deformation:

$$I = \iint_A z^2 dA = \int_{-Nh}^{Nh} wz^2 dz = \frac{2}{3}wN^3h^3 \quad (3.17)$$

The assumption has been made that the bender is sufficiently thin so that the moment M is uniform across one bender section at a distance x from the bender tip. According to the frame of reference for a beam bending downward, the moment M applied to the axis of rotation of a bender section at a given x -coordinate can be written as $M(x) = (L - x)(-F)$. From bending theory, the slope of the strain ϵ_m can be expressed as follows:

$$\epsilon_m = \frac{s_{11}}{I}M(x) = -\frac{3s_{11}(L - x)}{2h^3N^3w}F \quad (3.18)$$

which yields the final expression of the piezoelectric strain caused by the application of the upward force F with respect to the reference frame defined in Fig. 3.8:

$$S_{1,m}(z) = -\frac{3s_{11}(L - x)}{2h^3N^3w}F(z - Nh) \quad (3.19)$$

The slope of the mechanical strain is negative (Fig. 3.8), indicating that a positive applied force F will cause the tip of the bender to move upwards with respect to the reference frame, in opposition to the displacement caused by the piezoelectric strain.

3.3.3 Constitutive equations of the piezoelectric actuator

Displacement

According to bending theory, one can write that the curvature of the beam is $\rho = 1/\epsilon$. By integrating the slope of the strain along the length of the bender twice, one can determine the deflection of the beam for a given position on the x -axis. Due to the orientation of the reference frame (Fig. 3.8) and the way the moment $M(x)$ was calculated, this approach yields results that would be negative. The opposite of the double integration will thus be used for the deflection within the reference frame. Note that the expression of the neutral planes γ_m and γ_p were only necessary in solving the systems of equations for the strains. They do not directly intervene in the calculation of the displacement, as the displacement is directly related to the strain slope of each bending mechanism.

Integrating the slope of the piezoelectric strain along the length of the bender twice yields the expression of the displacement of the bender at a given position on the x -axis:

$$\delta_p(x) = - \int_0^x \int_0^x \epsilon_p dx dx \quad (3.20)$$

leading to the following expression of the displacement at a given coordinate x caused by the converse piezoelectric effect, due to the application of an input voltage V_{in} :

$$\delta_p(x) = \frac{3}{8} d_{31} \frac{x^2}{Nh^2} V_{in} \quad (3.21)$$

Similarly, integrating the slope of the mechanical strain along the length of the bender yields the expression of the displacement of the bender at a given position on the x -axis:

$$\delta_m(x) = - \int_0^x \int_0^x \epsilon_m dx dx \quad (3.22)$$

leading to the following expression of the displacement at a given coordinate x caused by the mechanical deformation of the bender, due to the application of an upward force F :

$$\delta_m(x) = \frac{s_{11} x^3}{2N^3 h^3 w} F \quad (3.23)$$

3.3. Analytical modelling of a piezoelectric cantilever

The displacement of the actuator corresponds to the total deflection at the tip of the bender (i.e. $x = L$). The principle of superposition makes it possible to add the two deflections, $\delta_m(L)$ and $\delta_p(L)$, in order to obtain the total deflection $\delta(x)$. Therefore, the constitutive equation of the actuator's displacement may be deduced from Eq. 3.21 and Eq. 3.23:

$$\delta = \frac{3}{8}d_{31}\frac{L^2}{Nh^2}V_{in} + \frac{s_{11}L^3}{2wN^3h^3}F \quad (3.24)$$

Charge

The application of Gauss' Law in conjunction with the expression of the electric displacement field D (Eq. 3.26) may be used to evaluate the amount of free electrical charges accumulated around the active piezoelectric layers:

$$Q = \oint_S D \, dA \quad (3.25)$$

The electric field E is null in all the layers of the actuator stack, except for the piezoelectric layers of the upper area upon which the voltage V_{in} is applied. Since the electrical charges of the actuator will only be measured on the electrodes that are connected to the active piezoelectric layers, only D_3^u in Eq. 3.4 will be considered in the application of Gauss' Law. With the previous observations, the electric displacement in these layers can be written as follows:

$$D_3^u = \epsilon_{33}E_3^u - d_{31}T_1^u \quad (3.26)$$

As shown in Eq. 3.26, the stress T_1^u must be evaluated in order to calculate the electric displacement field. While the neutral plane was not important for the determination of the displacement, it becomes necessary to calculate the charge accumulation since it intervenes in the expression of the stress T_1^u . In Eq. 3.3, in order to determine the stress T_1^u , the strain S_1^u is replaced by the sum of the piezoelectric strain $S_{1,p}^u$ and the mechanical strain $S_{1,m}^u$:

$$S_1(z) = \epsilon_m(z - \gamma_m) + \epsilon_p(z - \gamma_p) \quad (3.27)$$

This expression of the strain is a function of the z coordinate, and therefore it cannot be used as is in Eq. 3.26 which assumes a constant strain throughout the layer. The piezoelectric material within a single layer may be considered as a stack of infinitesimally small layers, each infinitesimal layer contributing to the free charge accumulation around that layer. This hypothesis, formulated by Dunsch [10], makes it possible to use the average stress within a layer to calculate the accumulated free charge:

$$T_1(k) = \frac{1}{h} \int_{(k-1)h}^{kh} \frac{1}{s_{11}} (S_1(z) + d_{31}E_3^u) \, dz \quad (3.28)$$

Chapter 3. Novel approach to high resolution self-sensing actuator design

where k denotes the position of the layer within the bender, starting from the bottom of the stack.

The effective stress in Eq. 3.28 can be used in Gauss' Law (Eq. 3.25) to finally calculate the total amount of free charges accumulated by the active layers of the piezoelectric actuator:

$$Q = \sum_{k=N+1}^N \int_0^L \int_0^w (\epsilon_{33} E_3^u - d_{31} T_1(k)) dy dx \quad (3.29)$$

which leads to the final expression of the electrical charges:

$$Q = \left(N \frac{\epsilon_{33} L w}{h} + \frac{3}{8} \frac{L w d_{31}^2}{h s_{11}} \right) V_{in} + \frac{3}{8} d_{31} \frac{L^2}{N h^2} F \quad (3.30)$$

Full model and parameter identification

The previously developed expressions for the outputs of the piezoelectric actuator under the effect of inputs F and V_{in} form the constitutive equations for the actuator. It follows the same form as the one predicted by the general model in Chapter 2 (Eq. 3.1). The total displacement δ and accumulated charge Q represent the state of the actuator, and are written

$$\begin{cases} \delta = \frac{3}{8} d_{31} \frac{L^2}{N h^2} V_{in} + \frac{s_{11} L^3}{2 w N^3 h^3} F \\ Q = \left(N \frac{\epsilon_{33} L w}{h} + \frac{3}{8} \frac{L w d_{31}^2}{h s_{11}} \right) V_{in} + \frac{3}{8} d_{31} \frac{L^2}{N h^2} F \end{cases} \quad (3.31)$$

From these equations, the actuator parameters may be determined by comparing the system in Eq. 3.31 to the general form of the model in Eq. 3.1:

$$K = \frac{2 w N^3 h^3}{s_{11} L^3} \quad (3.32)$$

$$\beta = \frac{3}{8} d_{31} \frac{L^2}{N h^2} \quad (3.33)$$

$$C_p = N \frac{\epsilon_{33} L w}{h} + \frac{4}{3} \beta^2 K \quad (3.34)$$

As expected, the β parameter (Eq. 3.33) is the same for the displacement equation and the charge equation. As for the capacitance (Eq. 3.34), its left hand term is the expected result for the capacitance of such a bender configuration, but its right hand term is expressed as a function of β and K . While the physical significance of this right hand term could be debated, estimations based on a known actuator, the Noliac CMBP03, show that it is lower than the left

hand term by two orders of magnitude. It may be neglected in the further developments for the sake of simplifying the equations.

3.4 Self-sensing actuator design

The constitutive equations for considered bender morphology now provide a direct relationship between the actuator characteristics and its design parameters, most notably the number of layers N . Knowing the impact of the latter on the actuator characteristics has been deemed essential to providing high resolution self-sensing actuators. As stated in Chapter 2, there is a tradeoff to be made in terms of actuator stiffness and SSA performance. Not only is a high number of layers strongly related to a higher stiffness, improving the actuation performance and the self-sensing position estimation, but it also has a negative impact on the β coefficient in the case of benders. As seen in Eq. 3.33, the coefficient is inversely proportional to N .

In the following section, the process for designing a monomorph bender based on the afore-described morphology (Fig. 3.7) is laid out. After analyzing the considerations and the objectives for the design, an analytical study is used to discover the best strategy to employ for the different design parameters.

3.4.1 Design considerations and objectives

Design space

The design parameters that have an impact on the final actuator characteristic constitute the design space for the actuator. Their scope, and their boundaries, have been chosen to fit the device within a restrained volume needed for some micro-robotic applications (e.g. operation in a SEM chamber). These parameters can be divided into two categories which will be described as follows.

The first category regroups all the parameters that describe the physical dimensions of the actuator's morphology. The length L and the width w are continuous parameters that describe the planar dimensions of the layers, and consequently of the bender itself. The layer thickness h is discrete and limited to a few pre-determined values that are tied to the fabrication processes. Finally, the number of layers in each area of the bender (Fig. 3.7) N is a natural number. Due to planarity concerns when fabricating the actuator, a minimum bender total thickness of $H_{\min} = 0.35 \text{ mm}$ is required. This implies that the lowest value N can be is always tied to the layer thickness h , such that $N_{\min} = H_{\min}/(2h)$. All of the parameters describing the physical dimensions of the morphology and their scopes for this design are provided in Tab. 3.1.

The second category of parameters pertains to the properties of the piezoceramic used in the fabrication process. The piezoelectric coefficients d_{ij} , the compliance s_{ij} , and the permittivity ϵ_{ij} are such parameters, and they cannot be modified independently from one another. A piezoelectric material must be chosen, and the d_{ij} , s_{ij} and ϵ_{ij} will be a consequence of

Table 3.1 – Physical parameters of the actuator design.

Parameter	Symbol	Unit	Range
Length	L	mm	[10, 25]
Width	w	mm	[1, 10]
Layer thickness	h	μm	{20; 50; 67}
Nb. of layers	N	-	$\{N_{\min}; \dots; 20\}$

that choice. Since the choice of materials is often limited, it is not necessary to take into account the material when designing the actuator. Instead, the study of the objective functions may be performed for each of the piezoelectric materials separately, and the material with the most suitable solution shall be selected. For the calculations performed in the coming developments, the NCE51 PZT ceramic developed by Noliac will be taken into account.

Objective function of the design

Before attempting to tackle the design, a clear objective must be determined. With the example provided in this chapter, the aim is to illustrate how to design an actuator with improved SSA performance for force estimation, all while guaranteeing sufficient actuator performance for micro-manipulation tasks. The estimation of the force through charge measurement has been discussed at length in Chapter 2, and serves as the basis to improve the SSA performance of an actuator design.

The sensing charge, a component of the total charge accumulated by the actuator, is directly related to the force applied on the actuator by the β coefficient. The other component that contributes to the total accumulated charge is a byproduct of the capacitive nature of piezoelectric materials, and is directly related to the driving voltage through its capacitance C_p . When measuring and integrating the current that flows through the actuator, both of these components are detected. A reference capacitor is thus supplied with an opposed driving voltage, suppressing the capacitive component of the charge accumulation and improving the charge measurement resolution prospects of the method.

Following these observations, and based on the knowledge provided by the constitutive equations (Eq. 3.1), the design goals are twofold:

1. The β coefficient must be maximised so that the sensing component of the total charge, $Q_p = \beta F$, is increased, improving the resolution of the force estimation.
2. Despite the compensation of the electrical component of the total charge, $Q_e = C_p V_{\text{in}}$, it is preferable to minimise it with respect to Q_p to reduce estimation errors.

An objective function representing the fitness of a particular actuator design to these goals may be defined. The analytical study of this objective function within the boundaries of the design

space (Tab. 3.1) shall provide insight into the preferences of each parameter for improved SSA performance. Since the aforescribed goals aim to maximise Q_p , and minimise Q_e with respect to Q_p , the following objective function $f(L, w, h, N)$ is defined:

$$f(L, w, h, N) = -\frac{Q_p}{Q_e} = -\frac{\beta F}{C_p V_{in}} \quad (3.35)$$

Note the assignment of a "-" sign in front of the ratio of the charge components. Since Q_p is negative, due to the β coefficient being negative, the sign of the function is inverted so that the design problem may be formulated as the maximisation of the objective function, as opposed to its minimisation.

The expression of the objective function in Eq. 3.35 can be further expanded by considering the reference voltage that shall be used. Since the worst case for the Q_p/Q_e ratio would be when the voltage is at its maximum, it is proposed to consider this value for V_{in} . Since the NCE51 PZT ceramic can support a maximum electric field of $E_3^{\max} = 3 \text{ V}/\mu\text{m}$ before undergoing depolarisation, the maximum applied voltage is a function of the layer thickness such that $V_{in}^{\max} = E_3^{\max} h$. This expression for the voltage will be substituted in Eq. 3.35.

The target application for the design is manipulation tasks of μm -scale objects, compatible with the experiments that were led in Section 3.2. To that end, it was determined that a displacement of at least $\delta = -\delta_{\min} = -25 \mu\text{m}$ needs to be guaranteed, and that forces of up to $F_{\max} = 100 \text{ mN}$ can be applied by the actuator throughout this displacement range. Due to the fact that the minimal displacement that can be achieved with the current design space (Tab. 3.1) is of $122 \mu\text{m}$, it is not necessary to constrain the objective function with this requirement. The main constraint will be the applied force, and a blocking force of F_{\max} under any displacement of the full range is guaranteed under the following condition (Eq. 3.31):

$$F(L, w, h, N) = -\frac{2wN^3h^3}{s_{11}L^3}\delta_{\min} - \frac{3wN^2h^2d_{31}}{4Ls_{11}}E_3^{\max} \geq F_{\max} \quad (3.36)$$

For the sake of brevity, the terms F_{\max} , E_3^{\max} and δ_{\min} will from now on respectively be written as F , E_3 and δ . Hence this formulation for the design's objective function (Eq. 3.36–3.35):

$$\begin{aligned} \underset{L, w, h, N}{\text{maximize}} \quad & f(L, w, h, N) = -\frac{3}{8} \frac{L}{wh^2N^2} \frac{d_{31}}{\epsilon_{33}E_3} \\ \text{subject to} \quad & F(L, w, h, N) \geq F \end{aligned} \quad (3.37)$$

3.4.2 Analysis of the objective function

The objective function $f(L, w, h, N)$ (Eq. 3.37) is represented in five dimensions. The study of its evolution, along with the evolution of the force constraint (Eq. 3.36), provides insight on the strategy to adopt for each parameter to match the design goals. For the convenience of

the analytical study, it is convenient to reduce the dimensionality of the objective function. A number of simplifications can be done to achieve this. To that end, with the layer thickness h being discrete, it makes sense to consider this parameter as a constant in the following study, as each of the three values of h (Tab. 3.1) can be studied separately. This first consideration reduces the dimensionality of the problem from five to four.

Reducing the dimensionality of the design problem

As it is a natural number, considering N as a real number does not make sense in a physical terms. However, for the analytical study, the lower case n will replace N and will be considered as a real in order to study the influence of the number of layers on the evolution of the objective function. Following this study, n can be discretised as N to the value closest to the solution. The objective function curves as a function of (L, w) for different values of n may be seen in Fig. 3.10. What can be said at first glance is that the objective function is seemingly monotonous, and that the solution to the design problem may be trivial.

The dimensionality of the design problem may be reduced further by expressing one of the remaining variables (i.e. L , w , or n) as a function of the other variables. One approach that would enable this is to find a set of design points $\{L, w, n\}$ that would satisfy the force constraint while maximising the objective function. Consider the following equation, which states that the maximum applied force of the actuator is equal to the requirement of minimum blocking force across the whole free displacement range: $F(L, w, h, n) = F$. By applying the force constraint from Eq. 3.36, one can write the width w as a function of the length L and the number of layers n that would satisfy this condition:

$$w(L, n) = -\frac{4Fs_{11}L^3}{h^2n^2(3d_{31}L^2E_3 + 8hn\delta)} \quad (3.38)$$

By substituting the width w in the objective function (Eq. 3.37 by its expression in Eq. 3.38, the objective function $f(L, w, n)$ may be reparametrised into a new, three dimension, objective function $f(L, n)$. The result of this reparametrisation may be written as:

$$f(L, n) = -\frac{9d_{31}^2E_3L^2 + 24d_{31}hn\delta}{32E_3L^2s_{11}\epsilon_{33}} \quad (3.39)$$

The parametric surface illustrated in red in Fig. 3.10 represents the set of design points $\{L, w, n\}$ that satisfies the force constraint all while maximising the objective function within the design space. This parametric surface may be described using Eq. 3.38 and Eq. 3.39 as follows:

$$\begin{cases} x = L \\ y = w(L, n) \\ z = f(L, n) \end{cases} \quad (3.40)$$

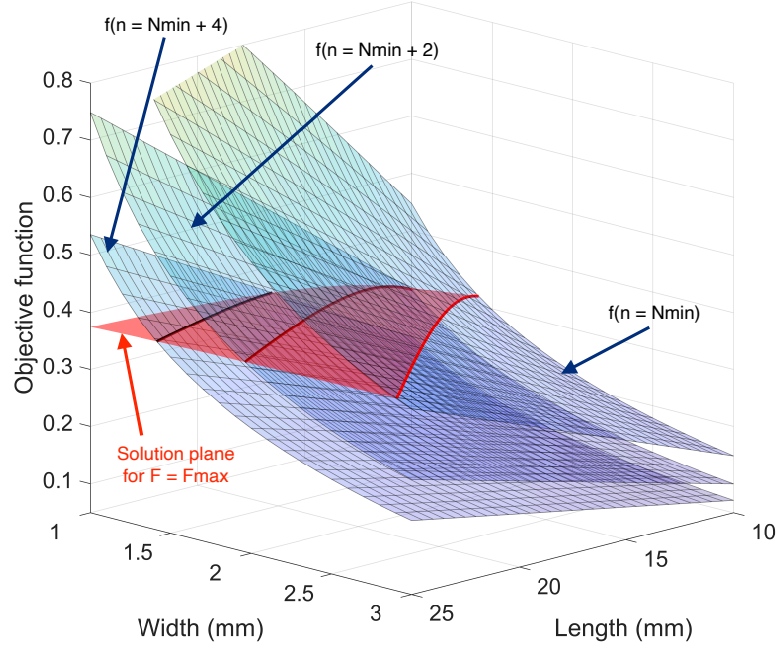


Figure 3.10 – Representation of the intersection between the objective function (blue) for different values of n with the solution plane satisfying the constraint (red).

It can be said with firm conviction that the set of design points $\{L, w, n\}$ that satisfies the $F(L, w, h, n) = F$ condition is also the one that maximises the objective function (Eq. 3.37) within that constraint. Indeed, the partial derivatives of Eq. 3.36 with respect to L , w , and n are of opposite sign to those of Eq. 3.37. This implies that attempting to modify the solution set of $\{L, w, n\}$ to maximise the objective function will also decrease the maximum applied force of the actuator below the required mechanical specification (Eq. 3.36). With the parametric surface described in Eq. 3.40, the dimensionality of the design problem has been brought from five down to three.

Study of the partial derivatives

It has been suggested that the maximisation of the objective function could be trivial, as its surface for any given n (Fig. 3.10) seemed monotonic. The same could be said for the parametric surface $f(L, n)$ (Eq. 3.40), in red in Fig. 3.10, representing the set of solutions that maximise $f(L, w, h, N)$ while guaranteeing the force constraint. This monotonicity needs to be proven before any certain claim can be made, however. To that end it is proposed to study the partial derivatives of the parametrised surface to analytically determine if it is concave, convex, or simply monotonic within the scope of the design space. First, the partial derivative of $f(L, n)$ with respect to L (i.e. x -axis in Fig. 3.10) is determined:

$$\frac{\partial f}{\partial x} = \frac{\partial f}{\partial L} = -\frac{3d_{31}nh\delta}{2E_3FL^3s_{11}\epsilon_{33}} \quad (3.41)$$

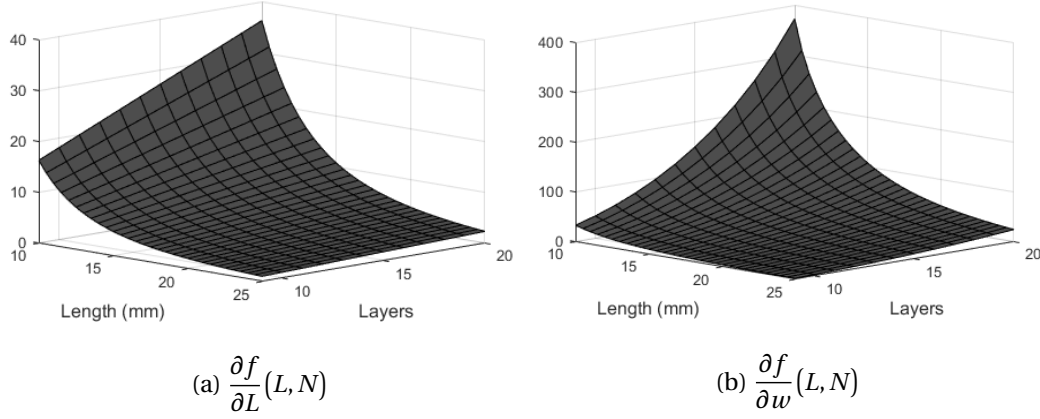


Figure 3.11 – Partial derivatives of f with respect to L and w .

Table 3.2 – Evolution of the partial derivative of f with respect to w .

n	$-\infty$	$n_{0,1}$		n_p	$n_{0,2}$		$+\infty$	
$\partial f/\partial w$		+	0	+	∞	+	0	-
$f(L, n)$		\nearrow		\nearrow	\parallel	\nearrow		\searrow

Since L and n are strictly positive by definition, the partial derivative of $f(L, n)$ with respect to L is strictly positive in the design space. It can be thus said that the parametric surface described in Eq. 3.40 is monotonic with respect to L , and increasing the latter will maximise the objective function. Finally, the partial derivative of $f(L, n)$ with respect to w (i.e. y -axis in Fig. 3.10) is determined. In this case, since w is a function of L and n , the partial derivative of $f(L, n)$ needs to be decomposed as such:

$$\frac{\partial f}{\partial y} = \frac{\partial f}{\partial w} = \frac{\partial f}{\partial n} \frac{\partial n}{\partial w} = \frac{\partial f}{\partial n} \left(\frac{\partial w}{\partial n} \right)^{-1} \quad (3.42)$$

The partial derivative of w with respect to n can be calculated from Eq. 3.38, while the partial derivative of f with respect to n can be calculated from Eq. 3.39:

$$\frac{\partial w}{\partial n} = \frac{24FL^3 s_{11}}{h^2 n^3} \frac{d_{31} E_3 L^2 + 4hn\delta}{(3d_{31} E_3 L^2 + 8hn\delta)^2} \quad (3.43) \quad \frac{\partial f}{\partial n} = \frac{3d_{31} h\delta}{4E_3 FL^2 s_{11} \epsilon_{33}} \quad (3.44)$$

Resulting in the following partial derivative of $f(L, n)$ with respect to w :

$$\frac{\partial f}{\partial w} = \frac{d_{31} h^3 n^3 \delta (3d_{31} E_3 L^2 + 8hn\delta)^2}{32E_3 F^2 L^5 s_{11}^2 (d_{31} E_3 L^2 + 4hn\delta) \epsilon_{33}} \quad (3.45)$$

Determining the sign of the partial derivative relies on finding its poles $n_{p,i}$ and zeros $n_{0,i}$:

$$n_{0,1} = 0 < n_p = -\frac{d_{31}E_3L^2}{4h\delta} < n_{0,2} = -\frac{3d_{31}E_3L^2}{8h\delta} \quad (3.46)$$

The evolution of the partial derivative of $f(L, n)$ with respect to w is summarised in Tab. 3.2. It is strictly positive within the interval $[n_{0,1}, n_p[$. Considering a length L between 10 mm and 25 mm (Tab. 3.1), and considering the material properties of the Noliac NCE51 piezoceramic, it can be shown that $n_p \in [29, 182]$. Since by definition $n \in [N_{\min}, 20]$ and $N_{\min} > 0$, it is possible to affirm that $n \in]0; n_p[$ and that the parametric surface described in Eq. 3.40 is monotonic and increasing with respect to w .

3.4.3 Design guidelines for piezoelectric self-sensing benders

From the analytical study of the objective function, multiple conclusions may be drawn regarding the design parameters. A set of solutions that both maximises the objective function and satisfies the force constraint has been evidenced, and is represented by a parametric surface (Eq. 3.40) in Fig. 3.10. The monotonicity of this parametric surface has been proven through the study of its partial derivatives with respect to (L, w) . The solution that maximises the objective function is found on the boundary of the design space visualised in Fig. 3.10.

The partial derivative of f with respect to L is strictly positive, and f is therefore monotonically increasing with respect to this parametr. The length L must be set to the upper boundary of its scope in the design space (Tab. 3.1). It can also be shown that the partial derivative of f with respect to h is strictly negative and, by the monotonically decreasing characteristic of f , imposes that h should be set to the lower boundary of its scope (Tab. 3.1). As for the width, the partial derivative of the objective function with respect to w is strictly positive in the interval of the design space, indicating that w should also be maximised. Unlike the other parameters, w may not simply be chosen on the boundary of its scope, since it is bound to the force constraint by Eq. 3.38, and is tied to the choice of the free parameters L , h , and N . Instead, the parameter N must be chosen so that it maximises w . The strategy to adopt is highlighted by looking at the partial derivative of w with respect to N (Eq. 3.43) which is strictly negative in the $[N_{\min}, 20]$ interval. The width w is therefore monotonically decreasing with respect to N , and the latter should be set to the lower boundary of its scope (Tab. 3.1). It is therefore a function of the minimum actuator thickness H_{\min} and layer thickness h . The design strategy may thus be summarised by the following points:

- Let h be the minimum value in Tab. 3.1
- Let L be the maximum value in Tab. 3.1
- Calculate N as $N_{\min} = H_{\min}/(2h)$.
- Calculate w as a function of L and n according to Eq. 3.38.

A self-sensing actuator suitable for the micro-robotic application that has been discussed may now be designed by applying the aforescribed methodology. Without any practical or fabrication considerations, the parameters for the self-sensing piezoelectric bender would be a length of $L = 25$ mm, a layer thickness of $h = 20$ μ m, a number of layers of $N = 9$, and therefore a width of $w = 2.8$ mm, resulting in an actuator thickness of 0.36 mm.

3.5 Conclusion

This chapter has presented a new angle of research to piezoelectric SSA. Where most publications have sought to use readily available commercial actuators to implement self-sensing implementations, albeit successfully, none have attempted to model then design an actuator that maximises the results of their sensorless estimation.

Prior to designing the prototype, the scope of its design has been established by performing typical micro-robotic tasks on μ m-scale samples: silicon micro-pillars that are 37 μ m in height and 3.5 μ m in diameter. Following these experiments, it has been determined that the force estimation would require a resolution of 0.1 mN, and that the position estimation would require a resolution of 0.5 μ m. In terms of actuator performance, the actuator would need to be able to apply forces of up to 100 mN across a free displacement range of 25 μ m. The lower stiffness of benders is more adapted to applications where precise force control is required (Chapter 2). This morphology has thus been considered for the prototype design, and a model has been developed from it. For the sake of design flexibility, the model has considered the number of layers of the actuator stack to be a variable. The resulting actuator characteristics calculated through the model may thus be influenced by this parameter.

Finally, with the design scope established by the measurements on the micro-pillar and with the analytical model of the actuator in hand, it has been possible to proceed with the design of the prototype. An objective function reflecting the design goals of the prototype was first established. The design sought to maximise the sensing component of the accumulated charges, while reducing the proportion of electrically induced charges. An analytical study has been performed on the objective function that had been constrained with design requirements, and its monotonicity with respect to the design parameters has been proven. Consequently, some concise guidelines to maximise the self-sensing performance could be formulated.

The following publications by the author are related to this chapter:

- Masson, L., Xinchang, L., and Perriard, Y. (2018). Design of an Optimized Self-Sensing Piezoelectric Cantilever for Micro-Robotic Applications. In *2018 International Conference on Manipulation, Automation and Robotics at Small Scales (MARSS)*, pages 1–6, Nagoya. IEEE
- Masson, L., Xinchang, L., and Perriard, Y. (2019b). An optimized self-sensing piezoelectric cantilever for micro-robotic applications. *Journal of Micro-Bio Robotics*, 15(2):91–103

4 Prototype fabrication and self-sensing performance assessment

4.1 Introduction

A design study of piezoelectric benders has provided clear guidelines for the fabrication of actuators tailored to specific Self-Sensing Actuation (SSA) applications. In the context of this thesis, a scope for actuation and self-sensing performances has been defined from measurements done in a benchmark scenario. The forces and displacements at play for the mechanical and electrical characterisation of P-N junction micro-pillars have hence been used to establish an actuator design space suited to this application. Using the previously established guidelines leads to the fabrication of a piezoelectric actuator that would be suitable for micro-robotic applications similar to that of the benchmark scenario. Nonetheless, proceeding from the design based on a theoretical model towards the practical implementation of that design may involve the adaptation of some parameters to the design process.

The development of a bender is the first step in designing a self-sensing prototype, which consists of two parts: the piezoelectric actuator itself, and the surrounding system referred to as the self-sensing test environment. The self-sensing prototype's goals are twofold. Firstly, it must facilitate the complete characterisation of the actuator integrated within the system. The assessment of the parameters shall also serve to validate the analytical model that has been developed in Chapter 3. Secondly, its purpose is to provide an environment for the implementation, testing, and assessment of SSA strategies with a fabricated actuator. Due to the tolerances of up to $\pm 20\%$ that are present in properties of the piezoceramics that are used in the fabrication of actuators, providing a modular environment that allows to test several actuators with ease is an important aspect of the prototype design.

The following sections of this chapter will present the self-sensing prototype that has been developed over the course of this thesis, beginning with fabrication of a batch of actuators and of the self-sensing system that surrounds it. With a clear picture of the complete system, the identification of actuation and self-sensing parameters that characterise the system shall be discussed. Finally, a self-sensing implementation with this system will be shown, leading into the qualitative and quantitative assessments of the resulting sensorless performance.

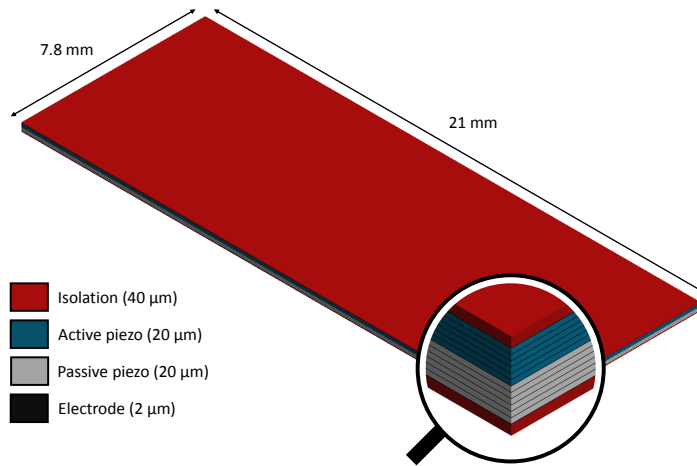


Figure 4.1 – Structure and topology of the fabricated actuator.

4.2 Prototype design and assembly

As mentioned, the prototype consists of two parts. The actuator fabricated according to the design guidelines in Chapter 3 is the centerpiece of the prototype and the focus of the SSA implementation. Surrounding the actuator, a supporting self-sensing testing system is responsible for providing an input voltage to drive the actuator, to integrate and measure the accumulated charges, to apply any compensation related to the measurement strategy that is required (e.g. reference capacitor), and finally to provide sensorless estimations of the actuator's mechanical state. In the experimental state of the self-sensing implementation, it is also necessary that this system includes non-invasive force and displacement sensing in order to validate the output of the self-sensing estimation. The following sections will discuss the bulk fabrication of an actuator design, and a general overview of the self-sensing test environment will be provided.

4.2.1 Fabrication of an actuator batch

The complexity of the fabrication of multi-layered piezoelectric actuators has led this research to turn to an industrial supplier for the handling of the process. The chosen supplier is Noliac, with whom discussions were held on the aforementioned design parameters. The real morphology of the actuator, illustrated in Fig. 4.1, differs slightly from the one that has been used to derive the model in Chapter 3. The first difference comes from the presence of two passive layers both on the top and the bottom of the actuator stack for electric isolation purposes. This, along the fact that the electrodes have a thickness of 2 μm, render the final actuator thickness greater than predicted by the model. Additionally, the active length and width of the actuator are slightly lower than outer dimensions of the bender, as isolation margins of 0.2 mm on the sides and of 3.8 mm along the length of the actuator need to be taken into account.

Table 4.1 – Final actuator specifications.

Param.	Material (–)	L (mm)	w (mm)	h (μm)	N –	H (mm)	β (nC/mN)	C_p (nF)	K (mN/ μm)
Value	NCE51F	21	7.8	20	6	0.35	-9.01	496	0.314

Table 4.2 – Inspection of the fabrication results.

Parameter	Unit	Specification			Measurement		
		Average	Min	Max	Average	Min	Max
Length	mm	21.0	20.6	21.5	21.13	21.12	21.15
Width	mm	7.80	7.65	7.95	7.84	7.83	7.86
Thickness	mm	0.35	0.25	0.45	0.481	0.457	0.495
Stroke	μm	290	232	348	301	273	317
Blocking force	N	0.22	0.18	0.26	0.27	0.26	0.28

Further parameter calculations made with the model shall only consider the effective dimensions of the actuator, which are obtained by subtracting the isolation margins from the external dimensions. To keep in line with the encumbrance requirements of the actuator, the design space for the external dimensions will be modified: the maximum length L is reduced from 25 mm to 21 mm, and the maximum width w is reduced from 10 mm to 9.6 mm. Furthermore, the calculation of the minimum amount of layers N_{\min} must now account for the added thicknesses of the electrodes and isolation layers. With these modifications to the design space in mind, and following the conclusions of the objective function study, the design should consist of a length of $L = 21$ mm, a number of layers of $N = 6$, and a layer thickness of $h = 20\mu\text{m}$. The width preserving the mechanical performance of the actuator can be calculated as a function of the other parameters as $w = 6.1$ mm.

Due to the fact that these chosen width and length parameters are close to that of some of Noliac's standardised actuators, i.e. $w_{\text{std}} = 7.8\text{mm}$ and $L_{\text{std}} = 21\text{mm}$, for which appropriate fabrication tools were already available, it has been decided to match these parameters to the standard. The resulting actuator would have identical length and width as these standard actuators, such as the CMBP03 produced by Noliac, but with customised internal parameters (i.e. layer thickness, number of layers) that are determined by applying the present chapter's design methodology. Setting the length and width to these standard values inevitably causes an 8.1% decrease of the design's objective function, but in 8.8% increase in the blocking force. Due to the fact that the β coefficient does not depend on the width w , this parameter of the actuator characteristic remains unchanged. Since this design still fits within the requirements specified in the previous section, this approach has been undertaken in order to drastically reduce the cost and lead time of the actuator's fabrication.

The final actuator parameters and its calculated characteristics are summarised in Tab. 4.1. The actuator has a free stroke of $\delta_{\max} = 290\mu\text{m}$ and a blocking force of $F_{\max} = 220\text{mN}$. Given

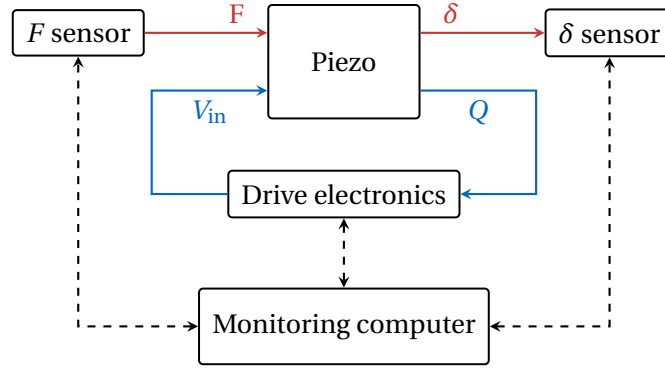


Figure 4.2 – Structure of the self-sensing prototype: mechanical signals in red, electrical signals in blue, digital communication busses in black.

a charge measurement resolution of 1 nC, such a design would be able to provide at best an estimation resolution of $0.35 \mu\text{m}$ for the displacement, and a resolution of 0.11 mN for the applied force. An inspection of the dimensions and actuation performance may be found in Tab. 4.2. Most parameters are within specifications of the fabrication process, however it should be noted that the measured blocking force is 23% greater on average. This seems to indicate that the resulting stiffness is greater than anticipated, and shall need to be confirmed with the testing that will follow in the present chapter.

4.2.2 Self-sensing test environment

The test environment component of the prototype is structured as shown in Fig. 4.2. It has been designed with the purpose of simultaneously measuring all of the electrical and mechanical state parameters of the actuator. To achieve this, a centralised architecture with a Cortex-M4F micro-controller running time critical software to coordinate all the measuring instruments has been adopted. In addition to this duty, it handles the processing of the data so as to provide sensorless estimations of the mechanical state. As such, the system provides a functional environment for implementing charge-based SSA strategies while also allowing for the validation of the outputs. The drive electronics, the position sensor, and the force sensor attached to a motorised linear positioning stage all communicate with the ST Microelectronics microcontroller, an STM32F446, through serial communication busses shown in black dashed lines in Fig. 4.2 (I²C and SPI).

When considering the piezoelectric as a system (Fig. 4.2), the electrical inputs and outputs (blue) of the actuator are contained within the same electrical loop. Since the charges are related to the current flowing through the electrodes, the circuit providing the driving voltage must also include charge amplification in series to the driven device. The drive electronics have been designed specifically for this project. However, with the amplification of charges in the order of nC being a delicate matter, the latter task is handled by a specialised Source Meter Unit (SMU): the Keithley 6517A configured as a coulombmeter. This instrument provides

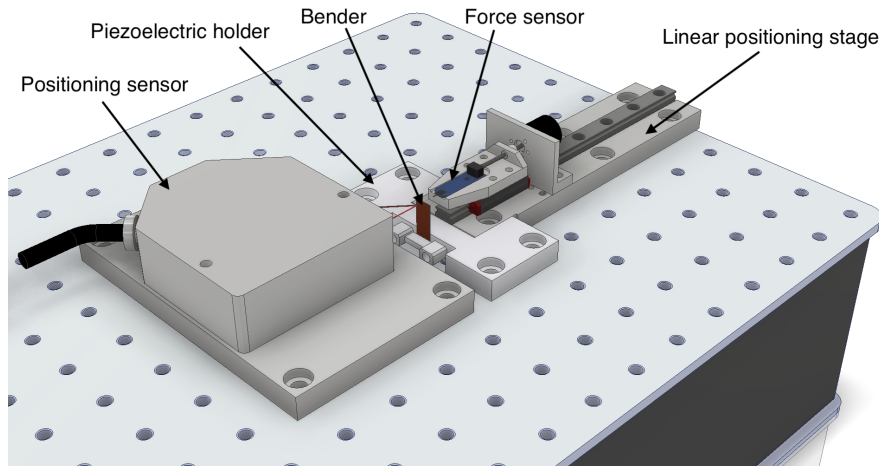


Figure 4.3 – Overview of the mechanical structure.

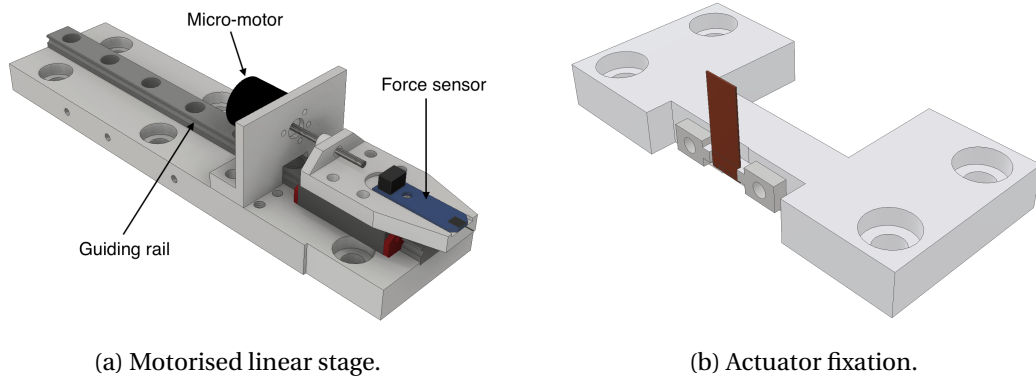


Figure 4.4 – Sub-systems of the self-sensing prototype.

charge measurement calibers ranging from $\pm 200 \text{ nC}$ to $\pm 2 \mu\text{C}$, with respective resolutions of 1 pC and 10 pC , which is befitting of the fabricated actuator's characteristics.

Regarding the mechanical inputs and outputs of the actuator in Fig. 4.2 (red), the use of non-invasive instruments has enabled the continuous determination of the mechanical state without affecting the actuator. All mechanical components are precisely positioned from one another by using machined pieces on an optical experimentation table with passive damping (Fig. 4.3). The relative displacement at the tip of the bender, i.e. end effector, is measured by a Keyence LK-G32 sensor head placed 2 cm away from the bender. It measures distance variations from a reference surface through triangulation using a laser beam. The fabricated actuators are glued using Araldite, a two-port epoxy adhesive, onto an actuator holder piece (Fig. 4.4b and Fig. 4.5). The latter component has been designed to be attached to the test environment by way of screws, making it possible to replace the bender under test with ease.

To accommodate the sub-mN force measurement, a high precision force sensor developed by Femto-Tools, the FT-ST100000, is used to measure and apply force to the piezoelectric

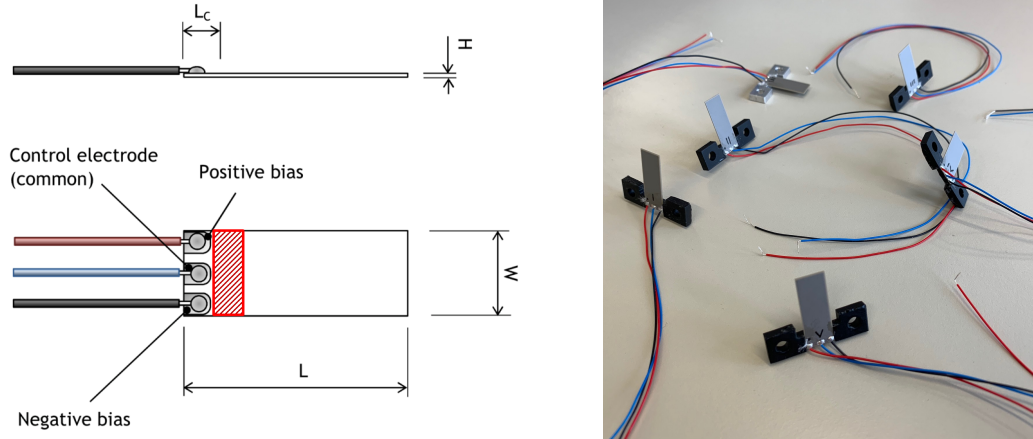


Figure 4.5 – Photo and schematic of the fabricated actuator; the hashed red area corresponds to the clamping / glueing surface for the actuator's assembly.

actuator with a range of 100 mN and a resolution of $5\mu\text{m}$. It is mounted on a motorised linear positioning stage powered by a Faulhaber micro-motor driving an endless screw with a pitch of $200\mu\text{m}$ (Fig. 4.4a). It is capable of providing a displacement resolution of $1\mu\text{m}$, and the mechanical setup provides a free stroke of 3 cm. The incentives for mounting the force sensor on a positioning stage are twofold. On the one hand, it allows to experiment with the mechanical properties of the benders with flexure tests: deforming the bender with the tip of a force sensor makes it possible to draw force-displacement and charge-force characteristics that make it possible to derive its stiffness K and its β coefficient. On the other hand, it allows to simulate real use cases for the self-sensing actuator by positioning the force sensor at a given distance from the bender tip and acting as a target sample: approach and force application control experiments may then be run with the SSA bender, with the manipulated force sensor tip providing validation data for the sensorless force estimation.

4.3 Identification of the actuation and self-sensing parameters

Before attempting to implement charge-based SSA strategies with the fabricated actuators, it is necessary to run an experimentation plan designed to characterise a batch of actuators. A set of six benders has been prepared and glued to plastic holders to that effect (Fig. 4.5), and they have been numbered for identification with the series of roman numerals I–VI. The characterisation of a batch of actuators allows for a statistical appreciation of the parameter spread, which is all the more justified by the usual $\pm 20\%$ tolerances on material properties. This tolerance is further compounded by the fact that the design parameters of the fabricated actuators aim for extremes in terms of dimensions and number of layers. The following paragraphs will detail a series of experiments that have been systematically run across the whole actuator batch to determine their stiffness K , capacitance C_p , and β coefficient. The knowledge of these parameters will also be necessary for the SSA implementation.

4.3. Identification of the actuation and self-sensing parameters

Table 4.3 – Results of the capacitance measurements.

Actuator No.	I	II	III	IV	V	VI
Upper area C_p (nF)	497	498	496	497	502	520
Lower area C_p (nF)	496	492	499	508	508	511

4.3.1 Capacitance measurement

The first experiment that can be done is to simply measure the capacitance of the piezoelectric actuator. This has been done with a Keysight 34450A digital multimeter. The impedance of a piezoelectric actuator inevitably varies under given stresses and applied voltages, therefore only its capacitance at rest may be evaluated. This is sufficient to determine the validity of the model prediction however, as the latter only considers the capacitance at rest. The model developed in Chapter 3 predicts a capacitance of $C_p = 496 \text{ nF} \pm 20\%$ given the fabrication parameters of the prototype's actuator. This prediction corresponds to the capacitance of either area of the bimorph, i.e. upper or lower which are symmetrical. As per the schematic in Fig. 4.5, let the positive bias be connected to the electrodes connected to the upper area of the bender, let the negative bias be connected to the bender's lower area, and let the common electrode be the ground voltage potential for both sets of electrodes. The measurements for the upper area (resp. lower area) are done by connecting the positive bias (resp. negative bias) to the HI port and both the negative bias (resp. positive bias) and the common electrode to the LO port of the multimeter, in order to short-circuit the unused area of the bender.

The results of these measurements are shown in Tab. 4.3, and the normal distribution of the results compared to the toleranced model prediction are represented in Section 4.3.5. The measured capacitance for the upper area has a mean value of 501.7 nF for a standard deviation of 9.2 nF, while the results for the lower area show a mean value of 502.3 nF for a standard deviation of 7.7 nF. The 90% confidence interval for both of these distributions encompasses the expectations provided by the model (Tab. 4.1), and the model prediction presents an error of 1.2% compared to the mean capacitance measured across all benders and areas. In that regard, the fit between model and empirical data is satisfactory.

4.3.2 Step response

To evaluate the dynamic behaviour of the benders, it is proposed to observe their response following a step in voltage application. Exercising precise control over a quasi-static bender's positioning requires an *a priori* understanding of its dynamic response to a ramped control scheme, as this is the most likely way it will be driven. Initially, the actuators's input voltage is left in a short-circuit state, and at $t = 1 \text{ s}$ a voltage step of 5 V is applied to the electrodes of the bender's upper area. While the voltage is maintained and no force is applied to the bender's tip, the deformation is continuously observed over the course of five minutes in order to be able to observe the creep effect of the piezoelectric material.

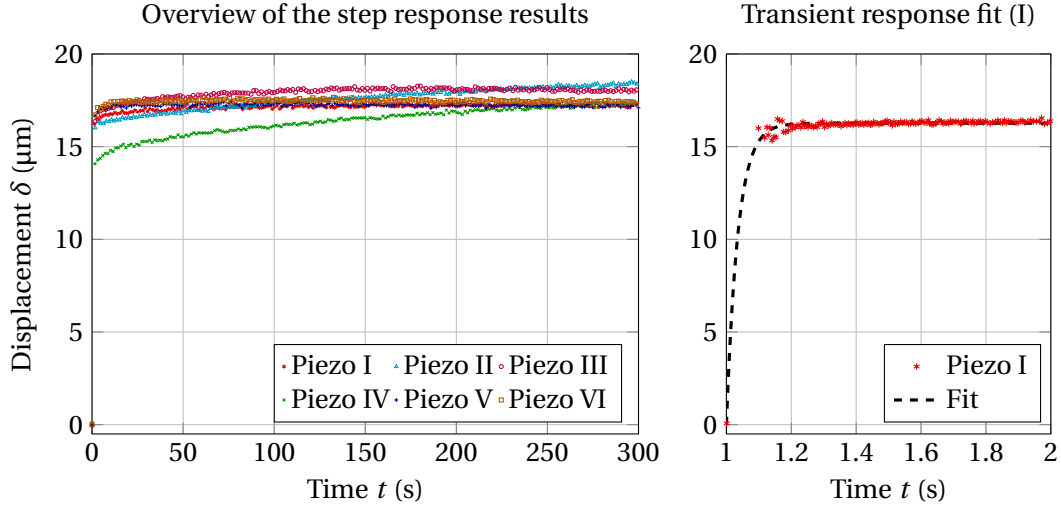


Figure 4.6 – Displacement measurements for the step response experiment (left), with an example of fitted curve for the transient response of an actuator (right).

From this experiment, one can hope to derive two pieces of information, as two signals are contained within the results shown in Fig. 4.6. Firstly, the study of the transient response occurring after the voltage step serves to derive the time constant τ that is important for the actuator's control. This response also provides a way to estimate the β coefficients, as the displacement will exponentially converge to the result of the voltage application, described as $\delta_{\text{free}} = \beta V_{\text{in}}$. Secondly, by observing the long term evolution of the displacement, an estimation of the severity of the creep effect for each bender may be estimated.

The results of the step response experiment performed on all six piezoelectric actuators are presented in Fig. 4.6. It is first proposed to examine the transient response of the benders. Both the τ and β parameters are found by fitting the measurement points of the first seconds after the $V_{\text{in}} = 5\text{V}$ voltage step at $t = 1\text{s}$ to a function that reflects the expected behaviour. As mentioned previously, the unconstrained actuator converges exponentially to the free displacement δ_{free} through a function in the form of:

$$\delta(t) = -5\beta(1 - e^{-(t-1)/\tau}) \quad (4.1)$$

The resulting parameters of these exponential fits to the transient responses of actuators I–VI may be found in Tab. 4.4. An example of fitted curve is also shown in the rightmost graph of Fig. 4.6. Across all actuators of the batch, an average $-\beta$ coefficient of $3.207\text{ }\mu\text{m/V}$ has been identified, along with a standard deviation of $0.192\text{ }\mu\text{m/V}$. Compared to the model estimation of $-\beta = 9.01\text{ }\mu\text{m/V}$, the β coefficient estimated through this experiment presents a high level of discrepancy with the theoretical expectations. More insight into this spread is provided in Section 4.3.5, and an updated model presented in Chapter 5 converges with the data provided by this experiment.

4.3. Identification of the actuation and self-sensing parameters

Table 4.4 – Extrapolated parameters of the fitted curves for the unit response experiment.

Actuator No.	I	II	III	IV	V	VI
$-\beta$ ($\mu\text{m}/\text{V}$)	3.253	3.206	3.272	2.830	3.327	3.356
τ (ms)	35.5	35.3	50.5	54.1	36.4	36.0

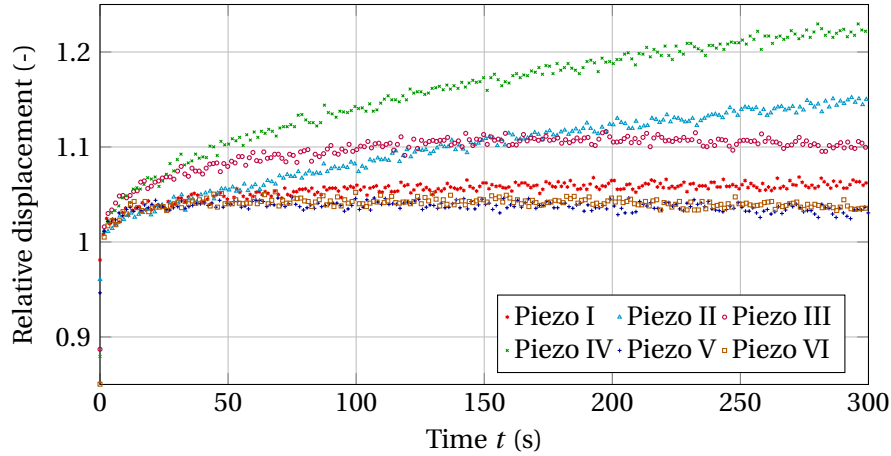


Figure 4.7 – Qualitative observation of the creep on the expected displacement.

Thanks to the transfer function of the transient responses (Eq. 4.1), the evolution of the creep effect can now be investigated. The creep is determined by subtracting the free displacement δ_{free} from the total measured displacement δ shown in Fig. 4.6. The resulting relative displacements are shown in Fig. 4.7, with a relative displacement of 1 corresponding to the absence of creep. Further characterisation experiments making use of charge measurements would be required to fully describe this phenomenon through a model. However, the result presented in Fig. 4.7 is sufficient for a qualitative observation of its effect. Varying amounts of creep are found for actuators I–VI, with relative displacements ranging from 3% to 23% after five minutes of observation.

4.3.3 Free stroke

In order to verify the repeatability of the previous estimations for the β coefficient, another experiment from which this parameter can be derived has been performed. In this experiment, the voltage V_{in} applied to a bender's upper area is swept across its complete nominal range, i.e. 0V – 60V, while the displacement δ is measured. The expected outcome for this experiment is the highlighting of the hysteretic relationship between voltage and displacement. The resulting $\delta - V_{\text{in}}$ characteristics also provide a way to estimate the β coefficient. The latter may be determined by calculating the initial slope of the hysteresis, starting at $V_{\text{in}} = 0\text{V}$. Another mechanical parameter may be found from this experiment, as the displacement at $V_{\text{in}} = 60\text{V}$ corresponds to the free stroke δ_{max} of the actuators.

Table 4.5 – Extrapolated β slopes and maximum displacements δ_{\max} for the free stroke experiment.

Actuator No.	I	II	III	IV	V	VI
$-\beta$ ($\mu\text{m}/\text{V}$)	3.255	3.285	3.130	2.715	3.110	3.255
δ_{\max} (μm)	298	308	303	273	291	314

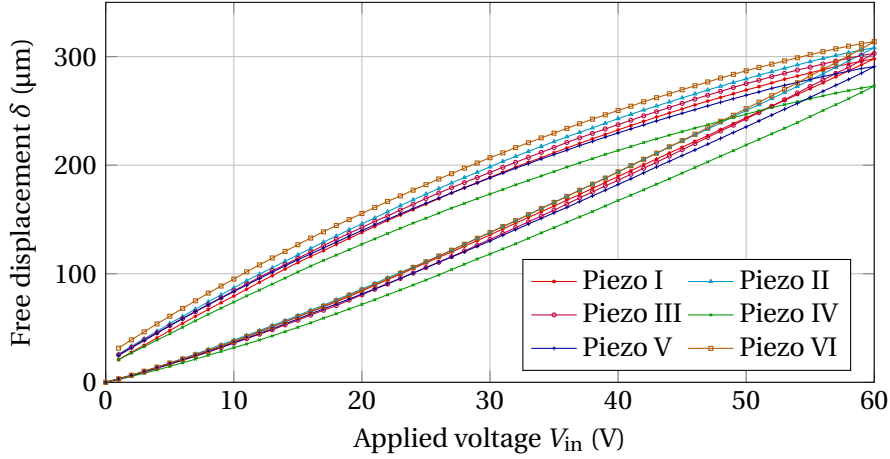


Figure 4.8 – Displacement measurements for the free stroke experiment.

The results of the voltage sweep are presented in Fig. 4.8, with the extrapolation of the free stroke δ_{\max} and β coefficient for actuators I–VI shown in Tab. 4.5. From this experiment, the average free stroke $\delta_{\max} = 301 \mu\text{m}$ in Tab. 4.2 across the whole batch coincides with the the average free stroke of $298 \mu\text{m}$ derived from this experiment. As for the $-\beta$ coefficient, its average estimation is of $3.125 \mu\text{m}/\text{V}$ for a standard deviation of $0.213 \mu\text{m}/\text{V}$. While it reflects the β coefficient of the previous experiment, the discrepancy with the expectations set by the model is still relevant. More information is provided in that regard within Section 4.3.5.

4.3.4 Flexure testing

The final electromechanical characterisation experiments that have been done are typical flexure tests. For this experimental protocol, the varied input becomes the applied force F . It is transmitted directly by the force sensor, and the amount of force is controlled through the motorised linear positioning stage on which the sensor is mounted on. By driving the force sensor's tip against the bender's end effector, an applied force sweep F from 0 to 45 mN is executed while the test environment collects displacement and charge measurements from the bender. This sweep is performed a total number of ten times on each bender to verify the repeatability of the experiment's results. Thanks to the readings on the mechanical and electrical outputs of the self-sensing actuator collected by the test environment, it is possible to characterise the benders in one of two ways through this experiment. First, the $\delta - F$

4.3. Identification of the actuation and self-sensing parameters

Table 4.6 – Extrapolated β and K slopes for the flexure experiment.

Actuator No.	I	II	III	IV	V	VI
$-\beta$ (nC/mN)	3.193	3.359	3.114	2.890	3.077	3.201
K (mN/ μ m)	0.834	0.838	0.925	0.958	0.982	0.933

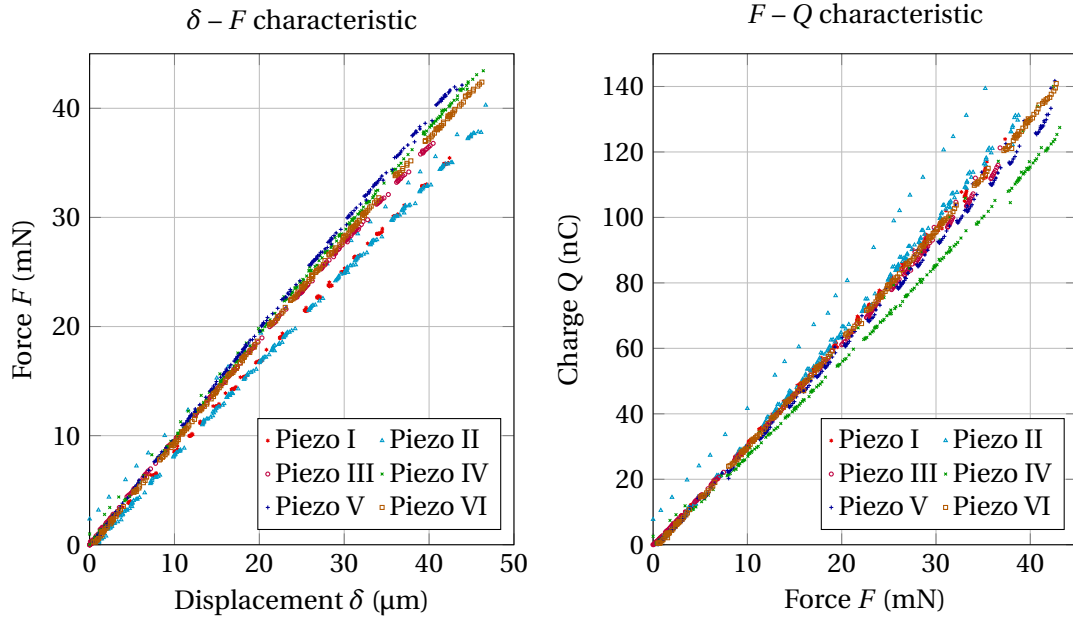


Figure 4.9 – Force, charge, and displacement measurement results for the flexure experiment.

characteristic function provides a way to estimate the stiffness K , as it corresponds to the slope of the curves which are expected to be linear. Similarly, the $F - Q$ characteristic function provides is related to the β coefficient, as it is equivalent to the slope of the curves which are once more expected to be linear, as per the SSA model established in Chapter 2. The latter estimation is a direct way to validate the results of the previous two experiments, as the relationship between force and charge through β is more straightforward than the one between the voltage and the displacement.

The results of the flexure tests across benders I–VI are shown in Fig. 4.9, and the K and β parameters that have been derived from these experiments are presented in Tab. 4.6. From the mechanical output of the experiments ($\delta - F$ characteristics), the estimated stiffnesses of the benders have a mean value of 0.912 mN/ μ m for a standard deviation of 61 μ N/ μ m. And from the electrical output of the experiments ($F - Q$ characteristics), the estimated $-\beta$ coefficients have a mean value of 3.139 nC/mN for a standard deviation of 0.156 nC/mN. Once more, these estimated β coefficients fit with the previous experiments while being lower than the -9.01 nC/mN predicted by the model. The same may be said for the estimated stiffness, where the model predicted a stiffness of 0.314 mN/ μ m. The reasons for this discrepancy and an updated model that converges with this experimental data are discussed in Section 4.3.5.

Table 4.7 – Results overview of the actuator characterisation experiments.

Actuator No.	I	II	III	IV	V	VI	μ	σ
K (mN/ μ m)	0.834	0.838	0.925	0.958	0.982	0.933	0.912	0.061
$C_{p,u}$ (nF)	497	498	496	497	502	520	501	9.2
$C_{p,l}$ (nF)	496	492	499	508	508	511	502	7.7
β_1 (μ m/V)	3.253	3.206	3.272	2.830	3.327	3.356	3.207	0.192
β_2 (μ m/V)	3.255	3.285	3.130	2.715	3.110	3.255	3.125	0.213
β_2 (μ m/V)	3.193	3.359	3.114	2.890	3.077	3.201	3.139	0.156
τ (ms)	35.5	35.3	50.5	54.1	36.4	36.0	41.3	7.9

4.3.5 Results overview

The results of all the characterisation experiments that have been presented in this section, along with the mean values and standard deviations, are summarised in Tab. 4.7. To further illustrate the results of this characterisation campaign, graphs showing the normal distribution of the characterisation results with respect to the model predictions are given in Fig. 4.10.

The three most important parameters that needed to be identified throughout these experiments were the stiffness K , the capacitance C_p , and the β coefficient. Not only correctly identifying these parameters is necessary for the implementation of SSA within the prototype, but they are also required to validate the predictions of the model established in Chapter 3. The latter model is referred to as *model 1* in Fig. 4.10. The following conclusions may be found for the three actuator parameters regarding their *model 1* predictions:

- The prediction for the capacitance $C_p = 496$ nF presents itself as satisfactory, as it overlaps with the 90% confidence intervals of the normal distributions of the capacitance measurements (Fig. 4.10). The error of the prediction of *model 1* with relation to the mean measured C_p is of 5 nF, amounting to a relative error of 1%.
- The same conclusion may not be drawn with the prediction for the stiffness $K = 0.314$ mN/ μ m. The error of the prediction of *model 1* with relation to the mean measured stiffness is of 0.598 mN/ μ m. In other words, the prediction is greater than the measured value by a factor of $\times 3$.
- As was the case for the stiffness, the *model 1* prediction for $\beta = -9.01$ nC/mN does not correlate with the experimental data. The prediction error with regards to the β measurements obtained from the flexure tests amounts to 5.871 nC/mN. In other words, the prediction is lower than the measured value by a factor of $\times \frac{1}{3}$.

The observation that there is a factor of $\times 3$ and $\times \frac{1}{3}$ between the *model 1* predictions and measurement data for K and β is not a coincidence, as the β coefficient is inversely proportional to the stiffness K [36]. However, such a large discrepancy did not occur when applying the same model to the commercial Noliac CMBP03 bender in Chapter 2.

4.3. Identification of the actuation and self-sensing parameters

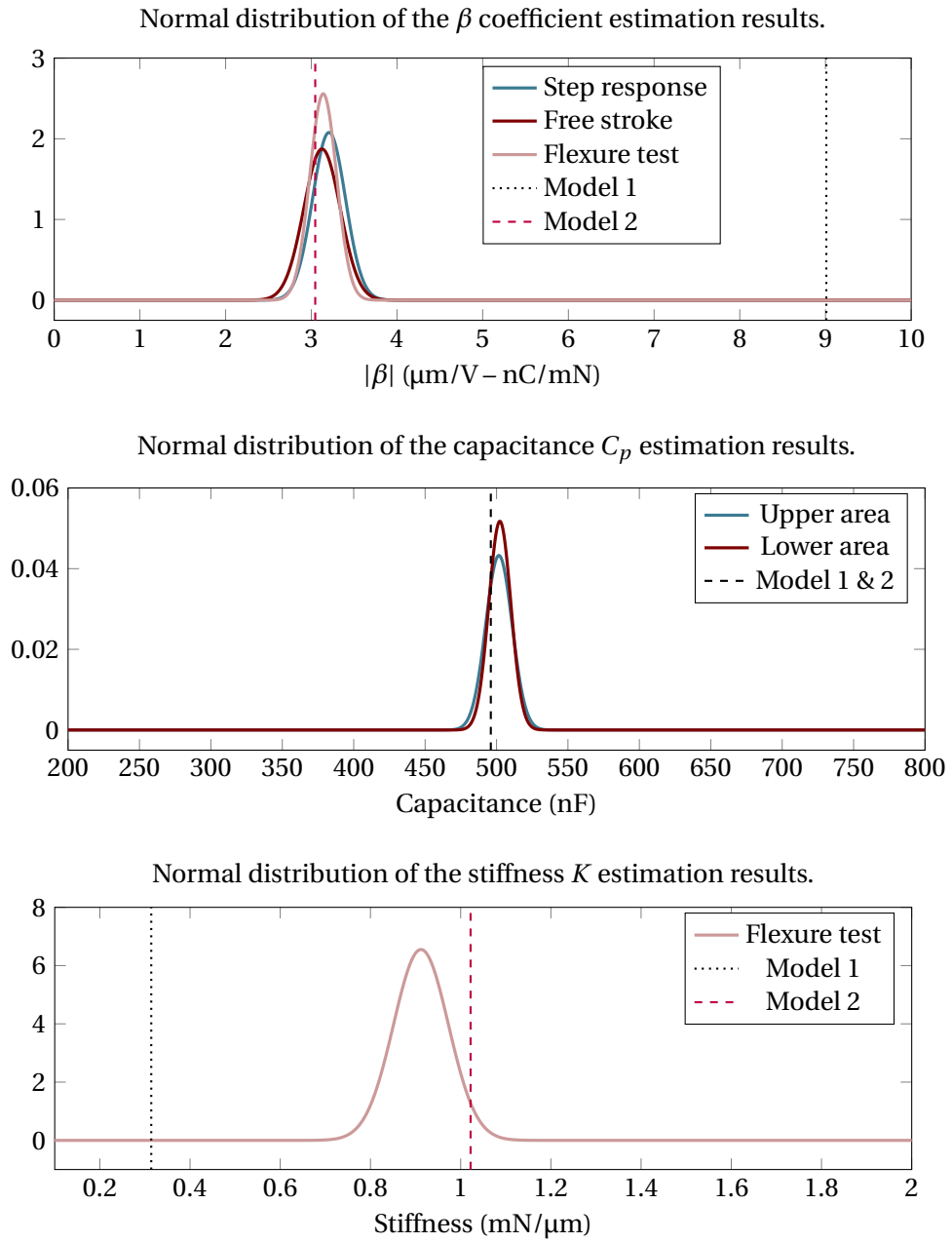


Figure 4.10 – Comparison between the characterisation results and the model predictions.

Table 4.8 – Comparison between *model 1*, *model 2*, and the measurement results.

Parameter	Model 1	Model 2	Measurement
$-\beta$ (nC/mN)	9.01	3.046	3.139
K (mN/ μm)	0.314	1.022	0.912

The source of this error is related to an incomplete evaluation of the bender stack's stiffness when establishing *model 1*. Some features of the stack have been neglected when establishing the model (Chapter 3), such as the electrode thickness and the presence of isolation layers at the top and bottom of the actuator stack. For thick and large numbers of layers, this assumption would not be cause for error. However, the guidelines derived from the design study have pushed for lowering the number of layers and opting for thinner layers, increasing the importance of these previously neglected features. Chapter 5 delves into that topic in detail and provides an updated model, referred to as *model 2* in the present chapter.

New conclusions may thus be drawn for the measurements of actuator parameters for benders I–VI shown in Tab. 4.7. While the expression of the capacitance stays the same for both models, the predictions for K and β of the new *model 2* converge with the experimental data in a more satisfactory manner than the predictions of *model 1* did (Tab. 4.8). As seen in Fig. 4.10, the *model 2* prediction of the β coefficient overlaps with the 90% confidence intervals of all three experimental estimations of this parameter. The error of this prediction amounts to 93 pC/mN, which corresponds to a relative error of 3%. Finally, the *model 2* prediction for the stiffness K converges with the experimental data (Fig. 4.10), albeit with less accuracy, as it does not overlap with the 90% confidence interval of the measurement spread. The absolute error with respect to the mean measurement amounts to 0.11 mN/ μ m, corresponding to a relative error of 12%. According to the supplier, a lower experimental stiffness than theoretically predicted is to be expected, as this is usually caused by multi-layered fabrication processes.

Three separate estimations for the β parameter have been obtained from the step response, free stroke, and flexure experiments. They are consistent with one another, however the estimation derived from the flexure tests shall be considered as more reliable from this point. Fitting an exponential curve to the transient response implies some *a priori* assumptions, as the number of measurement points that constitute the transient response is not clearly defined. Finally, the hysteretic aspect of the voltage – displacement characteristic may be cause for error when evaluating the initial slope of the curve.

4.4 Self-sensing actuation

The self-sensing prototype was designed with the goals of first validating the self-sensing model predictions for the fabricated actuators, and then of providing a development environment allowing to implement and test self-sensing implementations. Now that the design of the prototype has been discussed and the batch of benders have been characterised, the study can move on to the latter objective.

With a mean β coefficient of 3.139 nC/mN for benders I–VI, the accuracy of the charge measurement must be able to detect charge increments of 319 pC if the self-sensing estimator were to be intended for 0.1 mN accuracies. The charge measurement must also not greatly deteriorate over time if the SSA actuator is to be used with this accuracy in quasi-static applications. At this point, the charge measurement becomes the most critical component and will

determine the performance of the prototype. However, implementing such an accurate charge measurement is compounded by issues that arise when measuring low charges (sub- μC) that flow through high impedance devices such as piezos. Appendix C presents the parasitic effects that cause issues with the charge measurement.

A self-sensing implementation that has been applied to the fabricated benders will be discussed in the following paragraphs. The aim of this implementation is to provide a sensorless force estimation while the bender's end effector is being moved towards a sample, which will have been positioned at a fixed distance from the end effector at the beginning of the experiment. In essence, this experiment is identical to the scenario proposed for the simulation of a real use case at the end of Chapter 2. The goal of this manipulation is to determine if the actuator would be able to detect a threshold of force while it is manipulating an object, and at which resolution it could do so. This will help to determine the typical force estimation accuracy in manipulation tasks that could be expected from the self-sensing benders that have been fabricated for this thesis.

4.4.1 Calibrated approach

Despite the compensations and guards that have been put in place to counteract the parasitic effects that interfere with its procedure (Appendix C), the charge measurement has still proven to be difficult. While it has been possible to determine the bias current, it has been a complex matter to obtain a proper characterisation for the creep and the hysteresis of the piezoelectric actuator. Not only would the bias current i_b vary from one experiment to another, but as soon as an input voltage V_{in} were to be applied, the leakage current would also drastically increase past expectations. The variation of the bias current is not predictable, however the leakage current is consistent for a given applied voltage V_{in} . Therefore, instead of the compensated approach that has been discussed, a calibrated approach to the charge measurement has been chosen.

This approach implies that the charge measurement has to be calibrated prior to driving the actuator. The aim of this approach is to establish a charge – voltage profile which empirically describes the evolution of the charge with respect to the applied voltage. This is done in the absence of external mechanical interactions, in other words when the self-sensing actuator is not manipulating an object. The charge – voltage profiles that are created in calibration runs are then used to extract the sensing charge from the measured charge during the subsequent approach runs, as the electrical contribution of the charges are independent from the force interactions that occur between the actuator and the manipulated sample. The calibration and approach runs are performed as such:

- **Calibration runs:** During the calibration runs, the force sensor is removed from the proximity of the bender's end effector so that it may move freely without constraint. The calibration runs are then repeated a large number of times. During each runs, the actuator is subjected to a ramping applied voltage V_{in} in steps of 200 mV from 0 V to

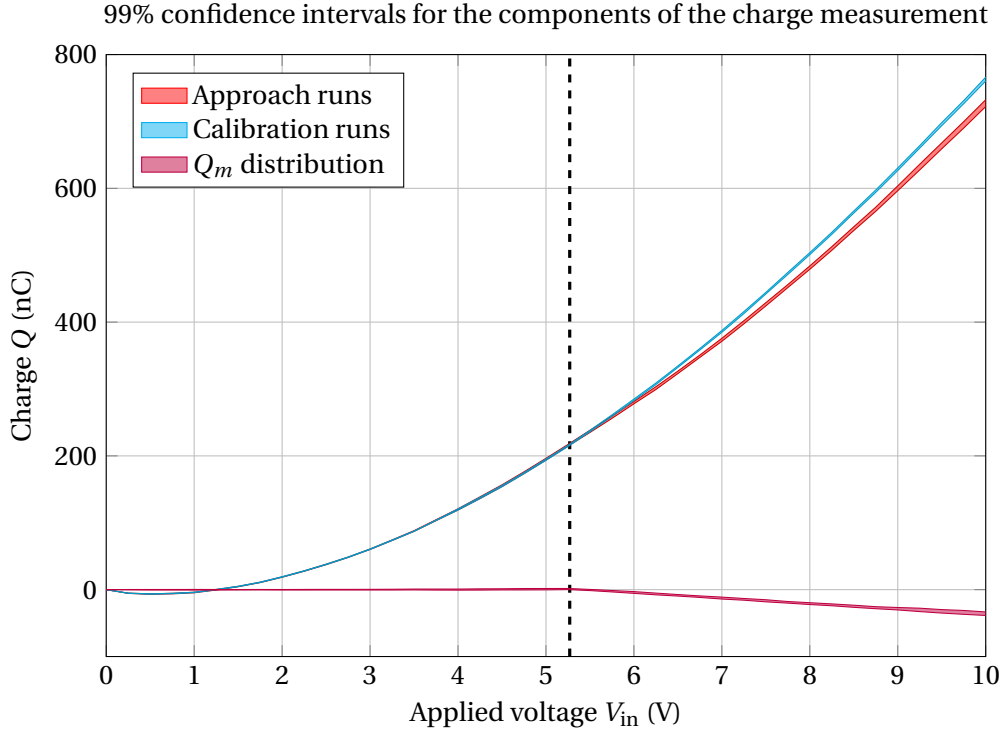


Figure 4.11 – Calibration of the self-sensing approach: the 99% confidence intervals are shown for the calibration runs, the approach runs, and for the resulting measured charge Q_m .

10 V, and the output charge is measured simultaneously. The output is then saved on the monitoring computer, and the normal distribution of the charge measurements is evaluated with respect to voltage to create a charge – voltage profile.

- **Approach runs:** The force sensor is used as a manipulated sample in these experiments, as it allows to validate the output of the self-sensing estimation. The tip of the sensor is first placed at a set distance (i.e. $5\mu\text{m}$ – $20\mu\text{m}$) from the bender's end effector, as shown in Fig. 4.12. For each approach run, the bender is then deformed by a ramping driving voltage V_{in} as it had been during the calibration runs. While the end effector approaches the force sensor and then applies a force upon it, the charge is measured by the electrometer. The sensing charge is extracted from the measured charge by subtracting the calibrated charge – voltage profile from it, and a force estimation can then be performed using the estimation equations shown in Chapter 2.

An example of the charge measurements for the calibration runs and the approach runs is provided in Fig. 4.11. Since the calibration runs are repeated a large amount of times to provide a statistical evaluation of the charge – voltage profile, the calibration measurements are represented by their 99% confidence intervals in this graph. The 99% confidence interval for a multitude of approach runs is also shown to show if there would be an overlap between both confidence intervals, which would make it impossible to extract the sensing charge.

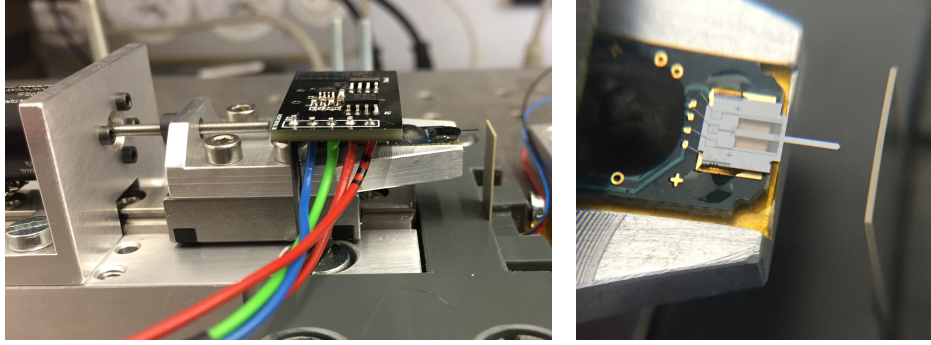


Figure 4.12 – Photos of the force sensor positioned close to the bender's tip.

For each separate approach run, the difference between the calibration profile and the real use case measurement corresponds to the sensing charge. The 99% confidence intervals for the estimated sensing charges are shown in purple in Fig. 4.11). As expected, before the contact between the force sensor and the bender's end effector, represented by a vertical dashed line in Fig. 4.11, the sensing charge is null. It starts increasing along with the force once the contact has been made, and expectedly by a factor described by the actuator's β coefficient.

4.4.2 Discussion on the resulting SSA performance

With the extracted sensing charges, it is possible to provide an estimation of the force by applying the estimator equations as discussed in Chapter 2. This has been done for multiple approach runs to determine if the performance remained consistent throughout. For these experiments, the force estimation is compared to the force measurement with respect to time in Fig. 4.13, and the absolute error of the estimation ϵ_F is calculated.

Across all three runs, the SSA performance could be qualitatively described as satisfactory. The estimated force converges with the measured force for the duration of the experiment ($\tau = 110$ s), whether it be during the approach of the bender's tip and or during the force application phase. For the approach runs 1 and 2, the absolute error ϵ_F does not usually exceed 0.25 mN, while it increases to up to 1 mN near the end of approach run 3 (after $t = 80$ s). Due to the statistical approach of the calibration measurements, it is not possible to point out the true cause for this drift near the end of approach run 3. However, it can be said that the sensorless force estimation implemented in this experiment would be sufficient to detect forces with a resolution of 0.25 mN for shorter experiments ($t \leq 60$ s), which is befitting of the micro-robotic use case studied in Chapter 3.

The calibrated strategy is not as precise as a full fledged compensated charge measurement would be, as occasional drifts could occur during the experiments. It must be also noted that a new set of calibration runs must be performed before a new set of experiments to account for changes in environmental factors, as the accuracy of the sensing charge extraction would degrade over very large periods of time (i.e. several hours). It is evident that more

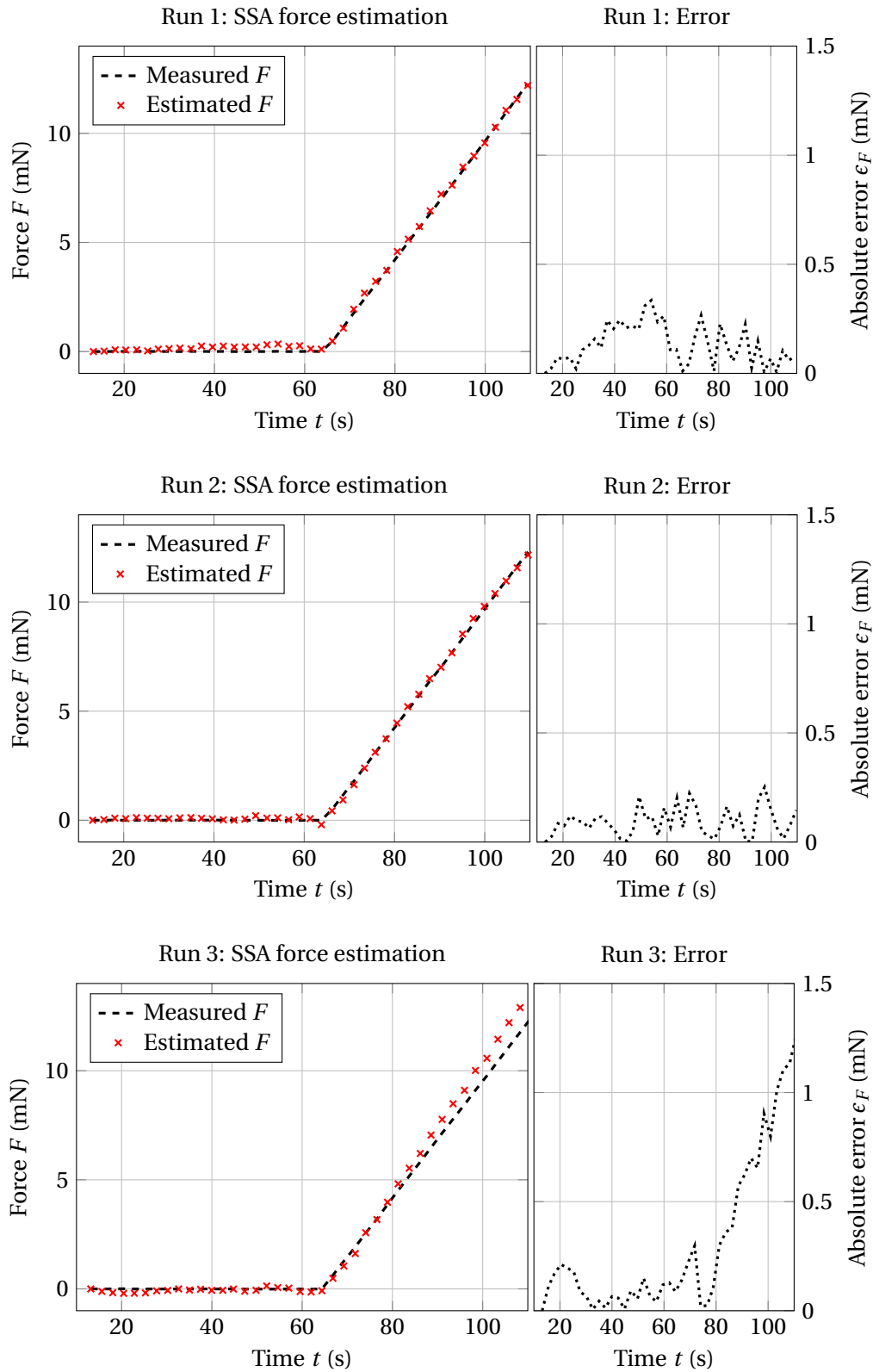


Figure 4.13 – Self-sensing force estimation result for three separate approach runs.

robust performances could be obtained by using the fabricated benders in setups capable of accurately compensating the charge measurement in order to determine the sensing charge. Despite these observations, the SSA results shown in Fig. 4.13 demonstrate that it is possible to obtain a sub-mN accuracy in the force estimation of the self-sensing benders by implementing a calibrated approach.

4.5 Conclusion

In this chapter, the design and implementation of a prototype for Self-Sensing Actuation (SSA) has been presented. It had been determined that a SSA prototype consisted of two parts: the piezoelectric bender, of which the constitutive equations and design have been studied at length in Chapter 3; and the test environment surrounding the actuator, responsible for driving the actuator and measuring all the electro-mechanical variables that describe the state of the piezoelectric system.

The first step in designing the SSA prototype has been the choice of an actuator design, following the guidelines that were established in Chapter 3. The initial design that has been derived from these guidelines aims to maximise the charge contributions of the bender's mechanical deformation. However, due to real considerations deriving from the fabrication process of the actuator, the final actuator parameters vary mildly from the initial design (Tab. 4.1). This has caused an 8.1% decrease in the objective function and an 8.8% increase in the blocking force. Despite these alterations of the maximised design, the prototype featured promising characteristics for the prospect of self-sensing. With a β coefficient of -9.01 nC/mN , it offered a $\times 17$ increase in its sensorless estimation's resolution compared to the commercial Noliac CMBP03 bender of similar morphology.

These expectations have unfortunately been dampened by the results of the characterisation campaign of six fabricated actuators that followed. The test environment of the prototype has been used with success to measure the parameters of bender I–VI: the capacitance C_p , the stiffness K , and the β coefficient. While the measurement of the capacitance C_p was shown to converge with the prediction offered by the model established in Chapter 3, the stiffness K and the β coefficient diverged from the predictions by factors of $\times 3$ and $\times \frac{1}{3}$ respectively.

When considering the probable causes for the discrepancy between model predictions and measurement results, it has been pointed out that some features of the bender design that were previously considered as negligible could be responsible: the thickness of the electrodes and the presence of isolation layers at the top and bottom of the stack. Since the model predictions were still correct for Noliac's commercial CMBP03 bender, it has been suspected that the error is exacerbated by the guidelines derived by the actuator's design study for thinner and less piezoceramic layers. While the results of this discussion and an model update are the topic for Chapter 5, the results for this new model are still compared to the characterisation results. The measurements converge with the new model's parameters, with an error of 3% for the β coefficient and an error of 12% for the stiffness K .

Finally, using the newly characterised actuators, a self-sensing implementation has been performed with the prototype. The aim has been to replicate the use case simulation provided at the end of Chapter 2, by driving the self-sensing actuator toward a manipulation sample and estimating the applied forces. This was done with the intent to determine the best accuracy that could be achieved for the force detection, so that a threshold detection could be implemented for manipulation tasks. Due to difficulties presented by the charge measurements in the pC–nC scale, a calibrated approach has been opted for instead. With this strategy, it has been shown across multiple runs that it is possible to expect an accuracy of 250 μN for durations of less than 60 s. However, as the charge measurement deteriorate over time, this accuracy is downgraded to 1 mN for experiments lasting up to 110 s. The results obtained with a simple calibrated approach are however greatly encouraging, and future work on this topic could focus on the critical charge measurement in order to push the envelope of what is possible in terms of self-sensing accuracy.

The following publication by the author is related to this chapter:

- Masson, L., Ren, X., and Perriard, Y. (2019a). Novel test environment for the development of self-sensing piezoelectric actuators. In *2019 22nd International Conference on Electrical Machines and Systems (ICEMS)*, pages 1–5, Harbin, China. IEEE

5 Definite improvement of self-sensing performance through optimisation

5.1 Introduction

In Chapter 3, it has been shown how one can model a multi-layered piezoelectric monomorph bender and express its characteristics as a function of all design parameters, including the number of layers N . To validate the analytical model and to obtain a working prototype, an actuator has been designed and manufactured according to design guidelines that have been laid out by the conclusions of the design study. Through the subsequent experimental validations presented in Chapter 4, it has been observed that the model predictions did not converge with the experimental data for the fabricated bender; estimation errors of the β coefficient by an alarming factor of $\times 3$ were evidenced.

The model predictions for the CMBP03 bender converged well with the experimental data, therefore it has been stipulated that this has been caused by the design guideline's push for thinner and fewer piezoelectric layers to increase the SSA sensitivity. This cause for model error becomes problematic when attempting to maximise the SSA performance of an actuator, as thinner and fewer layers lead to better estimation resolutions through the increase in the β coefficient. To be more specific, the drift between model predictions and experimental data has been correlated with the ratio of active thickness to the total thickness of the actuator stack. This active thickness corresponds to the layers that were effectively taken into account by the model, excluding some features that were thought to have a negligible impact on the model. These features have been identified as the thickness of the electrodes and the presence of isolation layers at the top and bottom of the actuator stack.

The present chapter endeavours to demonstrate a rigorous approach to providing a definite improvement in SSA performance. This improvement is obtained by starting from a more accurate model which will account for the entirety of the actuator stack. The initial design assumptions on topology are reconsidered in Section 5.2, and a more accurate updated model is presented. From there, by considering the actuator as a sensor and by aiming to optimise its *sensitivity* and *accuracy*, a multi-objective optimisation methodology with an original numerical approach is presented at length in Section 5.3.

5.2 Reconsidering the design assumptions on actuator topology

To reiterate on the analytical model established for the multi-layer piezoelectric monomorph bender, it is first necessary to reconsider the actuator topology that has been defined. This necessity stems from the observation that features originating from fabrication considerations could no longer be neglected when reaching for fringe values of certain parameters. When reducing the number of layers or the individual piezoelectric layer thickness, both improving the SSA performance of the design, the model neglecting these features became erroneous.

These features will hereby be included when elaborating the analytical model of the actuator, and the newly considered actuator topology is schematically described in Fig. 5.1. The following paragraphs will describe the new topology, and will provide an insight into why the exclusion of these features cause a wide gap between the β parameter estimation from the model and from experimental data.

5.2.1 Description of the topology and associated design parameters

The new topology is evidently based on the one described in Chapter 3. The section of the monomorph bender is composed of an upper active area of N piezoelectric layers and a lower passive area of an equal number of piezoelectric layers. As a reminder, even if this bender is configured as a bimorph, only the piezoelectric layers of the former are electrically driven to deform the piezoelectric actuator, hence the bender being considered monomorph. This was done to simplify the drive electronics of the actuator given that electronics for sub-nC charge measurement need to be added to it. Additionally, the usage of piezoelectric material in the lower area is convenient for the fabrication process itself. Should there be any need to explore the use of the bimorph configuration in an SSA setting, this actuator can be used and serve as a basis of comparison with the monomorph performance.

As mentioned in the preamble to this section, two features present in the bender's section will now be considered in addition to the upper and lower area. The new topology, along with its new features, is schematically described in Fig. 5.1. The two features are the following:

- Electrodes layered around each drivable piezoelectric layer, defined by their own thickness h_e and material properties, most notably their compliance s_e . Their thickness is fixed by the design process to $2\text{ }\mu\text{m}$, and there is a total of $2N + 1$ electrodes to surround all the piezoelectric layers. They are represented by the black layers in Fig. 5.1.
- A pair of high impedance isolation layers present at the top of the actuator stack, and another pair present at its bottom. As a security measure, they cover the bare electrodes that are driven with high voltages. The individual thickness of these 4 isolation layers is the same thickness h as the piezoelectric layers, and the material is the same piezoceramic due to the ease of the fabrication process when using the same materials. They are represented by the red layers in Fig. 5.1

5.2. Reconsidering the design assumptions on actuator topology

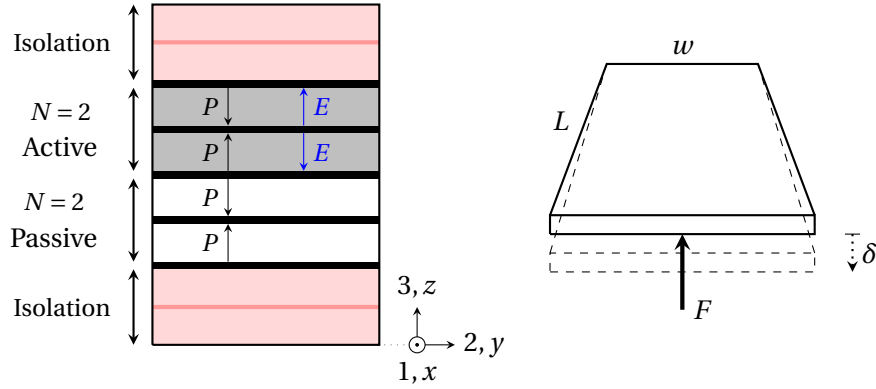


Figure 5.1 – Considered monomorph topology in the case where $N = 2$; electrodes in black, piezoelectric layers of the upper and lower areas in grey, and isolation layers in red.

The external dimensions of the actuator is described by the length of the bender L and its width w . The piezoelectric layers from the isolation, upper and lower areas are all described by their thickness h , while the electrodes are defined by their thickness h_e . For the sake of brevity in writing some lengthy equations in the following demonstrations, the μ coefficient has been defined as the ratio between the piezoceramic layer thickness and the electrode thickness. Due to the fact that the h_e parameter will remain a constant in the considered fabrication process, it may be replaced by $h_e = h/\mu$.

In total, the actuator stack is built from $2N + 4$ piezoceramic layers and of $2N + 1$ electrode layers. Knowing the electrode thickness h_e and the piezoelectric layer thickness h , the total thickness H of the bender can therefore be calculated as follows:

$$H = (2N + 1)h_e + (2N + 4)h \quad (5.1)$$

The following mathematical developments will require a frame of reference when elaborating the analytical model. As illustrated in Fig. 5.1, and in Fig. 5.3 during the following paragraphs, the origin of the frame of reference is placed at the bottom end of the stack: the x (index 1) axis along the length L , the y (index 2) axis along the width w , and the z (index 3) axis along the bender's total thickness H .

5.2.2 Influence of the electrodes and isolation layers

The assertion was made that the exclusion of the isolation layers and the electrodes from the first model caused estimation errors for the β parameter. It is proposed here to rationalise this gap between model and experimental estimations for given actuators. The model is accurate when considering piezoelectric layer thicknesses $h \geq 40 \mu\text{m}$ and a sufficient number of layers N , but the error appears when decreasing these parameters. To understand the cause of this deviation, the *active thickness* of the bender must be considered.

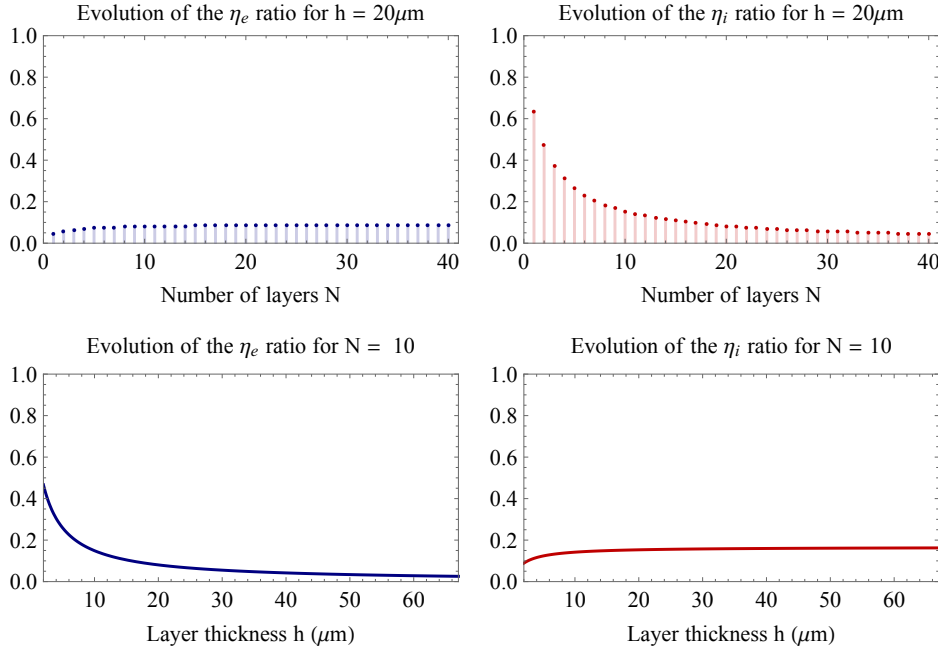


Figure 5.2 – Effect of the decrease in h and N parameters on the η_e and η_i thickness ratios.

This quantity, hereby labelled as η , is defined as the ratio of the added thicknesses of the piezoelectric layers in the upper and lower area of the bender section to the total thickness H of the bender's section defined in Eq. 5.1. In other words, the active thickness as it has been defined is the percentage of the bender's section that is taken into account by the model, with the unaccounted thickness corresponding to the electrodes and isolation layers.

In order to visualise the effect of decreasing N and h on the active thickness η , consider η_e (respectively η_i) as the ratio of the added thicknesses of the electrodes (respectively isolation layers) to the total thickness H . As per their definition, it is evident that $\eta = 1 - \eta_e - \eta_i$, and that increasing either of these ratios is detrimental to the active thickness η . The two ratios η_e and η_i may be written as follows:

$$\eta_e = \frac{(2N+1)h_e}{H} \quad (5.2)$$

$$\eta_i = \frac{4h}{H} \quad (5.3)$$

It can be verified that η_e is proportional to $1/h$ and that η_i is proportional to $1/N$. This can be visualised in Fig. 5.2, where η_e (left) and where η_i (right) are plotted as a function of N with h as a constant, then as a function of h with N as a constant. When $h = h_e$ and for $N = 10$, η_e corresponds to 46.7% of the total thickness. Similarly, when $N = 1$ and for $h = 20 \mu\text{m}$, η_i corresponds to 63.4% of the total thickness. Conversely, the N (respectively h) parameter has a minimal impact on the η_e (respectively η_i) ratio. Therefore, the concept of active thickness illustrates how the model does not consider a significant portion (as high as 63.4% for instance) of the bender's section when decreasing N and/or h .

The loss of accuracy from the model was correlated to the decrease in the active thickness η past a certain point in Chapter 3. As a consequence, this loss of accuracy may in turn be correlated to the decrease in h and N parameters studied above. This can be explained by the fact that the bender section is central to the study of a bending cantilever.

Given this rationale, it is now evident that a new model must be formulated by taking accounting for the isolation and electrode layers present in the bender's section. This holds especially true when aiming to optimise the bender's design in a way that maximises the β parameter, which has been shown to be done when decreasing the number of layers N and the piezoelectric layer thickness h .

5.2.3 Updating the model for the monomorph bender

With this modelling objective and the new actuator topology (Fig. 5.1) in mind, the new model can now be established. The process for doing so is entirely based on the demonstration shown in Chapter 3, using a combination of the principle of superposition, piezoelectric theory, and bending theory. The novelty of the new approach will consist in modelling a bender for which the actuator stack is heterogeneous, meaning that it is composed of layers of differing mechanical properties. Let the index u (resp. l) denote the piezoelectric layers in the upper and active (resp. lower and inactive) area of the actuator. Additionally, let the index t (resp. b) denote the piezoelectric isolation layers at the top (resp. bottom) of the actuator stack, and let e denote the electrode layers.

Displacement equation

As a reminder, two phenomena are simultaneously causing the mechanical deformation of the actuator. On the one hand, the applied voltage V_{in} strains the active piezoelectric layers within the actuator through the converse piezoelectric effect, reverberating this strain throughout the whole section of the stack of layers. On the other hand, the applied force F on the bender's tip uniformly spreads a strain throughout all the layers of the actuator stack section. Due to the linearity of these phenomena, the displacement equation of the piezoelectric actuator can be evaluated by applying the principle of superposition. Independently from one another, the actuator displacement caused by each phenomenon can be modelled, after which both displacements can be summed to express the total displacement δ caused by the external application of inputs V_{in} and F .

The parameters of the piezoelectric strain $S_{1,p}(z)$ are first evaluated. The deflection of the beam due to the converse piezoelectric effect, referred to as δ_p , can be tied to the applied voltage V_{in} . The application of the theory of piezoelectricity allows for the evaluation of the strain S within the piezoelectric layers of the material thanks to the knowledge of the electric field E . With the disposition of the electrodes illustrated in Fig. 5.1, it is possible to relate the applied voltage V_{in} to the electric field E and layer thickness h .

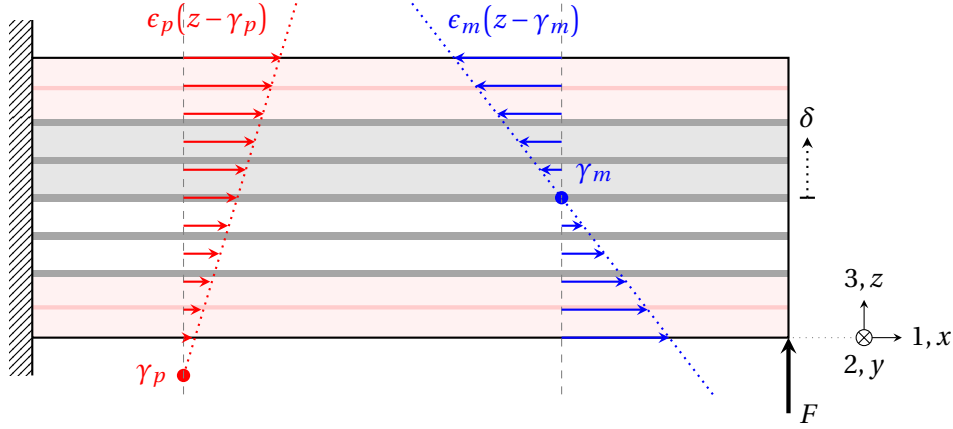


Figure 5.3 – Representation of the frame of reference and of the strains in sections of the actuator stack: piezoelectric strain in red and mechanical strain in blue.

Let γ_p be the position of the neutral plane and let ϵ_p be the slope of the strain along the bender section. With respect to the neutral plane, the strain caused by the piezoelectric effect may be written as $S_{1,p}(z) = \epsilon_p z$. When considering a section of the beam at equilibrium, the sum of internal forces F_{int} and internal moments M_{int} is zero. The μ ratio has been defined earlier in order to simplify the equations of this demonstration: the constant electrode thickness will from then on be replaced by $h_e = h/\mu$. Solving the equilibrium leads to the following expression for the slope of the strain:

$$\epsilon_p = -\frac{6d_{31}N^2s_e\mu^2(1+\mu)}{h^2P}V_{\text{in}} \quad (5.4)$$

where P is expressed as:

$$P = s_{11}(1+2N)\left(1+4N(1+\mu)^2+4N^2(1+\mu)^2\right) + 2s_e\mu\left(6+24\mu+32\mu^2+24N^2(1+\mu)^2+N^3(1+\mu)^2+N(23+70\mu+48\mu^2)\right) \quad (5.5)$$

The expression of the position of the neutral plane γ_p is also found by solving the system of equations:

$$\gamma_p = -\frac{h(s_{11}R_1 + s_eR_2)}{6N\mu(1+\mu)((2N+1)s_{11} + (2N+4)s_e\mu)} \quad (5.6)$$

where R_1 is expressed as:

$$R_1 = (1+2N)\left(-1+2N^2(1+\mu)^2+N(-1+7\mu+8\mu^2)\right) \quad (5.7)$$

and where R_2 is expressed as:

$$R_2 = 2\mu\left(-9N^2(1+\mu)+2N^3(1+\mu)^2-2(3+12\mu+16\mu^2)-N(17+40\mu+24\mu^2)\right) \quad (5.8)$$

5.2. Reconsidering the design assumptions on actuator topology

The mechanical strain $S_{1,m}$ is now evaluated. Let γ_m be the position of the neutral plane and ϵ_m be the slope of the strain. With respect to the neutral plane, the strain caused by the mechanical deformation may be written as $S_{1,m}(z) = \epsilon_m z$. Due to the symmetrical nature of the bender's morphology, it is evident that the neutral plane for the mechanical deformation can be found at the center of the beam section:

$$\gamma_m = (N + 2)h + (N + \frac{1}{2})h_e \quad (5.9)$$

According to bending theory, the slope of the strain ϵ_m is related to the compliance of the material, the moment of inertia, and the moment of force. It can be expressed as follows:

$$\epsilon_m = \frac{s_{11}}{I} M(x) = -\frac{12s_e s_{11} \mu^3}{wh^3 P} (L - x) F \quad (5.10)$$

With the expressions of the piezoelectric strain slope ϵ_p , the mechanical strain slope ϵ_m , and their respective neutral planes, the expressions of the strains $S_{1,p}(z)$ and $S_{1,m}(z)$ may be fully written. Bending theory dictates that the curvature of a beam ρ is related to the slope of its strain ϵ such that $\rho = 1/\epsilon$. Due to the orientation of the reference frame and to the way the moment $M(x)$ was calculated, the application of bender theory yields a negative result. The opposite of the double integration will thus be used for the deflection within the reference frame. The total displacement δ of the piezoelectric bimorph at its tip, when subjected to an applied force F and a driving voltage V_{in} , may now be expressed by applying the principle of superposition with the mechanical deflection $\delta_m(L)$ and the piezoelectric deflection $\delta_p(L)$:

$$\delta = \frac{3d_{31}N^2 s_e L^2 \mu^2 (1 + \mu)}{h^2 P} V_{in} + \frac{4L^3 s_{11} s_e \mu^3}{wh^3 P} F \quad (5.11)$$

Charge equation

In order to derive the electrical output of the actuator, Gauss' law is used to evaluate the free electrical charges accumulated at the electrodes around the piezoelectric layers. It requires knowledge of the electric displacement field D and of the effective stress $T(k)$, the latter being the average stress across one layer's thickness. By doing so, one can express the total amount of electrical charges accumulated by the piezoelectric actuator as such:

$$Q = \frac{3d_{31}N^2 s_e L^2 \mu^2 (1 + \mu)}{h^2 P} F + \left(N \frac{Lw\epsilon_{33}}{h} + C_\delta \right) V_{in} \quad (5.12)$$

where C_δ is a term that is related to the d_{31} piezoelectric coefficient and the actuator morphology parameters. Its expression will be left out of this manuscript due to the length of the equation. However, using calculations based on the actuator design from Chapter 3, it is possible to verify that C_δ is two orders of magnitudes lower than the main capacitance term, and this term will therefore be neglected from now on.

Complete model and parameter identification

It is now possible to write the constitutive equations as predicted by the general form defined in Chapter 2 and the piezoelectric equations (Eq. 3.2). Note that in this instance, the force F is negative with respect to the reference frame, hence the sign change from the general model for the terms in front of F . The state of the self-sensing actuator subject to an upward applied force and driving voltage is described by its displacement δ and accumulated electrical charge Q , both of which can be described by a system of equations:

$$\begin{cases} \delta = \frac{3d_{31}N^2s_eL^2\mu^2(1+\mu)}{h^2P}V_{in} + \frac{4L^3s_{11}s_e\mu^3}{wh^3P}F \\ Q = N\frac{Lw\epsilon_{33}}{h}V_{in} + \frac{3d_{31}N^2s_eL^2\mu^2(1+\mu)}{h^2P}F \end{cases} \quad (5.13)$$

The K , C_p and β parameters can now be identified. The expression of δ in Eq. 5.11 can be compared with its equivalent in the general model in order to identify K and β . Similarly, the expression of Q in Eq. 5.12 may be compared with its equivalent in the general model in order to identify C_p and confirm the expression of β .

$$K = \frac{wh^3P}{4L^3s_{11}s_e\mu^3} \quad (5.14)$$

$$C_p = N\frac{Lw\epsilon_{33}}{h} \quad (5.15)$$

$$\beta = \frac{3d_{31}L^2N^2s_e\mu^2(1+\mu)}{h^2P} \quad (5.16)$$

This confirms that the β parameters in both constitutive equations of the system Eq. 5.13 are the same, lending credence to the model being established in these demonstrations.

5.2.4 Experimental validation of the complete model

The validity of the updated model has been assessed with the SSA prototype that has been developed for this thesis. The measurements and the comparison with the updated model parameters have already been presented in Chapter 4, the results of which are reminded in Tab. 5.1. In this table, *model 1* refers to the initial model that has been presented in Chapter 3, while *model 2* refers to the updated model that has been presented in the preceding paragraphs.

As discussed earlier, the predictions for the stiffness K and the β coefficient of *model 1* have presented large discrepancies with respect to the experimental data. The predicted K was lower than the measured stiffness by a factor of $\times \frac{1}{3}$, while the predicted β was greater than the measured coefficient by a factor of $\times 3$. Including the previously neglected features of the

5.3. Multi-objective optimisation study based on the complete model

Table 5.1 – Reminder of the experimental results presented in Chapter 4.

Parameter	Model 1	Model 2	Measurement
$-\beta$ (nC/mN)	9.01	3.046	3.139
K (mN/ μm)	0.314	1.022	0.912

actuator stack in the updated *model 2* has reduced the error of the β prediction down to 3%, and the K prediction down to 12%. These results lend credence to the validity of the model update presented in this chapter.

5.3 Multi-objective optimisation study based on the complete model

Now that an accurate analytical model of the piezoelectric actuator has been formulated, it is possible to perform an optimisation study based on it. Before proceeding with an optimisation study, a reflexion must be carried out on the aspects of the actuator's characteristics that must be improved for the optimisation of the SSA performance. Beneficial aspects must be maximised, while the ones detrimental to SSA must be minimised. In order to do so, it is convenient to consider the SSA actuator as a sensor: not only its purpose is to actuate, but it also must provide feedback on its state. In that light, it is possible to discuss the accuracy, precision, or linearity of the SSA actuator, much like the same would be discussed for a sensor.

In this section, an approach is proposed to optimise an SSA bender's *sensitivity* and *accuracy*. The objective functions of the optimisation study will be defined along with the constraints that are imposed on the design. Following this preamble, a novel multi-objective optimisation approach based on a solution searching algorithm will be discussed, after which the Pareto frontier of the set of solutions will be evidenced and discussed.

5.3.1 Optimisation problem definition

This study relies on two sensor concepts to define the SSA performance of a given piezoelectric actuator design: *sensitivity* and *accuracy*. Sensors usually convert a signal from one physics domain (e.g. mechanical, thermal, magnetic) into a signal from another domain. This converted signal can then be interpreted by an electronics system, and this signal can thus be used for instance in a control feedback loop. The self-sensing implementation of a piezoelectric actuator is analogous to a sensor's purpose by allowing a system to interpret the mechanical state of the actuator through electrical signals produced by the actuator itself. The *precision*, in other words the resolution, of a self-sensing piezoelectric actuator depends entirely on the measurement electronics and not on the design of the actuator itself, therefore it does not fall within the purview of this study.

To proceed with the definition of the objective functions, knowledge of the measurement set up that will be connected to the actuator is necessary. As discussed in previous chapters,

the charge based self-sensing approach is the preferred method for the implementation of a quasi-static actuator intended for micro-robotic applications. The charge measurement set up is inspired by the implementation of Rakotondrabe in [46] with the use of a reference capacitor C_r . This capacitor is supplied with a voltage in opposition to the piezoelectric actuator's drive voltage V_{in} in order to attenuate the amount of electrical charges accumulated by the actuator's capacitance. This approach improves the charge measurement range of the electrometer by a substantial margin. The charge contributions due to application of V_{in} are indeed demonstrably greater, by up to two orders of magnitude, than the charge contributions due to an applied force.

First objective function: Sensitivity (f_β)

With the analogy of a sensor in mind, the concept of *sensitivity* for an SSA actuator refers to the variation of the charge measurement in response to a given variation of force or displacement. An optimal SSA actuator would aim to maximise this sensitivity, so that a charge measurement system will be able to detect smaller variations in force or displacement with its given sensing resolution. This forms the basis for the first objective function of this study.

When considering the previously presented analytical model, this sensitivity can be directly represented by the β parameter, a coefficient expressed in C/N representing the amount of electrical charges accumulated as a result of the application of a given force F . With the d_{31} piezoelectric coefficient being negative and all other parameters in its equation being positive, β is therefore strictly negative. In order to maximise $|\beta|$, it is proposed to add a negative sign in front of the expression of β in (Eq. 5.16), resulting in the following objective function to maximise:

$$f_\beta(L, w, \{h, \mu\}, N) = -\beta = -\frac{3d_{31}L^2N^2s_e\mu^2(1+\mu)}{h^2P} \quad (5.17)$$

where P is expressed in Eq. 5.5.

Second objective function: Accuracy (ϵ_f)

In a similar fashion, the concept of *accuracy* for an SSA actuator corresponds to the maximum error of the estimation. In terms of self-sensing actuator optimisation, this is a parameter that needs to be minimised, and will therefore dictate the second objective function of this optimisation study. The charge-based self-sensing approach is usually affected by phenomena that cause drift over time, in particular bias currents produced by the measurement electronics and drift currents that are inevitable. Both of these currents are picked up by the charge measurement electronics, and will create a drift in the charge measurement over time. When discussing quasi-static SSA, where it may be necessary to maintain a position or an applied force for long periods of time, it is necessary to define a measurement time constant. It will be referred to as τ from now on, and it shall define the amount of time during which a given estimation accuracy can be guaranteed.

5.3. Multi-objective optimisation study based on the complete model

The maximum error ϵ_f accumulated after a lapse of time τ must be expressed as a function of τ and all the actuator parameters. To that end, considering the measurement circuit from Chapter 4, the expression of the measured charge Q_m should be considered:

$$Q_m = \beta F + V_{in} C_d + Q_l + Q_b = \beta \hat{F} \quad (5.18)$$

where C_d is the difference between actuator capacitance C_p and the reference capacitance C_r , V_{in} the applied voltage, Q_l the charge drift caused by leakage currents, Q_b the charge drift caused by bias currents, and \hat{F} the force estimation.

When considering that the difference between the estimation \hat{F} and the applied force F defines the estimation error ϵ_f , such that $\epsilon_f = \hat{F} - F$, one can write:

$$\epsilon_f = (V_{in} C_d + Q_l + Q_b) \beta^{-1} \quad (5.19)$$

The charge drift components can be written as:

$$Q_l + Q_b = \int_0^\tau \frac{V_{in}}{R_l} dt + \int_0^\tau i_b dt \quad (5.20)$$

where R_l is the leakage resistance of the circuit, and i_b the bias current. Both of these quantities can be either estimated or measured experimentally, and can therefore be used in the expression of the estimation error ϵ_f .

Considering the worst case for each parameter allows the ϵ_f parameter to estimate the highest possible estimation error after a lapse of time τ . In that regard, the maximum electric field $E_{3,\max}$ will be used in the following calculations, with $V_{in,\max} = E_{3,\max} h$. This maximum electric field causes the highest accumulation of unwanted charges caused by C_p , which the addition of the capacitance C_r intends to compensate for. From the expression of β in Eq. 5.16, the expression of the estimation error ϵ_f can be written as a function of the actuator parameters and of the P coefficient described in Eq. 5.5:

$$\epsilon_f = -h^2 \frac{E_{3,\max} h N \rho C_d + E_{3,\max} L w \tau + i_b N \rho \tau}{3 d_{31} L^2 N^3 s_e \mu^2 (1 + \mu) \rho} P \quad (5.21)$$

The electrometer that is intended for use in the charge measurement electronics for the SSA actuator is the Keithley 6517A. Therefore, in keeping with the spirit of considering the worst case for each parameter, the value of i_b will be set to the highest possible value provided by its datasheet, i.e. 4 fA. In this section, the leakage resistance R_l will be modelled on the basis of the piezoelectric material resistivity ρ measurements performed by Hooker [20]. While it is a complex matter to estimate the impedance of a piezoelectric component at quasi-static frequencies, this study regarding the properties of PZT-based piezoelectric ceramics provides a realistic expectation of the order of magnitude of the piezoelectric actuator's resistance. In the context of a charge based SSA actuator, the exactitude of this estimation is not a high

Table 5.2 – Actuator morphology parameters.

Parameter	Symbol	Unit	Range
Length	L	mm	[5, 35]
Width	w	mm	[2, 10]
Layer thickness	h	μm	{20; 50; 67}
Thickness ratio	μ	-	{10; 25; 33.5}
Nb. of layers	N	-	$\{N_{\min}; \dots; 40\}$

priority. Indeed, the ϵ_f component does not represent the exact estimation error of the SSA actuator, as the SSA method presented in the following Chapter attempts to compensate these charge measurement drifts as much as possible. The point of studying ϵ_f in this optimisation study is therefore only to minimise these estimation errors as much as possible.

Design space and constraints

For the optimisation study to produce meaningful results, the solutions must answer to realistic expectations. This implies, for instance, that the resulting dimensions should be within manufacturing capabilities, or that the resulting characteristics of the actuator such as stiffness or capacitance are within expected ranges. For instance, a very high capacitive load would be problematic for the drive electronics, while a low stiffness will reduce the manipulation strength of the piezoelectric actuator.

To that end, it is necessary to define a design space along with design constraints prior to the optimisation study. A design space is defined by the parameters that can be tuned during the optimisation, and they can be divided into two categories: material properties, and actuator morphology properties. Design constraints tie these parameters to conditions imposed on the design. They enable the expression, for instance, of some parameters as a function of the other parameters. This reduces the dimensionality of the optimisation problem and further facilitates the optimisation study. The list of parameters that define the design space, along with their respective symbols, units and ranges, are presented in Tab. 5.2, and are discussed at length in the following paragraphs.

Material properties pertain to parameters such as the piezoelectric coefficients d_{ij} , the compliance s_{ij} and the permittivity ϵ_{ij} . As they depend on the choice of piezoceramic material for the fabrication, they cannot be chosen independently from one another. With the amount of choices for the material being limited, it is not necessary to consider the piezoelectric material as a design parameter that needs to be optimised. The same calculations that will be presented in this study can be made for each set of material properties, and a choice can be made from the results of these calculations. For the subsequent demonstrations, the NCE51 piezoceramic by Noliac will be the baseline for the material properties, as it has been used for the previous manufacturing of piezoelectric actuators.

Actuator morphology properties describe the shape and configuration of the piezoelectric actuator illustrated in Fig. 5.1, and are evidently the principal parameters to be tuned throughout the optimisation study. The length L and width w are continuous parameters directly describing the external dimensions of the actuator. The parameter pair $\{h, \mu\}$ is discrete and limited to three possible sets of values. To each h is associated a μ parameter value describing the ratio between the thickness of the piezoelectric layers h and the constant electrode layers $h_e = 2 \mu\text{m}$. As explained in Section 5.2.3, the μ parameter has been defined to simplify the writing of some of the model equations. Finally, the number of layers N for each area of the actuator is discrete. The lower boundary N_{\min} must be chosen as a function of the $\{h, \mu\}$ parameter pair such that it verifies through Eq. 5.1 that the total actuator thickness H is greater than $H_{\min} = 0.35 \text{ mm}$. The actuator morphology parameters and their boundaries are all summarised in Tab. 5.2.

The first constraint to be imposed upon the design is the value of the piezoelectric capacitance C_p which must not exceed $C_{p,\max} = 500 \text{ nF}$. A higher capacitance would be detrimental to the self-sensing estimation due to the higher amount of undesirable electrical charges accumulated by the driving voltage V_{in} , but also to the power supply of the actuator which would need to be designed to drive more capacitive loads. From the previous developments, the expression of the design constraint on the capacitance C_p can be written:

$$C_p(L, w, \{h, \mu\}, N) = N \frac{Lw}{h} \epsilon_{33} \quad (5.22)$$

A mechanical performance constraint is also imposed on the actuator's design. Given that it is intended to be used in micro-manipulation tasks, it must be capable of maintaining blocking forces of up to $F_{\min} = 150 \text{ mN}$ at a displacement of at least $\delta_{\min} = 37.5 \mu\text{m}$. The expression of the maximum blocking force F can be derived from the expression of the displacement δ , leading to:

$$F(L, w, \{h, \mu\}, N) = wh^2 \frac{3d_{31}E_{3,\max}L^2N^2s_e\mu^2(1+\mu) - hP\delta_{\min}}{4L^3s_{11}s_e\mu^3} \quad (5.23)$$

The terms $E_{3,\max}$ and δ_{\min} will from now on respectively be written as E_3 and δ for the sake of brevity. As for the constraining variables, C_d must not exceed 10 nF , the measurement time constant is set to $\tau = 100 \text{ s}$, the bias current is $i_b = 4 \text{ fA}$, and the maximum electric field before depolarization of Noliac's NCE51 piezoceramic is $E_3 = 3 \text{ V}\mu\text{m}^{-1}$.

5.3.2 Multi-Objective Optimisation

The multi-objective optimisation problem can now be formally defined. The aim is to maximise the *sensitivity* of the sensor described by the f_β objective function (Eq. 5.17), and to improve the *accuracy* by minimising the estimation error ϵ_f (Eq. 5.21). These objective functions must be optimised while also guaranteeing design conditions defined by the constraints imposed on the maximum actuator capacitance C_p (Eq. 5.22) and the required blocking force

F (Eq. 5.23) at a given displacement δ_{\min} . The multi-objective optimisation problem can thus formally be written as follows:

$$\begin{aligned}
 & \underset{L, w, \{h, \mu\}, N}{\text{minimise}} && \epsilon_f(L, w, \{h, \mu\}, N) \\
 & \underset{L, w, \{h, \mu\}, N}{\text{maximise}} && f_\beta(L, w, \{h, \mu\}, N) \\
 & \text{subject to} && F(L, w, \{h, \mu\}, N) \geq F_{\min}, \\
 & && C_p(L, w, \{h, \mu\}, N) \leq C_{p, \max}.
 \end{aligned} \tag{5.24}$$

Analytical Study

The analytical model describing the behaviour of the piezoelectric actuator makes it possible to take a rigorous analytical approach. Indeed, the evolution of the objective functions over the design space can be studied by examining the partial derivatives of the function, and it can be demonstrated whether a maxima (or minima) exists within that design space. As a first step, it is proposed to study the evolution of both objective functions f_β and ϵ_f with respect to the two continuous parameters: actuator length L and width w . The partial derivatives of the *sensitivity* objective function f_β with respect to L and w are as follows:

$$\begin{aligned}
 \frac{\partial f_\beta}{\partial L} &= - \frac{6d_{31}LN^2s_e\mu^2(1+\mu)}{h^2P} \\
 \frac{\partial f_\beta}{\partial w} &= 0
 \end{aligned} \tag{5.25}$$

Since all the design parameters are positive (Tab. 5.2), the P coefficient described in Eq. 5.5 is demonstrably strictly positive within the design space. The same can be said for all the parameters present in the partial derivative of f_β with respect to L , with the exception of the negative d_{31} coefficient. This partial derivative is therefore strictly positive, and it can be said that f_β is monotonous and ascending with respect to L within the design space. Since the partial derivative with respect to w is always null, f_β is independent of w . The partial derivatives of the *accuracy* objective function ϵ_f with respect to L and w are as follows:

$$\begin{aligned}
 \frac{\partial \epsilon_f}{\partial L} &= h^2P \frac{E_3(2hN\rho C_d + Lw\tau) + 2i_bN\rho\tau}{3d_{31}L^3N^3s_e\mu^2(1+\mu)\rho} \\
 \frac{\partial \epsilon_f}{\partial w} &= -h^2P \frac{E_3\tau}{3d_{31}LN^3s_e\mu^2(1+\mu)\rho}
 \end{aligned} \tag{5.26}$$

The same reasoning used in the demonstration for the partial derivatives of f_β can be used for the partial derivatives of ϵ_f . It is worthy to note that the sign of i_b will depend on the measurement circuit, and that it has been verified to be positive in the case presented in Chapter 4. Considering the design space, the numerator of the partial derivative with respect to L is strictly positive, and its denominator is strictly negative due to all parameters being

positive with the exception of d_{31} . The partial derivative of ϵ_f with respect to L is therefore strictly negative, and it can be said that ϵ_f is monotonous and descending with respect to L within the design space. The same reasoning leads to the conclusion that the partial derivative of ϵ_f with respect to w is strictly positive, and therefore ϵ_f is monotonous and ascending with respect to w within the design space.

Conclusions to this initial analytical study are that the f_β (resp. ϵ_f) function is maximised (resp. minimised) when increasing the length L , and that the ϵ_f function is minimised by decreasing the width w . Without the presence of constraints, an optimal solution would be the maximum possible length L and the smallest possible width w . These constraints will however impose restrictions on the values of L and w that are eligible. It is thus proposed to consider L as a variable to maximise, while using the constraints of the optimisation problem to impose boundaries to the possible values of w . By solving $F = F_{\min}$ and $C_p = C_{p,\max}$, the minimum width w_{\min} and maximum width w_{\max} can respectively be written as a function of L , N , and $\{h, \mu\}$, as seen in Eq. 5.27 and Eq. 5.28 respectively.

On the one hand, the w_{\min} expression (Eq. 5.27) provides the minimum width w required to be able to satisfy the minimum blocking force application constraint, as a lower width would reduce the stiffness of the actuator.

$$w_{\min} = \frac{4F_{\min}L^3s_{11}s_e\mu^3}{-3d_{31}E_3L^2h^2N^2s_e\mu^2(1+\mu) + h^3\delta P} \quad (5.27)$$

On the other hand, the w_{\max} expression (Eq. 5.28) provides the maximum width w required to be able to satisfy the maximum actuator capacitance constraint, as a greater width would increase the surface of the electrodes and therefore the total capacitance.

$$w_{\max} = C_{p,\max} \frac{h}{LN\epsilon_{33}} \quad (5.28)$$

It is possible to replace w with the expressions of w_{\min} and w_{\max} in the f_β and ϵ_f objective functions in order to create parametric curves representing the boundaries of w as a function of all the other parameters. Both of the parametric curves have been plotted over the objective functions in Fig. 5.4, in red for w_{\min} and in purple of w_{\max} . The surface of the plotted objective functions colored in pink corresponds to the design points satisfying the condition imposed on the width w by the optimisation constraints: $w \in [w_{\min}; w_{\max}]$. Since both objective functions are compatible in terms of optimisation with respect to L and w , i.e. increasing L and decreasing w is beneficial to both, it can be asserted that the intersection between the two parametric curves, in other words the point (L, w) satisfying the condition $w_{\min} = w_{\max}$, corresponds to the optimal solution for a given N and $\{h, \mu\}$.

Since one optimal solution can be associated to a N and $\{h, \mu\}$ pair of parameters, the optimisation could proceed with a study of the evolution of the objective functions with respect to these parameters. This reduces the dimensionality of the optimisation study further by

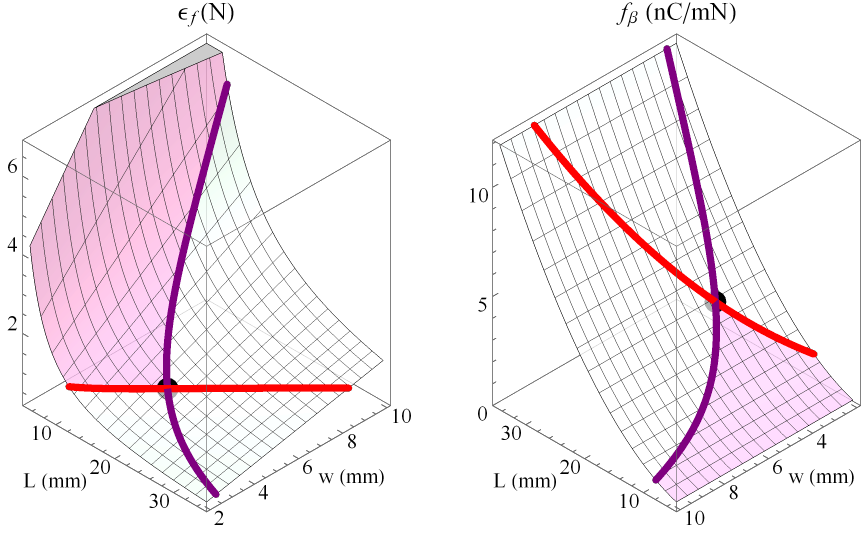


Figure 5.4 – Graphical representation of the ϵ_f and f_β objective functions for a $N = 1$ and layer thickness h ; w_{\max} (Purple), w_{\min} (Red).

tying the values of L and w to a given N and $\{h, \mu\}$ pair of parameters. Two problems arise from this approach and render it impossible to achieve analytically, however. The first issue is that it is impossible to solve N in equations using the f_β and ϵ_f objective functions, since the dependency of these functions to N is polynomial to the m^{th} degree, where $m > 3$. The second issue is that there is no guarantee that the (L, w) intersection between w_{\min} and w_{\max} is within the design space. It is then proposed to proceed with the optimisation study numerically, as both N and $\{h, \mu\}$ are discrete parameters with a limited number of possible values, especially in the case of the latter.

Numerical approach: Finding the Pareto frontier

The remaining parameters to fine tune in order to optimise the actuator design are the number of layers N as well as the thickness pair $\{h, \mu\}$, both discrete in nature. The former may have up to 40 possible values, while the latter can only have three. It is thus more efficient to solely study the evolution of the objective functions with respect to N , and to repeat the same study across the three possible values of $\{h, \mu\}$. The approach will hereafter be to plot the objective functions for each layer thickness h with respect to N , then to determine the Pareto frontier of the optimisation problem. As previously demonstrated, when considering the optimisation constraints, there exists an optimal solution (L, w) for a given N that both maximises f_β and minimises ϵ_f at the intersection of the w_{\min} and w_{\max} curves. It has also been mentioned that this solution could be outside of the boundaries of the design space.

Hence, the first step to plotting all the optimal solutions with respect to N is to establish an algorithm which will find the second best (L, w) solution which fits within the design space.

5.3. Multi-objective optimisation study based on the complete model

This is possible due to the monotonicity of the f_β and ϵ_f objective functions within the design space, and due to their compatibility in terms of goals, i.e. L must be maximised and w minimised in order to optimise both functions. With this in mind, the compatible approach to maximising each objective function can be described in two steps. Let w_0 be the minimum value of w , w_f the maximum value of w , L_0 the minimum value of L , and L_f the maximum value of L in the design space defined in Tab. 5.2.

Considering the initial (L, w) optimal solution found analytically at the intersection of the w_{\min} and w_{\max} constraint functions, the length L must first be reduced to $L' = L_{\max}$ if necessary, or left to $L' = L$ otherwise. Following this initial step, the width w must be adjusted according to four identified cases. In accordance with the relationship of ϵ_f to the width w , the algorithm must pick the lowest possible value of w that still conforms to the design space and constraints. The adjustment of w will thus depend on the relationship between the boundaries of the design space $[w_0, w_f]$ and the constraints $w_{\min}(L')$ and $w_{\max}(L')$. The four identified cases, which are illustrated in Fig. 5.5, are the following:

- **Case 1:** Both $w_{\min}(L')$ and $w_{\max}(L')$ are greater than the boundaries, such that $w_f < w_{\min}$. The length L must be reduced further by solving L'' for $w_{\min}(L'') = w_f$, and the best solution is therefore (L'', w_f) .
- **Case 2:** At least $w_{\min}(L')$ is within boundaries, such that $w_0 \leq w_{\min}(L') \leq w_f$. Considering the w_{\min} constraint, the best solution is $(L', w_{\min}(L'))$.
- **Case 3:** Only $w_{\max}(L')$ is within boundaries, such that $w_{\min}(L') < w_0 \leq w_{\max}(L') \leq w_f$. The width can be set to its lowest boundary, and the best solution is (L', w_0) .
- **Case 4:** Both $w_{\min}(L')$ and $w_{\max}(L')$ are lower than the boundaries, such that $w_{\max}(L') < w_0$. The length L must be reduced further by solving L'' for $w_{\max}(L'') = w_0$, and the best solution is (L'', w_0) .

As shown in the example for a width of $h = 50\mu\text{m}$ in Fig. 5.5, the lowest possible w that maximises L and satisfies all imposed conditions is always picked by the algorithm (black circle). The highest value of w that maximises L is represented by a red dot, and is considered the worst outcome for a maximised L in that it increases the ϵ_f objective function. Furthermore, this example shows that the new optimal (L, w) solution, replacing the analytically determined optimal solution, is always within boundaries of the design space and conforms with the design constraints imposed on F and C_p . It is possible that, after following the steps of the algorithm, the new length L' is lower than its lower boundary L_0 . In this situation, none of the (L, w) solutions within the design space satisfy the design constraints on F and C_p for the considered N and $\{h, \mu\}$ pair of parameters. Since there is no solution satisfying the constraints, the solution in this case is rejected.

The described algorithm is represented in pseudocode form in Fig. 5.6. The numerical approach to solving the multi-objective optimisation problem can therefore be pursued with

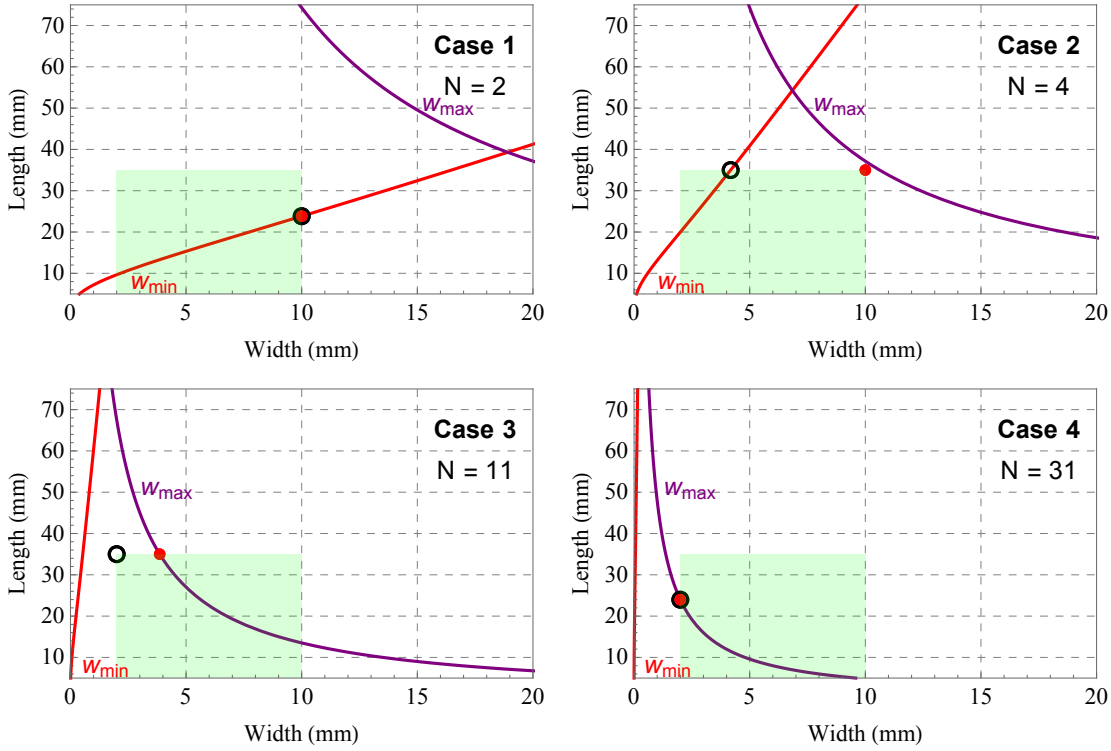


Figure 5.5 – Illustration of the four cases considered by the algorithm for $h = 50 \mu\text{m}$, with the valid design space for (L, w) drawn in green, the solution chosen by the algorithm circled in black, and the solution that is considered the worst as a red dot.

```

1: if  $L > L_{\max}$  then
2:    $L' = L_{\max}$ 
3: end if
4: if  $w_f < w_{\min}(L')$  then
5:   Solve  $L'$  for  $w_{\min}(L') = w_f$ 
6:   Calculate  $f_\beta$  and  $\epsilon_f$  with  $L'$  and  $w = w_f$ 
7: else if  $w_0 \leq w_{\min}(L') \leq w_f$  then
8:   Calculate  $f_\beta$  and  $\epsilon_f$  with  $L'$  and  $w_{\min}$ 
9: else if  $w_{\min}(L') < w_0 \leq w_{\max}(L') \leq w_f$  then
10:  Calculate  $f_\beta$  and  $\epsilon_f$  with  $L'$  and  $w_0$ 
11: else if  $w_{\max}(L') < w_0$  then
12:  Solve  $L'$  for  $w_{\max}(L') = w_0$ 
13:  Calculate  $f_\beta$  and  $\epsilon_f$  with  $L'$  and  $w = w_0$ 
14: end if

```

Figure 5.6 – Pseudocode of the (L, w) solution correction algorithm.

the digital implementation of the aforescribed steps. With there being a single optimal (L, w) solution after the application of the algorithm, it is possible to study the evolution of the objective functions with respect to N for each given $\{h, \mu\}$ pair of parameters, from which a maxima (respectively minima) for f_β (respectively ϵ_f) can be potentially singled out. This implementation produces the plots presented in Fig. 5.7 for the three possible $\{h, \mu\}$ pairs of parameters. These plots not only show the evolution of the objective functions f_β and ϵ_f with respect to N , but also the evolution of the corresponding design parameters L and w , as well as the evolution of the actuator characteristics F and C_p .

The series of plots in Fig. 5.7 clearly illustrate how the algorithm brings the initial analytical solutions in line with the design space (i.e. L, w) and constraints (i.e. F, C_p). The valid ranges for L, w, F and C_p are illustrated in white in their respective plots, with the exterior of their boundaries represented in grey. The leftmost column of plots in Fig. 5.7a show the evolution of the optimal objective functions with respect to N by analytically determining the optimal solution (L, w) at the $w_{\min} = w_{\max}$ intersection. In some cases, the (L, w) solution determined this way conforms with the imposed conditions, as can be seen for $h = 20\mu\text{m}$ for $N < 11$ for instance. For greater layer thicknesses, however, the length of the actuator is immediately out of bounds. The values of C_p and F are, as would be expected by solving the $w_{\min} = w_{\max}$ equation, constant and equal to their respective constraint values. In parallel, the evolution of the optimal objective functions with respect to N after the application of the algorithm can be seen in rightmost column of equations in Fig. 5.7b. These plots show that the optimal design points conform with the imposed conditions for all values of N and $\{h, \mu\}$, at the cost of a reduced overall optimality of the f_β and ϵ_f objective functions. The values of C_p and F are increased or decreased as a function of the w chosen by the algorithm, in accordance with the four identified cases of the algorithm illustrated in Fig. 5.5.

5.3.3 Closing remarks of the optimisation study

Were the design space not a concern, it would be clear that the objective functions would be monotonous with respect to N , and that increasing N to its highest value would be the answer to the optimisation problem. Additionally, the lefthand plots of Fig. 5.7 show that picking the greatest value for the layer thickness h would also provide the optimal solution. Both of these observations are counter intuitive to the observations that were made in the previous chapter regarding the optimisation goals for h and N .

However, this improved multi-objective optimisation study shows that, when considering realistic limitations of an actuator's parameters and its characteristics, the SSA performance of the actuator is greatly improved by reducing h to a minimum. This rectification of the optimal solutions is in line with the aforementioned observations made in the previous chapter that reducing h to a minimum is beneficial to the SSA performance of a design. The evolution of the new optimal solutions with respect to N indicates that, for each $\{h, \mu\}$ pair of parameters, there is a local maxima for f_β and a local minimal for ϵ_f . This is evidenced in the magnified

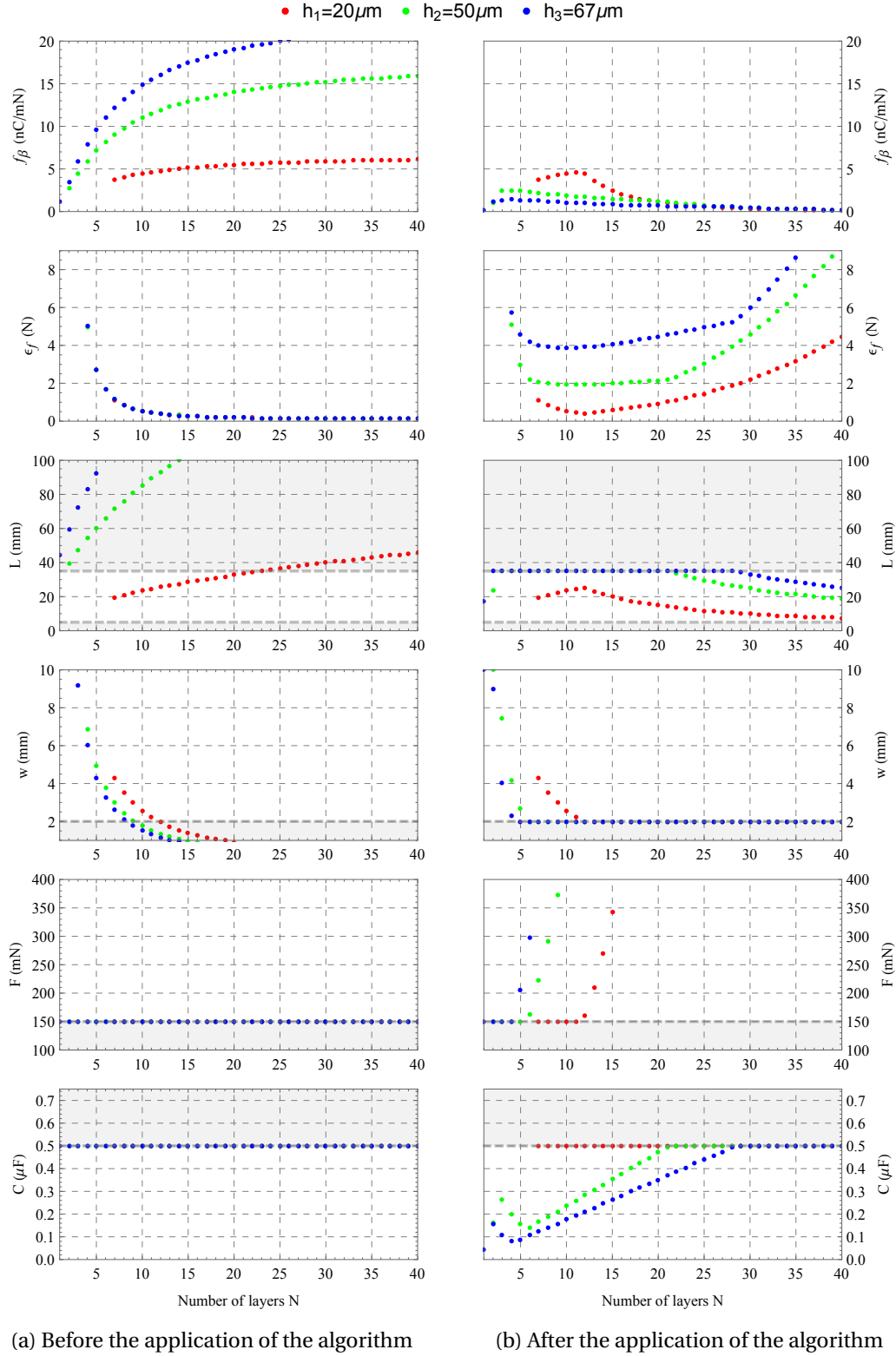


Figure 5.7 – Evolution of the objective functions f_β and ϵ_f , design parameters L and w , and constraint functions F and C_p , and after the application of the correction algorithm.

5.3. Multi-objective optimisation study based on the complete model

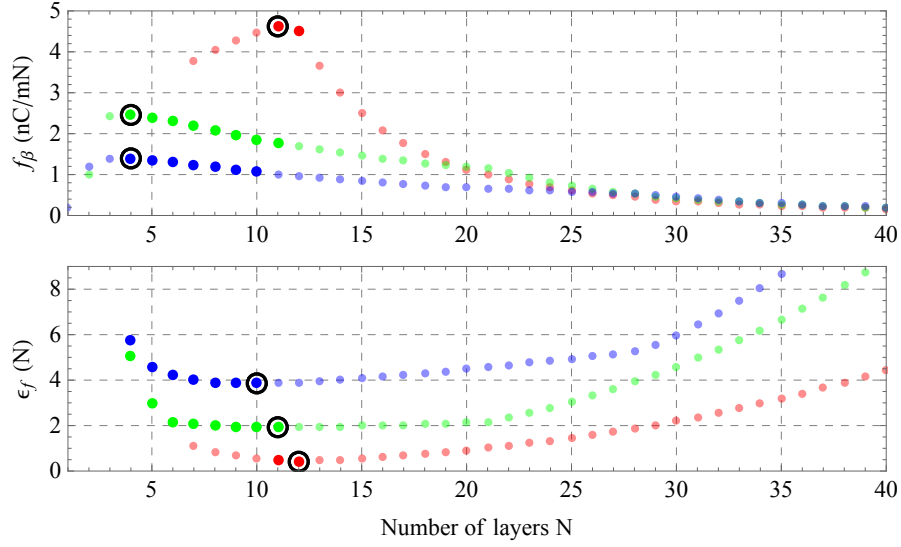


Figure 5.8 – Evolution of f_β and ϵ_f as a function of N ; the optimal solution for each objective function is circled in black, and the points making up each Pareto front in emboldened.

optimised objective functions plots with respect to N (Fig. 5.8), where the single optimal solution for each layer thickness is circled in black. Moreover, this plot indicates that for each h there exists a series of Pareto efficient values of N that optimise f_β and ϵ_f . This implies that, within these sets, it is not possible to improve one objective function without degrading the other. The sets constitute the Pareto frontiers of the multi-objective optimisation problem, and the points corresponding to each set are emboldened in Fig. 5.8.

The existence of these Pareto frontiers can be better observed by plotting all the optimal solutions (f_β, ϵ_f) across the complete range of the N and $\{h, \mu\}$ parameters. This is shown in Fig. 5.9, where ϵ_f is represented on the abscissa and f_β is represented on the ordinate. The range of (f_β, ϵ_f) solutions for each N is shown as a horizontal bar. These bars correspond to the range of values between the optimal w chosen by the algorithm and the worst viable w , as illustrated in Fig. 5.5. They are horizontal in these plots because w has no effect on the f_β objective function. The leftmost extremity of each bar corresponds to the w chosen by the optimisation algorithm, and therefore to the optimised points illustrated in Fig. 5.8.

Given the arrangement of the plot axes, the Pareto frontier for each h would correspond to the upper-left boundary of their respective body of solutions. The Pareto frontiers, circled in black in Fig. 5.9, are identical to the sets of Pareto efficient solutions evidenced in Fig. 5.8. When considering the optimisation of one objective function regardless of the other, the extremities of the Pareto efficient sets are found. The solutions that optimise f_β or ϵ_f the most are shown with their respective design parameters and final actuator characteristics in Tab. 5.3. The two points that constitute the Pareto frontier for the $h = 20\mu\text{m}$ body of solutions (Fig. 5.9) also form the Pareto frontier of the whole multi-objective optimisation problem, when grouping the bodies of solutions for all values of h .

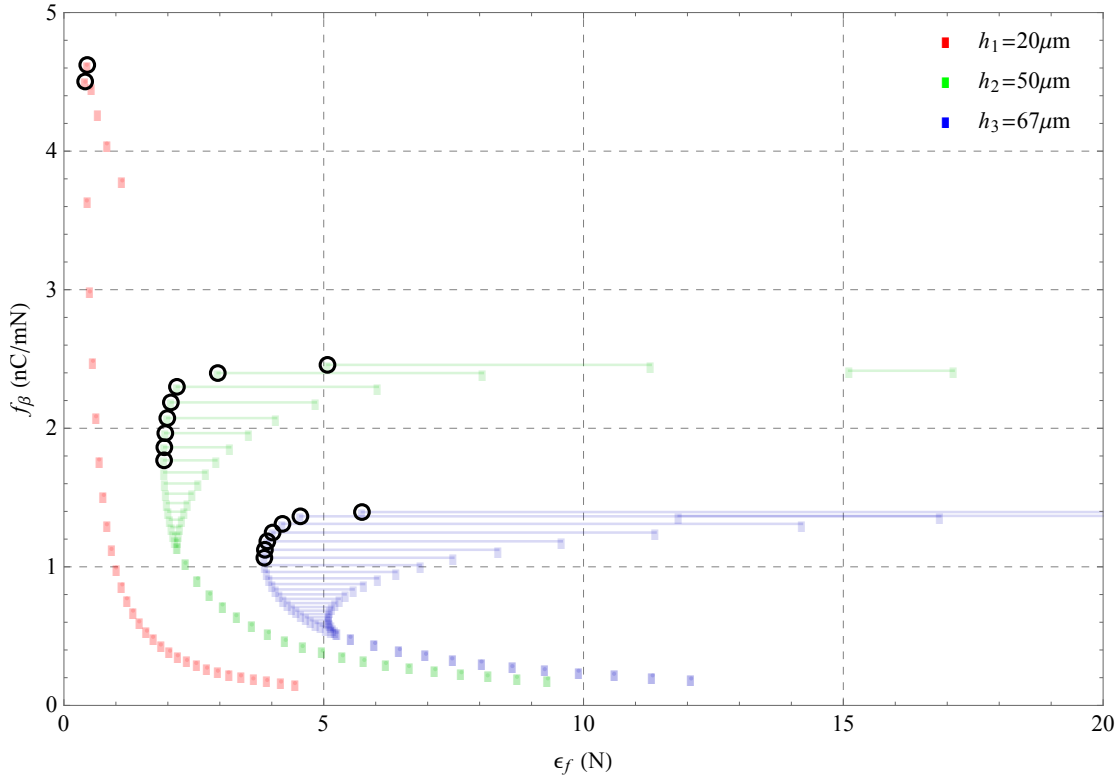


Figure 5.9 – Representation of all solution ranges for different values of N , with the leftmost extremity of each range corresponding to the solution chosen by the optimisation algorithm; the Pareto efficient points of the Pareto frontiers for each h are circled in black.

Among those two Pareto efficient points, a tradeoff must be made between maximising f_β and minimising ϵ_f in order to single out one best solution at the end of this multi-objective optimisation study. Since the most critical aspect of an SSA piezoelectric actuator is its *sensitivity* $|\beta|$, and that its *accuracy* may be improved using proper error compensation techniques, the solution maximising the f_β objective function ($N = 11$) is preferred. This results in an actuator within design specifications with a *sensitivity* of $|\beta| = 4.62 \text{ nC/mN}$, and with an *accuracy* defined by a maximum error of $\epsilon_f = 0.45 \text{ N}$. This amount of error may appear to be alarming for an SSA actuator intended for sub-mN accuracies. It is essential, however, to keep in mind that this error ϵ_f is not representative of the true estimation errors of the final SSA implementation. In such a case, the post-processing of the charge measurement will account for errors introduced by piezoelectric creep, hysteresis, and drift from the measurement electronics.

As a closing remark, the results of the optimisation study may be considered as intuitive. In a less restrained design space for the intervals of the length L and the width w , the optimal solution will always be found by applying the design guidelines formulated in Chapter 3. This can be analytically proven by demonstrating the monotonicity of both objective functions through the study of their partial derivatives. However, a local maxima for f_β and a local minima for ϵ_f have been introduced into the study by the inclusion of engineering considerations. These

Table 5.3 – Summary of the optimal solutions for each possible value of h , with an optimisation priority either on f_β or ϵ_f , and corresponding design parameters and characteristics.

h (μm)	Priority	L (mm)	w (mm)	N (-)	H (mm)	C_p (nF)	F (mN)	f_β (nC/mN)	ϵ_f (N)
20	f_β	24.4	2.2	11	0.57	500	150	4.62	0.45
20	ϵ_f	24.8	2.0	12	0.61	500	160	4.50	0.41
50	f_β	35.0	4.2	4	0.62	197	150	2.46	5.07
50	ϵ_f	35.0	2.0	11	1.35	259	563	1.77	1.93
67	f_β	35.0	2.3	4	0.82	80	150	1.40	5.74
67	ϵ_f	35.0	2.0	10	1.65	176	851	1.07	3.86

considerations are in part related to the fabrication process, for which adapted dimensions are needed to ensure planarity as much as they are needed to ensure realistic proportions for the actuator. The stability of the extrema imposed by engineering considerations may be asserted. This is due to the fact that the numerical correction of the optimal (L, w) solutions for a given $\{h, \mu\}$ follows itself the design guidelines of Chapter 3 by first choosing the longest possible length L , and then adapting the width w to the imposed performance constraints.

5.4 Conclusion

After providing an understanding of the causes of the initial model's inaccuracies, this chapter has successfully proposed a more accurate model for monomorph cantilevers intended for SSA implementations. The crux of the matter of this chapter has been the demonstration of a rigorous approach to achieving high SSA accuracies and sensitivities through actuator design. In order to maximise both of these aspects, the proposed design approach relies on a multi-objective optimisation study for which an original numerical optimisation algorithm has been provided. Two objective functions have been defined, with f_β describing the *sensitivity* of the actuator to be maximised, and the *accuracy* ϵ_f describing the estimation error of the self-sensing implementation to be minimised. These two functions formed the basis of the multi-objective optimisation study, and were associated with conditions in the form of a design space and characteristics constraints. A first pass of analytical study has provided a way to find an optimal (L, w) solution as a function of the other actuator morphology parameters, N and $\{h, \mu\}$. From this point onward, the optimisation study has proceeded with a numerical approach due to limitations of the analytical approach, and an algorithm has provided a way to find the Pareto frontier of the optimisation problem.

For each thickness of layer, i.e. 20 μm , 50 μm , and 67 μm , a best solution for maximising either the *sensitivity* or the *accuracy* has been identified. As expected from the initial design study provided in Chapter 3, the highest theoretical SSA performance would be obtained

Chapter 5. Definite improvement of self-sensing performance through optimisation

with thinner piezoelectric layers. The preferred solution on the Pareto frontier has been characterised with a β coefficient of -4.62 nC/mN , which offers a promising leap in SSA performance. To understand the performance gain due to this design approach, it is relevant to look at other actuators that have been discussed throughout this thesis:

- Compared to the commercial CMBP03 bender manufactured by Noliac presented in Chapter 2, and featuring a coefficient of $\beta = -0.486 \text{ nC/mN}$, the optimised offers a sensitivity increase by a factor of $\times 9.5$.
- Similarly, compared to the actuator manufactured following the design guidelines presented in Chapter 3 with a coefficient of $\beta = -3.139 \text{ nC/mN}$, the optimised design offers a sensitivity increase of 52%.
- A final point of comparison that could be made which would bring to light the potential of this optimised design would be the bender used by Rakotondrabe et al. in [46] in similar publications. They use a bender for which they identify a coefficient of $\beta = -1.03 \text{ nC/mN}$, and are capable of achieving sub-mN and sub- μm accuracies with their advanced SSA implementations. The optimised design used in similar implementations could then offer a theoretical sensitivity increase by a factor of $\times 4.5$.

Great strides of progress have been achieved in piezoelectric SSA since its inception, most of the advances having been made on the grounds of improving the error compensation, dynamic capabilities, and robustness of the sensorless estimation. With the definite improvement of SSA performance through actuator design methodologies presented in this chapter, a rather unexploited subject has been brought to light within the research field of piezoelectric self-sensing. This has been made possible by considering the SSA actuator as a sensor as much as an actuator, and bringing the focus onto the characteristics pertaining to its performance as a sensor when designing the actuator.

The following publications by the author are related to this chapter:

- Masson, L. and Perriard, Y. (2019a). Improved modelling of a monomorph piezoelectric actuator for linear self-sensing applications. In *2019 12th International Symposium on Linear Drives for Industry Applications (LDIA)*, pages 1–6, Neuchatel, Switzerland. IEEE
- Masson, L. and Perriard, Y. (2019b). Multi-objective optimisation methodology for self-sensing piezoelectric monomorph benders. In *2019 12th International Symposium on Linear Drives for Industry Applications (LDIA)*, pages 1–6, Neuchatel, Switzerland. IEEE

Conclusion and perspectives

Research overview

A broad variety of research topics pertaining to piezoelectric Self-Sensing Actuation (SSA) have been covered throughout this thesis. With the goal of achieving an actuator design capable of sensorless sub-mN estimation resolution and accuracy in mind, the work has adopted a bottom-up approach after a detailed overview of the current state of the art on the matter. This has entailed laying down the theoretical groundwork in order to understand the impact an actuator design might have on SSA prospects. This groundwork has provided an expectation for the general model of self-sensing piezoelectric actuators in the form of constitutive equations. With the assumption of the linearity of material properties, the latter related the mechanical and electrical inputs, the applied force and the driving voltage, to the mechanical and electrical outputs, the displacement and the accumulated charges.

Despite the objective of operating at quasi-static frequencies, i.e. working frequencies below 1 Hz, a dynamic model was still required to provide a tool to model step responses. Such a model has been assembled with the help of Bond Graph Models (BGM), and with it came valuable insight into the internal dynamics of the multi-physics system that is a piezoelectric actuator. The BGM provides the added benefit of enabling the study of the force and displacement estimation accuracies over time, and has served as a valuable tool to understand how an actuator's characteristics, i.e. capacitance and stiffness, potentially affected the sensorless estimation accuracies. Consequently, the firm expectation that properly designing an actuator for SSA would lead to greater results in terms of sensorless estimation had been sowed.

Before going into the design study of a particular morphology of self-sensing actuators, an experiment has been performed on a typical micro-robotic application. The aim has been to collect data on the manipulation forces and displacements required of the micro-robot to fulfil its task. Among several actuator morphologies, the monomorph bender has been selected for the design. This educated choice has been made upon the understanding of the positive effect of a lower stiffness on force estimation. From this choice, an analytical model of the bender has been formulated, tying every design parameter to the final characteristics of the actuator. After defining the design goals in terms of estimation resolution and error, an analytical study of the actuator fitness function has determined its monotonicity. This has thus provided a clear guideline to maximising the self-sensing performance within a pre-defined design space.

With these tools in hand, it has been possible to approach the conception of a prototype to demonstrate a high accuracy self-sensing piezoelectric actuator. The prototype is built around two subsystems: the piezoelectric actuator, fabricated according to the guidelines that have been derived from the design study; and the test environment surrounding the actuator, providing validation measurements for the displacement, the force, and electrically driving and sensing the actuator. By following the design guidelines, thin benders have been fabricated in bulk with the help of a commercial supplier. From the model that had been derived earlier, the fabricated actuators had a promising β coefficient of -9.01 nC/mN , offering a theoretical self-sensing performance increase of $\times 17$ over Noliac's commercial CMBP03 bender with a β coefficient of 0.486 nC/mN .

Before attempting to implement self-sensing estimation, it has been necessary to experiment on the batch of actuators with the prototype's test environment. The aim was not only to validate the self-sensing model, but also to determine the real parameters of the actuator that would be used in the sensorless estimation. Unfortunately, despite the great success in characterising the piezoelectric actuator, it was found that the measured β coefficient was of 3.139 nC/mN , lower than the model prediction by a factor of $\times \frac{1}{3}$. Despite these discrepancies, which were later solved in the final chapter of this thesis, a sensorless force estimation demonstration has been implemented on the prototype. Following the simulation scenario provided at the end of Chapter 2, the goal was to approach the bender to the force sensor's tip, which was acting as a simulated manipulation sample, with a ramping input voltage. The force would be determined while the actuator was live, demonstrating what kind of force estimation accuracy could be expected when attempting to detect a force threshold. Using a calibrated approach, it has been possible to achieve force estimation accuracies of 0.25 mN for experiments that were shorter than 60 s .

From the measurement campaign that has been held on the batch of actuators, it had become apparent that there is a significant difference between the actuator characteristics predicted by the analytical model and those that were measured experimentally. Hence the conclusion that one or several aspects of the main design had been made based on wrong assumptions. After analysing the aspects of the design that were considered negligible, the sources of the model error had been identified as the neglect of the electrode thicknesses and of electrical isolation layers at the top and bottom of the actuator stack. A new and complete model has been reformulated based on these observations, and the updated model provides an estimation of 3.046 nC/mN for the β coefficient of the fabricated benders, corresponding to an error of 3% .

The new model functions showed that a design solution that would maximise the self-sensing performance while guaranteeing proper actuator performance would be complex and offer no obvious solution, which had been the case with the first model. The opportunity has thus been seized to demonstrate a more rigorous design approach through multi-objective optimisation, once again based on the analytical study of the updated model. The study has resulted in a Pareto frontier, providing solutions that offer a tradeoff between estimation sensitivity and resolution. The optimal actuator design offered a β coefficient of 4.62 nC/mN ,

hence providing a 52% improvement over the first design that had been fabricated in bulk. Compared to the state of the art, the bender used by Rakotondrabe in [46] with great success in self-sensing applications has a β coefficient of 1.03 nC/mN. Hence, the optimised actuator discussed in this thesis would offer a sensitivity increase of $\times 4.5$. These promising results pave the way for future research that would push the envelope of what is possible in terms of accuracy and resolution with piezoelectric self-sensing actuation.

Original contributions

The original research that has been conducted for this thesis has brought forward some novel contributions to the state of the art of self-sensing piezoelectric actuators. These contributions are outlined in the following points of this section.

- *Piezoelectric self-sensing framework:*

There has been a lack of presentation on how to approach piezoelectric SSA from the scientific literature, as most examples made use of readily available commercial actuators to implement their successful strategies. The research proposed in this thesis has sought to address this by proposing a bottom-up approach to self-sensing. A theory has been formulated by considering the actuator as a system receiving force and voltage as inputs, and resulting in charge and displacement outputs. Constitutive equations describing the relationship between the four signals have been derived from the model, and it has been shown that the form of this model is the same for every actuator morphology. The main strengths of Bond Graph Models (BGM) have been exploited to complement the theory with a dynamic model. The BGM of a complete self-sensing system including the actuator, the charge sensing electronics, and the mechanical interface offers an high-level intuitive understanding of the multi-physics system.

- *Insight into the relationship between actuator characteristic and SSA performance:*

In addition to its qualitative insight, the use of a BGM to perform a dynamic simulation has been demonstrated. This simulation has provided a quantitative evaluation of the self-sensing performance of a system over time. This has been used to bring to light the impact of actuator characteristics on self-sensing estimation accuracy. Aside from the expected tradeoff between actuation performance and self-sensing resolution, a tradeoff between displacement control and force control has been evidenced: for instance, a lower stiffness leads to greater force estimation resolution while reducing the free stroke of the actuator. This intuition serves a purpose in understanding what actuator morphology to choose from depending on the target application.

- *Model-driven self-sensing optimisation for piezoelectric actuators:*

Several examples of piezoelectric bender modelling exist in the state of the art, but all featured a fixed configuration in terms of layers in the actuator stack. Two instances of modelling are available in the present thesis, and they have demonstrated how to

approach benders with a variable number of piezoelectric layers. Such analytical models are useful, as they bring more design flexibility in self-sensing piezoelectric actuators. From this model, analytical studies and multi-objective optimisations have shown that there is a tradeoff for the actuator stack.

- *Modular environment providing grounds for SSA experimentation:*

The prototype consisting of custom fabricated piezoelectric benders surrounded by a modular test environment has provided flexibility in researching self-sensing implementations. The possibility of measuring the complete electro-mechanical state of the operated actuator makes it possible to validate the output of the self-sensing estimation. The self-sensing implementation that has been demonstrated in this thesis has made use of a calibrated approach, and the repeatability of the approach has been satisfactory while offering good force estimation accuracies.

Outlook and future prospects

While this thesis has explored a broad array of topics, the field may still benefit from more research interest. Some aspects of piezoelectric SSA in particular have not been explored in depth in the scope of this research,

- *Strengthening piezoelectric SSA theory:*

While tests on multiple actuators have been made and have shown that the pre-calculated analytical model fit the general SSA models, the understanding of the effect of design morphologies on actuation and self-sensing performances may benefit from additional research. By systematically modelling and experimentally characterising a wide variety of morphologies, e.g. piezotubes, shear stacks, membranes, one could compile a robust catalogue of solutions to various ranges of micro-robotic applications. Expanding the model capabilities beyond the linear aspects of the actuator's behaviour should also be considered. With such possibilities in hand, it would become possible to reduce the impact of non-linear effects such as creep and hysteresis in the actuator design by accounting for them in the multi-objective optimisation.

- *Dynamic considerations of self-sensing:*

Quasi-static applications have been the target working frequency of the prototype. While the working dynamic models constructed with BGMs allow for a quantitative description of a self-sensing system's dynamic responses, this aspect of the actuator performance has not been taken into account during the optimisation and design of the prototype. To extend the improvement of piezoelectric SSA performance further, more research needs to consider working the dynamic aspects of actuation and sensing into the model-driven approach that has been presented in this thesis.

- *Robust charge measurement accounting for piezoelectric non-linearities:*

The most critical aspect to the implementation of SSA is the measurement of trace

amounts of electrical charge (i.e. pC–nC), in particular in quasi-static applications where the charge measurement must be accurate for long periods of time. This challenge is made more difficult by parasitic effects that plague the charge measurement, such as the creep and hysteresis inherent to piezoelectric properties, or the presence of leakage and bias currents within the drive electronics. Leaps and bounds of progress could be achieved if research effort were invested into this particular aspect of the charge-based self-sensing topic, as this would be the key to extending the duration of the self-sensing accuracy above 60 s.

- *Towards a more engineered micro-robotic integration:*

The developed prototype has been used to position with respect to and apply force on a manipulation target. Such experiments are sufficient to demonstrate the increases in performance through model-driven self-sensing actuator design, however it remains distant to real micro-robotic applications. In the latter, tools are used to interact with μm -scale samples (e.g. electrical probes, diamond points, graspers), while in the former, the end tip of the piezoelectric actuator directly interacts with the sample. The path to large-scale use of piezoelectric SSA, and therefore the furtherment of miniaturised micro-robotics, requires the study of kinematic chains and configurations making use of optimised self-sensing actuators.

Scientific literature

Over the course of this thesis, the following publications have been submitted and published by the author:

- Masson, L., Civet, Y., Germano, P., and Perriard, Y. (2017). Design of a generalised charge-based self-sensing model for quasi-static piezoelectric actuators. In *2017 20th International Conference on Electrical Machines and Systems (ICEMS)*, pages 1–6, Sydney, Australia. IEEE
- Masson, L., Xinchang, L., and Perriard, Y. (2018). Design of an Optimized Self-Sensing Piezoelectric Cantilever for Micro-Robotic Applications. In *2018 International Conference on Manipulation, Automation and Robotics at Small Scales (MARSS)*, pages 1–6, Nagoya. IEEE
- Masson, L. and Perriard, Y. (2019a). Improved modelling of a monomorph piezoelectric actuator for linear self-sensing applications. In *2019 12th International Symposium on Linear Drives for Industry Applications (LDIA)*, pages 1–6, Neuchatel, Switzerland. IEEE
- Masson, L. and Perriard, Y. (2019b). Multi-objective optimisation methodology for self-sensing piezoelectric monomorph benders. In *2019 12th International Symposium on Linear Drives for Industry Applications (LDIA)*, pages 1–6, Neuchatel, Switzerland. IEEE

Conclusion and perspectives

- Masson, L. and Perriard, Y. (2019c). Study of self-sensing actuation strategies for quasi-static piezoelectric actuators. In *2019 22nd International Conference on Electrical Machines and Systems (ICEMS)*, pages 1–5, Harbin, China. IEEE
- Masson, L., Ren, X., and Perriard, Y. (2019a). Novel test environment for the development of self-sensing piezoelectric actuators. In *2019 22nd International Conference on Electrical Machines and Systems (ICEMS)*, pages 1–5, Harbin, China. IEEE
- Masson, L., Xinchang, L., and Perriard, Y. (2019b). An optimized self-sensing piezoelectric cantilever for micro-robotic applications. *Journal of Micro-Bio Robotics*, 15(2):91–103

A Equations of piezoelectricity

To model, optimise and design piezoelectric actuators, it is necessary to have a grasp on the theory of piezoelectricity. To that end, this appendix provides the constitutive equations for piezoelectric materials. After a brief on the discovery and the basic principles of piezoelectricity, the equations that describe the direct and converse effects will be presented, after which a short introduction on how a model may be derived is presented. For a complete overview of piezoelectric theory, the following sources are suggested:

- Tichý, J., Erhart, J., Kittinger, E., and Přívratská, J. (2010). *Fundamentals of Piezoelectric Sensorics*. Springer Berlin Heidelberg, Berlin, Heidelberg. ISBN: 978-3-540-43966-0
- Heywang, W., Lubitz, K., and Wersing, W., editors (2008). *Piezoelectricity: evolution and future of a technology*. Number 114 in Springer series in materials science. Springer, Berlin. ISBN: 978-3-540-68680-4

A.1 History of piezoelectric discovery

The precursor to the discovery of piezoelectricity has been the research of Carl von Linné and Franz Aepinus on pyroelectricity in the middle of the XIXth century. Both von Linné and Aepinnus had proven the existence of pyroelectric materials which, when subjected to temperature variations, saw a change in their electric polarization. Following these observations, other researchers had then stipulated that there would be another type of material that could present a change in electric polarization in response to a mechanical stress, without being able to prove or disprove the theory.

It was not until the year 1880, with the work of brothers Jacques and Pierre Curie, that the direct piezoelectric effect had been observed and experimentally validated. They had posited that the piezoelectric properties of a material would arise from the asymmetrical nature of its crystal structure. The hypothesis was successfully validated by measuring the variation of electric potential of crystals under mechanical stress, such as quartz, tourmaline and Rochelle salt. This experimental proof was however limited to the direct piezoelectric effect, as the converse effect

had not been considered at that point. It was in 1881 that Gabriel Lippmann had predicted that the piezoelectric effect was in fact reversible, on the basis of thermodynamics calculations. This indirect effect, named converse piezoelectric effect, would cause a piezoelectric material to strain under the application of an electric potential. Based on this mathematical proof, the Curie brothers would immediately go on to experimentally demonstrate the converse piezoelectric effect.

Even though Pierre and Marie Curie would develop a quartz piezoelectric electrometre to assist them in their research in 1889, piezoelectric theory saw little evolution until the contribution of Woldemar Voigt in 1910. In his *Lehrbuch der Kristallphysik (mit ausschluss der kristalloptik)* publication, Voigt rigorously described piezoelectric theory using tensor calculus using piezoelectric constants he defined. The aspects of the theory that are relevant to the work of this thesis will be laid out in the following paragraphs.

A.2 Equations

In the mechanical domain, the behaviour of linear elastic materials is described by Hooke's law, describing the relationship between the strain of a material (i.e. deformation) and the stress it is subjected to (i.e. pressure) [47]:

$$\mathbf{S} = \mathbf{s}\mathbf{T} \quad (\text{A.1})$$

where \mathbf{S} is the material strain, \mathbf{T} the associated stress, and \mathbf{s} the mechanical compliance. These parameters are represented in the form of tensors in the generalised form of Hooke's law. For simple isotropic materials, the tensor form of Hooke's law may be simplified into a scalar or matricial operation.

The electrical domain behaviour of any materials subjected to an electric field may be described by the following equation in matricial form [9]:

$$\vec{D} = \epsilon \vec{E} \quad (\text{A.2})$$

where \vec{E} is the electric field vector, \vec{D} the electric displacement field vector, and ϵ the permittivity coefficient matrix. Due to the three dimensional aspect of these quantities, the tensor form is not necessary for this physics domain.

Piezoelectric materials act as electro-mechanical transducers that cause both the electrical domain and mechanical domain to interact directly. This mutual interaction is described by the piezoelectric tensor \mathbf{d} which is appended to the two previous equations. As such, the electric field generated by the direct piezoelectric effect is described by $\mathbf{d}\mathbf{T}$, while the strain caused by the converse piezoelectric effect is described by $\mathbf{d}\mathbf{E}$ [58]. These updated equations constitute a system of two equations that completely describe a given material's behaviour in the two physics domains.

Let the superscripts T and E respectively denote a constant stress and electric field. By simplifying the tensorial notation with Einstein's notation, the equations describing piezoelectric theory are written as follows [19]:

$$\begin{cases} S_{ij} = s_{ijkl}^E T_{kl} + d_{ijk} E_k \\ D_i = d_{ikl} T_{kl} + \epsilon_{ij}^T E_j \end{cases} \quad (\text{A.3})$$

Tensors are mathematical entities that are complex to manipulate. For anisotropic materials, the \mathbf{d} tensor may require up to 18 independant coefficients to fully describe the piezoelectric properties of a material. Thankfully, the most commonly used crystals, i.e. barium titanate and lead zirconate titanate (PZT), belong to the 4 mm crystal class. The symmetry present in these crystals allow for simplifications of the property tensors of these materials, hence making it possible to use matricial notations to describe the phenomenon:

$$\begin{cases} \vec{S} = \{s\} \vec{T} + \{d\}^t \vec{E} \\ \vec{D} = \{d\} \vec{T} + \{\epsilon\} \vec{E} \end{cases} \quad (\text{A.4})$$

The coefficients of strain and stress tensors \mathbf{S} and \mathbf{T} have been linearised into vectors \vec{S} and \vec{T} , which is made possible by the symmetrical properties of PZT crystals. Indexes **1**, **2**, and **3** correspond the othorgonal deformations caused by the σ_x , σ_y , and σ_z stresses, while indexes **4**, **5**, and **6** correspond to the shearing deformations caused by the τ_{yz} , τ_{zx} , and τ_{xy} stresses:

$$\vec{S}^t = \begin{pmatrix} S_1 & S_2 & S_3 & S_4 & S_5 & S_6 \end{pmatrix} \quad \vec{T}^t = \begin{pmatrix} T_1 & T_2 & T_3 & T_4 & T_5 & T_6 \end{pmatrix} \quad (\text{A.5})$$

The axes **1**, **2**, and **3** used in the referential frame for the piezoelectricity equation in Eq. A.4 correspond to the crystallographic axes \mathbf{a} , \mathbf{b} , and \mathbf{c} of the tetragonal PZT crystal [58]. The **3**-axis hence corresponds to the polarisation direction of the piezoelectric material. Consequently, in order to simplify the tensorial notation into a matricial one, the coefficients of the material property matrices $\{d\}$, $\{s\}$, and $\{\epsilon\}$ are arranged as follows:

$$\{d\} = \begin{pmatrix} 0 & 0 & 0 & 0 & d_{15} & 0 \\ 0 & 0 & 0 & d_{24} & 0 & 0 \\ d_{31} & d_{32} & d_{33} & 0 & 0 & 0 \end{pmatrix} \quad (\text{A.6}) \quad \{\epsilon\} = \begin{pmatrix} \epsilon_{11} & 0 & 0 \\ 0 & \epsilon_{22} & 0 \\ 0 & 0 & \epsilon_{33} \end{pmatrix} \quad (\text{A.7})$$

$$\{s\} = \begin{pmatrix} s_{11}^E & s_{12}^E & s_{13}^E & 0 & 0 & 0 \\ s_{21}^E & s_{22}^E & s_{23}^E & 0 & 0 & 0 \\ s_{31}^E & s_{32}^E & s_{33}^E & 0 & 0 & 0 \\ 0 & 0 & 0 & s_{44}^E & 0 & 0 \\ 0 & 0 & 0 & 0 & s_{55}^E & 0 \\ 0 & 0 & 0 & 0 & 0 & 2(s_{11}^E - s_{12}^E) \end{pmatrix} \quad (\text{A.8})$$

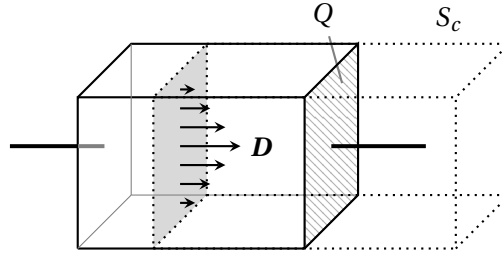


Figure A.1 – Integration surface used in the application of Gauss' law.

A.3 Deriving a model

The constitutive equations of the piezoelectric actuator are derived from the ground up by defining the actuator topology and its polarity, and by resolving the piezoelectricity tensors according to this definition [19]:

$$\begin{cases} D = dT + \epsilon^T E \\ S = s^E T + dE \end{cases} \quad (\text{A.9})$$

where the tensor D is the electric displacement field, E is the electric field, S is the strain, T is the stress, s the compliance constants, ϵ the dielectric constants, and d the piezoelectric constants of the material. Due to the symmetrical properties of common piezoelectric materials (e.g. PZT), the tensors of piezoelectricity may be written in matrix form [58] [19].

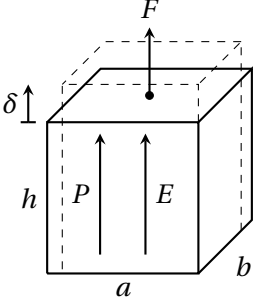
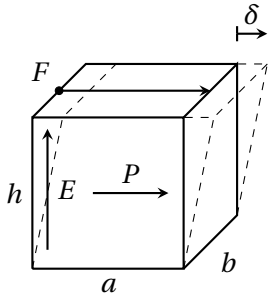
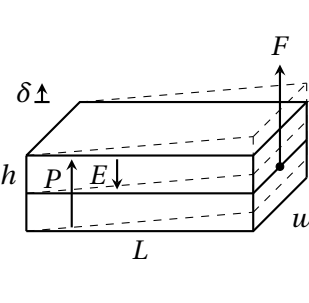
The accumulated electric charges on the electrode surface connected to the piezoelectric material may be derived by applying Gauss' law with the electric displacement field D evaluated in Eq. A.9. This law provides a relationship between the integration of the electric displacement vector D on a closed surface and the amount of electrical charges Q within the contained volume:

$$Q = \oint_{S_c} D \, dA \quad (\text{A.10})$$

where the closed surface S_c is chosen in a way that it encapsulates one of the actuator's electrodes, as illustrated in Fig. A.1. Only one of the faces of S_c presents a non-zero electric displacement field D , which greatly simplifies the integral in Eq. A.10.

The use of the piezoelectricity tensors (Eq. A.9) and of Gauss' law (Eq. A.10) are sufficient to derive the constitutive equations for any piezoelectric actuator. This approach is analytical by nature, and it is assumed that the properties of the piezoelectric material remain linear. This is evidently not the case, as these properties are affected by the electric field applied to the actuator. The non-linearities that affect the piezoelectric actuator, such as creep and hysteresis, need to be modelled aside for accurate control of the actuator. Despite these issues, these constitutive equations serve to examine the parameters of an actuator, and to determine its mechanical and self-sensing performances. Examples of parameters derived for basic actuators may be found in Tab. A.1: δ is the displacement, F the applied force, K the stiffness, C_p the capacitance, and β an electro-mechanical coupling coefficient related to the

Table A.1 – Constitutive equation parameters for three elementary deformations.

Traction	Shearing	Flexure
		
$\beta = d_{33}$	$\beta = d_{15}$	$\beta = \frac{3}{8} d_{31} \frac{L^2}{h^2}$
$K = \frac{ab}{hs_{13}}$	$K = \frac{ab}{hs_{55}}$	$K = \frac{2wh^3}{L^3 s_{11}}$
$C_p = \epsilon_{33} \frac{ab}{h}$	$C_p = \epsilon_{11} \frac{ab}{h}$	$C_p = \epsilon_{33} \frac{Lw}{h} + \frac{4}{3} \beta^2 K$

d_{ij} piezoelectric coefficients. The constitutive equations for the piezoelectric actuators in Tab. A.1 are all found by substituting the expressions of the β , K , and C_p parameters in the general model equations in Eq. 2.2, presented in Chapter 2.

Each of these examples demonstrates what shall be referred to as *elementary deformations*, as they provide simple examples of the main ways to produce motion with piezoelectric materials: flexure deformation, shearing deformation, and traction (or conversely compression) deformation. Traction (respectively shearing) deformations is created by ensuring that the electric field E and the polarity of the piezoelectric material P are colinear (respectively orthogonal), thus making use of the d_{33} (respectively d_{15} or d_{24}) piezoelectric coefficient. As for flexure deformation, the example provided here is that of a monomorph cantilever. An inactive piezoelectric layer is superimposed with one that is activated by an electric field aligned with its polarization. Through the d_{31} piezoelectric constant, the active layer is elongated, which results in flexure deformation of the whole beam due to the mechanical resistance of the attached passive layer. This type of motion can also be achieved and greatly amplified with bimorph benders, where both layers are activated with opposite electrical fields, therefore causing them to deform in opposite directions.

B Introduction to bond graph modelling

Bond graph modelling is a powerful and versatile approach to dynamic modelling of complex systems. This rather recent discipline proposes to study the energy exchanges that occur within a system, as well as those that occur between the system itself and its environment. From these modelled energy flows, constitutive equations for the system may be derived and its behaviour given specific inputs and conditions may be understood. The elegance of the bond graph approach stems from the fact that energy may be exchanged from one energy domain to another, and therefore it is easy to study multi-physics system and predict how the physics domains interact with each other. This is especially relevant when the studied systems are transducers, actuators, and sensors, which often have two or even three physics domain intervening in their operating principles. The choice of using bond graph modelling for self-sensing piezoelectric actuators has hence been self-explanatory in this thesis work. The present appendix serves as a brief introduction to bond graph modelling, the purpose of which is to familiarise the reader with the modelling concepts that will be manipulated.

Bond graphs are built up from two main categories of modelling objects: nodes and bonds. Nodes are components, or subsystems, of a system. For instance, the mechanical domain would include nodes that would portray masses, springs, and dampers, which the electrical domain would include resistors, capacitors, and inductors. The bonds are the energetic interactions that take place between these nodes. The particularity of these bonds is that they introduce the notion of computational causality. The model allows scientists to consider the order in which the energy flow is propagated within a system, which inevitably influences how the results of such an energy flow will be calculated: either through derivation or integration.

The theory of bond graph modelling has been formally defined by Henry Paynter in 1959. Since its inception, the method has been discussed in a myriad of scientific publications that have provided their own contributions. In the following sections, it is principally the work of Borutzky [4], Gawthrop [15], and Karnopp [33] that have been used to compile this summary. The variables that describe a bond will first be introduced, followed by an illustration of how these bonds are represented, after which the concept of causality is discussed. Finally, the nodes that constitute the basic building blocks of bond graph elements shall be enumerated.

B.1 Power conjugated variables

Bond graph models deal with the instantaneous energy exchanges that occur within a system, which are characterised by the instantaneous power $P(t)$. Two power conjugated variables are introduced: the effort $e(t)$, and the flow $f(t)$. These variables are related to the instantaneous power $P(t)$ through the following relationship:

$$P(t) = e(t) \cdot f(t) \quad (\text{B.1})$$

The proper analogy to illustrate the power conjugated variables would be the mechanical force F or the voltage u for the effort, and the velocity v or the current i for the flow. In fact, an equivalence for the effort and the flow may be drawn across multiple physics domain, as illustrated in Tab. B.1. These variables help to define the amount of power flowing between two components of a system.

In addition to the power conjugated variables, two energy variables are defined: the generalised displacement $q(t)$, and the generalised momentum $p(t)$. These variables quantify the total amount of energy transferred by the power $P(t)$ in a given time period, and are accumulated within energy stores of the system. These energy variables' equivalent physical quantities for each physical domain are also provided in Tab. B.1. They are each related to one of the power conjugated variables as such:

$$q(t) = q(t_0) + \int_0^t f(\tau) d\tau \quad (\text{B.2})$$

$$p(t) = p(t_0) + \int_0^t e(\tau) d\tau \quad (\text{B.3})$$

The relationship between the effort e , the flow f , the displacement q , and the momentum p are best illustrated by the so-called tetrahedron of state, as shown in Fig. B.1. By properly interpreting this tetrahedron, one may find how a flow is converted into an effort and, likewise, how a flow is caused by an effort. Depending on the order in which these variables are propagated within a system, the relationships are either integral or derivative. This concept is important to keep in mind when later considering the concept of computational causality for the elaboration of these models.

Three type of components are identified in the conversions between the four state variables: the generalised reactance R , inertance I , and compliance C . Analogies are often drawn between systems from different domains, the most common of which being between hydraulics and electronics to explain and contextualise how current and voltage interact within a closed circuit. In these analogies, components from different domains are often compared due to their similar impact on the constitutive equations of the system. This is where the generalised reactance, inertance, and compliance intervene. For instance, capacitors and springs behave as compliances for their respective domains. Furthermore, a generalised reactance is equivalent to a damper in the mechanical domain, and to a resistor in the electric domain. Finally, the inertance pertains to the mechanical mass and to the inductance.

B.1. Power conjugated variables

Table B.1 – Power conjugated variables pertaining to multiple physics domains.

Energy domain	Effort $e(t)$	Flow $f(t)$	Generalised momentum $p(t)$	Generalised displacement $q(t)$
Translational mechanics	Force F [N]	Velocity v [m/s]	Momentum p [Ns]	Displacement x [m]
Rotational mechanics	Moment M [Nm]	Angular velocity ω [rad/s]	Angular momentum L [Nms]	Angle θ [rad]
Electro- magnetic	Voltage u [V]	Current i [A]	Linkage flux λ [Vs]	Charge Q [C]
	Magnetomotive force Θ [A]	Magnetic flux rate $\dot{\phi}$ [Wb/s]	–	Magnetic flux ϕ [Wb]
Hydraulics	Total pressure p [N/m ²]	Flow rate Q [m ³ /s]	Pressure momentum P_p [Ns/m ²]	Volume V [m ³]
Thermodynamics	Temperature T [K]	Entropy flow \dot{S} [J/K/s]	–	Entropy S [J/K]
Chemical domain	Chemical potential μ [J/mol]	Molar flow \dot{N} [mol/s]	–	Molar mass N [mol]

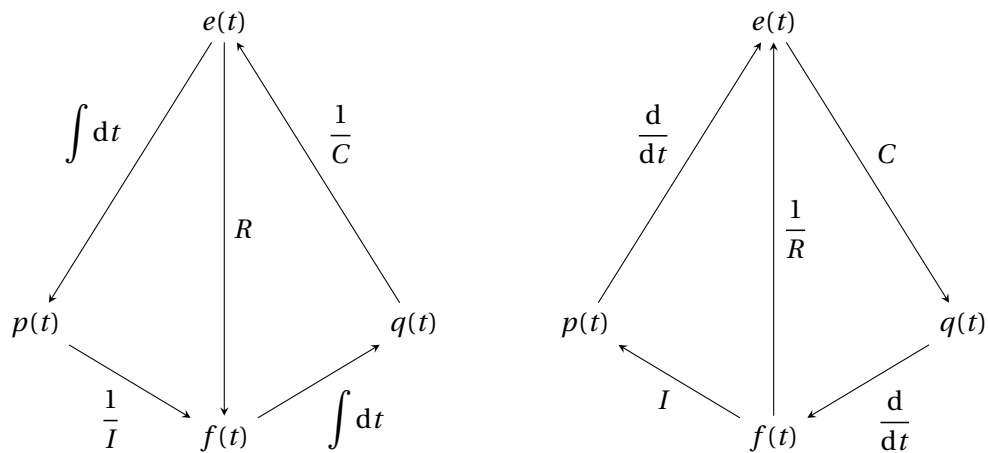


Figure B.1 – Tetrahedron of state [33], and relationship between its variables.

B.2 Power bonds

A power bond is the graphical representation of an energy exchange between two nodes of the bond graph. It is quantified by the instantaneous power $P(t)$, and its conjugated power variables $e(t)$ and $f(t)$. Given knowledge of the nodes and their bonds, it is possible to deduce a set of equations at each of the system's nodes. Due to the fact that an energy exchange, or flow, has a concept of directionality, a sign convention must be provided so that the power conjugated variables of the energy exchange $P(t)$ are consistent with respect to their sign. This is achieved by adding a half-arrow in the graphical representation of the power bond (Fig. B.2). Any variable flowing in the direction of the bond's half-arrow reference be positive.

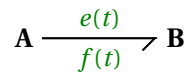


Figure B.2 – Graphical representation of a power bond.

In the example of Fig. B.2, positive energy flows from node **A**, an energy source, into node **B**, an energy sink. For nodes that are energy sources in a specific power bond, the positive direction of power $P(t) > 0$ flows away from the node itself. On the contrary, the positive direction of power $P(t) > 0$ flows into energy sink nodes. To further describe a bond, labels for the effort (top) and for the flow (bottom) may be provided around the half-arrow.

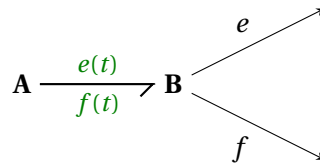


Figure B.3 – Graphical representation of activated bonds (i.e. signals).

There exists a special kind of bond, labelled as *activated bond*, which merely conveys an information. They are generally represented as a simple arrow flowing out of a node, with a label of the power conjugated variable that is conveyed by the signal. This signal can then be fed into a block diagram for signal processing and for feedback control. Since ideal measurements only carry the information of one power conjugated variable while the other variable is zero, the effective energy flow $P(t)$ within that bond is null. As such, activated power bonds do not affect the power balance of the node it originates from.

B.3 Concept of computational causality

As mentioned earlier, bond graph nodes each have an associated constitutive equation that may be derived from the bonds they are connected to. Determining the constitutive equation for each node of the bond graph provides the user with a set of equations that completely describes the system. Bonds carry two variables, the effort $e(t)$ and the flow $f(t)$, and one constitutive equation is not enough to solve both variables.

Hence the need for one of the variables to be considered as imposed by the node at the other end of a bond. In this manner, each node's equation may be solved to provide an expression for either $e(t) = F(f(t))$ or $f(t) = F(e(t))$, enabling the possibility of systematically deriving the constitutive equations for a full system through its bond graph model. This is done by assigning the computational causality within a bond.

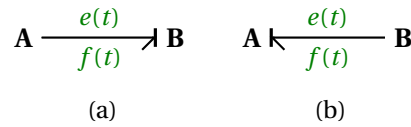


Figure B.4 – Standard graphical representation for the causality of a power bond.

The graphical representation for the assignment of computational causality is a straight line orthogonal to the bond placed at either node (Fig. B.4). This line indicates which side of the bond is imposing the flow $f(t)$. Consequently, the absence of a line on one side indicates that this side is imposing the effort $e(t)$. As such, the following may be said of node **A** in each case represented in Fig. B.4:

- a. $f(t)$ is imposed by node **B**, and $e(t) = F(f(t))$ is derived from node **A**.
- b. $e(t)$ is imposed by node **B**, and $f(t) = F(e(t))$ is derived from node **A**.

B.4 Bond graph elements

Nodes are the building blocks of bond graph models, and several types of basic nodes have been defined so that all systems may be schematically represented from them. While energy storage nodes are single-port, most nodes are multi-port, implying that they can be connected with two or more bonds. All nodes are associated with one or more constitutive equations describing their influence over the bonds they are connected to. More specifically, these constitutive equations describe the behaviour of a multi-port element at a given port as a function of its power conjugated variables. Due to the non-spatial properties described by bond graph nodes, the constitutive equations of the latter may be considered as lumped parameter models. They each represent a single effect of a more complex physical phenomenon.

B.4.1 Elements and their constitutive equations

The following paragraphs will describe the basic bond graph nodes that are used to model most multi-physics systems. Each node will be presented with its constitutive equations. As a means of concluding this overview of bond graph nodes, the next section provides a table summarising all the presented nodes along with their constitutive equations.

Power conserving junctions

As Henry Paynter, the creator of bond graphs, put it in *The Gestation and Birth of Bond Graphs* (2000), the power conserving junctions have a capital role in rendering bond graphs a complete and formal discipline. These nodes serve to split and distribute the power conjugated variables among several other nodes. They neither dissipate nor store energy, as they are energy conservative. They are a multi-port node, featuring two to as many ports as required to distribute and propagate a variable.

The first of these nodes is the 0-junction, otherwise known as a *flow junction*. These nodes propagate an input effort throughout all their ports, and split the incoming flows among all the outgoing flows. In this manner, they behave much like Kirchhoff's voltage law. The constitutive equations for a 4-port 0-junction as depicted in Fig. B.5 may be written as:

$$\begin{aligned} e_1 + e_2 &= e_3 + e_4 \\ f_1 &= f_2 = f_3 = f_4 \end{aligned} \tag{B.4}$$

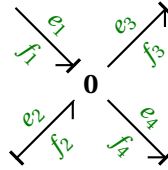


Figure B.5 – Bond graph node for a 0-junction with 4 ports.

The second node is the 1-junction, otherwise known as a *effort junction*. It is the dual of the flow junction, hence the naming convention opposing the 0-junction to the 1-junction. These nodes propagate an input flow throughout all of their ports, and split the incoming efforts into all outgoing efforts. As an analogy, it behaves similarly to Kirchhoff's current law. The constitutive equations for a 4-port 1-junction as depicted in Fig. B.6 may be written as:

$$\begin{aligned} e_1 &= e_2 = e_3 = e_4 \\ f_1 + f_2 &= f_3 + f_4 \end{aligned} \tag{B.5}$$

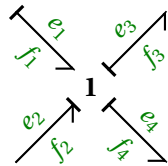


Figure B.6 – Bond graph node for a 1-junction with 4 ports.

Both 0-junctions and 1-junctions need to observe strict causality requirements. Indeed, since they propagate an input effort (respectively flow) to all of their ports, there needs to be one and only bond that imposes the propagated power variable. The required causality for both junctions is depicted in Fig. B.7. Note that *input* effort or flow does not mean whether the direction of the bond is directed toward the junction or not, hence the lack of half-arrows in Fig. B.7. Instead, the causality of one of the bonds imposes the propagated variable to the junction while the causality of all other bonds are reversed.



Figure B.7 – Expected causality for 0-junctions and 1-junctions.

Should a 0-junction or 1-junction fail to meet this strict causality requirement, the system would be in a causal conflict. Such a conflict makes it impossible to systematically derive the constitutive equations of the system. This is generally remedied by toggling the causality of the bonds that connect the junction with its surrounding nodes, often alternating the equations of adjacent nodes between integral and derivative causalities.

Energy storage elements

Energy stores are 1-port nodes that describe how energy is stored in a system. The energy is generally stored in the form of a momentum or a displacement, and these nodes are considered energy conservative. Two main types of energy stores are defined: C-stores which are related to the generalised compliance component C of a physics domain, and I-stores which are related to the generalised inertance component I of a physics domain.

The C-store nodes store energy in the form of generalised displacements $q(t)$, and the latter are tied to the effort through the characteristic function of the node ϕ_C as follows:

$$q(t) = \phi_C(e(t)) \quad (\text{B.6})$$

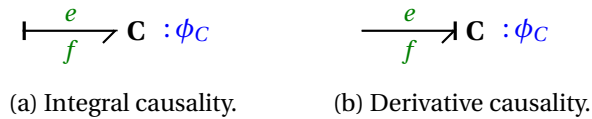


Figure B.8 – Bond graph nodes for 2-port C elements.

Depending on the defined causality of the node's bond, the constitutive equation of C-store nodes may be written as such, with the lefthand equation being the integral causality, and the righthand equation being the derivative causality:

Appendix B. Introduction to bond graph modelling

$$e(t) = \phi_C^{-1} \left(\int_0^t f(\tau) d\tau \right) \quad (\text{B.7})$$

$$f(t) = \frac{d}{dt} \phi_C(e(t)) \quad (\text{B.8})$$

The I-store nodes store energy in the form of generalised momenta $p(t)$, and the latter are tied to the flow through the characteristic function of the node ϕ_I as follows:

$$p(t) = \phi_I(f(t)) \quad (\text{B.9})$$

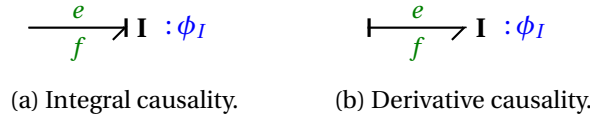


Figure B.9 – Bond graph nodes for 2-port I elements.

Depending on the defined causality of the node's bond, the constitutive equation of I-store nodes may be written as such, with the lefthand equation being the integral causality, and the righthand equation being the derivative causality:

$$f(t) = \phi_I^{-1} \left(\int_0^t e(\tau) d\tau \right) \quad (\text{B.10})$$

$$e(t) = \frac{d}{dt} \phi_I(f(t)) \quad (\text{B.11})$$

The difference between integral and derivative causalities may be understood when examining the tetrahedron of state describing the relationship between the four state variables (Fig. B.1). The integral causality is generally preferred when modelling engineering systems, but it may happen that the derivative causality is sometimes required. This generally happens when a causal conflict needs to be solved. Note that in their preferred causalities, C-stores impose the flow to their adjacent node while I-stores impose the effort to their adjacent node.

Dissipators

Dissipators are nodes that provide a direct relationship between the effort and the flow, and they are related to the generalised reactance component R of a physics domain. They model the energy losses that occur within a system, whether it's due to friction, heat dissipation, or magnetic losses.

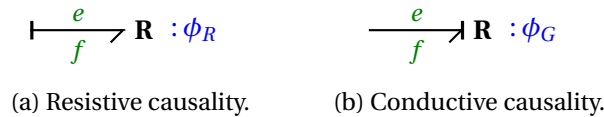


Figure B.10 – Bond graph nodes for R elements.

The constitutive equation of the R node may be written as such, with the lefthand equation describing the resistive causality, and the righthand equation describing the conductive causality:

$$e(t) = \phi_R(f(t)) \quad (\text{B.12})$$

$$f(t) = \phi_G(e(t)) \quad (\text{B.13})$$

The resistive characteristic function of the R node ϕ_R is the inverse of its conductive characteristic function ϕ_G . These nodes are not as sensitive to the causality assigned to their bond, as they are not defined by an integral or derivative characteristic.

Ideal energy sources and sinks

Ideal energy sources and sinks are non-physical elements. Energy cannot be created or destroyed, it is exchanged. The system modelled by a bond graph does not encompass the whole universe, but a piece of it which is the scope of the system. Therefore, rather than describing actual components of a system, ideal energy stores and sinks are used to describe the interaction of the system with its external environment.

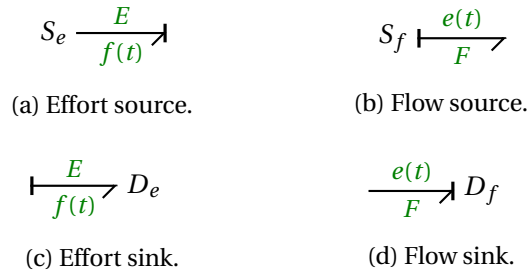


Figure B.11 – Bond graph nodes for ideal energy sources and sinks.

The bonds of ideal energy sources (respectively sinks) impose an outgoing (respectively ingoing) effort E or flow F . They are graphically represented as shown in Fig. B.11

Ideal couplers

Finally, ideal couplers are 2-port nodes that convert energy from one physics domain into another. They are energy conservative, implying that they do not dissipate energy, and they do not store energy. Instead, couplers merely exchange energy between their two ports. There are two kinds of couplers used in bond graphs: transformers (TF) and gyrators (GY).



Figure B.12 – Bond graph nodes for transformers (TF).

Transformers (Fig. B.12) establish a direct transformation of the power conjugated variables from one physics domain into another. Note that transformers may have either an effort or a flow as input, and that their output retains the same causality. The constitutive equations for these 2-port couplers constrain the efforts and the flows of its bonds as follows, where the

modulus m is a positive real constant:

$$\begin{aligned} e_1(t) &= m \cdot e_2(t) \\ f_2(t) &= m \cdot f_1(t) \end{aligned} \quad (\text{B.14})$$



Figure B.13 – Bond graph nodes for gyrators (GY).

Gyrators (Fig. B.13) on the other hand establish a crossed relationship between the power conjugated variables of its two bonds, from one physics domain into another. This implies that the effort of the input is related to the flow of the output, and that the flow of the input is related to the effort of the output, hence the opposite causalities of the coupler's two bonds. The constitutive equations for these 2-port couplers constrain the efforts and the flows of its bond as follows, where the gyrator ratio w is a positive real constant:

$$\begin{aligned} e_1(t) &= w \cdot f_2(t) \\ f_2(t) &= w \cdot f_1(t) \end{aligned} \quad (\text{B.15})$$

Modulated variants of transformers and gyrators exist where the coefficients m and w are replaced by controllable, modulated, functions $f(t)$ and $g(t)$. The **M** prefix is appended to the name of the nodes, and they are represented as in Fig. B.14. Note that modulated sinks and sources may also be defined in a similar way. Special care must be taken that modulated elements such as sources and sinks do not violate the principles of energy conservation.

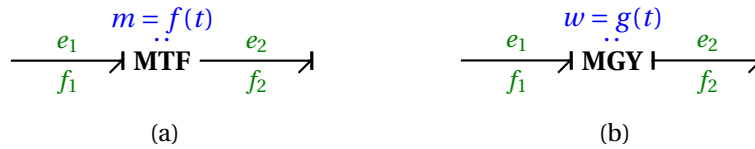
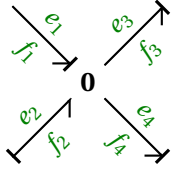
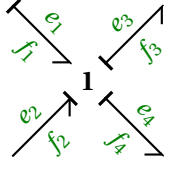
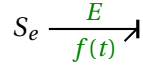
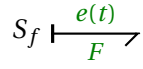
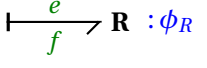
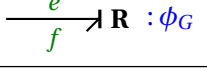
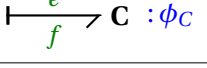
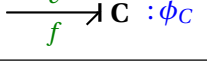
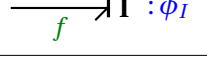
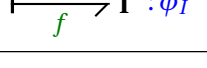
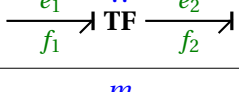
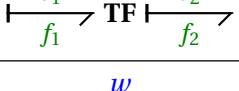
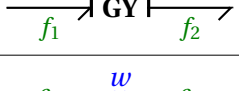
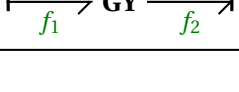


Figure B.14 – Examples of modulated elements: modulated (a) transformer, (b) gyrator.

B.4.2 Summary

Now that an overview of the basic elements used to build bond graphs has been provided, it is proposed to summarise all of this information into a table in Tab. B.2. When working with or reading about bond graph models, it is a helpful resource to better grasp all the notions that are being worked with.

Table B.2 – Summary of the bond graph elements and their constitutive equations.

Element	Bond graph node	Constitutive equations
0-junction		$e_1 = e_2 = e_3 = e_4$ $f_1 + f_2 = f_3 + f_4$
1-junction		$e_1 + e_2 = e_3 + e_4$ $f_1 = f_2 = f_3 = f_4$
Effort source		$S_e = E(t)$
Flow source		$S_f = F(t)$
Dissipator		$e(t) = \phi_R(f(t))$
		$f(t) = \phi_G(e(t))$
1-port C element		$e(t) = \phi_C^{-1}\left(\int_0^t f(\tau) d\tau\right)$
		$f(t) = \frac{d}{dt} \phi_C(e(t))$
1-port I element		$f(t) = \phi_L^{-1}\left(\int_0^t e(\tau) d\tau\right)$
		$e(t) = \frac{d}{dt} \phi_L(f(t))$
2-port TF element		$e_1(t) = m \cdot e_2(t)$ $f_2(t) = m \cdot f_1(t)$
		$e_1(t) = m \cdot e_2(t)$ $f_2(t) = m \cdot f_1(t)$
2-port GY element		$e_1(t) = w \cdot f_2(t)$ $f_2(t) = w \cdot f_1(t)$
		$e_1(t) = w \cdot f_2(t)$ $f_2(t) = w \cdot f_1(t)$

C Charge measurement techniques for high impedance devices

Initial charge measurement attempts that have been performed on the fabricated benders in Chapter 4 have shown that, if uncompensated for various parasitic effects, the charge measurement has a tendency to drift by an order of magnitude after sufficiently long experiments, i.e. $\tau \geq 60$ s. The slightest unwanted current flowing in the actuator's drive and measurement electronics will be integrated by the charge amplifier, the Keithley 6517A, and is responsible for these drifts. Some of these phenomena can be modelled and therefore compensated in the measurement's post-processing. However, as it will be shown, some of these effects appear random, and must therefore passively be shielded against. In these paragraphs, the causes for these drifts shall be presented, and a solution to counter them will be discussed.

C.1 Parasitic effects inherent to the supporting electronics

The first category of measurement drift that will be discussed is caused by the measurement electronics itself. As a reminder from Chapter 2, the electronics is set up as shown in Fig. C.1. The piezoelectric actuator and a reference capacitor are connected to the HI terminal of the Keithley 6516A electrometer, of which the LO terminal is connected to the circuit's ground. The actuator and the reference capacitor C_r are supplied by symmetrical and opposite voltages $+V_{in}$ and $-V_{in}$ respectively. This is done to increase the dynamic range of the charge measurement for the Keithley 6516A, as this set up cancels in large part the electrical contribution of the voltage application if C_r is sufficiently close to C_p .

Let $Q(t)$ be the charges amplified by the electrometer, $Q_p(t)$ the charges accumulated by the piezoelectric actuator, and $Q_c(t)$ be the charges accumulated by the reference capacitor C_r . Given this measurement setup, the charges measured by the electrometer may be written as:

$$Q(t) = Q_p(t) + Q_c(t) = \beta F(t) + C_p V_{in}(t) - C_r V_{in}(t) \quad (C.1)$$

There are two other phenomena that affect the charge measurement from within the electronics. The first of these is the bias current i_b , an effect that is present at the input of circuits using

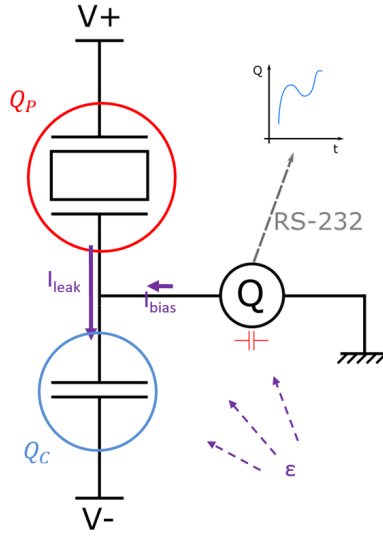


Figure C.1 – Charge components and parasitic charges.

operational amplifiers. For instance, the Keithley 6517A is designed to have a bias current lower than 4 fA. It is sufficiently low to be ignored in the majority of applications. However, this is not negligible when attempting to detect charges in the pC–nC range in long experiments, as its contribution is integrated over time. To characterise the bias current of the measurement electronics, the input voltage V_{in} is grounded and the current i_b is measured.

In addition to the bias current, the second phenomenon impacting the charge measurement over long periods of time is the leakage current. It is caused by the application of the voltage V_{in} on the piezoelectric actuator and the reference capacitor. Despite their great impedances, these leakage currents in the order of the fA–pA are also integrated by the electrometer and cause drift in the charge measurement. The leakage resistance is measured by applying a non-null input voltage V_{in} to the actuator and reference capacitor. The charge contribution of the bias current $i_b t$ is subtracted from the measured charge in order to obtain the leakage current, and therefore the leakage resistance R_l . With these phenomena in mind, the charges integrated by the electrometer in the measurement electronics may be written as such:

$$Q(t) = \beta F(t) + C_p V_{in}(t) - C_r V_{in}(t) + i_b t + \int_0^t \frac{V_{in}(t)}{R_l} dt \quad (C.2)$$

Let $Q_m(t) = \beta F(t)$ be the mechanical contribution to the charges, otherwise referred to as the sensing charge. This is the component that needs to be isolated from the electrical charge contribution and the parasitic effects in order to provide a sensorless estimation of the

actuator's mechanical state. From Eq. C.2, the sensing charge is thus written:

$$Q_m(t) = Q(t) - C_p V_{in}(t) + C_r V_{in}(t) - i_b t - \int_0^t \frac{V_{in}(t)}{R_l} dt \quad (C.3)$$

C.2 Parasitic effects inherent to the piezoelectric actuator

Some of the currents flowing through the bender that offput the charge measurement are produced by the actuator itself, due to the non-linearities inherent to piezoelectric materials. The two main causes of drifts are usually identified as creep and hysteresis, both of which are all the more important when considering quasi-static applications. Fortunately, these effects are well understood by now, and a great number of examples dealing with their compensation may be found in the scientific literature. In the specific context of piezoelectric SSA, Clévy has discussed how these effects are compensated from the charge measurement [7]. In fact, Clévy proposes that the $-C_p V_{in}$ term in Eq. C.3 should be replaced by operators describing the hysteresis and the creep : $Q_H(V_{in})$ and $Q_C(V_{in})$.

Hysteresis is a well known particularity of piezoelectric materials, and to a further extent ferroelectric materials. The non-linearities of the piezoelectric material's properties create a hysteretic relationship between the actuator's displacement and the applied voltage. This hysteresis is reflected upon the mechanical component of the charge accumulation, as the charge is directly related to the material's strain. After applying a triangular signal onto the actuator and compensating the output of the electrometer for bias and leakage currents, the hysteresis can be modelled by means of a Prandtl-Ishlinskii operator $Q_H(V_{in})$.

Caused by the non-linearity of the piezoelectric material's properties, the creep causes the displacement of the piezoelectric bender to continuously drift over the course of several minutes after the application of a driving voltage. This creeping deformation also provokes a drift in charge measurement, since the charge is related to the strain within the piezoelectric material. It may be modelled thanks to a Linear Time Invariant (LTI) function $Q_C(V_{in})$ after applying a voltage step, which is fitted to the resulting charge measurement after subtracting the hysteresis, bias, and leakage contributions. The resulting charge measurement with all the modelled compensations is thus written as such:

$$Q(t) = \beta F(t) + Q_H(V_{in}) + Q_C(V_{in}) - C_r V_{in}(t) + i_b t + \int_0^t \frac{V_{in}(t)}{R_l} dt \quad (C.4)$$

C.3 Parasitic effects caused by environmental contributions

The third and last category of parasitic effect that will be discussed are caused by the environment surrounding the actuator and the electronics. As such, they can not be modelled and

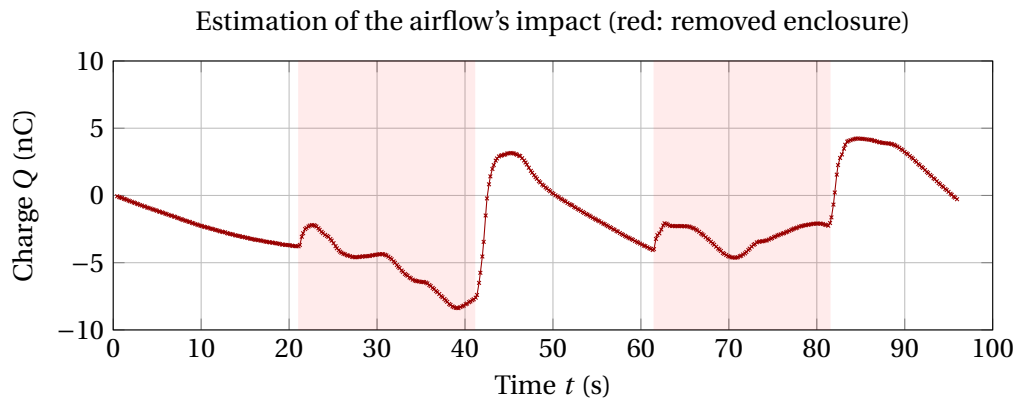


Figure C.2 – Effect of the airflow on the charge measurement: the enclosure is removed from the test bench in the red areas of the plot.

compensated from the charge measurement, and are prone to apparent randomness. The prototype's design must minimise these effects as much as possible. These effects are typically related to room temperature, electrostatic and electromagnetic interferences, and relative humidity, which all become a source of error when measuring small.

The first issue that arose when attempting to measure the leakage and bias currents was a random component that affected the charge measurement. After troubleshooting, the cause of this error has been identified to be the airflow within the room. To validate this hypothesis, an experiment was carried out with a charge measurement performed for over 100 s. During this experiment, an enclosure that has been designed to cover the piezoelectric actuator and its surrounding sensors is periodically taken out and put back on. The resulting charge measurement may be seen in Fig. C.2. Whenever the enclosure is removed, the current (i.e. derivative of the charge) varies over time, and whenever it is put back on, it becomes stable once more. The exact cause of the measurement's perturbation other than the fact that it is related to the airflow is unknown and hasn't been verified: it could be related to electrostatic charges carried by the air, or it could be that the self-sensing actuator is sensitive enough that small deformations caused by the airflow will impact the charge measurement.

Another issue that needs to be accounted for is the effect of electric perturbations caused by electrostatic and electromagnetic interferences. To that effect, the drive and measurement electronics must be carefully designed to limit these effects and be well guarded against external interference. In the self-sensing prototype, a double shielding setup as illustrated in Fig. C.4 has been used. The electrometer is connected to the electronics by way of a triaxial cable connected to two different shields. The inner shield, referred to as the noise shield, is connected to the ground of the electronics. It is meant to reduce the interference caused by external signals by absorbing currents and dissipating them in the ground plane, instead of in the tracks conducting sensitive signals. The outer shield, referred to as the safety shield, is connected to the earth. Its main function is to protect the user from electrocution hazard, but it also helps with guarding the electronics by acting as a secondary Faraday cage.

C.3. Parasitic effects caused by environmental contributions

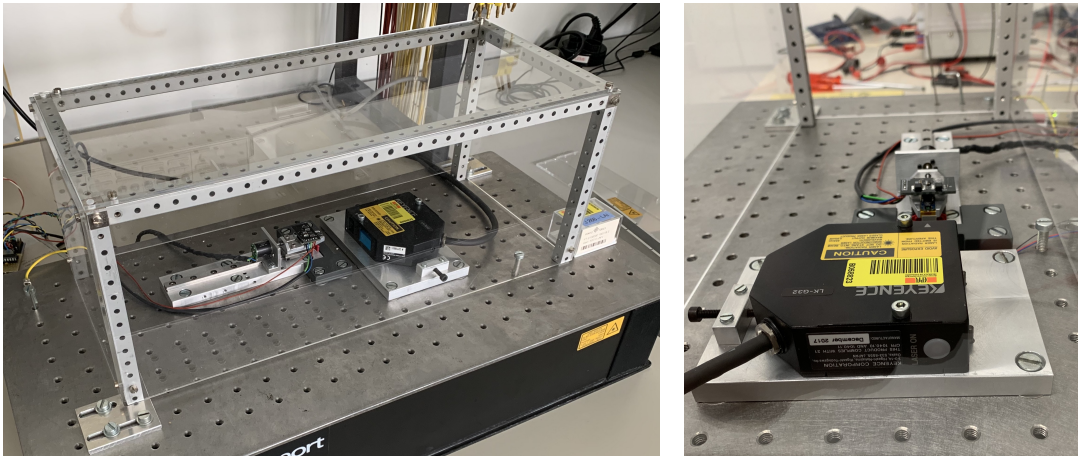


Figure C.3 – Photos of the enclosure surrounding the prototype.

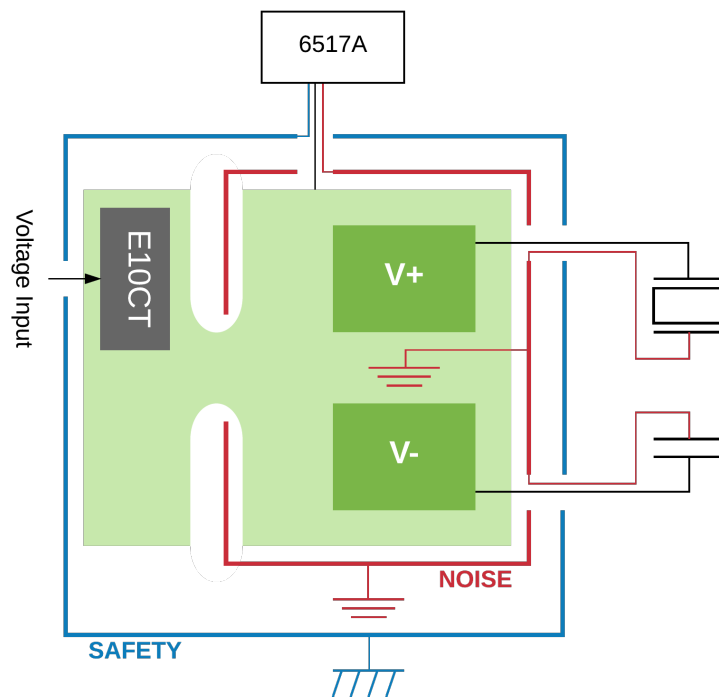


Figure C.4 – Schematic of the double shielding for the electronics.

Bibliography

- [1] Badel, A., Qiu, J., and Nakano, T. (2008). Self-sensing force control of a piezoelectric actuator. *IEEE Transactions on Ultrasonics, Ferroelectrics, and Frequency Control*, 55(12):2571–2581.
- [2] Badel, A., Qiu, J., Sebald, G., and Guyomar, D. (2008). Self-sensing high speed controller for piezoelectric actuator. *Journal of Intelligent Material Systems and Structures*, 19(3):395–405.
- [3] Bleuler, H., Clavel, R., Baur, C., Bouri, M., Kral, M., and Henein, S. (2009). *Robotique et Microrobotique*. Presses Polytechniques et Universitaires Romandes, Lausanne, Suisse, polycopié - septembre 2009 edition.
- [4] Borutzky, W. (2010). *Bond graph methodology: development and analysis of multidisciplinary dynamic system models*. Springer, London. ISBN: 978-1-84882-881-0.
- [5] Burkart, I., Klocke, V., and Maynicke, E. (2014). The Nanoworkbench: Automated Nanorobotic system inside of scanning electron or focused ion beam microscopes. In *Nano/Micro Engineered and Molecular Systems (NEMS), 2014 9th IEEE International Conference on*, pages 89–92. IEEE.
- [6] Chee Khiang Pang, Guoxiao Guo, Chen, B., and Tong Heng Lee (2006). Self-sensing actuation for nanopositioning and active-mode damping in dual-stage HDDs. volume 11, pages 328–338.
- [7] Clévy, C., Rakotondrabe, M., and Chaillet, N., editors (2011). *Signal Measurement and Estimation Techniques for Micro and Nanotechnology*. Springer New York, New York, NY.
- [8] Copt, F. L. (2018). *Integrated approach for auto-adaptive synchronous motor winding*. PhD thesis. Thèse 8903.
- [9] Coulon, F. d. and Jufer, M. (2006). *Introduction à l'électrotechnique: Traité d'Electricité volume I*. Presses Polytechniques et Universitaires Romandes. ISBN: 978-2-88914-213-2.
- [10] Dunsch, R. and Breguet, J.-M. (2007). Unified mechanical approach to piezoelectric bender modeling. *Sensors and Actuators A: Physical*, 134(2):436–446.

Bibliography

- [11] Fallahinia, N., Zareinejad, M., Talebi, H., and Ghafarirad, H. (2018). Robust Force Control of Piezoelectric Precision Positioning Actuators Using Self-Sensing Method. In *2018 IEEE/ASME International Conference on Advanced Intelligent Mechatronics (AIM)*, pages 533–538, Auckland, New Zealand. IEEE.
- [12] Fallahinia, N., Zareinejad, M., Talebi, H. A., and Ghafarirad, H. (2015). Robust control of piezoelectric micro positioning actuator using self-sensing method. In *Robotics and Mechatronics (ICROM), 2015 3rd RSI International Conference on*, pages 714–719. IEEE.
- [13] Flueckiger, M., Zogg, W., and Perriard, Y. (2010). Optimal design and sensorless position control of a piezoelectric motor integrated into a mechatronic cylinder lock. In *Energy Conversion Congress and Exposition (ECCE), 2010 IEEE*, pages 3428–3433. IEEE.
- [14] Flückiger, M. (2010). *Sensorless Position Control of Piezoelectric Ultrasonic Motors: a Mechatronic Design Approach*. PhD thesis, École Polytechnique Fédérale de Lausanne. Thèse 4752.
- [15] Gawthrop, P. and Smith, L. (1996). *Metamodelling: for bond graphs and dynamic systems*. Prentice Hall international series in systems and control engineering. Prentice Hall, London; New York. ISBN: 978-0-13-489824-7.
- [16] Grivon, D. (2017). *Design, Modelling and Sensing Possibilities of Magneto-Rheological Based Devices*. PhD thesis, École Polytechnique Fédérale de Lausanne, Lausanne. Thèse 7372.
- [17] Hagood, N. W. and Anderson, E. H. (1992). Simultaneous sensing and actuation using piezoelectric materials. In Ealey, M. A., editor, *Active and Adaptive Optical Components*, volume 1543, pages 409 – 421. International Society for Optics and Photonics, SPIE.
- [18] Henein, S. (2004). *Conception des guidages flexibles*. Presses polytechniques et universitaires romandes, Lausanne. ISBN: 978-2-88074-481-6.
- [19] Heywang, W., Lubitz, K., and Wersing, W., editors (2008). *Piezoelectricity: evolution and future of a technology*. Number 114 in Springer series in materials science. Springer, Berlin. ISBN: 978-3-540-68680-4.
- [20] Hooker, M. W. (1998). Properties of PZT-based piezoelectric ceramics between -150 and 250°C. Technical report, National Aeronautics and Space Administration (NASA), Langley Research Center.
- [21] Ikeda, H. and Morita, T. (2011). High-precision positioning using a self-sensing piezoelectric actuator control with a differential detection method. *Sensors and Actuators A: Physical*, 170(1-2):147–155.
- [22] Islam, M., Seethaler, R., and Mumford, D. (2011). Hysteresis independent on-line capacitance measurement for piezoelectric stack actuators. In *Electrical and Computer Engineering (CCECE), 2011 24th Canadian Conference on*, pages 001149–001153. IEEE.

-
- [23] Islam, M. N. and Seethaler, R. J. (2011). Identification of constitutive parameters for piezo stack actuators based on online capacitance measurements. In *ASME 2011 International Design Engineering Technical Conferences and Computers and Information in Engineering Conference*, pages 457–463. American Society of Mechanical Engineers.
- [24] Islam, M. N. and Seethaler, R. J. (2014). Sensorless Position Control For Piezoelectric Actuators Using A Hybrid Position Observer. *IEEE/ASME Transactions on Mechatronics*, 19(2):667–675.
- [25] Ivan, I. A., Aljanaideh, O., Agnus, J., Lutz, P., and Rakotondrabe, M. (2017). Quasi-Static Displacement Self-Sensing Measurement for a 2-DOF Piezoelectric Cantilevered Actuator. *IEEE Transactions on Industrial Electronics*, 64(8):6330–6337.
- [26] Ivan, I. A., Rakotondrabe, M., Lutz, P., and Chaillet, N. (2009a). Current integration force and displacement self-sensing method for cantilevered piezoelectric actuators. *Review of Scientific Instruments*, 80(12):126103.
- [27] Ivan, I. A., Rakotondrabe, M., Lutz, P., and Nicolas Chaillet (2009b). Quasistatic displacement self-sensing method for cantilevered piezoelectric actuators. *Review of Scientific Instruments*, 80(6):065102.
- [28] Ivanov, A., Masson, L., Rossi, S., Belloni, F., Wiesendanger, R., Gass, V., Rothacher, M., Hollenstein, C., Männel, B., Fleischmann, P., Mathis, H., Klaper, M., Joss, M., and Styger, E. (2014). Cubeth: low cost gnss space experiment for precise orbit determination. page 13. The 4S Symposium.
- [29] Ivanov, A. B., Masson, L., and Belloni, F. (2016). Operation of a concurrent design facility for university projects. In *2016 IEEE Aerospace Conference*, pages 1–9. IEEE.
- [30] Ivanov, A. B., Masson, L., Rossi, S., Belloni, F., Mullin, N., Wiesendanger, R., Rothacher, M., Hollenstein, C., Mannel, B., Willi, D., et al. (2015). Cubeth: Nano-satellite mission for orbit and attitude determination using low-cost gnss receivers. In *66th International Astronautical Congress. Jerusalem, Israel: International Astronautical Federation, IAF*.
- [31] J. J. Dosch, Inman, D. J., and Garcia, E. (1992). A Self-Sensing Piezoelectric Actuator for Collocated Control. *Journal of Intelligent Material Systems and Structures*, 3(1):166–185.
- [32] Jones, L., Garcia, E., and Waites, H. (1994). Self-sensing control as applied to a PZT stack actuator used as a micropositioner. *Smart Materials and Structures*, 3(2):147–156.
- [33] Karnopp, D., Margolis, D. L., and Rosenberg, R. C. (2012). *System dynamics: modeling, simulation, and control of mechatronic systems*. Wiley, Hoboken, NJ, 5th edition. ISBN: 978-1-118-15281-2.
- [34] Klocke, V. and Jones, G. (2011). The SEM/FIB workbench: Automated nanorobotics system inside of scanning electron or focussed ion beam microscopes. In *2011 11th IEEE International Conference on Nanotechnology*, pages 1510–1515.

Bibliography

- [35] Mansour, S. Z. and Seethaler, R. J. (2017). Simultaneous Displacement and Force Estimation of Piezoelectric Stack Actuators Using Charge and Voltage Measurements. *IEEE/ASME Transactions on Mechatronics*, 22(6):2619–2624.
- [36] Masson, L., Civet, Y., Germano, P., and Perriard, Y. (2017). Design of a generalised charge-based self-sensing model for quasi-static piezoelectric actuators. In *2017 20th International Conference on Electrical Machines and Systems (ICEMS)*, pages 1–6, Sydney, Australia. IEEE.
- [37] Masson, L. and Perriard, Y. (2019a). Improved modelling of a monomorph piezoelectric actuator for linear self-sensing applications. In *2019 12th International Symposium on Linear Drives for Industry Applications (LDIA)*, pages 1–6, Neuchatel, Switzerland. IEEE.
- [38] Masson, L. and Perriard, Y. (2019b). Multi-objective optimisation methodology for self-sensing piezoelectric monomorph benders. In *2019 12th International Symposium on Linear Drives for Industry Applications (LDIA)*, pages 1–6, Neuchatel, Switzerland. IEEE.
- [39] Masson, L. and Perriard, Y. (2019c). Study of self-sensing actuation strategies for quasi-static piezoelectric actuators. In *2019 22nd International Conference on Electrical Machines and Systems (ICEMS)*, pages 1–5, Harbin, China. IEEE.
- [40] Masson, L., Ren, X., and Perriard, Y. (2019a). Novel test environment for the development of self-sensing piezoelectric actuators. In *2019 22nd International Conference on Electrical Machines and Systems (ICEMS)*, pages 1–5, Harbin, China. IEEE.
- [41] Masson, L., Xinchang, L., and Perriard, Y. (2018). Design of an Optimized Self-Sensing Piezoelectric Cantilever for Micro-Robotic Applications. In *2018 International Conference on Manipulation, Automation and Robotics at Small Scales (MARSS)*, pages 1–6, Nagoya. IEEE.
- [42] Masson, L., Xinchang, L., and Perriard, Y. (2019b). An optimized self-sensing piezoelectric cantilever for micro-robotic applications. *Journal of Micro-Bio Robotics*, 15(2):91–103.
- [43] McPherson, T. and Ueda, J. (2011). Piezoelectric self-sensing technique for tweezer style end-effector. In *2011 IEEE/RSJ International Conference on Intelligent Robots and Systems*, pages 1940–1945.
- [44] McPherson, T. and Ueda, J. (2014). A Force and Displacement Self-Sensing Piezoelectric MRI-Compatible Tweezer End Effector With an On-Site Calibration Procedure. *IEEE/ASME Transactions on Mechatronics*, 19(2):755–764.
- [45] Micky Rakotondrabe (2013). Combining self-sensing with an unknown-input-observer to estimate the displacement, the force and the state in piezoelectric cantilevered actuators. In *American Control Conference (ACC), 2013*, pages 4516–4523. IEEE.
- [46] Micky Rakotondrabe, Ivan, I. A., Khadraoui, S., Lutz, P., and Chaillet, N. (2015). Simultaneous Displacement/Force Self-Sensing in Piezoelectric Actuators and Applications to Robust Control. *IEEE/ASME Transactions on Mechatronics*, 20(2):519–531.

-
- [47] Pedro, M.-E. d., Gmür, T., and Botsis, I. (2012). *Introduction à la mécanique des solides et des structures*. Presses Polytechniques et Universitaires Romandes, Lausanne. ISBN: 978-2-88074-979-8.
- [48] Putra, A. S., Huang, S., Tan, K. K., Panda, S. K., and Lee, T. H. (2008). Self-Sensing Actuation With Adaptive Control in Applications With Switching Trajectory. *IEEE/ASME Transactions on Mechatronics*, 13(1):104–111.
- [49] Péclat, C. (1995). *Conception et Réalisation d'un Micromoteur Piézoélectrique*. PhD thesis, École Polytechnique Fédérale de Lausanne. Thèse 1434.
- [50] Péclat, C. and Trumpy, K. (1998). Piezoelectric motor having an arrangement which provides information relative to the rotor position and/or the rotor's number of revolutions.
- [51] Rakotondrabe, M., Clévy, C., and Lutz, P. (2010). Complete Open Loop Control of Hysteretic, Creeped, and Oscillating Piezoelectric Cantilevers. *IEEE Transactions on Automation Science and Engineering*, 7(3):440–450.
- [52] Rakotondrabe, M., Ivan, I. A., Khadraoui, S., Cleve, C., Lutz, P., and Chaillet, N. (2010). Dynamic displacement self-sensing and robust control of cantilever piezoelectric actuators dedicated for microassembly. In *2010 IEEE/ASME International Conference on Advanced Intelligent Mechatronics*, pages 557–562.
- [53] Rodriguez-Fortun, J., Orus, J., Buil, F., and Castellanos, J. (2010). General bond graph model for piezoelectric actuators and methodology for experimental identification. *Mechatronics*, 20(2):303–314.
- [54] Saigusa, K. and Morita, T. (2015). Self-sensing control of piezoelectric positioning stage by detecting permittivity. *Sensors and Actuators A: Physical*, 226:76–80.
- [55] Scaglione, O. (2013). *Iron Hysteresis and Enhanced Kalman Filtering for Sensorless Position Detection of Synchronous Motors*. PhD thesis, École Polytechnique Fédérale de Lausanne. Thèse 5630.
- [56] Suzuki, K., Chee, S. K., and Morita, T. (2018). Self-sensing grasping with piezoelectric manipulator. In *ACTUATOR 2018; 16th International Conference on New Actuators*, pages 1–3.
- [57] Takigami, T., Oshima, K., Hayakawa, Y., and Ito, M. (1998). Application of self-sensing actuator to control of a soft-handling gripper. In *Proceedings of the 1998 IEEE International Conference on Control Applications (Cat. No.98CH36104)*, volume 2, pages 902–906 vol.2.
- [58] Tichý, J., Erhart, J., Kittinger, E., and Přívratská, J. (2010). *Fundamentals of Piezoelectric Sensorics*. Springer Berlin Heidelberg, Berlin, Heidelberg. ISBN: 978-3-540-43966-0.
- [59] Yan Liang Zhang, Changhai Ru, Brandon K. Chen, and Yu Sun (2011). A Load-Lock-Compatible Nanomanipulation System for Scanning Electron Microscope. Technical report.

Bibliography

- [60] Yeh, T.-J., Ruo-Feng, H., and Shin-Wen, L. (2008). An integrated physical model that characterizes creep and hysteresis in piezoelectric actuators. *Simulation Modelling Practice and Theory*, 16(1):93–110.
- [61] Yusuke Ishikiriyama and Takeshi Morita (2010). Improvement of Self-sensing Piezoelectric Actuator Control Using Permittivity Change Detection. *Journal of Advanced Mechanical Design, Systems, and Manufacturing*, 4(1):143 – 149.

Nomenclature

Acronyms

<i>Symbol</i>	<i>Description</i>
BGM	Bond Graph Model
BM	Bridge Measurement (self-sensing)
CM	Charge Measurement (self-sensing)
FFT	Fast Fourier Transform
HPF	High-Pass Filter
LPF	Low-Pass Filter
LTI	Linear Time Invariant
MEMS	Microelectromechanical Systems
MRI	Magnetic Resonance Imaging
OA	Operational Amplifier
MCU	Micro-Controller Unit
MOO	Multi-Objective Optimisation
PLL	Phase-Locked Loop
PUM	Piezoelectric Ultrasonic Motor
PZT	Lead-Zirconate Titanate (piezoceramic material)
SEM	Scanning Electron Microscope
SMU	Source Meter Unit
SNR	Signal-to-Noise Ratio
SSA	Self-Sensing Actuation
UIO	Unknown-Input Observer

List of symbols

<i>Symbol</i>	<i>Unit</i>	<i>Description</i>
β	CN^{-1}	Charge accumulation coefficient
	mV^{-1}	Electro-mechanical conversion coefficient
γ_m	m	Position of the mechanical deformation neutral plane
γ_p	m	Position of the piezoelectric deformation neutral plane
δ	m	Actuator displacement
δ_0	m	Initial distance between end effector and sample
δ_m	m	Mechanically induced displacement
δ_p	m	Piezoelectrically induced displacement
η	(%)	Active thickness ratio
η_e	(%)	Electrode layers thickness ratio
η_i	(%)	Inactive layers thickness ratio
ϵ_δ	m	Displacement estimation error
ϵ_f	N	Force accuracy objective function (MOO)
ϵ_F	N	Force estimation error
ϵ_{ij}	F m^{-1}	Element of the permittivity matrix
ϵ_m	m^{-1}	Slope of the mechanically induced strain
ϵ_p	m^{-1}	Slope of the piezoelectrically induced strain
μ	(%)	Ratio between layer thickness and electrode thickness
ρ	$\Omega \text{ m}$	Resistivity
τ	s	Experiment duration
C_d	F	Difference in capacitance between C_p and C_r
C_i	F	Integration capacitor of the charge amplifier
C_p	F	Piezoelectric capacitance
C_r	F	Reference capacitor of the charge amplifier
d_{ij}	CN^{-1}	Element of the piezoelectric coefficient tensor
D	C m^{-2}	Electric displacement field
e	–	Effort power conjugated variable (multi-physics)
E	Vm^{-1}	Electric field

f	–	Flow power conjugated variable (multi-physics)
f_β	CN ⁻¹	Force sensitivity objective function (MOO)
F	N	Mechanical force
F_{ext}	N	External mechanical force
F_{int}	N	Internal mechanical force
h	m	Layer thickness for the actuator stack
h_e	m	Electrode thickness
H	m	Total thickness of the actuator stack
H_{min}	m	Minimum total thickness of the actuator stack
i	A	Instantaneous current
I	kgm ²	Moment of inertia
i_b	A	Bias current
K	Nm ⁻¹	Stiffness
L	m	Cantilever length
M_{ext}	Nm	External mechanical moment
M_{int}	Nm	Internal mechanical moment
N	–	Number of layers in the actuator stack
N_{min}	–	Minimum number of layers in the actuator stack
p	–	Generalised momentum (multi-physics)
P	Cm ⁻²	Electric polarisation field
q	–	Generalised displacement (multi-physics)
Q	C	Free charges
Q_e	C	Electrical component of the accumulated charges
Q_p	C	Mechanical component of the accumulated charges
Q_r	C	Free charges accumulated by the reference capacitor
\dot{Q}	A	Piezoelectric actuator instantaneous current
R_L	Ω	Leakage resistance
s_{ij}	m ² N ⁻¹	Element of the compliance tensor
S	(%)	Mechanical strain
$S_{1,m}$	(%)	Mechanically induced strain

Nomenclature

$S_{1,p}$	(%)	Piezoelectrically induced strain
T	Nm^{-2}	Mechanical stress
V_{in}	V	Actuator input voltage
V_p	V	Direct piezoelectric effect voltage
V_Q	V	Output voltage of the charge amplifier
V_s	V	Measurement bridge sensing voltage
w	m	Cantilever width

Curriculum Vitae

Louis Masson

Born December 12th, 1990

Dutch, French, and Swiss Citizen

louis@lesmasson.com

Professional experience

- 12.2015 – 07.2020 **École Polytechnique Fédérale de Lausanne, Lausanne,**
PhD student of the Robotics, Control and Intelligent Systems doctoral school, and doctoral assistant of the Integrated Actuators Laboratory.
- 10.2013 – 09.2015 **Swiss Space Center, Lausanne,**
Scientific assistant endorsing systems engineering and embedded software engineering roles for multiple satellite projects, in addition to teaching assistant duties.

Education

- 2016 – 2020 **Ph.D. thesis, Integrated Actuators Laboratory (LAI), EPFL**
Doctoral School of Robotics, Control, and Intelligent Systems (EDRS)
- 2008 – 2013 **M.Sc in Microengineering, École Polytechnique Fédérale de Lausanne,**
Master Project: Development of the Command and Data Management Sub-system (CDMS) for the CubETH microsatellite.
- 2005 – 2008 **Baccalauréat Scientifique, Lycée français de La Haye,**
Mention TB, Section Européenne.

Nomenclature

Journal Articles

- Masson, L., Xinchang, L., and Perriard, Y. (2019b). An optimized self-sensing piezoelectric cantilever for micro-robotic applications. *Journal of Micro-Bio Robotics*, 15(2):91–103

Conference Publications

- Masson, L. and Perriard, Y. (2019b). Multi-objective optimisation methodology for self-sensing piezoelectric monomorph benders. In *2019 12th International Symposium on Linear Drives for Industry Applications (LDIA)*, pages 1–6, Neuchatel, Switzerland. IEEE
- Masson, L. and Perriard, Y. (2019a). Improved modelling of a monomorph piezoelectric actuator for linear self-sensing applications. In *2019 12th International Symposium on Linear Drives for Industry Applications (LDIA)*, pages 1–6, Neuchatel, Switzerland. IEEE
- Masson, L., Ren, X., and Perriard, Y. (2019a). Novel test environment for the development of self-sensing piezoelectric actuators. In *2019 22nd International Conference on Electrical Machines and Systems (ICEMS)*, pages 1–5, Harbin, China. IEEE
- Masson, L. and Perriard, Y. (2019c). Study of self-sensing actuation strategies for quasi-static piezoelectric actuators. In *2019 22nd International Conference on Electrical Machines and Systems (ICEMS)*, pages 1–5, Harbin, China. IEEE
- Masson, L., Xinchang, L., and Perriard, Y. (2018). Design of an Optimized Self-Sensing Piezoelectric Cantilever for Micro-Robotic Applications. In *2018 International Conference on Manipulation, Automation and Robotics at Small Scales (MARSS)*, pages 1–6, Nagoya. IEEE
- Masson, L., Civet, Y., Germano, P., and Perriard, Y. (2017). Design of a generalised charge-based self-sensing model for quasi-static piezoelectric actuators. In *2017 20th International Conference on Electrical Machines and Systems (ICEMS)*, pages 1–6, Sydney, Australia. IEEE
- Ivanov, A. B., Masson, L., and Belloni, F. (2016). Operation of a concurrent design facility for university projects. In *2016 IEEE Aerospace Conference*, pages 1–9. IEEE
- Ivanov, A. B., Masson, L., Rossi, S., Belloni, F., Mullin, N., Wiesendanger, R., Rothacher, M., Hollenstein, C., Mannel, B., Willi, D., et al. (2015). Cubeth: Nano-satellite mission for orbit and attitude determination using low-cost gnss receivers. In *66th International Astronautical Congress. Jerusalem, Israel: International Astronautical Federation, IAF*
- Ivanov, A., Masson, L., Rossi, S., Belloni, F., Wiesendanger, R., Gass, V., Rothacher, M., Hollenstein, C., Mannel, B., Fleischmann, P., Mathis, H., Klaper, M., Joss, M., and Styger, E. (2014). Cubeth: low cost gnss space experiment for precise orbit determination. page 13. The 4S Symposium